MICROFLUIDIC DEVICES FOR ACCESIBLE MEDICAL DIAGNOSTICS

Thesis by

George Manuel Maltezos

In Partial Fulfillment of the Requirements for the Degree of Doctor of Philosophy

California Institute of Technology
Pasadena, California
2006
(Defended November 20th, 2006)

There are easily over a hundred people who helped me write this thesis, I will try to thank them individually and dedicate this book to my wife and family who contributed in the most important ways.

Introduction

This thesis covers a wide array of topics, all focused on technologies which are the core elements of future diagnostic devices that will cheaply, simply, and quickly monitor patient status in order to deliver better patient outcomes. The addition of massive amounts of microfluidically captured data to the medical decision-making process will bring precision to the art of medical decision making.

Pandemic prevention is the most pressing need for this technology, however the greatest promise for accessible microfluidic diagnostic devices is that it allows data to be collected and shared on a large scale with little cost or trauma. Doctors and patients will be able to monitor proteins on even a daily basis in order to evaluate treatments, causes, and effects. If networked, this ability on a global scale could lead to a functioning planetary immune system in which patient data is shared in order to make better medical decisions.

Abstract

This thesis covers devices exploring basic areas of physical and biological research including: surface plasmon enhanced InGaN light-emitting diode, analysis of using AlGaN emitters coupled with thin film heaters to cure onychomycosis infections, tunable organic transistors that use microfluidic source and drain electrodes, as well as an electrical microfluidic pressure gauge for PDMS MEMS. Also analyzed are devices created through the use of novel three-dimensional rapid prototyping techniques, such as: the replication of three-dimensional valves from printed wax molds, chemically robust three-dimensional monolithic SIFEL fluoropolymer microfluidics, microfluidic valves for customized radioactive positron emission dyes, reduction of microfluidic control inputs through the use of pressure multiplexing, bicuspid-inspired microfluidic check valves and microfluidic three-dimensional separation column. Devices created to analyze blood are also treated including: a microfluidic device to extract blood plasma from a finger-stick; inexpensive, portable immunoassay devices and their use in in small cell lung carcinoma and multiple sclerosis; as well as a device to screen metastasizing cancer cells. Devices created to perform polymerase chain reactions are also studied, including: an evaporative cooler for microfluidic channels, thermal management in microfluidics using micro-Peltier junctions in a microfluidic polymerase

chain reaction system, and an accessible polymerase chain reaction system.

Table of Contents

Summary

I. Devices exploring basic areas of physical and biological research

This section deals with projects exploring new areas of nanofabrication, fungal infections, and basic microfluidic devices.

1. Surface plasmon enhanced InGaN light-emitting diode

We report a dramatic increase in the photoluminescence (PL) emitted from InGaN/GaN quantum wells (QW), obtained by covering these sample surfaces with thin metallic films. Remarkable enhancements of PL peak intensities were obtained from $In_{0.3}Ga_{0.7}N$ QWs with 50 nm thick silver and aluminum coating with 10 nm GaN spacers. These PL enhancements can be attributed to strong interaction between QWs and surface plasmons (SPs). No such enhancements were obtained from samples coated with gold, as its well-known plasmon resonance occurs only at longer wavelengths. We also showed that QW-SP coupling increases the internal quantum efficiencies ($\bullet_{int}$) by measuring the temperature dependence of PL intensities. QW-SP coupling is a very

promising method for developing the super-bright light-emitting diodes (LEDs). Moreover, we found that the metal nano-structure is very important fact in deciding the light extraction. A possible mechanism of QW-SP coupling and emission enhancement has been developed, and high-speed and efficient light emission is predicted for optically, as well as electrically, pumped light emitters.

2. Analysis of using AlGaN emitters coupled with thin film heaters to cure onychomycosis infections

This is a description of work that is still ongoing in which the sensitivity of fungi that cause onychomycosis to ultraviolet radiation from AlGaN emitters and thin film heaters is explored. The recent commercial availability of AlGaN LEDs has made light and heat treatment a possibility for the 30 million Americans who suffer from this disease.

3. Tunable organic transistors that use microfluidic source and drain electrodes

This chapter describes a type of transistor that uses conducting fluidic source and drain electrodes of mercury which flow on top of a thin film of the organic

semiconductor pentacene. Pumping the mercury through suitably designed microchannels changes the width of the transistor channel and, therefore, the electrical characteristics of the device. Measurements on transistors with a range of channel lengths reveal low contact resistances between mercury and pentacene. Data collected before, during, and after pumping the mercury through the microchannels demonstrate reversible and systematic tuning of the devices. This unusual type of organic transistor has the potential to be useful in plastic microfluidic devices that require active elements for pumps, sensors, or other components. It also represents a noninvasive way to build transistor test structures that incorporate certain classes of chemically and mechanically fragile organic semiconductors.

4. Electrical Microfluidic Pressure Gauge for PDMS MEMS

The first electrical microfluidic pressure sensor is presented herein. An electrolyte-filled valved microchannel in a PDMS (polydimethylsiloxane) chip experiences a drastic increase in electrical resistance when and only when it is completely pinched off by the microvalve. This in effect establishes a 1-1 correspondence between electrical resistance (low or

high) and valve status (open or closed), thereby providing an electrical means of reporting valve status.

Valve status (open or closed) is determined by applied pressure being below or above the characteristic closing pressure of the valve; therefore, the valve reports an upper or lower bound for the applied pressure, respectively. An array of such valves of varying closing pressures reports a set of inequalities that produce an interval estimate for the pressure. That estimate is reported as a set of resistance values of the respective microchannels, due to the 1-1 correspondence above. Hence, the overall system acts as an electrical microfluidic pressure gauge. This sensor would form a useful subunit within PDMS MEMS (micro-electro-mechanical systems), e.g., by reporting pressure values to electrical feedback control loops.

II. Devices created through the use of novel three-dimensional rapid prototyping techniques

This section deals with devices created through the three dimensional microfluidic “lost wax” process developed at Caltech. A number of previously impossible or very difficult problems were solved, including high-pressure microfluidic valving, fluorinated microfluidics for chemical resistivity

(including to radioactive compounds), novel check valves, and microfluidic separation columns.

1. Replication of three-dimensional valves from printed wax molds

We describe microfluidic vias, channels, and valves fabricated by replication molding of polydimethylsilicone (PDMS) into printed wax molds. Additionally we show how completely polymer-embedded microfluidic circuits can be realized with this technique. A novel three-dimensional microfluidic valve is also demonstrated, which is robust against swelling and which operates at up to 30 psi flow pressure. This method for defining microfluidic devices offers higher pressure tolerance and more resistance to corrosive solvents, as delamination problems can be avoided. It also enables a great flexibility in choice the of replicated polymers and three-dimensional interconnection topologies in forming complex microfluidic circuits for microbiochemical analysis.

2. Chemically robust three-dimensional monolithic SIFEL fluoropolymer microfluidics

The three-dimensional nature of the “lost wax” valves allows fluoropolymers such as SIFEL to be used as

valves for microfluidics. This is important because PDMS, the standard polymer used for microfluidics, cannot be used with most organic solvents – putting the most interesting applications of microfluidics out of reach of the current technologies. Sifel microfluidics will allow a wider range of solvents and reactions to be performed in microfluidics.

3. Microfluidic valves for customized radioactive positron emission dyes

The “lost wax” process was used to create specialized chips and newly designed, chemically robust, high-pressure microfluidic valves for making radioactive positron emission dyes. This is important because these species typically have very short half-lives, meaning that all PET scan machines must be within a certain time-distance from a central manufacturing site. In turn this causes the central plant to only produce the standard dye, even though researchers have been able to create target-specific dyes for use in more informative diagnostics. The development of local capacity to create dye as needed in a microfluidic device would also easily be able to make the more specific dyes in order to improve patient outcomes.

4. Reducing Microfluidic Control Inputs Through the Use of Pressure Multiplexing

An important problem in microfluidics is reducing the number of input pins needed to control as many valves as possible. Each input pin takes up space on the chip and requires a leak-free connection to outside plumbing and large control valves. Using our new three-dimensional valves created by rapid prototyping we were able to conceive of and prove a new system of pressure multiplexing that can greatly reduce the number of needed inputs beyond the previously reported minimum of controlling n valves with $2 \log_2 n$ inputs. We were able to control n valves with $2 \log_{24} n$ inputs. Furthermore, our pressure multiplexing technique is general and can be applied to standard 2D microfluidics. Minimizing the number of control inputs is extremely important in creating simplified and more robust microfluidic chips for practical purposes.

5. Bicuspid-inspired microfluidic check valve

Complicated “check valves” can be made using the “lost wax” process which mimic the operation of the heart’s valves. These one-way valves promise to be a robust check valve for an electrically operated microfluidic valve. All of the variables for making these complex

three-dimensional valves are analyzed and a one input pump is demonstrated, as opposed to the three normally required for traditional peristaltic microfluidic pumps.

6. Microfluidic Three-Dimensional separation column

The three dimensional rapid prototyping machine is used to create microfluidic separation columns. Silica is poured into a tall vertical column and sodium silicate is used to form the frit. These columns can be easily made in parallel and complex combinatorial chemical reactions can be carried out with the products being purified simultaneously.

III. Devices created to analyze blood

This section deals with microfluidic devices that process whole blood from a fingerprick and analyzes for various different proteins

1. Microfluidic Device to extract Blood Plasma from a finger stick

With the increased use of microfluidic technology in the fields of physics, chemistry, engineering, biotechnology, and especially medicine, it has become

increasingly more important to discover more viable and more efficient means through which to incorporate existing technology into a microfluidic context. One such example is the analysis of blood through microfluidics. For the practical application of microfluidic analysis, it is necessary to create a system of blood filtration and anti-coagulation, a procedural practice necessary for microscale whole-blood analysis.

In the context of microfluidic blood analysis, the system of blood filtration and anti-coagulation is necessary to handle blood samples in a miniaturized format. That is to say, there must be a way to separate blood cells and plasma from whole blood, on a microfluidic scale, for proper microfluidic blood analysis.

2. Inexpensive, portable immunoassay device

We have developed an inexpensive and rapid read-out system for multi-antigen microfluidic fluorescence immunoassay systems. The fluidic analysis chips can be fabricated in polydimethylsiloxane PDMS, and have been shown to perform high-throughput analysis on multiple analytes and manage the measurement of over 100 fluorescent readings with sensitive detection down to .01mg/ml concentrations. In a fluorescence assay, the

intensity of fluorescence is used to read the concentration of the antigen, and is typically measured with a fluorescence microscope or a laser scanner. This serial measurement process is both time-consuming and expensive, and limits the speed with which an immuno-assay can be completed. Here we show that it is possible to perform fluorescence detection with digital imaging to obtain multiple immunoassay readings in parallel.

a. Use in small cell lung carcinoma

Here we describe the application of a microfluidic fluorescent noncompetitive immunoassay system for the detection of the CRMP5 protein, a marker for SCLC (Small Cell Lung Carcinoma), and the miniaturization of the detector. Using monoclonal rat antibodies, an immunoassay stack specific to the CRMP5 marker was built and tested for specificity and sensitivity. A microfluidic filter able to separate serum from blood allowed for tests to examine marked blood. A detector consisting of an excitation and emission filter set, lens, LED, and CCD digital camera replaced bulkier optical microscope detectors and allowed for images to be taken simultaneously off all chambers in the microfluidic device. By achieving appropriate signal to noise ratios with

the miniaturized detector and using the immunoassay chip in tandem with microfluidic blood filters we approach cost-efficient handheld devices capable of detecting SCLC with high specificity and sensitivity.

b. Use in multiple sclerosis

Recent advances in microfluidics have allowed for the fabrication of miniaturized, highly efficient immunoassay chips that minimize the quantities of reagent and patient serum needed for disease detection. This technology is especially applicable for detection and diagnosis of multiple sclerosis (MS), a debilitating auto-immune disease. We were able to demonstrate disease detection by identifying matrix metalloproteinase 9 (MMP-9), a biomarker for MS, in simulated patient serum. This is a proof-of-concept for the viability of a handheld multiple sclerosis symptom detector. Such a detector could prove invaluable in the treatment of this disease. Multiple sclerosis is a disease that progresses through a series of excacerbations. If these excacerbations can be predicted through constant monitoring of blood species, treatments can be developed for use at the onset of MS attacks in order to minimize or eliminate the damage caused by the attack.

3. Device to screen metastasizing cancer cells

With nanofabricated microfluidic systems, we studied the migration behaviors of two cell lines *in vitro*. Cells were allowed to migrate through areas of 15 µm in height, containing a microfluidic channel of 15 µm (height) by 15 µm (width) and 45 µm to 1cm in length. We observed that cells left their monolayer origin as individual cells to enter the entrance of the channel. After migration through the channel, the daughter cells resulting from the first division migrated away from each other to form two colonies. When each of the two colonies expanded into 32-cell colonies, the colonies disassociated into multiple small colonies. Our results indicate that cells can break off from the monolayer to actively search their environment, and the dissociation of cells from each other is highly regulated. Future gene expression profiling study on cells prior and post disassociation should reveal genes that regulate the disassociation of cells from the monolayer. These genes are potential candidate genes which regulate cancer cells to leave the original tumor and become the metastasis. We demonstrated here that a microfluidic system can be a powerful means to study genes that regulate cell disassociation, which is a first step of cancer metastasis. Our system can be easily converted

to an inexpensive high throughput device to screen drugs for inhibiting metastasis in the pharmaceutical industry.

IV. Devices created to perform polymerase chain reactions

This section deals with temperature control in microfluidics and its use in PCR

1. Evaporative cooling in microfluidic channels

Evaporative cooling is an effective and energy efficient way to rapidly remove heat from a system. Specifically, evaporative cooling in microfluidic channels can provide a cost-effective solution for the cooling of electronic devices and chemical reactors. Here we present microfluidic devices fabricated by using soft-lithography techniques to form simple fluidic junctions between channels carrying refrigerant and channels carrying N2 gas. The effects of channel geometry and delivery pressure on the performance of refrigeration through vaporization of acetone, isopropyl alcohol, and ethyl ether were characterized. By varying gas inlet pressures, refrigerants, and angles of the microfluidic junctions, optimal cooling conditions were found. Refrigeration rates in excess of 40 °C/s were measured, and long lasting subzero cooling in the junction could be observed.

2. Thermal management in microfluidics using micro-Peltier junctions

We report refrigeration and heating of nanoliter fluid volumes with micro-Peltier junctions. The temperature of small liquid reservoirs can be rapidly changed and controlled within a range between −3 °C to over 120 °C with good long-term stability. These thermal management systems enable the fabrication of complex chip-based chemical and biochemical reaction systems in which the temperature of many processes can be controlled independently.

3. Microfluidic Polymerase Chain Reaction

We implement Microfluidic technology to miniaturize a thermal cycling system for amplifying DNA fragments. By combining microfluidic thermal heat exchanger to cool a Peltier junction, we have demonstrated very fast heating and cooling of small volumes of solution. We use a miniature K-type thermocouple to provide a means for in-situ sensing of the temperature inside the micro-refrigeration system. By combining the thermocouple, two power supplies controlled with a relay system, and computer automation, we reproduce the function of a commercial PCR thermal cycler and have

demonstrated amplification of a DNA sample of about 1000 bp.

4. Accessible Polymerase Chain Reaction

Since the mid-1990s, real-time polymerase chain reactions (PCR) have been used with selective primers to amplify and identify DNA and RNA molecules within large and expensive thermal cyclers. Recently, it has become possible to build compact heating and cooling systems for the amplification of DNA with greater accuracy at a 100 times lower cost. Such inexpensive PCR identification could serve remote regions of the world, leading to an early warning system for pandemic outbreaks. Here we compare a portable PCR system with a conventional desk-top unit. We show that H5N1 (avian influenza) and HIV (AIDS), as well as many other common virus strains can be identified within a clinical setting at low viral loads. Our portable instrument results in superior amplification as more precise temperature control is possible. This improvement in performance also enables the use of less expensive intercalating dyes as fluorescent probes, further reducing the cost of PCR tests.

I

Devices exploring basic areas of physical and biological research

1. Surface plasmon enhanced InGaN light emitting diode

ABSTRACT

We report a dramatic increase in the photoluminescence (PL) emitted from InGaN/GaN quantum wells (QW), obtained by covering these sample surface with thin metallic films. Remarkable enhancements of PL peak intensities were obtained from $In_{0.3}Ga_{0.7}N$ QWs with 50 nm thick silver and aluminum coating with 10 nm GaN spacer. These PL enhancements can be attributed to strong interaction between QWs and surface plasmons (SPs). No such enhancements were obtained from samples coated with gold, as its well-known plasmon resonance occurs only at longer wavelengths. We also showed that QW-SP coupling increase the internal quantum efficiencies ($\bullet_{int}$) by measuring the temperature dependence of PL intensities. QW-SP coupling is a very promising method for developing the super bright light emitting diodes (LEDs). Moreover, we found that the metal nano-structure is very important facto to decide the light extraction. A possible mechanism of QW-SP coupling and emission enhancement has been developed, and high-speed and efficient light emission is predicted for optically as well as electrically pumped light emitters.

1. INTRODUCTION

Since 1993, InGaN quantum wells (QW)-based light emitting diodes (LEDs) have been continuously improved and commercialized as light sources in the ultraviolet and

visible spectral regions.[1-3] Moreover, white light LEDs, in which a blue LED is combined with a yellow phosphor, have been commercialized and offer a replacement for conventional incandescent and fluorescent light bulbs.[4] However, the promise of inexpensive solid state lighting has so far been delayed by the relatively poor extraction efficiency of light from semiconductor light sources. We believe that the development of efficient and bright white LEDs will rapidly result in commercialization of efficient solid state illumination sources. The most important requirement for a competitive LED for solid state ligthing is the development of new methods to increase its quantum efficiency of light emission.

The external quantum efficiency ($\bullet_{ext}$) of light emission from an LED is given by the light extraction efficiency (C_{ext}) and internal quantum efficiency ($\bullet_{int}$). $\bullet_{int}$ in turn is determined by the ratio of the radiative (k_{rad}) and nonradiative (k_{non}) recombination rates of carriers.

$$\eta_{ext} = C_{ext} \times \eta_{int} = C_{ext} \times \frac{k_{rad}}{k_{rad} + k_{non}} \quad (1)$$

Often, k_{non} is faster than k_{rad} at room temperature, resulting in modest $\bullet_{int}$. There are three methods to increase $\bullet_{ext}$; (1) increase C_{ext}, (2) decrease k_{non}, or (3) increase k_{rad}. Previous work has focused on improving C_{ext} from InGaN LEDs by using the patterned sapphire substrates and mesh electrodes.[5] However, further improvements of extraction of light through these methods are rapidly approaching fundamental

limitations. Although much effort has recently been placed into reducing k_{non} by growing higher quality crystals,[6-7] dramatic enhancements of $\bullet_{ext}$ have so far been elusive. [8-9] On the other hand, there have been very few studies focusing on increasing k_{rad},[10-11] though that could prove to be most effective for development of high $\bullet_{ext}$ light emitters. In this article, we propose the enhancement of k_{rad} by coupling between surface plasmon (SP) and the InGaN QWs. If the plasmon frequency is carefully selected to match the QW emission frequency, the increase of the density states resulting from the SP dispersion diagram can result in large enhancements of the spontaneous emission rate. Therefore, energy coupling between QW and SP as described in this article is one of the most promising solutions to increase k_{rad}. SPs, excited by the interaction between light and metal surfaces,[12-13] are known to enhance absorption of light in molecules[14], increase Raman scattering intensities[15-16] and light transparencies[17-18], and also generate photonic band gap[19-20]. Since 1990, SPs have also received much attention when used in LEDs[21-30]. Gianordoli et al optimized the emission characterization of GaAs-based LED by SP.[25] Vuckovic et al. reported the SP enhanced LED analyzing by both theoretically and experimentally.[26] Thus, great attention has been focused on SP enhanced emission. Hobson et al. reported the SP enhanced organic LEDs.[27] For InGaN QWs, Gontijo and co-workers reported the coupling of the spontaneous emission from QW into the SP on silver thin firm[28] and showed

increased absorption of light at the SP frequency. Neogi et al. confirmed that the recombination rate in an InGaN/GaN QW could be significantly enhanced by the time-resolved PL measurement.[29] However, in this early work, light could not be extracted efficiently from the silver/GaN surface. Therefore, the actual PL enhancement of InGaN/GaN by coupling into SP had not so far been observed directly. Quite recently, we have reported for the first time large photoluminescence (PL) increases from InGaN/GaN QW material coated with metal layers.[30] In order to design even more efficient structures and to fabricate electrical pumped LED devices by using SP coupling, we have to understand and optimize both mechanism and dynamics of energy transfer and light extraction. Here we fabricate and test nano-structured metal layers to explore the dependence of the plasmon enhancement on metal composition, thickness and grain shapes and sizes. The purpose of this work is to predictably use our control over metal geometries and composition to improve light emission and localization.

2. EXPERIMENT

Fig 1 shows the setup of the PL measurement and the sample structure. $In_{0.3}Ga_{0.7}N$/GaN QW wafers were grown on a (0001) oriented sapphire substrate by a metal-organic chemical vapor deposition (MOCVD). The QW heterostructure consists of a GaN (4 •m) buffer layer, an InGaN QW (3 nm) and a GaN cap layer (10, 40 or 150 nm), and the PL peak wavelength of the wafers is located at 470 nm. A 50nm thick silver film was

evaporated on top of the surface of these wafers. After polishing the bottom surface of the QW samples, we photoexcite and detect emission from the backside of the samples through the transparent substrate. Such back side access to the QWs permit us the rapidly compare the PL from QWs with and without the influence of SPs, and to measure the dependence of the emission intensity on the distance between the QW and the metal films by changing the GaN spacer thickness. Topography measurements were performed by a twin-SNOM system manufactured by OMICRON. Fluorescence microscopy was used with X40 objective, a mercury lamp, and a color CCD camera. Metal grating structures were fabricated by electron beam lithography on a 50 nm thick polymethylmethacrylate (PMMA) mask coated on the metal surface. The pattern was transferred into the top metal layer by using Ar ion milling.

To perform the photoluminescence (PL) measurements, a cw-InGaN diode laser (406 nm) was used to excite the QWs from the bottom surface of wafer. Luminescence was collected and focused into an optical fiber and subsequently detected with a multichannel spectrometer (Ocean optics). Neutral density filters were used to

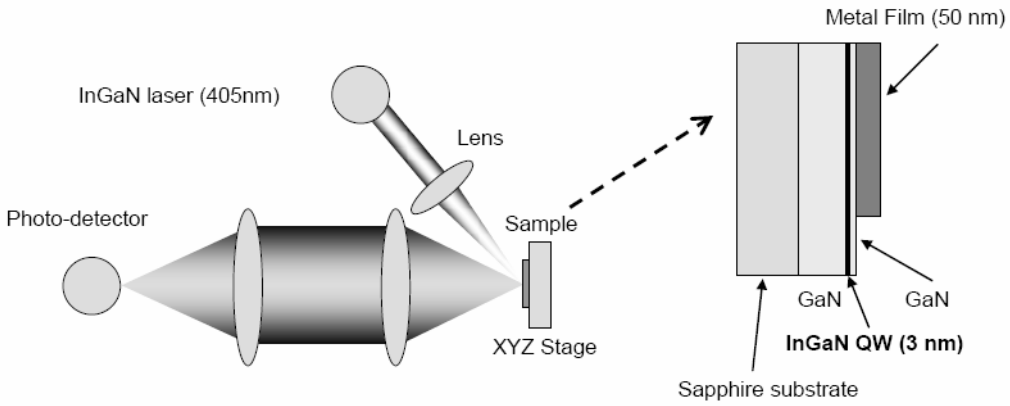

Fig. 1 Experimental setup of the photoluminescence measurement and the sample structure.

excitation power (from 0.18 to 4.5 mW) to determine the power dependence of the luminescence intensities, and their temperature dependence was studied by using a by cryostat with the ability of cooling from room temperature to 6K. To perform time-resolved PL measurements, frequency doubled beams of a mode-locked Al_2O_3:Ti laser pumped by an Ar^+ laser were used to excite the QW from the backside of the wafer. A 1.5 ps pulse width, 400 nm pump wavelength, and 80 MHz repetition rate were chosen to excite luminescence in the QW. A streak camera system (Hamamatsu) was used as the detector.

3. RESULTS AND DISCUSSIONS

3.1 Enhanced photoluminescence spectra

Fig. 2a shows typical emission spectra from InGaN/GaN QW samples covered with silver layers. As the PL peak of the uncoated wafer at 470 nm was normalized to 1, it is clear that a dramatic enhancement in the PL intensity from the silver coated InGaN QWs can be obtained when the cap layer

thicknesses is limited to 10 nm. On the other hand, the PL intensities are no longer strongly influenced from the silver in samples with 150 nm thick cap layers. The enhancement ratios of 10 nm capped QW samples covered with silver are 14-fold at the peak wavelength and 17-fold when comparing the luminescence intensity integrated over the emission spectrum with un-coated InGaN samples. We also compared the PL spectra of our QW samples after coating them with silver, aluminum, and gold layers (Fig. 2b). For InGaN QWs with a 10nm cap, such measurements indicate that a 8-fold peak intensity and 6-fold integrated intensity enhancement is obtained after coating with aluminum, and no enhancement in PL is found to occur in gold-coated samples. In such a measurement, a small (2x) increase in the luminescence efficiency could be expected after metallization as the deposited metal reflects light back into the QW, and this may double the effective path-length of the incident pump light. Although the reflectivity of gold at 470 nm is smaller than that of silver or aluminum, this difference alone cannot explain the large difference in the enhancement ratio of each metal.

The dramatic PL enhancement of samples after coating with Ag and Al can be attributed to the strong interaction between the QW and SPs. We propose a possible mechanism of QW-SP coupling and light extraction shown in Fig. 3a. Electron-hole pairs created in the QW can couple to the electron vibration at the metal/semiconductor surface when the

bandgap energy ($\bullet\bullet_{BG}$) of InGaN active layer is close to the electron vibration energy ($\bullet\bullet_{SP}$) of SP. Then, electron-hole recombination may produce a SP instead of a photon, and this new path of the recombination increases the spontaneous recombination rate. If the metal/semiconductor surface were perfectly flat, it would be difficult to extract light emission from the SP, since it is a non-propagating evanescent wave. However, in evaporated metal coatings, light emission can be observed as the SP is scattered through roughness and imperfections in the metal layers. The coupling rate (k_{SP}) between the QW and SP is expected to be much faster than k_{rad} as a result of the large electromagnetic fields introduced by the large density of states (Fig. 3b). Actually, we observed such the enhanced spontaneous emission rates

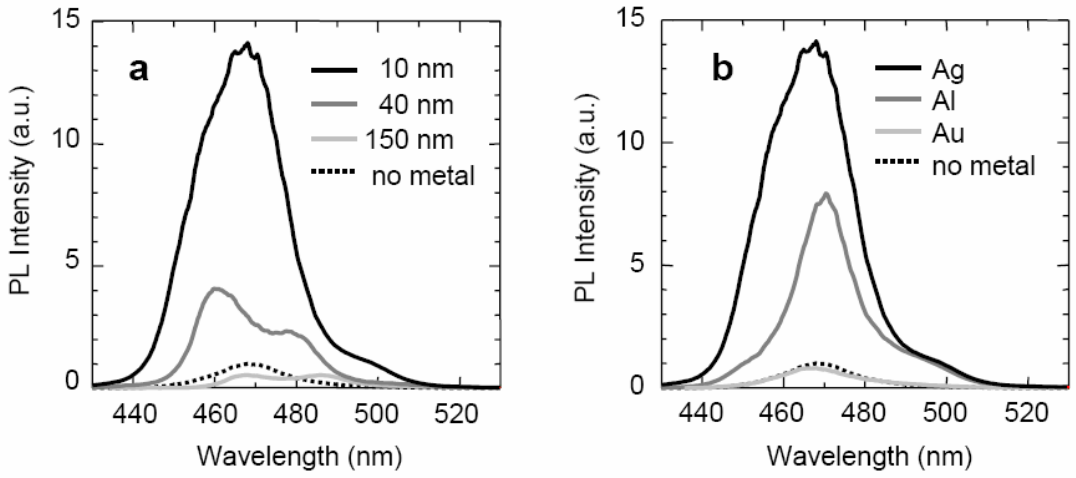

Fig. 2 a, PL spectra of InGaN/GaN QWs coated with silver layers with 10 nm, 40 nm and 150 nm thick GaN spacers. b, PL

spectra of InGaN/GaN coated with Ag, Al and Au with 10 nm GaN spacers.

by the time-resolved PL measurement. All profiles could be fitted to single exponential functions and PL lifetimes (τ_{PL}) were obtained. We found that the time-resolved PL decay profiles of the Ag-coated sample strongly depend on the wavelength and become faster at shorter wavelengths, whereas those of the uncoated sample show little spectral dependence.[31] We attribute the increases in both emission intensities and decay rates from Ag-coated samples to the coupling of energy between the QW and the SP.

3.2 Surface plasmon dispersion diagram

The dispersion diagrams of the SP modes at the metal/GaN interfaces are shown in Fig. 4a. The SP wave-vector (momentum) $k(\omega)$ was obtained by the following equation.[12-13]

$$k(\varpi) = \frac{\omega}{c}\sqrt{\frac{\varepsilon'_{metal}(\omega)\varepsilon'_{GaN}(\omega)}{e'_{metal}(\omega)+\varepsilon'_{GaN}(\omega)}} \quad (2)$$

where, $\varepsilon'_{metal}(\omega)$ and $\varepsilon'_{GaN}(\omega)$ are the real part of the dielectric functions for metal and GaN, respectively. The plasmon energy (ω_p) of silver is well known as 3.76 eV.[32] The SP energy (ω_{SP}) must be modified for a silver/GaN surface, and can be estimated to be approximately ~2.8 eV (~440 nm) (Fig. 4a) when using the dielectric constant of silver[33] and GaN[34]. $k(\omega)$ approaches infinity around ~2.8 eV by $\varepsilon'_{metal}(\omega)$ + $\varepsilon'_{GaN}(\omega)$ ~ 0. We have plotted a typical measured PL spectrum from the InGaN QW in Fig. 4a. The position of the PL peak

was very close to $\bullet\bullet_{SP}$, and large SP enhancements in luminescence intensity were observed especially at the higher energy side of the PL spectrum. This observation supports the existence of the QW-SP coupling phenomenon. Thus, silver is suitable for SP coupling to blue emission, and we attribute the large increases in luminescence intensity from Ag-coated samples to such resonant SP excitation. In contrast, the estimated $\bullet\bullet_{SP}$ of gold on GaN is below ~2.2 eV (~560 nm), and no measurable enhancement is observed in Au-coated InGaN emitters as the SP and QW energies are not matched. In the case of aluminum, the $\bullet\bullet_{SP}$ is higher than ~5 eV (~250 nm), and the real part of the dielectric constant is negative over a wide wavelength region for visible light.[35] Thus, a substantial and useful PL enhancement is observed in Al-coated samples, although the energy match is not ideal at 470 nm and a better overlap is expected at shorter wavelengths. Fig. 4b shows the enhancement ratios of PL intensities with metal layers separated from the QWs by 10 nm spacers as a function of wavelength. We find that the enhancement ratio increases at shorter wavelengths for Ag samples, while it is independent of wavelength for Al coated samples. The clear correlation between Figs.4a and 4b suggests that the obtained emission enhancement with Ag and Al is due to SP coupling.

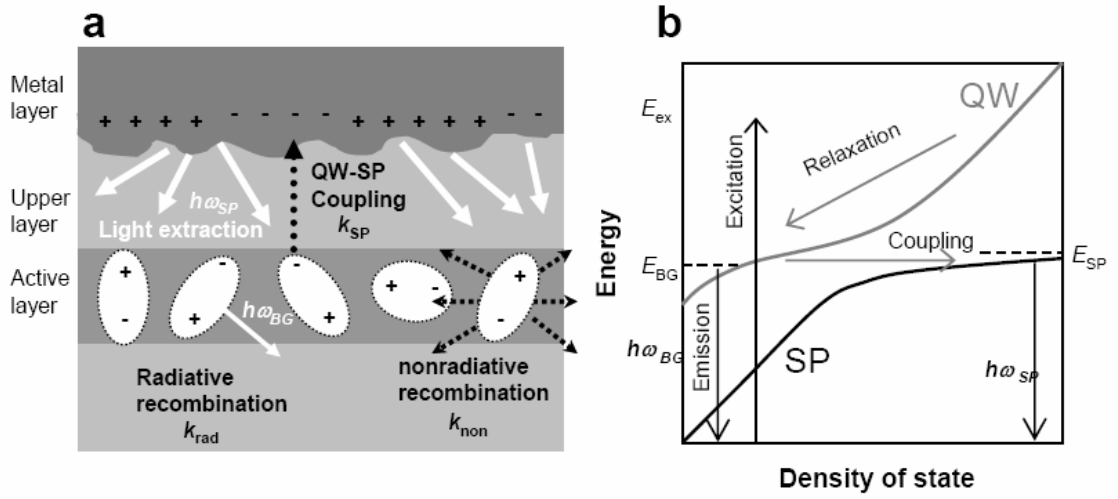

Fig. 3 a, Schematic diagram of the electron-hole recombination and QW-surface plasmon (SP) coupling mechanism. b, Energy diagram of excitation, emission and QW-SP coupling.

3.3 Spacer trickiness and excitation power dependences

PL intensities of Al and Ag coated samples were also found to strongly depend on the distance between QWs and the metal layers, in contrast to Au coated samples. Fig. 5a shows this dependence of the PL enhancement ratios taken for three different GaN spacer thicknesses (of 10nm, 40nm, and 150nm) with each metal coating. These show an exponential increase in intensity as the spacer thickness is decreased for Ag and Al, but no significant improvement in the PL intensity for samples coated with gold. This figure suggests that coupling between SP should be main component to contribute to the PL enhancement, because the SP is an evanescent wave, which decays exponentially with increasing distance from the metal

surface. Only electron-hole pairs located within the near-field from the surface can couple to the SP mode. The penetration depth $Z(\bullet)$ of the SP fringing field into GaN from metal can be calculated from[11-12]

$$Z(\omega) = \frac{c}{\omega}\sqrt{\frac{\varepsilon'_{GaN}(\omega) - \varepsilon'_{metal}(\omega)}{\varepsilon'_{metal}(\omega)^2}} \quad (3)$$

$Z(\bullet)$ is predicted to be Z= 47, 77, and 33 nm for Ag, Al, and Au, respectively at 470 nm. The inset of Fig. 5a shows good agreement between these calculated penetration depths (dashed lines) and measured values for Ag and Al coated samples. This again indicates that the emission enhancement results from QW-SP coupling.

We also find that the luminescence enhancement ratio increases with increasing excitation power (Fig. 5b). In InGaN QWs, electron-hole pairs are often localized by spatial modulations in bandgap energy produced by fluctuations of indium composition, QW width, or piezoelectric field. Such localization centers serve as radiative recombination centers for electron-hole pairs and explain the strong emission and insensitivity to growth defects in InGaN/GaN QW material. The emission efficiency may be reduced at high excitation intensities by saturation of these localization centers. When metal layers are coated within the near field of the QW, both localized and un-localized electron-hole pairs can immediately couple to the SP mode. In that situation, the saturation of the localized centers can be avoided and this leads to high emission

efficiencies even under intense excitation. We consider this very advantageous in light emitting diodes, since generally the emission efficiencies of such emitters are reduced under the high current pumping. Thus, by using the SP coupling, higher current operation and brightness should be achievable.

3.4 Internal quantum efficiencies and Purcell enhancement factor

We expect that the SP coupling will increase the efficiency ($\bullet_{int}$) by enhancing the spontaneous recombination rate. In order to estimate the $\bullet_{int}$ and to separate the SP enhancement from other effects (mirror effect, photon recycling, etc.), we have also measured the temperature dependence of the PL intensity. Fig. 6a shows the linear and Arrhenius plots of the integrated photoluminescence intensities of InGaN-SQWs coated with Ag and Al and compares these to un-coated

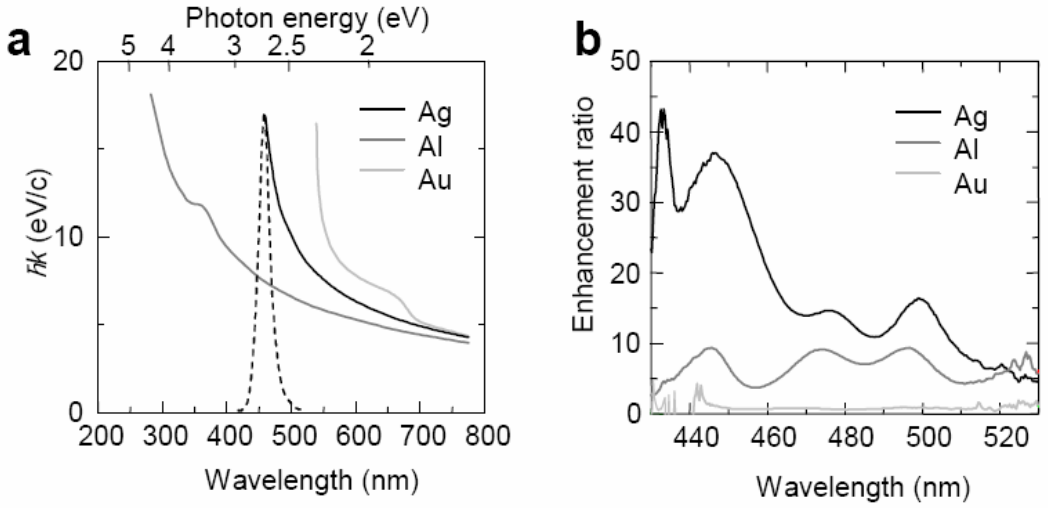

Fig. 4 a, Dispersion diagrams of surface plasmons generated on metal/GaN. The dashed line was the PL spectrum of

InGaN/GaN. b, PL enhancement ratios at several wavelengthsfor same samples with Fig. 2b.

samples with 10 nm GaN spacer layer thicknesses. The $\bullet_{int}$ values of un-coated InGaN was estimated as 6 % at room temperature by assuming $\bullet_{int}$ ~100% at ~6 K.[36] We found that the $\bullet_{int}$ values were increased by 6.8 times (41%) by Ag coating and by 3 times (18%) by Al coating. We expect this actual enhancement of the $\bullet_{int}$ values to be a result of the enhancement of the spontaneous recombination rate of electron-hole pairs by SP coupling. 6.8-fold increasing of $\bullet_{int}$ means that 6.8-fold improvement of the efficiency of electrically pumped LED devices should be achievable because $\bullet_{int}$ is a fundamental property and not depend on the pumping method. Such improved efficiencies of the white LEDs, in which a blue LED is combined with a yellow phosphor, are expected to be larger than those of current fluorescent lamps or light bulbs. The luminous efficacy of commercial white LEDs is 25 lm/W under a current of 20 mA at room temperature.[37] This value is still lower than that of fluorescent tubes (75 lm/W). A 3-fold improvement is necessary to exceed the current fluorescent lamps or light bulbs. We expect that the SP coupling technique is very promising for even larger improvements of solid-state light source.

Wavelength depended enhanced efficiencies $\eta_{int}^{*}(\lambda)$ can be related the coupling rate $k_{SP}(\lambda)$ between QWs and SPs by the relationship:

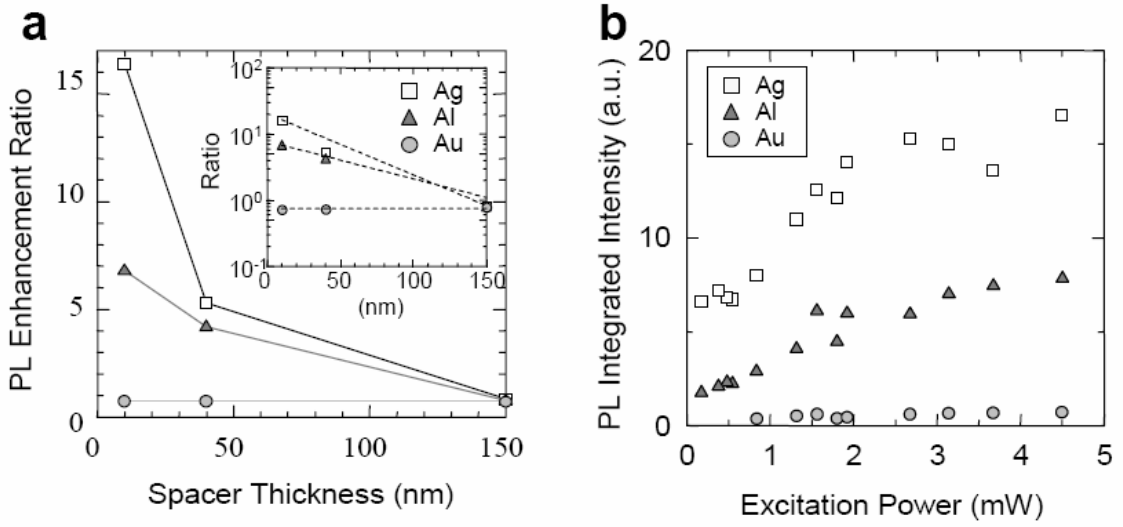

Fig. 5. GaN spacer thicknesses (a) and excitation power (b) dependence of the PL enhancement ratios.

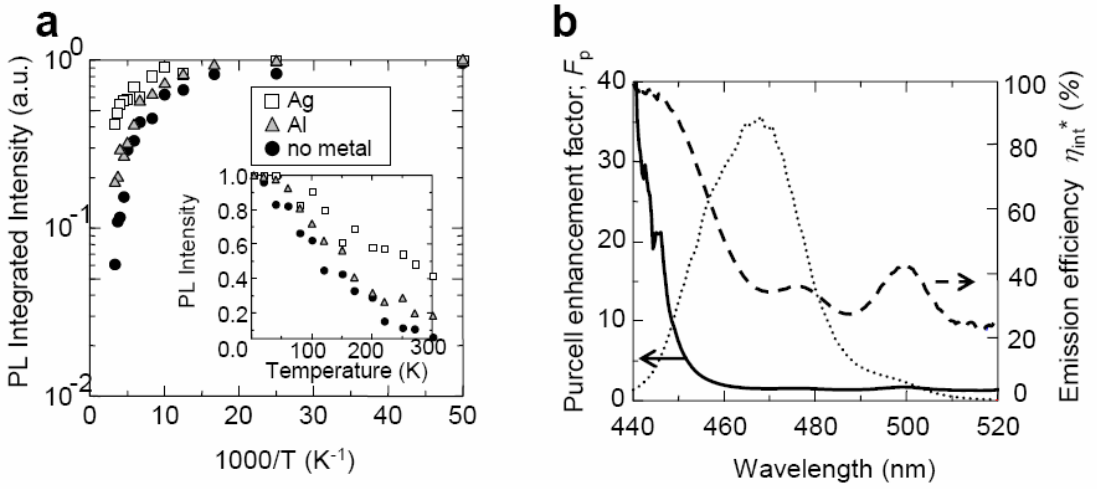

Fig. 6 a, Temperature dependence of integrated PL intensities. b, Wavelength dependent emission efficiencies [$\eta_{int}^{*}(\lambda)$] was plotted as dashed line. The Purcell enhancement factor $F_p(\lambda)$ estimated by $\eta_{int}^{*}(\lambda)$ was also potted

(solid line). The dotted line was the PL spectrum of the same sample.

$$\eta_{\text{int}}^{*}(\omega) = \frac{k_{rad}(\omega) + C_{ext}^{'}(\omega)k_{SP}(\omega)}{k_{rad}(\omega) + k_{non}(\omega) + k_{SP}(\omega)} \quad (4)$$

where $C'_{ext}(\bullet)$ is the probability of photon extraction from the SPs energy and is decided by the ratio of light scattering and dumping of electron vibration through non-radiative loss. Fig, 6b shows the $\bullet_{int}^{*}(\bullet)$ of Ag coated sample estimated from PL enhancement ratio (Fig. 6b) by normalizing the integrated $\bullet_{int}^{*}$ should be 41%. We find that $\bullet_{int}^{*}(\bullet)$ increases at shorter wavelengths where the plasmon resonance more closely matches the QW emission, and reaches almost 100% at 440 nm.

The Purcell enhancement factor F_p[38] quantifies the increase in the spontaneous emission rate of a mode for a particular mode, and can be described by $\bullet_{int}(\bullet)$ and $\bullet_{int}^{*}(\bullet)$ when $C'_{ext} \bullet 1$:

$$F_p(\omega) = \frac{k_{rad}(\omega) + k_{non}(\omega) + k_{SP}(\omega)}{k_{rad}(\omega) + k_{non}(\omega)} \approx \frac{1 - \eta_{\text{int}}(\omega)}{1 - \eta_{\text{int}}^{*}(\omega)} \quad (5)$$

Fig.6b also shows $F_p(\bullet)$ estimated at each wavelength by assuming a constant $\bullet_{int}(\bullet)$ = 6 %. $F_p(\bullet)$ is significantly higher at wavelengths below 470 nm, well in agreement with previous work[28-29]. The PL spectrum shape (plotted as dotted line) also indicates that $F_p(\bullet)$ values are higher at the shorter wavelength region. That should be a possible reason for the asymmetry in the luminescence peak of Fig. 2. Fig. 6b suggests that a InGaN QW with a peak position at around

440 nm should be best matched for SP enhancement from a silver layer. In that case, the enhanced $\bullet_{int}^{*}(\bullet)$ value is expected to approach 100% throughout the PL spectrum. The SP frequency could be geometrically tuned to match our $\bullet$ ~ 470 nm QW by fabricating nanostructures, for example, using a grating structure, or using alloys.

3.5 Surface roughness and grating structures

The SP energy can be extracted as light by providing roughness or nano-structuring the metal layer. Such roughness allows SPs of high momentum to scatter, lose momentum and couple to radiated light.[39] $C'_{ext}(\bullet)$ in Eq.(4) should depend on the roughness and nano-structure of the metal surface. We succeeded in controlling the grain structure within nano-sizes. Such roughness in the metal layer was observed from topographic images obtained by shear-force microscopy of the original GaN surface (Fig. 7a) and the coated Ag surface (Fig. 7b). The depth profiles along the

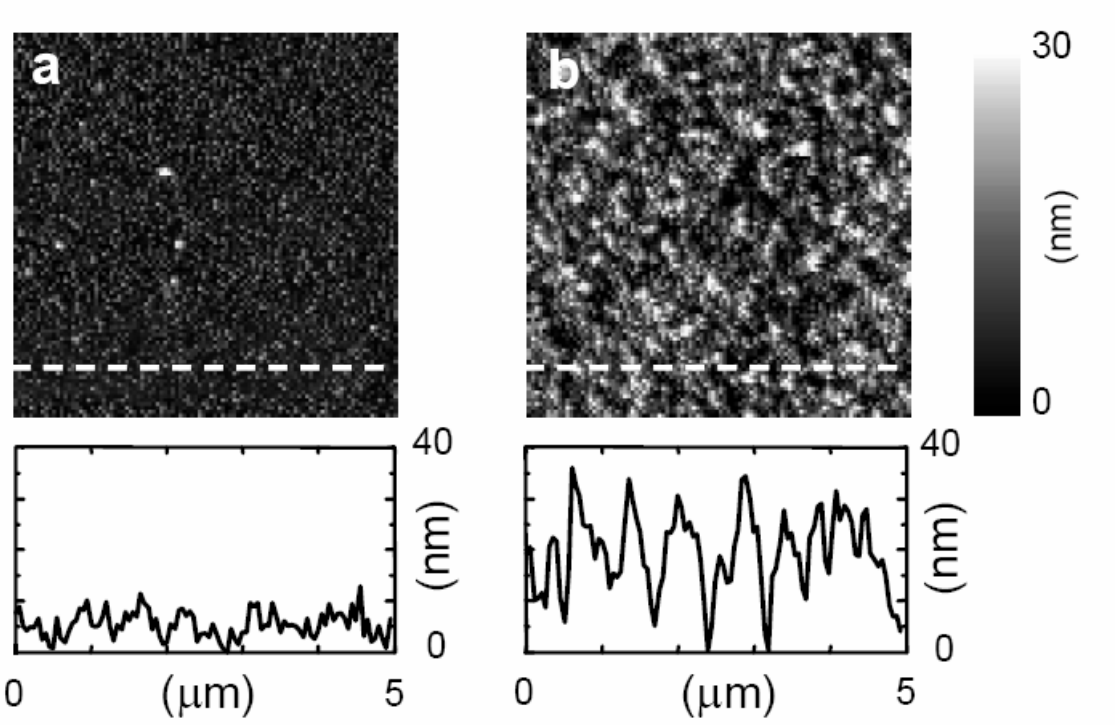

Fig. 7 Topographic image of the uncoated GaN surface (a) and the 50 nm thick Ag film evaporated on GaN (b). The depthprofilealong the dashed line in the topographic images are also plotted.

dashed lines of the Ag surface of approximately 30-40 nm while the GaN surface roughness was below 10 nm. Higher magnification SEM images of Ag and GaN surface are shown in Figs. 8a and 8b. The length scale of the roughness of Ag surface was determined to be a few hundred nanometers. Fig. 8c shows a fabricated metal grating, a geometry that has previously been used to couple SP and photons [21, 23-26]. Micro-luminescence images of uncoated, coated, and patterned grating structures of Ag on InGaN QWs with 10 nm spacers are shown in Fig. 8d. We found a doubling of the emission from

133 nm wide Ag stripes forming a 400 nm period grating, whereas such an emission increase was not observed from 200 nm wide Ag stripes within a 600 nm period grating. This measurement suggests that the size of the metal structure determines the SP-photon coupling and light extraction. We also found that the PL peak position of grating structured regions was dramatically blue-shifted (Fig. 9). This suggests that the nano-grating structure modulate not only light extraction but also localized SP frequency. Such geometrical tuning of the SP frequency is one of the most important next subjects and is now on progress by experimentally and theoretically.

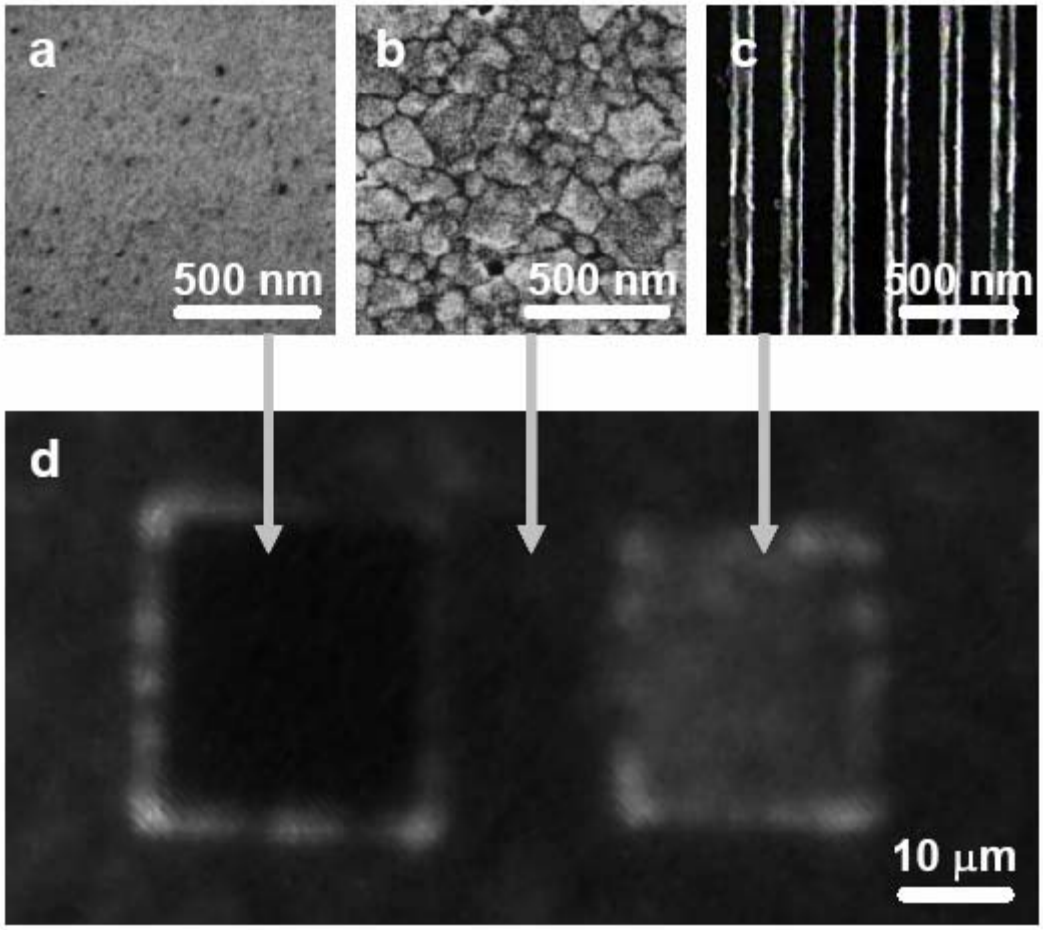

Fig. 8 SEM images of (a) the uncoated GaN surface, (b) the 50 nm Ag film on GaN, and (c) the grating structure with 33% duty cycle fabricated within a 50 nm thick Ag layer on GaN. (d) Micro-luminescence image including the areas of Figs. 3a-c.

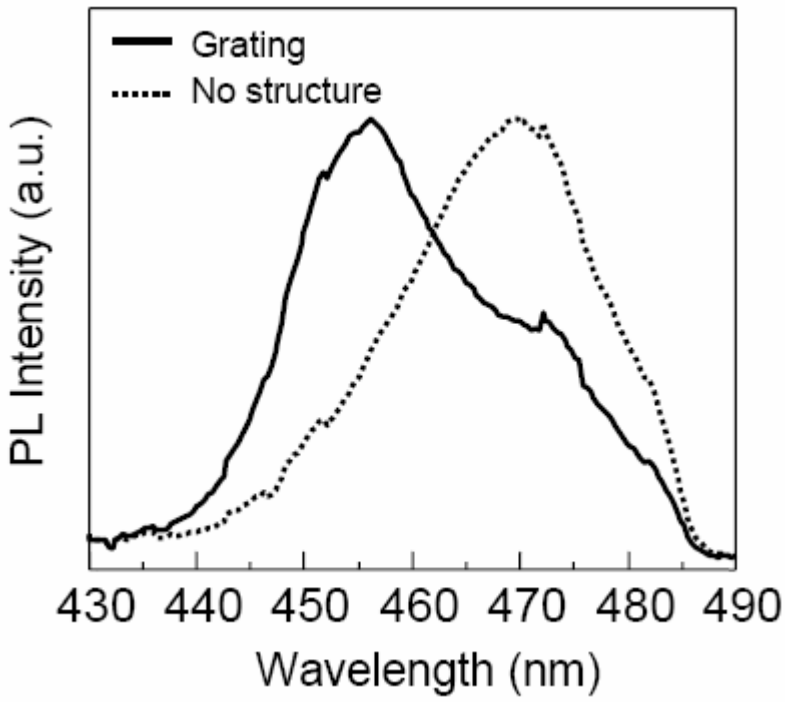

Fig. 9 PL spectra of InGaN/GaN QW with nano-grating structured and unstructured silver layers with 10 nm GaN

4. CONCLUSIONS

We conclude that the SP enhancement of PL intensities of InGaN is a very promising method for developing solid state light sources with high emission efficiencies. We have directly measured significant enhancements of $\bullet_{int}$ and the spontaneous recombination rate, and shown how distance and choice of patterned metal films can be used to optimize light emitters. Even when using un-patterned metal layers, the SP energy can be extracted by the submicron scale roughness on the metal surface. SP coupling is one of the most interesting solutions for developing efficient photonic devices, as the metal can be used both as an electrical

contact and for providing high electromagnetic fields from SPs. We believe that this work provides a foundation for the rapid development of highly efficient and high-speed solid state light emitters alternative to conventional light bulbs.

REFERENCES

1. S. Nakamura, T. Mukai and M. Senoh, "Candela-class high-brightness InGaN/AlGaN double-heterostructure blue-light-emitting diodes", Appl. Phys. Lett. **64**, 1687-1689, 1994.

2. S. Nakamura, T. Mukai, M. Senoh and N. Iwase, "High-brightness InGaN/AlGaN double-heterostructure blue-green-light-emitting diodes", J. Appl. Phys. **76,** 8189-8191, 1994.

3. T. Mukai, M. Yamada, S. Nakamura, "Current and temperature dependences of electroluminescence of InGaN-based UV/blue/green light-emitting diodes", Jpn. J. Appl. Phys. **37**, L1358-L1361, 1998.

4. S. Nakamura and G. Fasol, *The blue laser diode: GaN based light emitting diode and lasers*, Springer, Berlin, 1997.

5. M. Yamada, T. Mitani, Y. Narukawa, S. Shioji, I. Niki, S. Sonobe, K. Deguchi, M. Sano, and T. Mukai, "InGaN-based near-ultraviolet and blue-light-emitting diodes with high external quantum efficiency using a patterned sapphire substrate and a mesh electrode", Jpn. J. Appl. Phys. **41**, L1431-L1433, 2002.

6. S. Nakamura, “The roles of structural imperfections in InGaN-based blue light-emitting diodes and laser diodes”, Science, **281**, 956-961, 1998.

7. S. Nakamura, M. Senoh, S. Nagahama, N. Iwasa, T. Yamada, T. Matsushita, H. Kiyoku, Y. Sugimoto, T. Kozaki, “InGaN/GaN/AlGaN-based laser diodes with modulation-doped strained-layer superlattices grown on an epitaxially laterally overgrown GaN substrate”, Appl. Phys. Lett. **72**, 211-213, 1998.

8. T. Mukai, K. Takekawa, S. Nakamura, “InGaN-based blue light-emitting diodes rrown on epitaxially laterally overgrown GaN substrates”, Jpn. J. Appl. Phys. **37**, L839-L841, 1998.

9. T. Mukai, and S. Nakamura, “ultraviolet InGaN and GaN single-quantum-well-structure light-emitting diodes grown on epitaxially laterally overgrown GaN substrates”, Jpn. J. Appl. Phys., **38**, 5735-5739, 1999.

10. P. Walterelt, O. Brandt, A. Trampert, H. T. Grahn, J. Menniger, M. Ramsteiner, M. Reiche, and K. H. Ploog, “Nitride semiconductors free of electrostatic fields for efficient white light-emitting diodes”, Nature, **406**, 865-868, 2000.

11. J. J. Wierer, M. R. Krames, J. E. Epler, N. F. Gardner, M. G. Craford, J. R. Wendt, J. A. Simmons, and M. M. Sigalas, “InGaN/GaN quantum-well heterostructure light-emitting diodes employing photonic crystal structures” Appl. Phys. Lett., **84**, 3885-3887, 2004.

12. H. Raether, *Surface plasmon on smooth and rough surface and on grating*, Springer, Berlin, 1988.

13. A. Liebsch, *Electronic Excitations at Metal Surfaces, Physics of Solids and Liquids*, Ansgar, Libsch, 1997

14. G. W. Ford and W. H. Weber, "Electromagnetic-interactions of molecules with metal-surfaces", Phys. Rep. **113**, 195-287, 1984.

15. M. Fleischmann, P. J. Hendra, and A. J. McQuillan, "Raman spectra of pyridine adsorbed at a silver electrode", Chem. Phys. Lett. **26**, 163-166, 1974.

16. J. F. García-Vidal, and J. B. Pendry, "Collective theory for surface enhanced Raman scattering", Phys. Rev. Lett. **77,** 1163-1166, 1996.

17. T. W. Ebbesen, H. J. Lezec, H. F. Ghasemi, T. Thio, and P. A. Wolff, "Extraordinary optical transmission through sub-wavelength hole arrays", Nature, **391**, 667-669, 1998.

18. U. Schroter and D. Heitmann, "Surface-plasmon-enhanced transmission through metallic gratings", Phys. Rev. B, **58**, 15419-15421, 1998.

19. S. C. Kitson, W. L. Barnes, and J. R. A. Sambles, "full photonic band gap for surface modes in the visible", Phys. Rev. Lett. **77**, 2670-2673, 1996.

20. W. T. Barnes, T. W. Preist, S. C. Kitson, and J, R. Sambles, “Physical origin of photonic energy gap in the propagation of surface plasmon on grating”, Phys. Rev.B. **54**, 6227-6244, 1996.

21. A. Köck, E. Gornik, M. Hauser, and M. Beinstingl, “Strongly directional emission from AlGaAs/GaAs light-emitting diode”, Appl. Phys. Lett. **57**, 2327-2329, 1990.

22. N. E. Hecker, R. A. Hopfel, and N. Sawaki, Physica E, “Enhanced light emission from a single quantum well located near a metal coated surface”, **2**, 98-101, 1998.

23. N. E. Hecker, R. A. Hopfel, N. Sawaki, T. Maier, and G. Strasser, “Surface plasmon-enhanced photoluminescence from a single quantum well”, Appl. Phys. Lett. **75**, 1577-1579, 1999.

24. W. L. Barnes, “Electromagnetic crystals for surface plasmon polaritons and the extraction of light from emissive devices”, J. Light. Tech., **17**, 2170-2182, 1999.

25. S. Gianordoli, R. Hainberger, A. Kock, N. Finger, E. Gornik, C. Hank, and L. Korte, “Optimization of the emission characteristics of light emitting diodes by surface plasmons and surface waveguide modes”, Appl. Phys. Lett. **77**, 2295-2297, 2000.

26. J. Vuckovic, M. Loncar, and A. Scherer, “Surface plasmon enhanced light-emitting diode”, IEEE J. Qunt. Elec. **36**, 1131-1144, 2000.

27. P. A. Hobson, S. Wedge, J. A. E. Wasey, I. Sage, and W. L. Barnes, “Surface plasmon mediated emission from organic light emitting diodes”, Advanced Materials, **14,** 1393-1396, 2002.

28. I. Gontijo, M. Borodisky, E. Yablonvitch, S. Keller, U. K. Mishra, and S. P. DenBaars, “Enhancement of spontaneous recombination rate in a quantum well by resonant surface plasmon coupling” Phys. Rev. B, **60**, 11564 -11567, 1999.

29. A. Neogi, C.-W. Lee, H. O. Everitt, T. Kuroda, A. Tackeuchi, and E. Yablonvitch, “Enhancement of spontaneous recombination rate in a quantum well by resonant surface plasmon coupling”, **66**, 153305, 2002.

30. K. Okamoto, I. Niki, A. Shvartser, Y. Narukawa, T. Mukai, A. Scherer, “Surface-plasmon-enhanced light emitters based on InGaN quantum wells”, Nature Mater., **3**, 601-605, 2004.

31. K. Okamoto, I. Niki, Y. Narukawa, T. Mukai, Y. Kawakami, and A. Scherer, “Surface plasmon enhanced high-speed spontaneous emission”, *submitted for publication*

32. A. Liebsch, “ Surface plasmon dispersion of Ag”, Phys. Lev. Lett, **71**, 145-148, 1993.

33. E. D. Palik, *Handbook of Optical Constants of solids*, Academic, San Diego, 1985.

34. T. Kawashima, H. Yoshikawa, S. Adach, S. Fuke, and K. Ohtsuk, “Optical properties of hexagonal GaN”, J. Appl. Phys., **82**, 3528-3535, 1997.

35. A. Bagchi, C. B. Duke, P. J. Feibelman, and J. O. Porteus, " Measurement of Surface-Plasmon Dispersion in Aluminum by Inelastic Low-Energy Electron Diffraction", Phys. Rev. Lett., **27**, 998–1001, 1971.

36. Y. Kawakami, K. Omae, A. Kaneta, K. Okamoto, T. Izumi, S. Saijo, K. Inoue, Y. Narukawa, S. Nakamura, and S. Fujita, "Radiative and nonradiative recombination processes in GaN-based semiconductors", Phys. Stat. Sol. (a), **183**, 41-50, 2001.

37. Y. Narukawa, I. Niki, K. Izuno, M. Yamada, Y. Murazaki and T. Mukai, "hosphor-conversion white light emitting diode using InGaN near-ultraviolet chip", Jpn. J. Appl. Phys. **37**, L371-L373, 2003.

38. E. M. Purcell, "Spontaneous emission probabilities at radio frequencies", Phys. Rev. **69**, 681, 1946.

39. W. Barnes, "Light-emitting devices: Turning the tables on surface plasmons", Nature Mater., **3**, 588-589, 2004.

2. Analysis of using AlGaN emitters coupled with thin film heaters to cure onychomycosis infections

Onychomycosis affects more than 35 million Americans and is sometimes life threatening in immunocompromised patients and can lead to amputations in people with diabetes. Current FDA approved treatments work very poorly with a 5.5-8.5% chance of cure for Ciclopirox and a 38% chance for terbinafine hydrochloride. Additionally terbinafine hydrochloride is toxic to the liver and has a 15% chance of reinfection. The recent advances in creating low cost, commercially available AlGaN LED's which emit in the UV range, coupled with thin film heaters has led us to explore the use of these devices for the treatment of onychomycosis. These systems are theorized to work through a number of pathways. First the 247-275nm center wavelengths of the LED's is known to be at a DNA and RNA absorption peak and light in this energy wavelength will break fungal nucleic acid bonds (fig. 1).

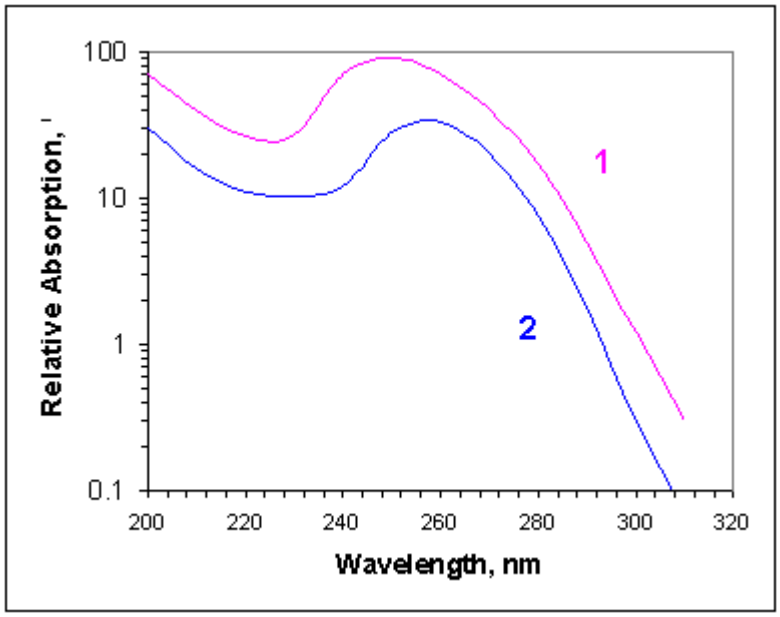

Figure 1 Absorption peak of 1. DNA and 2. RNA

The UV absorption of the keratin sheet of the nail can be measured and a proper UV dose can be used in order to not overdose the patient. It seems reasonable to assume that a dose lower than the average daily dose of an exposed digit would be safe, and our research suggest that this would be more than enough to kill the fungus. Additionally these fungi typically grow not only due to dark confines, but also because the temperature of the nail bed is typically 1-2 degrees lower than body temperature, ideal growing conditions for these fungi. In addition to the UV light treatment, a thin film heater is used to create a "localized fever" in order to create conditions that inhibit fungal growth. The resistive heater both raises the temperature and drives off moisture in order to kill the fungi (fig. 1). These treatments are predicted to be used either by

themselves or in combination with existing treatments in order to increase the effectiveness of those treatments. For the general population it may simply be a matter of shifting the balance in the person-pathogen interaction in the favor of the person such that their normal immune system can overcome the fungus.

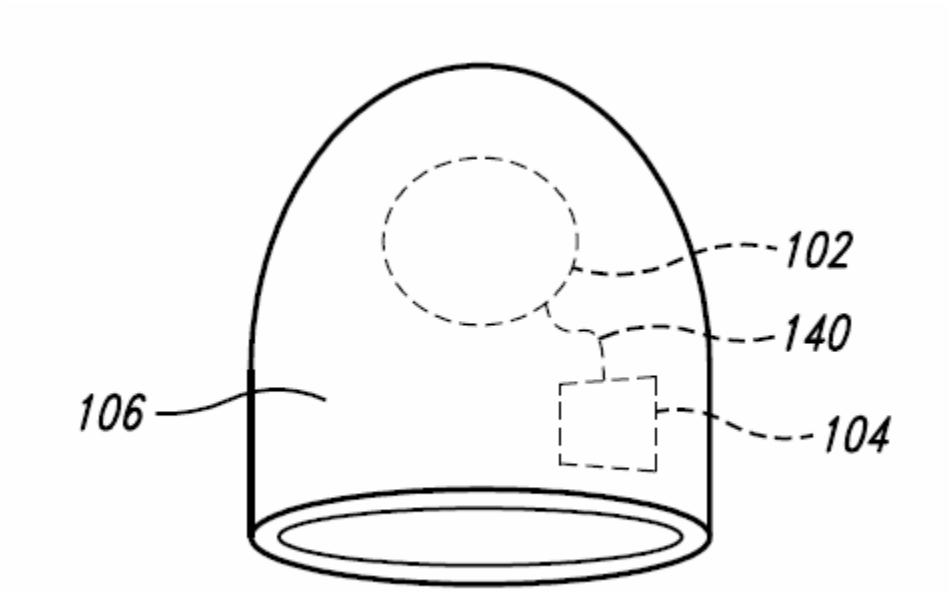

Figure 2 The device as envisioned over the nail, 102 is the combination UV LED and thin film heater, 104 is the power supply, 106 and 140 are the mechanical and electrical connections

We have made some start on the fungus growth, with four strains (two Trichophyton rubrum and two T. mentagrophytes - the two most common nail fungi) and about two weeks ago set up a suit of conditions for one of the T. rubrum. At first we had some difficulties, likely due to the Tween 20 (fatty acid) added to the water to resuspend the spores that killed

or inhibited the fungus. It is known that some of the long chain fatty acids inhibit the fungus.

Next one of the T. mentagrophytes species was grown, with excellent growth at 30°C and 37°C but nothing at 39-40°C, and a UV does of 0.3 min seems to have kill the fungus. However, this was done on the spores rather than a growing mat of the fungus, this is less informative as spores can become dormant, be less (usually more) resistant to stresses, etc. Interestingly the fungus grows very poorly on minimal medium, which is strange as many mutants of other fungi unable to grow on this type of media are unable to cause disease.

The next step is to test all four strains at once under the same types of conditions, as well as use the fungus when it is growing actively rather than in the spore stage.

The devices provided to our collaborators at Duke University where Petri dishes with embedded LEDs and thin film heaters and control electronics. The sterility was guaranteed by wiping around the lid with ethanol, and the LED was allowed to self-sterilize. The Petri dishes where poured with 30 ml of growth medium, which gives the agar a thickness of 5 - 5.5 mm. Depending on the age of the fungus there can be some distortion in the media, so the light was made to hit somewhere between 5 and 7 mm. (closer to 5.5 was ideal). The distance between bottom of the plate to the top is ~13 mm.

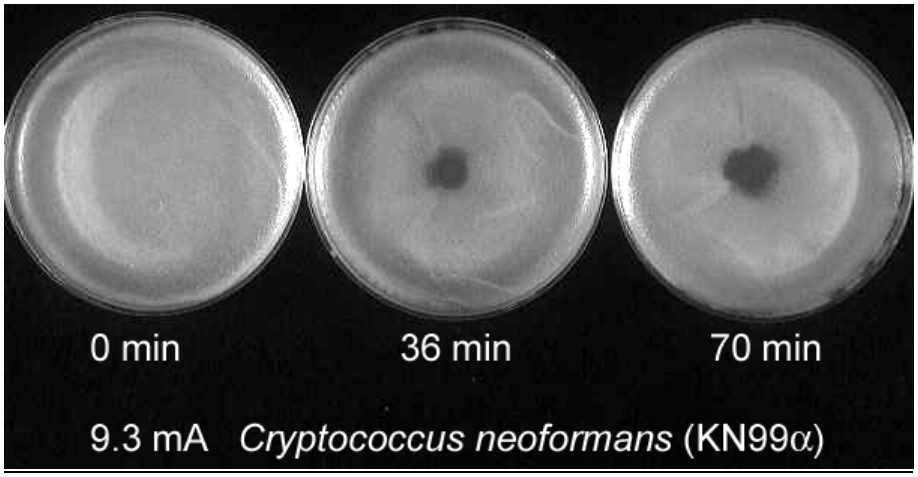

Figure 3 Cryptococcus neoformans exposed to UV light

Cryptococcus fungi was very sensitive to the UV light (fig. 1). A lawn of Cryptcoccus yeast cells was spread on plates and treated at 9.3mA for 36 and 70 min, then grown on the plates overnight. A good clearing of the fungus in the middle is clearly visible. It is clear that much less exposure is needed to kill the fungus - probably for Cryptococcus a few minutes at lower power would work. We suspect that with this sort of action the nail fungus will not need days of treatment to be killed.

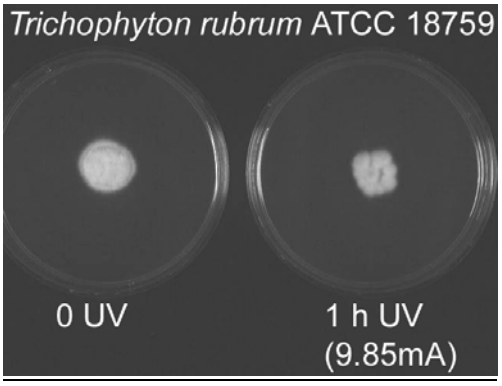

Figure 4 Tricophyton rubrum exposed to UV light , note the blotchy texture of the exposed fungus this indicates fungal death

A trial run on Trichophyton was similarly carried out. Figure 3 shows a representative sample dosed at 9.85mA, which while it looks like there is almost even growth, the clumped look of the UV treated plates are indicative that only a subset of the fungus survived the treatment, and later grew back fine - at an earlier time point the difference is more dramatic. This suggest several further experiments:

(a) smaller inoculation area - The light is very focused, so anything on the edge is not exposed

(b) increase the dose up to 2 and 4 h, and

(c) try re-hitting the fungus the next day with a second treatment.

The treatment of onychomyosis is an important area, and novel devices such as the AlGaN LEDs and thin film heaters could present an effective, low side effect treatment options for millions. As research in this area continues will be have better dose characteristic data, coupled with temperature data. The next steps will be to obtain infected nails from volunteers in order to measure the UV absorption of keratin in order to ascertain safe doses of ultraviolet radiation. Next clinical trials, with and without antifungal compounds can be started.

References:

[1] CHANG JCH, OSSOFF SF, LOBE DC, et al.

UV INACTIVATION OF PATHOGENIC AND INDICATOR MICROORGANISMS APPLIED AND ENVIRONMENTAL MICROBIOLOGY 49 (6): 1361-1365 1985

[2] Brasch J, Menz A. UV susceptibility and negative phototropism of dermatophytes, Mycoses 38, 197-203 (1995)

[3] Robbins WJ, Growth Requirements of Dermatophytes, Annals New York Academy of Sciences, 1357

[4] http://www.steribeam.com/puv-rev.htm

[5] Gupta A, Fleckman P, Baran R, Ciclopirox nail lacquer topical solution 8% in the treatment of toenail onychomycosis, American Academy of Dermatology, (2000)

[6] Young C, Range of variation among isolates of tricophyton Rubrum, Sabouraudia, 10, 164-170 (1972)

3. Tunable organic transistors that use microfluidic source and drain electrodes

This letter describes a type of transistor that uses conducting fluidic source and drain electrodes of mercury which flow on top of a thin film of the organic semiconductor pentacene. Pumping the mercury through suitably designed microchannels changes the width of the transistor channel and, therefore, the electrical characteristics of the device. Measurements on transistors with a range of channel lengths reveal low contact resistances between mercury and pentacene. Data collected before, during, and after pumping the mercury through the microchannels demonstrate reversible and systematic tuning of the devices. This unusual type of organic transistor has the potential to be useful in plastic microfluidic devices that require active elements for pumps, sensors, or other components. It also represents a noninvasive way to build transistor test structures that incorporate certain classes of chemically and mechanically fragile organic semiconductors.

The integration of active electronics directly with molded microfluidic channel arrays represents a promising way to increase the functionality, lower the cost, and reduce the size of microfluidic reactors, separation, and analysis systems. Organic electronic circuits have certain

characteristics—intrinsic compatibility with plastics, ease of fabrication and processing, ability to be patterned with the types of soft lithographic methods that are useful for building microfluidic devices,[1–3] etc.—that make them attractive for this purpose. Here we explore one route for directly combining the active elements of plastic circuits (i.e., the transistors themselves) with moving fluids that can be coupled in various ways to the microfluidic elements of the system. We demonstrate, in particular, that microchannels filled with mercury can serve as dynamically tunable source and drain electrodes in transistors that incorporate the p-type organic semiconductor pentacene. This letter begins with a description of the layout of these devices and the sequence of steps for their fabrication. Measurements on transistors with channel lengths between 25 and 200 mm demonstrate the good performance of these devices and the low contact and parasitic resistances associated with them. Pumping the mercury back and forth in the channels reversibly adjusts the electrical characteristics of the transistors in a systematic and easily understandable way. Devices with this design could find applications as sensors or elements of drive circuits for pumps in microfluidic systems. In addition, the noninvasive and low resistance microchannel mercury contacts may be useful for basic studies of charge transport in chemically and mechanically fragile classes of organic semiconductors, in a

way that is analogous to the recent application of mercury droplets for probing organic molecular-scale diodes [4]. Figure 1(a) shows a schematic view of a typical device.

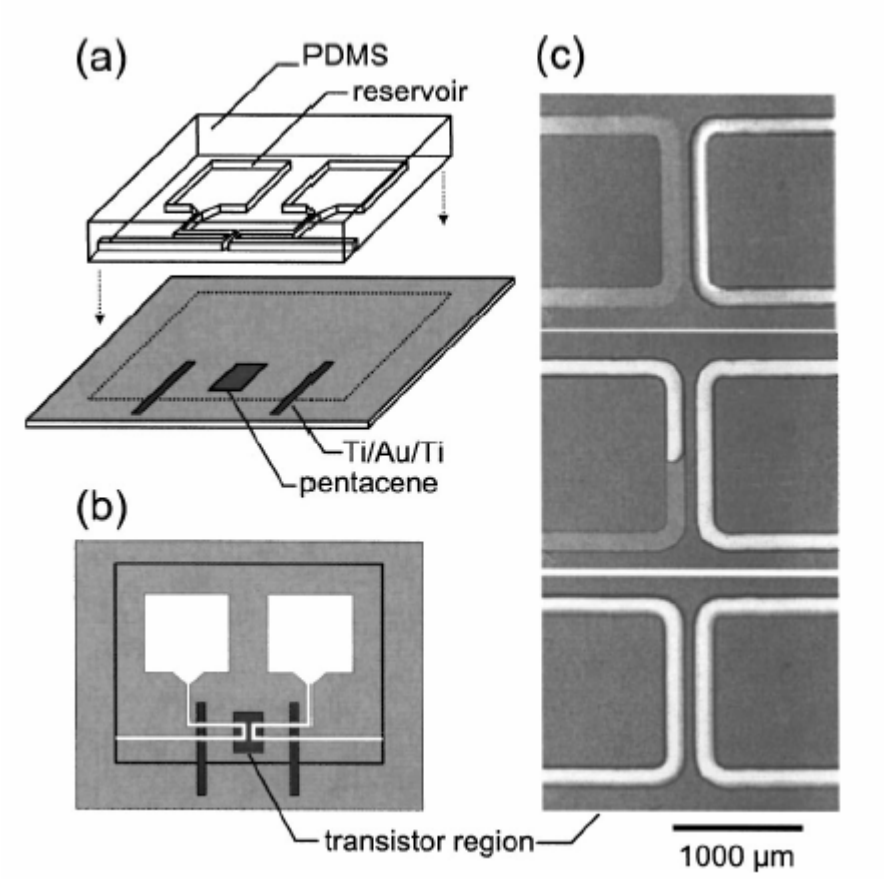

Figure 1 Part (a) shows a schematic angled view of a PDMS element with relief on its surface (top) and a substrate that supports the semiconductor, gate dielectric, Ti/Au/Ti contact lines, and gate electrode. Part (b) shows a schematic illustration of the assembled device as viewed from the top through the transparent PDMS. Part (c) presents optical micrographs of the transistor region with mercury (white) pumped into the channel on the left hand side to various degrees. The extent that the mercury fills the channels defines the effective transistor channel width.

It consists of a bottom substrate that supports a thin film of an organic semiconductor (pentacene; 25 nm, deposited by thermal evaporation through a shadow mask at 0.02 nm/s) on

a gate dielectric (SiO2 ; 300 nm, thermally grown) and a gate electrode (highly doped Si wafer). The microfluidic channels are formed by conformal contact of this substrate with an elastomeric element that is built using the techniques of soft lithography. In particular, casting and curing a prepolymer to poly(dimethylsiloxane) (PDMS) (Dow Corning) against a ‘‘master’’ structure of patterned negative photoresist (SU-8, Microchem Corp.; thickness ;15 mm) forms a transparent element with relief in the geometry of the resist. For the photolithography, we used printed transparencies for photomasks; the resolution of these masks (~25μm) determined the smallest features in our devices. As shown in Fig. 1(a), for the microfluidic transistors illustrated here, the relief consists of two square (~2mmx2mm) ‘‘reservoirs,’’ each of which is connected to a narrow channel. These channels travel from the reservoirs to a region where they are parallel and separated by a small distance. This area, which we refer to as the ‘‘transistor region,’’ forms the part of the device that defines the source and drain electrodes. After this transistor region, the channels lead to exits on opposite edges of the PDMS element. Depositing small droplets of mercury at the positions of the reservoirs, flipping the PDMS element over (the mercury clings to the surface of the PDMS) and then placing it against the substrate that supports the other components of the device leads to a ‘‘wetting’’ contact that seals the mercury in the reservoirs and forms closed

microchannels. When the surfaces of the SiO2 and the PDMS have been exposed briefly to an oxygen plasma, this contact leads to a strong, permanent bond between these two elements [5]. Experiments described elsewhere show that contact of the PDMS against the top surface of the pentacene film does not change the electrical properties of the accumulation channel that develops at the interface between the dielectric and the semiconductor or other characteristics of the transistors (e.g., the off currents, etc.)[6].

The PDMS element is aligned so that the transistor region overlaps with the rectangular area of the substrate that supports the pentacene. See Fig. 1(b). Applying slight mechanical pressure to the PDMS above the reservoirs (the low modulus of the PDMS allows it to be easily deformed) pumps the mercury into the channels. By adjusting the applied pressure, it is possible to control the distance that the mercury travels through the channels. Pumping the mercury so that it completely fills the channels causes it to flow over the pentacene and to complete a transistor whose source/drain electrodes are defined by the geometry of the PDMS element (i.e., the separation between the channels, and the distance along which they are parallel in the transistor region). In other words, in this configuration, the microchannels define the width (W) and length (L) of the transistor channel. When the mercury is only partially pumped through the transistor region, then the position of the fluid plug determines the transistor channel width.

Figure 1(c) shows optical micrographs collected by viewing the device through the transparent PDMS element in the transistor region, at three stages of pumping the mercury through the channel on the left. The mercury appears bright in these images. The curved corners of the channels facilitate flow. The microfluidic channels and the mercury overlap lines of Ti (2.5 nm)/Au (50 nm)/Ti (30 nm) which are formed on the substrate by electron beam evaporation through a shadow mask. These lines extend beyond the edges of the PDMS elements to enable electrical connection with conventional probe tips. See Figs. 1(a) and 1(b). The resistance at the contact between the mercury and the Ti/Au/Ti lines is negligible.

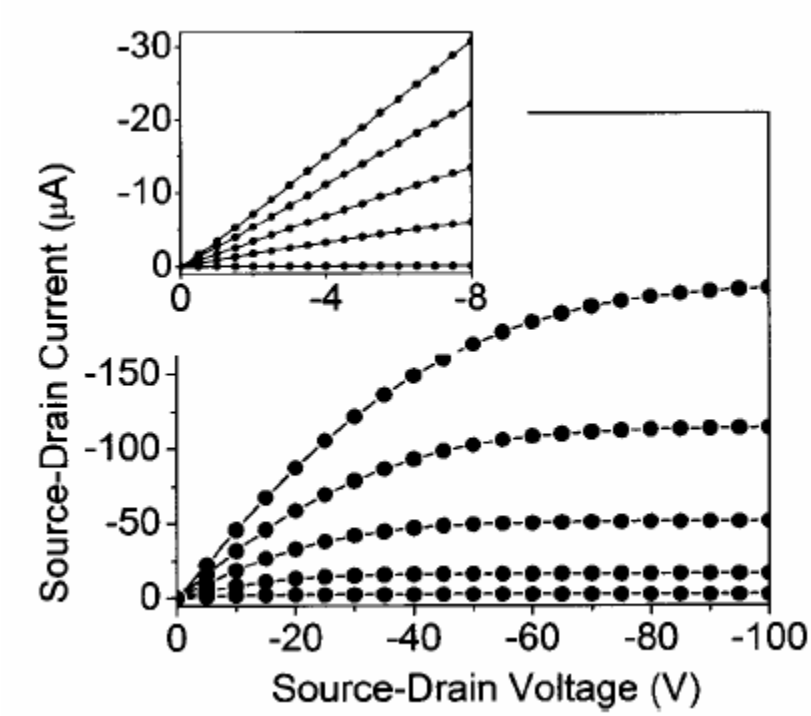

FIG. 2. Current-voltage characteristics of a microfluidic transistor that uses mercury for the source/drain electrodes and pentacene for the semiconductor. The top inset illustrates the response for source/drain voltages that are small compared to the gate voltage. The gate voltages for the inset are (from bottom to top curves): 0, -40, -60, -80, and -100 V. The gate voltages for the main part of this figures are (from bottom to top curves): -20, --40, -60, -80, and -100 V.

The current-voltage characteristics of the devices were determined with a semiconductor parameter analyzer (Agilent 4155). Figure 2 shows the properties of a device that has mercury pumped all the way through the transistor region of the microfluidic channels [i.e., in the geometry of the micrograph at the bottom of Fig. 1(c)]. The L and W of this device are 110 μm and 2.5 cm, respectively. The inset shows the response at source/drain voltages that are small compared to the gate voltage. The linear behavior is

consistent with ohmic contacts between the mercury and the pentacene.

The mobilities and threshold voltages computed using the standard expressions [7] in the saturation and linear regimes are, to within uncertainties, the same: 0.18 $\pm$0.02 cm^2/Vs and -18$\pm$2 V. We did not observe a systematic dependence of the linear or saturation regime mobilities or threshold voltages on L. These results are consistent with negligible effects of contacts for this range of transistor geometries.

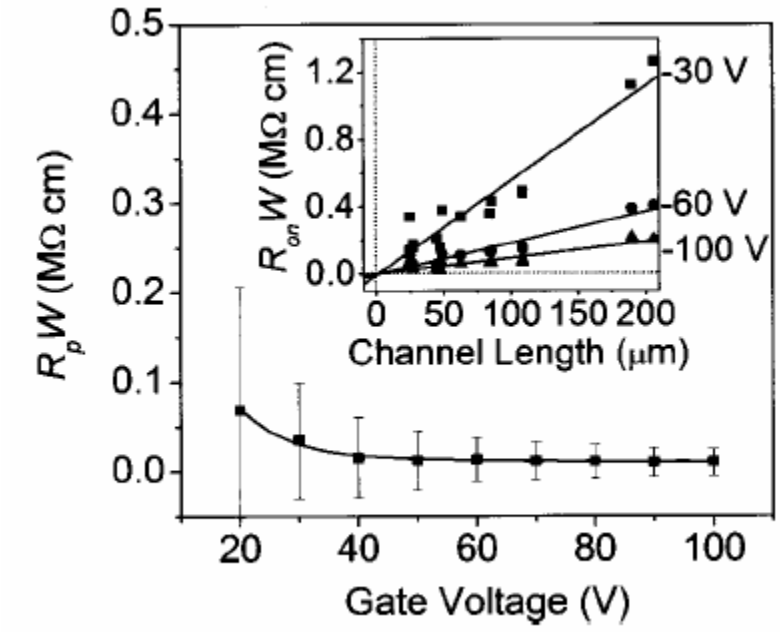

FIG. 3. Parasitic resistances associated with microfluidic transistors, as evaluated from the dependence of the device resistance on transistor channel length (as shown in the inset).

Figure 3 shows parasitic resistances computed by analyzing the linear regime behavior of 12 devices with a range

of channel lengths between 25 and 200 mm. This set of devices includes pentacene deposited in several different evaporations. The inset shows the overall width-normalized device resistance measured at small source/drain voltages and at different gate voltages; the y intercepts determine the parasitic resistances (i.e., the component of the device resistance that remains when the length of the channel is zero). These parasitics (which include the mercury–pentacene contact resistance) are sufficiently small that they are difficult to measure accurately in the devices described here. The transistor channel sheet conductances (S) can be measured from the inverse of the slope of the line fits shown in the inset to Fig. 3. The intrinsic mobility and threshold voltage (0.14 ±0.02 cm^2/Vs and -18±2V, respectively) follow from linear fits to these data according to

$$S = \mu_i C(V_G - V_{T,i}) \quad (1)$$

where μ_i and $V_{T,i}$ are the intrinsic mobility and threshold voltage, respectively, C is the capacitance of the gate dielectric, and V_G is the gate voltage [8]. These intrinsic channel properties are consistent with the saturation and linear regime results. They are also similar to intrinsic values determined from analysis of devices fabricated on the same substrate by evaporating gold electrodes (1 nm/s; 50 nm thick) onto the pentacene through a shadow mask. The parasitic resistances associated with evaporated gold

devices [7] are typically higher than those associated with the mercury microchannel electrodes.

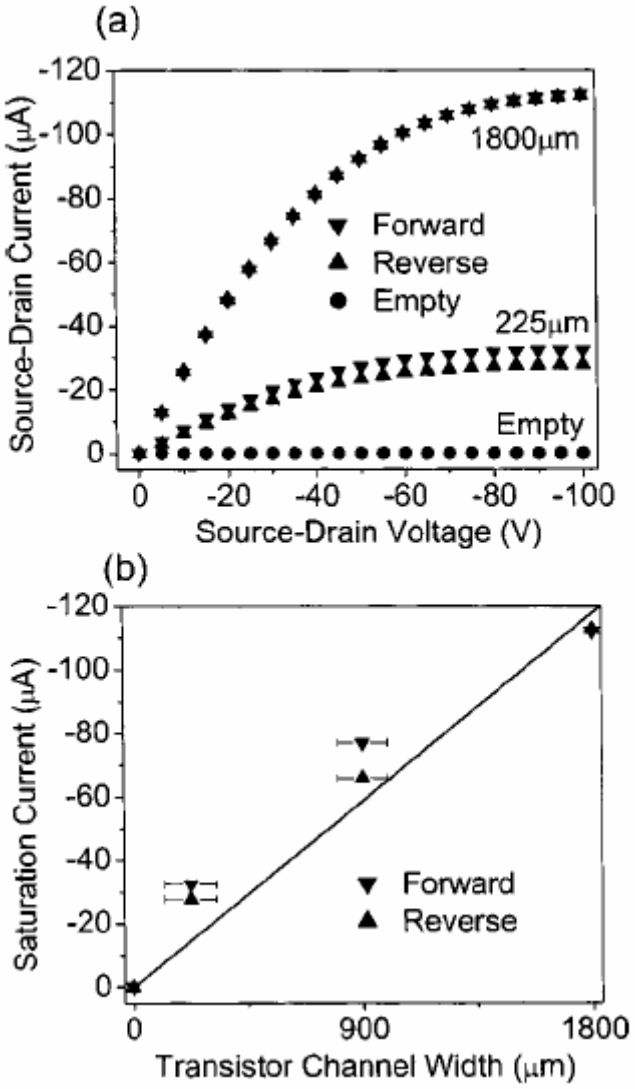

FIG. 4. Part (a) shows current/voltage characteristics of a microfluidic transistor evaluated at three tuning states with a gate voltage of -100 V. Curves measured during filling and emptying cycles (forward and reverse) are presented. Part (b) shows the associated saturation currents.

Pumping the mercury through the transistor region of the microfluidic system changes the width of the transistor channel. Figure 4 illustrates current-voltage responses of

a device pumped to configurations that yield different effective channel widths. For these data, the mercury was pumped to a fixed location in one of the two channels while the current–voltage measurements were made. The other of the two channels was filled completely with mercury for all measurements.

The results show a large tuning contrast ($>10^6$), which is limited partly by small leakage currents through the gate dielectric. Measurements performed as the mercury is pumped into and out of overlap with the pentacene in the transistor region yield the same results, to within uncertainties associated with determining the position of the front of the mercury plug. Although we did not perform long term reliability or cycling tests, there was no noticeable degradation in device performance during the several hours of measurements on several different devices before, during and after pumping.

The results presented in this letter demonstrate that (i) pumped microfluidic mercury source/drain electrodes and organic semiconductors provide the basis for a type of tunable transistor that can be integrated directly with plastic microfluidic systems, and (ii) the contact resistances between mercury and the organic semiconductor pentacene are <0.02 M• cm at large gate voltages, and the performance of the associated transistors are comparable to or better than those that are built in the conventional way. The fabrication procedures are compatible with plastic

substrates and with transistor channel lengths that are considerably shorter than those described here. (Similar fluidic channel systems have been used to mold source/drain electrodes for organic transistors with channel lengths of ~2 μm.)[9] They are also suitable for building microfluidic transistors with other fluidic conductors and organic or inorganic semiconductors. Designs in which fluid motion alters the transistor channel length rather than, or in addition to, the channel width are also possible. The simplicity of the fabrication procedures, the flexibility of the tuning approach, and its inherent compatibility with ‘‘soft’’ semiconductor materials and plastic microfluidic networks, all suggest that devices of this type have the potential to be useful for fundamental studies and applied work in organic electronics and microfluidics.

References:

[1] J. C. McDonald and G. M. Whitesides, Acc. Chem. Res. 35, 491 (2002).

[2] HT. Thorsen, S. J. Maerkl, and S. R. Quake, Science 298, 580 (2002).

[3] T. B. H. Jo, L. M. Van Lerberghe, K. M. Motsegood, and D. J. Beebe, J. Microelectromech. Syst. 9, 76 (2000).

[4] M. A. Rampi and G. M. Whitesides, Chem. Phys. 281, 373 (2002).

[5] O. J. A. Schueller, D. C. Duffy, J. A. Rogers, S. T. Brittain, and G. M. Whitesides, Sens. Actuators A 78, 149 (1999).

[6] Y.-L. Loo, T. Someya, K. W. Baldwin, P. Ho, Z. Bao, A. Dodabalapur, H.E. Katz, and J. A. Rogers, Proc. Natl. Acad. Sci. U.S.A. 99, 10252 (2002).

[7] S. Sze, Semiconductor Devices: Physics and Technology (Wiley, New York, 1985).

[8] J. Zaumseil, K. Baldwin, and J. A. Rogers, J. Appl. Phys. 93, 6117 (2003).

[9] J. A. Rogers, Z. Bao, and R. V. Raju, Appl. Phys. Lett. 72, 2716 (1998).

4. Electrical Microfluidic Pressure Gauge for PDMS MEMS

ABSTRACT

The first electrical-microfluidic pressure sensor is presented herein. An electrolyte-filled valved microchannel in a PDMS (polydimethylsiloxane) chip experiences a drastic increase in electrical resistance when and only when it is completely pinched off by the microvalve. This effect establishes a 1-1 correspondence between electrical resistance (low or high) and valve status (open or closed), thereby providing an electrical means of reporting valve status. Valve status (open or closed) is determined by applied pressure being below or above the characteristic closing pressure of the valve; therefore, the valve reports an upper or lower bound for the applied pressure, respectively. An array of such valves of varying closing pressures reports a set of inequalities that produce an interval estimate for the pressure. That estimate is reported as a set of resistance values of the respective microchannels, due to the 1-1 correspondence above. Hence, the overall system acts as an electrical microfluidic pressure gauge. This sensor would form a useful subunit within PDMS MEMS (micro-electro-mechanical systems), e.g. by reporting pressure values to electrical feedback control loops.

INTRODUCTION

The past ten years have witnessed the rapid development of PDMS (polydimethylsiloxane) microfluidic technology from the simplest of channels **[1]** to an extended family of devices integrated by the thousands within the same chip **[2]**. Such chips have emerged as the micro-scale hydraulic elastomeric embodiment of Richard Feynman's dreams of infinitesimal machines **[3, 4]**. PDMS microfluidics has been driven by applications from the beginning, with every advance being rapidly employed in devising solutions to specific problems **[5]**. Thus it is no surprise that many exciting specialized chips have emerged to offer new capabilities, e.g. in protein crystallization **[6]**, DNA sequencing **[7]**, nanoliter PCR **[8, 9]**, cell sorting and cytometry **[10, 11]**, nucleic acids extraction and purification **[12]**, immunoassays **[13-20]**, and cell studies **[21-25]**. After the development of pure microfluidic technology and the subsequent vigorous pursuit of its biological applications, it is becoming clear that the next generation of microfluidic devices would combine the fundamental technology with integrated electrical and/or optical systems for control and measurement. Such integration offers new analytical and functional capabilities, as well as true overall device miniaturization.

A few steps in this new direction have already been taken, producing a capacitance cytometer **[11]**, a thermal cycler **[8],** and a spectrophotometer **[26]**. Moreover, such

devices can be arranged as independent but interconnected modules functioning within the boundaries of a single chip **[27]**. Our program is developing such next-generation chips with specific emphasis on devices for medical applications **[5]**. We call this new class of devices **nanomedicine chips**. They are anticipated to have the plumbing, electronics, temperature control, and functional capabilities to allow significant miniaturization of many of the current clinical laboratory machines.

As part of this emerging wave of new devices, we present the first (to our knowledge) electrical microfluidic pressure gauge. It utilizes the fundamental effect that an electrolyte-filled valved microfluidic channel experiences a drastic increase in electrical resistance when and only when it is completely closed off by the microfluidic valve. This effect establishes a 1-1 correspondence between electrical resistance (low/high) and valve status (open/closed), thereby offering an electrical means of reporting valve status. On the other hand, each valve remains open up to some characteristic pressure determined by its dimensions **[28, 29]**. Therefore, there is another 1-1 correspondence, this time between valve status (open/closed) and applied pressure (below/above the valve's characteristic pressure). In essence, valve status is equivalent to an upper or lower bound on the applied pressure. Then, an array of valves closing at different characteristic pressures would offer a set of inequalities that combine to produce an

interval estimate of the applied pressure. The 1-1 correspondence between valve status and electrical resistance allows reporting this estimate electrically as a set of resistance states of the respective microchannels. The resulting system acts as a microfluidic pressure gauge with electrical readout. The device compatibility with standard PDMS microfluidic technology and electrical control make it ideally suitable for integration in the future PDMS MEMS.

MATERIALS AND METHODS

Microfluidic Device Fabrication

Substrate fabrication. DWL66 direct mask writer (Heidelberg Instruments GmbH, 69126 Heidelberg, Germany) with a 20mm head is used to create the respective pattern on glass slides coated with 90nm non-oxidized chrome and 530nm Az1500 photoresist (Telic Co., Valencia, CA 91355). The photoresist is developed for 20 sec in Microposit MF-322 (Rohm and Haas Electronic Materials). The sample is washed with deionized water. The exposed chrome is etched for 3 min in CR-7 Chromium Photomask Etchant, Surfactant Added (Cyantek Corp.). The sample is washed with deionized water, blown dry, and stored as is. Immediately before assembly to the PDMS slabs, the substrate is washed with acetone (to remove the remaining protective photoresist), washed with ethanol, and blown dry.

Chip Fabrication.

Standard fabrication techniques **[28]** and a recipe of ours **[20]** are employed to produce the molds and PDMS devices. The latter are washed in ethanol and blown dry before being bound to the ready metallized glass substrate. The now assembled chips undergo final bake in an 80degC oven overnight **(Figure 1)**.

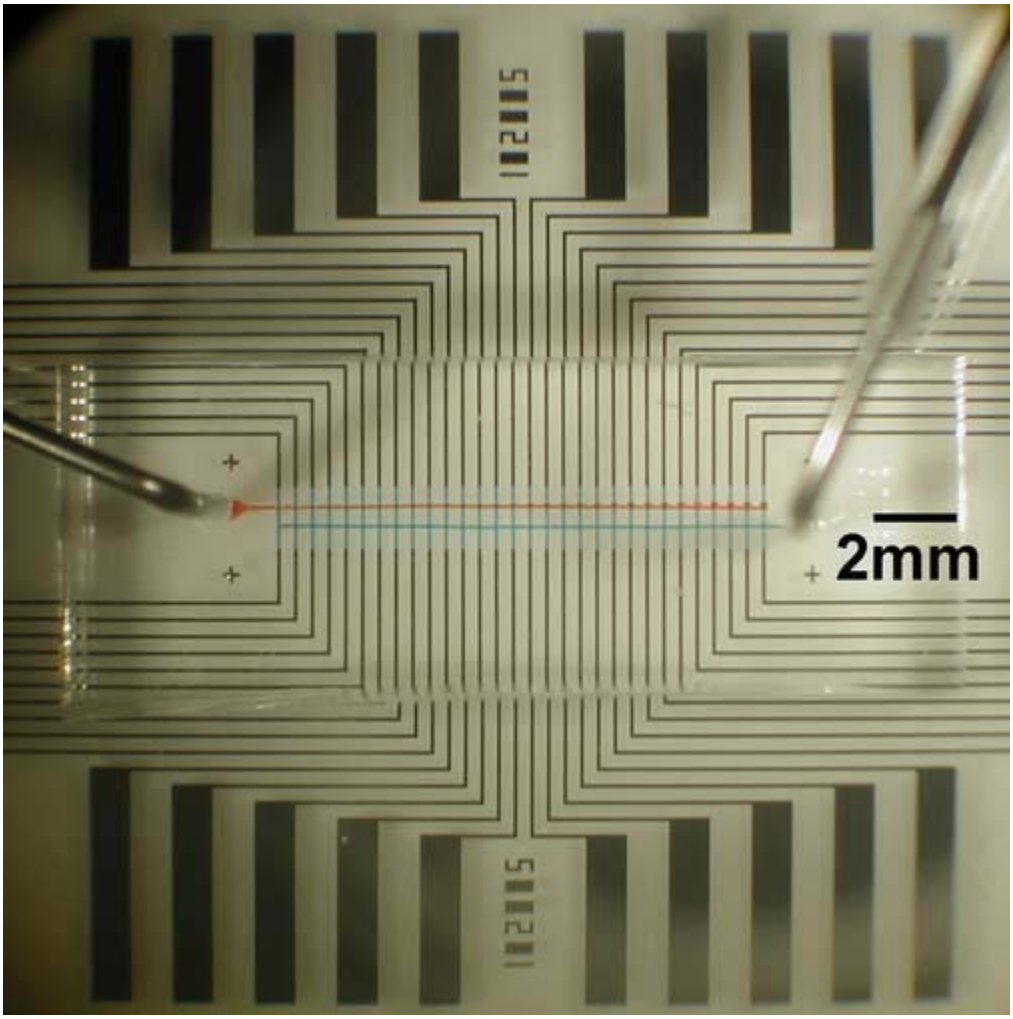

Figure 1. Device Architecture. A two-layer PDMS device is bound to a glass slide with chrome contacts in such a way that each pair of electrodes is matched to a short transverse segment of the lower-layer microchannel (blue dye; normally filled with salty buffer) **(A)**. The upper-layer channel (red dye; normally filled with deionized water) forms an array of microfluidic pushdown valves of varying dimensions (note valve length increasing from left to right in the picture) and thus varying characteristic closing pressures **(B)**.

Experimental Setup

The macrofluidic setup includes an inverted IX50 Olympus microscope, pressure regulators from AirTrol Components Inc (New Berlin, WI 53146), and a digital pressure gauge from TIF Instruments Inc (Miami, FL 33150). 23-gauge steel tubes

from New England Small Tube Corp. (Litchfield, NH 03052) are plugged into the chip's control channel ports. Their other ends are connected through Tygon® tubing (Cole-Parmer, Vernon Hills, IL 60061) to Lee-valve arrays (Fluidigm Corp. South San Francisco, CA 94080) operated by LabView software on a PC computer. A Nikon stereoscope SMZ-2T is equipped with a Nikon CoolPix990 color camera. Resistance measurements are conducted with a multimeter MiniRangemaster from Extech Instruments.

Basic Scheme

Standard multilayer soft lithography **[30]** is used to fabricate PDMS microfluidic chips. A comb-like array of 100•m-wide channels in the lower layer is crossed with a single channel in the upper layer to produce an array of pushdown microfluidic valves of varying length (55 to 200 •m). This PDMS two-layer device is then bound to a metallized glass substrate in such a way that each prong of the comb is aligned with its own pair of electrical contacts, thereby completing the chip fabrication **(Figure 1)**.

A salty buffer (Tris 10mM, NaCl 10 mM, MgCl2 0.1M, pH 8) is introduced in the lower (flow) layer by applying pressure and letting the preceding air escape through the polymer matrix. Filtered distilled water is similarly introduced in the upper (control) channel. The flow channel is then left at atmospheric pressure, while pressure is

applied to the control channel. For each value of the applied pressure, resistance is measured between the contacts of each prong. The status of the respective valve is also checked visually.

Ionic redistribution in response to the applied DC field tends to increase the resistance of the channel over time. While rapid measurements make this a small effect in the presented system, the polarity of applied voltage is reversed at every pressure setting to decrease the effect further.

RESULTS AND DISCUSSION

As PDMS and glass are electrical insulators, it is a reasonable expectation that an uninterrupted channel filled with a salty solution would drastically increase its electrical resistance if and only if it is pinched off by a closed valve. Simple preliminary experiments confirmed that expectation. The observed effect establishes a 1-1 correspondence between channel resistance (low/high) and valve status (open/closed). The mechanical properties of the valve establish another 1-1 correspondence, this time between the valve status (open/closed) and the applied pressure (insufficient/sufficient). Note that a single valve does not directly report the value of the pressure, but reports if the applied pressure is below or above the valve’s closing pressure. In essence, a single valve status produces a single inequality.

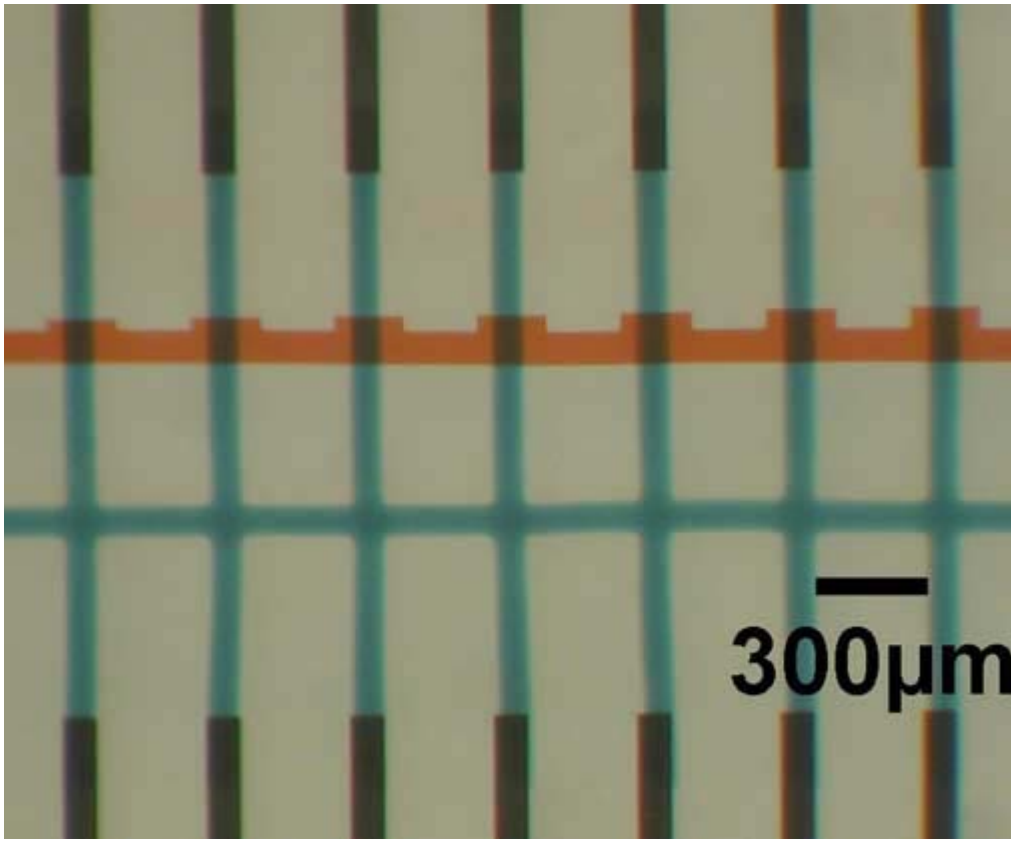

Figure 2. Device Function. Each valve closes if and only if the applied pressure exceeds the valve's characteristic pressure **(A)**. Thus the status of each valve determines applied pressure to an upper or lower bound. Then the status of a set of valves produces an interval estimate of the applied pressure. On the other hand, the electrical resistance of the electrolyte-filled channel segment under each valve (see Figure 1B) increases drastically if and only if the valve is closed **(B)**. Thus pressure determines valve array status determines electrical resistances status. Hence, the overall device functions as a microfluidic pressure gauge with electrical readout. **B** shows the resistance behavior of the channel segments under the valves from **A**, coded by same color.

Several such inequalities would narrow down the estimated pressure value better, especially if the respective bounds are judiciously selected. These bounds are the valves' closing pressures. Closing pressure is tuned by varying the valve's dimensions **[28, 29]**. Then an array of valves of different dimensions would provide the sought set

of pressure inequalities. Larger valves generally close at lower pressures **[28, 29]**. Hence, in principle, the applied pressure would be bound by the characteristic closing pressures of the largest open and the smallest closed valve. The resulting interval estimate for the applied pressure would be as narrow as the interval between the bounds. This analysis suggested the basic scheme described above. The scheme was implemented for applied pressures of 0.5 to 19 psi, in steps of 0.5 psi. The maximal value was set by the pressure at which all valves were closed. Further increase in the pressure would not change the result, while pressures in excess of 20 psi significantly increase the risk of layer delamination. All flow-channel prongs had resistances between 26 and 64 M• when the valves were open, while the resistance increased beyond the dynamic range of the multimeter (2 G•) when and only when the respective valve closed completely. Figure 2A shows the characteristic closing pressure versus valve length, for each valve. Figure 2B shows the resistance pattern versus applied pressure. Since in certain cases multiple valves closed at the same pressure, their resistance patterns practically overlapped. Consequently, multiple valves in one color in Figure 2A share one curve of the same color in Figure 2B. The system can be used as a pressure gauge, wherein the measured resistance of each channel indicates the status of the corresponding valve while the calibration ties

that status to the applied pressure. For example, if all valves up to and including "blue" are in "high resistance" state, while all valves above it (light green, red, black) are in "low resistance state", then according to Figure 2A, the applied pressure is between 10.5 and 11 psi. Alternatively, Figure 2B can be similarly used to arrive at the same conclusion.

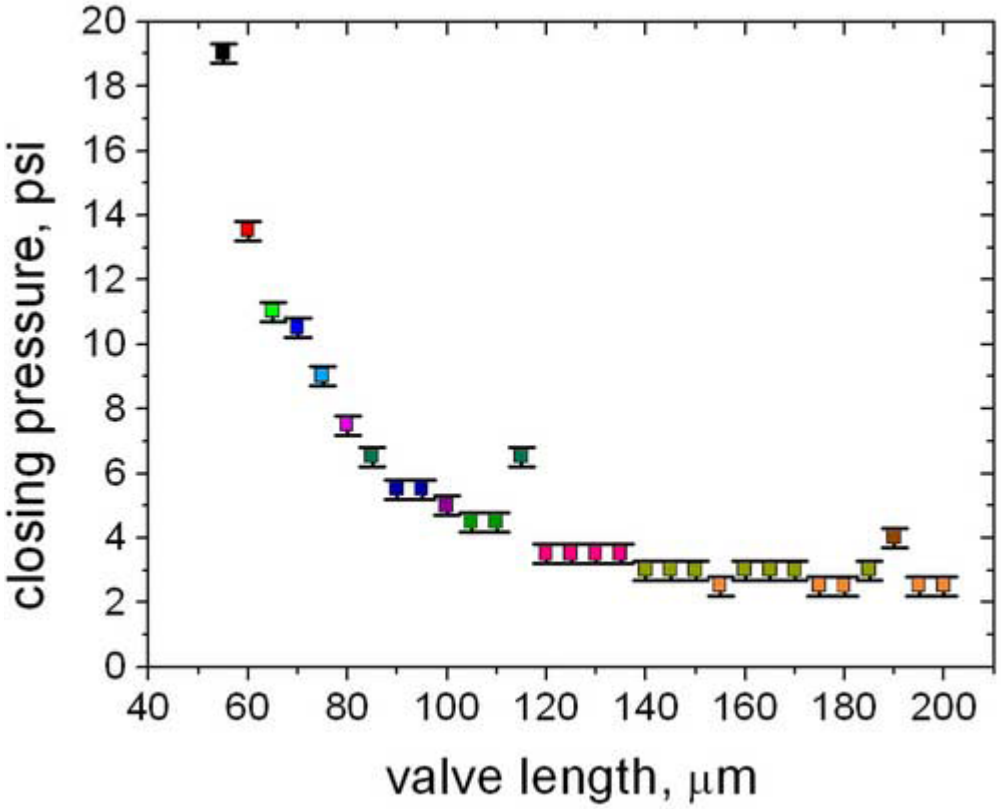

Figure 3 A graph of valve closing pressure with respect to the length of the valve. A highly sensitive region exists above 4psi

It is clear that the accuracy of pressure measurement is dependent on the pressure spacing of datapoints in Figure 2A, or of curves in Figure 2B. The desired accuracy in each particular application would require different closing pressures and thus different dimensions. Figure 2 shows that

high accuracy at high pressures cannot be achieved by varying *only* the valve length. However, if that restriction is relaxed, more values for the closing pressures become available **[29]** and the pressure spacing can be shrunk accordingly, thereby improving accuracy.

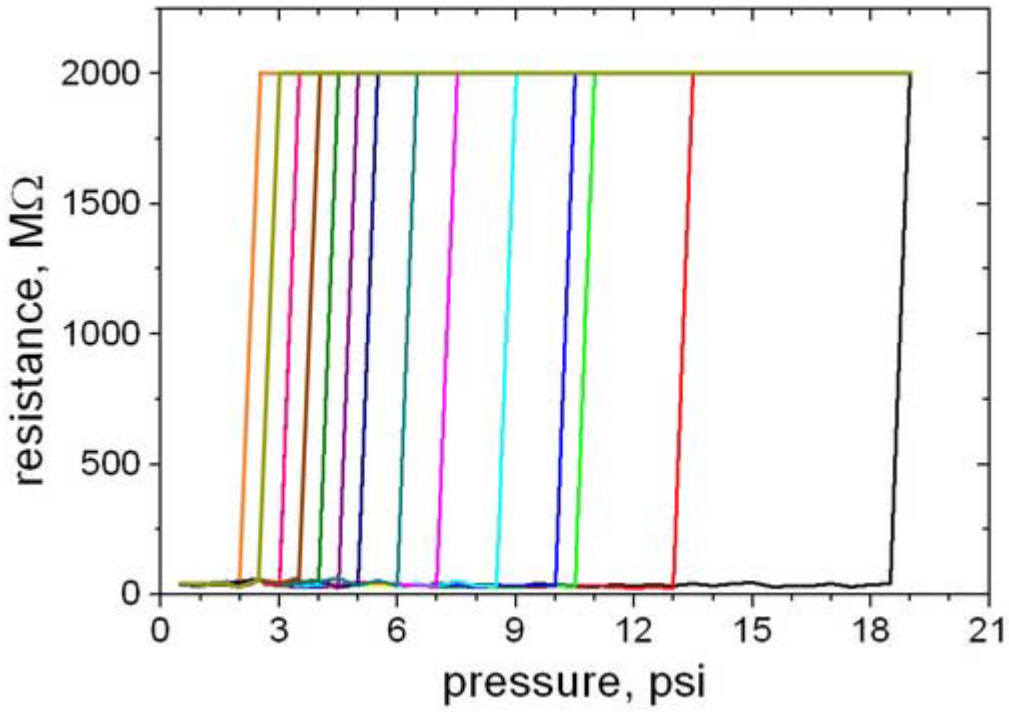

Figure 4. A graph showing the resistance measured across various valves (shown by the different colors) at different pressures. The graphs exhibit highly nonlinear behavior at a set pressure, allowing them to be used as excellent pressure gauges

Figure 2A shows that valves of lowest closing pressures generally break the rule that larger valves close at lower pressures. Of course a simple initial calibration can allow the device to function correctly, but if a better programmability of properties is required, then fabrication parameters can be changed to shift the sensitive part of the Figure 2A curve to lower pressures. For example, decreasing

valve membrane thickness would decrease the closing pressure for the same lateral dimensions **[29]**. Finally, a random fabrication artifact must be responsible for the significant deviation of the 115•m valve from the general dependence in Figure 2A. An individual glitch like that can be factored out trivially, as the pressure estimate is based on the results of the entire array. The presented pressure gauge is one of a set of components that would become increasingly important as microfluidics is developed further into hybrid integrated architectures **[27]** wherein microfluidic and electrical components are combined to form advanced novel devices. In particular, this sensor can be used to monitor pressure and electrically report the result to the logic circuitry that controls the overall PDMS MEMS device.

CONCLUSIONS

The first electrical-microfluidic pressure sensor is described herein. Applied pressure determines the status of an array of PDMS microfluidic valves of varying closing pressures. The electrical resistance of each valved channel is high if and only if the respective valve is closed. Thus valve array status and, therefore, an interval estimate of the pressure, are reported electrically. The overall microdevice functions as a pressure gauge with electrical readout. Its compatibility with both electrical circuitry and the basic PDMS microfluidic technology make it a

suitable subsystem for the next generation of hybrid PDMS MEMS.

REFERENCES

1. D.C. Duffy, J.C. McDonald, O.J.A. Schueller, and G.M. Whitesides, Rapid Prototyping of Microfluidic Systems in Poly(dimethylsiloxane), *Anal. Chem.* 70 (1998), 4974-4984

2. T. Thorsen, S.J. Maerkl, and S.R. Quake, Microfluidic Large-Scale Integration, *Science* 298 (2002), 580-584

3. R.P. Feynman, There's Plenty of Room at the Bottom, *J. MEMS* 1:1 (1992), 60-66

4. R.P. Feynman, Infinitesimal Machinery, *J. MEMS* 2:1 (1993), 4-14

5. E.P. Kartalov, W.F. Anderson, and A. Scherer, The Analytical Approach to PDMS Microfluidics and its Biological Applications, *J. Nanosci. Nanotech.*, (2006)

6. C.L. Hansen, E. Skordalakes, J.M. Berger, and S.R. Quake, A robust and scalable microfluidic metering method that allows protein crystal growth by free interface diffusion, *Proc. Natl. Acad. Sci. USA* 99:26 (2002), 16531-16536

7. E.P. Kartalov and S.R. Quake, Microfluidic device reads up to four consecutive base pairs in DNA sequencing-by-synthesis, *Nucl. Acids Res.* 32:9 (2004), 2873-2879

8. J. Liu, M. Enzelberger, and S. Quake, A nanoliter rotary device for polymerase chain reaction, *Electrophoresis* 23 (2002), 1531-1536

9. J. Liu, C. Hansen, and S.R. Quake, Solving the "World-to-Chip" Interface Problem with a Microfluidic Matrix, *Anal. Chem.* 75 (2003), 4718-4723

10. A.Y. Fu, H.-P. Chou, C. Spence, F.H. Arnold, and S.R. Quake, An Integrated Microfabricated Cell Sorter, *Anal. Chem.* 74 (2002), 2451-2457

11. L.L. Sohn, O.A. Saleh, G.R. Facer, A.J. Beavis, R.S. Allan, and D.A. Notterman, Capacitance cytometry: Measuring biological cells one by one, *Proc. Natl. Acad. Sci. USA* 97:20 (2000), 10687-10690

12. J.H. Hong, V. Studer, G. Hang, W.F. Anderson, and S.R. Quake, A nanoliter-scale nucleic acid processor with parallel architecture, *Nat. Biotech.* 22:4 (2004), 435-439 7

13. X. Jiang, J.M.K. Ng, A.D. Stroock, S.K.W. Dertinger, and G.M. Whitesides, A Miniaturized, Parallel, Serially Diluted Immunoassay for Analyzing Multiple Antigens, *J. Am. Chem. Soc.* 125 (2003), 5294-5295

14. M.E. Piyasena, T. Buranda, Y. Wu, J. Huang, L.A. Sklar, and G.P. Lopez, Near-Simultaneous and Real-Time Detection of Multiple Analytes in Affinity Microcolumns, *Anal. Chem.* 76 (2004), 6266-6273

15. K.S. Phillips and Q. Cheng, Microfluidic Immunoassay for Bacterial Toxins with Supported Phospholipid Bilayer Membranes on Poly(dimethylsiloxane), *Anal. Chem.* 77 (2005), 327-334

16. H. Tani, K. Maehana, and T. Kamidate, Chip-Based Bioassay Using Bacterial Sensor Strains Immobilized in Three-Dimensional Microfluidic Network, *Anal. Chem.* 76 (2004), 6693-6697

17. E. Eteshola and D. Leckband, Development and characterization of an ELISA assay in PDMS microfluidic channels, *Sensors and Actuators B* 72 (2001),129-133

18. E. Eteshola and M. Balberg, Microfluidic ELISA: On-Chip Fluorescence Imaging, *Biomed. Microdevices* 6:1 (2004), 7-9

19. Y. Murakami, T. Endo, S. Yamamura, N. Nagatani, Y. Takamura, and E. Tamiya, On-chip micro-flow polystyrene bead-based immunoassay for quantitative detection of tacrolimus (FK506), *Anal. Biochem.* 334 (2004), 111-116

20. E.P. Kartalov, J. Zhong, A. Scherer, S.R. Quake, C.R. Taylor, and W.F. Anderson, High-throughput multi-antigen microfluidic fluorescence immunoassays, *BioTechniques*, 40 (2006)

21. H. Wu, A. Wheeler, and R. Zare, Chemical cyotmetry on a picoliter-scale integrated microfluidic chip, *Proc. Natl. Acad. Sci USA* 101:35 (2004), 12809-12813

22. A.M. Taylor, M. Blurton-Jones, S.W. Rhee, D.H. Cribbs, C.W. Cotman, and N.L. Jeon, A microfluidic culture platform

for CNS axonal injury, regeneration and transport, *Nat. Methods* 2:8 (2005), 559-605

23. J.V. Rocheleau, G.M. Walker, W.S. Head, O.P. McGuinness, and D.W. Piston, Microfluidic glucose stimulation reveals limited coordination of intracellular Ca2+ activity oscillations in pancreatic islets, *Proc. Natl. Acad. Sci. USA*, 101:35 (2004), 12899-12903

24. C. Ionescu-Zanetti, R.M. Shaw, J. Seo, Y.-N. Jan, L.Y. Jan, and L.P. Lee, Mammalian electrophysiology on a microfluidic platform, *Proc. Natl. Acad. Sci USA* 102:26 (2005), 9112-9117

25. F.K. Balagadde, L. You, C.L. Hansen, F.H. Arnold, and S.R. Quake, Long-Term Monitoring of Bacteria Undergoing Programmed Population Control in a Microchemostat, *Science* 309 (2005), 137-140

26. M.L. Adams, M. Loncar, A. Scherer, and Y. Qiu, Microfluidic Integration of Porous Photonic Crystal Nanolasers for Chemical Sensing, *IEEE J. on Selected Areas in Communications* 23 (7) (2005), 1348-1356

27. K.A. Shaikh, K.S. Ryu, E.D. Goluch, J.-M. Nam, J, Liu, C.S. Thaxton, T.N. Chiesl, A.E. Barron, Y. Lu, C.A. Mirkin, and C. Liu, A modular microfluidic architecture for integrated biochemical analysis, *Proc. Natl. Acad. Sci. USA* 102:28 (2005), 9745-9750

28. V. Studer, G. Hang, A. Pandolfi, M. Ortiz, W.F. Anderson, and S.R. Quake, Scaling properties of a low-

actuation pressure microfluidic valve, *J. Appl. Phys.* 95:1 (2004), 393-398

29. E.P. Kartalov, A. Scherer, S.R. Quake, C.R. Taylor, and W. F. Anderson, Experimental Study and Theoretical Modeling of the Mechanical Behavior of PDMS Microfluidic Valves, *in press*

30. M.A. Unger, H.-P. Chou, T. Thorsen, A. Scherer, and S.R. Quake, Monolithic Microfabricated Valves and Pumps by Multilayer Soft Lithography, *Science* 288 (2000), 113-116

II
Devices created through the use of novel Three-Dimensional rapid prototyping techniques

1. Replication of three-dimensional valves from printed wax molds

Abstract

We describe microfluidic vias, channels and valves fabricated by replication molding of polydimethylsilicone (PDMS) into printed wax molds. Additionally we show how completely polymer embedded microfluidic circuits can be realized with this technique. A novel three-dimensional microfluidic valve is also demonstrated which is robust against swelling and which operates at up to 30psi flow pressure. This method for defining microfluidic devices offers higher pressure tolerance and more resistance to corrosive solvents, as de-lamination problems can be avoided. It also enables a great flexibility in choice of replicated polymers and three-dimensional interconnection topologies to form complex microfluidic circuits for microbiochemical analysis.

Introduction

Recently, lithographic techniques have been successfully applied towards the miniaturization of fluidic elements, such as valves, pumps and limited three dimensional structures (1-9). The integration of many devices on a single fluidic chip has enabled the development of powerful and flexible analysis systems with applications ranging from cell sorting to protein synthesis (10-14). Through replication molding and embossing from photolithographically

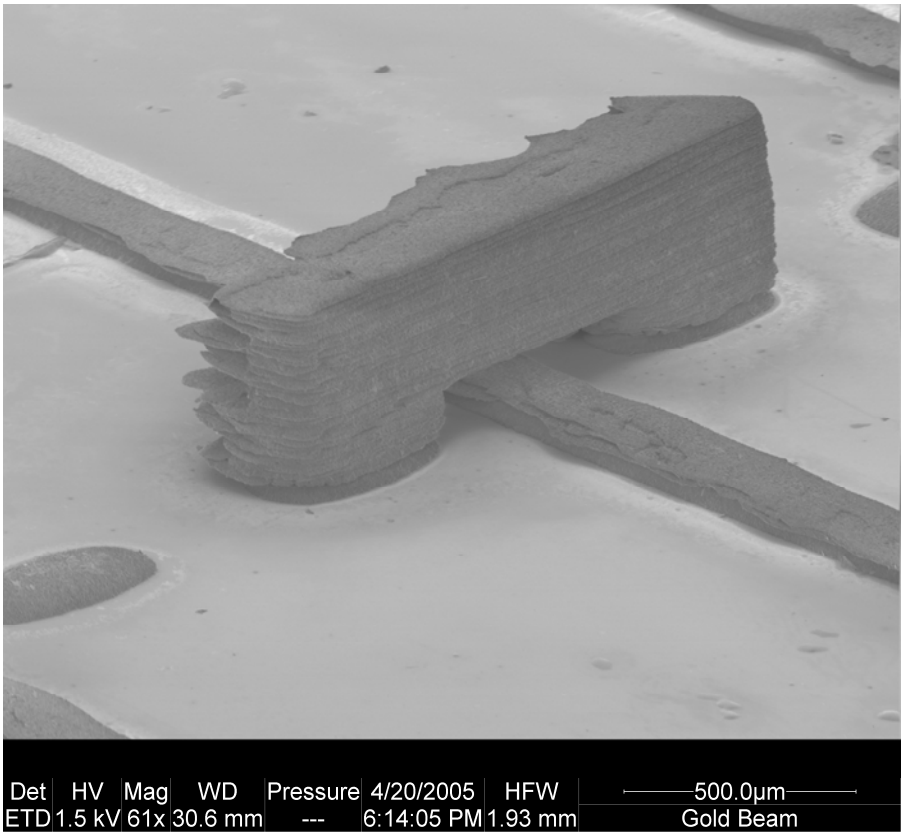

Figure 1. SEM picture showing a 115µm wide wax mold for a fluid line printed on a glass slide

patterned dies, inexpensive fluidic systems with pneumatic actuation have been developed, by several groups (15-18). Hermetically sealed valves, pumps and flow channels can be formed in polydimethylsilicone (PDMS) and related compounds (RTV, etc.), and in multilayer soft lithography, two or more replication molded layers are aligned and subsequently bonded to create systems of pneumatic actuation channels controlling flow within a layer of flow channels (8). As the geometry of the pneumatic valve determines the actuation pressure, it is possible to define pneumatic multiplexing geometries that permit the control of many valves on a microfluidic chip by a much smaller number of control valves

off-chip (19). Unfortunately, the two-dimensional nature of the flow channel arrangement limits the interconnection of

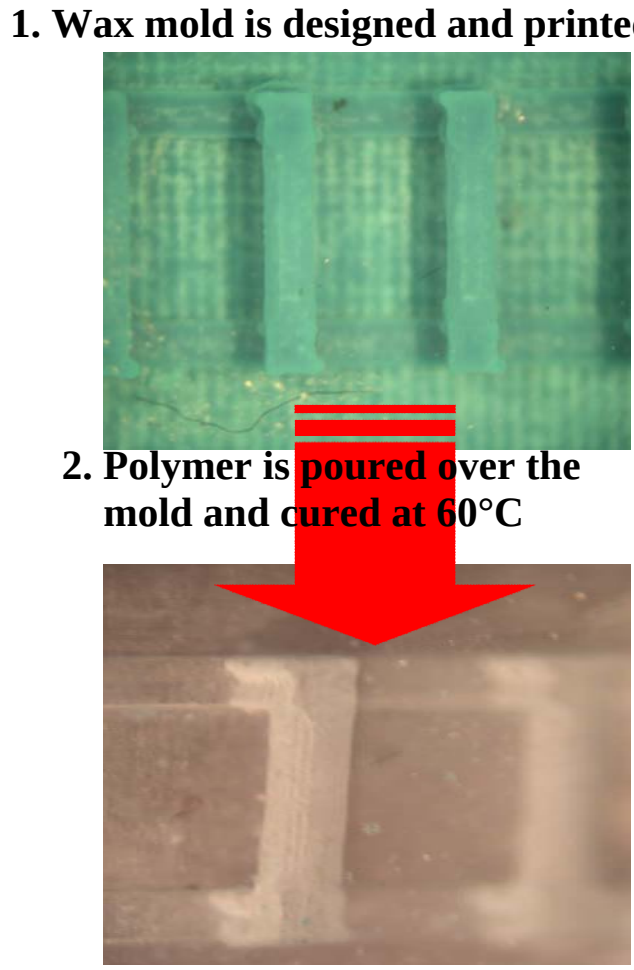

Figure 2. Wax printed via holes connecting two flow channels before and after removal of the wax. The basic fabrication steps are described: 1. First the mold is designed and printed, the mold is then placed in solvent (mineral oil) in order to dissolve the sacrificial wax and then dried. 2. PDMS is poured over the wax mold and allowed to cure at 60°C. 3. The wax is then melted out of the PDMS at 150°C, leaving a three-dimensional microfluidic chip.

this kind of two-dimensional fluidic system. Moreover, multi-layer soft lithography requires the use of elastomeric

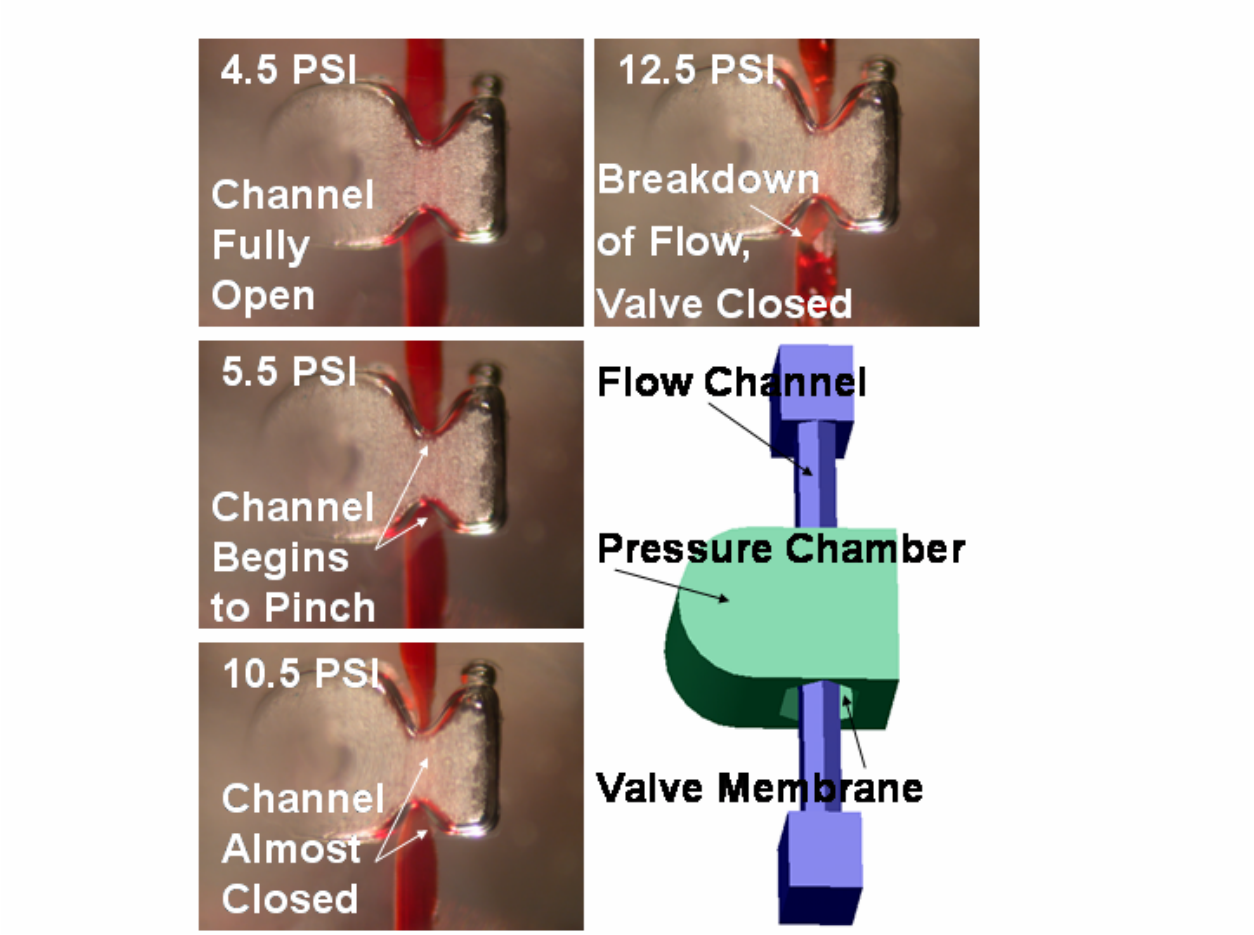

Figure 3. Three-dimensional valve constructed by wax printing and replication. The actuation pressure is only 62kPa (9psi) larger than the channel pressure. The disruption of flow caused by closing the valve is visible as air bubbles in this picture.

materials that can bond well to each other to avoid delamination of the pneumatic film layer from the fluid flow layer. Our approach in this report was to create a truly three-dimensional mold that could be embedded in a polymer, and the melted out in order to eliminate the requirement of traditional microfluidics that the chip be multilayer and bonded to a substrate in order to form a complete channel with valves. We also sought to eliminate the two-

dimensional restrictions on fluid and control line routing

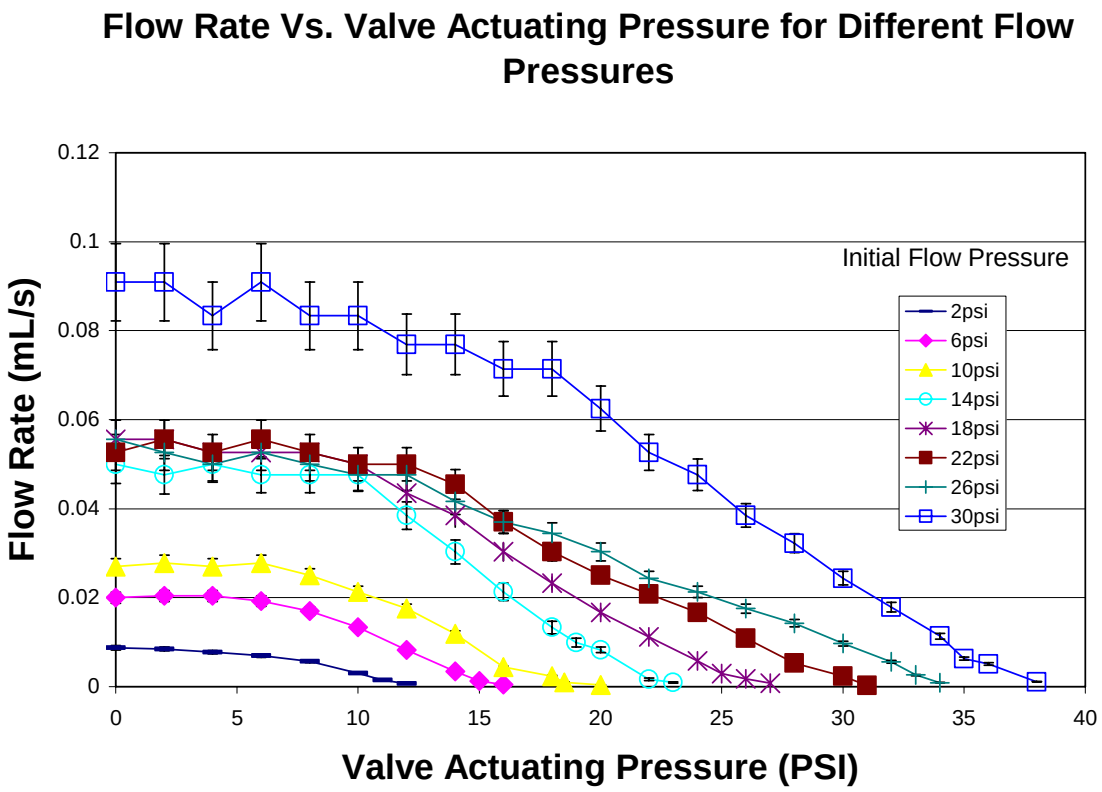

Figure 4. The valve enters a tunable region in which the flow pressure is strongly affected by the actuating pressure. Toward the right of the graph we enter a region of cutoff and have leak-tight flow of less than .1 ml over 1 hour of testing.

and alignment by creating three-dimensional vias to enable crossed paths. Finally we sought to make a completely embedded chip with control lines and fluid lines made only of polymer.

Fabrication

To solve these limitations of two-dimensional layered systems and to enable more flexible microfluidic plumbing topologies, we disclose here a three-dimensional replication

molding scheme that permits the construction of valves and pumps that are interconnected in all dimensions. To create three-dimensional replication dies, we use a commercial wax printing system (Solidscape T66) which can define features as small as 12.5 microns high by 115 microns wide (Fig. 1) when printing directly on a glass or silicon substrate. The apparent surface roughness of the wax mold has little influence on valve performance other than to slightly increase the closing pressure required for a leak tight valve. The combination of printed wax droplets with precise milling heads and stage positioning enables wax molds to be constructed with feature sizes comparable to those made by photolithography. The wax mold can be computer designed and printed directly onto a flat substrate without the need for any photolithography masks. The designer can fabricate three-dimensional microfluidic components interconnected with great flexibility. Three-dimensional connections between fluidic layers offer more flexible design opportunities that are inaccessible with planar techniques. Printing is carried out with 2 waxes – one that forms the structures which are "negatives" of the desired microchannels, and the other that acts as a sacrificial material and temporarily supports suspended structures during fabrication. After dissolution of the sacrificial wax material, PDMS or another prepolymer can be poured onto the mold and cured. Finally, the sacrificial wax mold is melted away to provide the completed microfluidic device

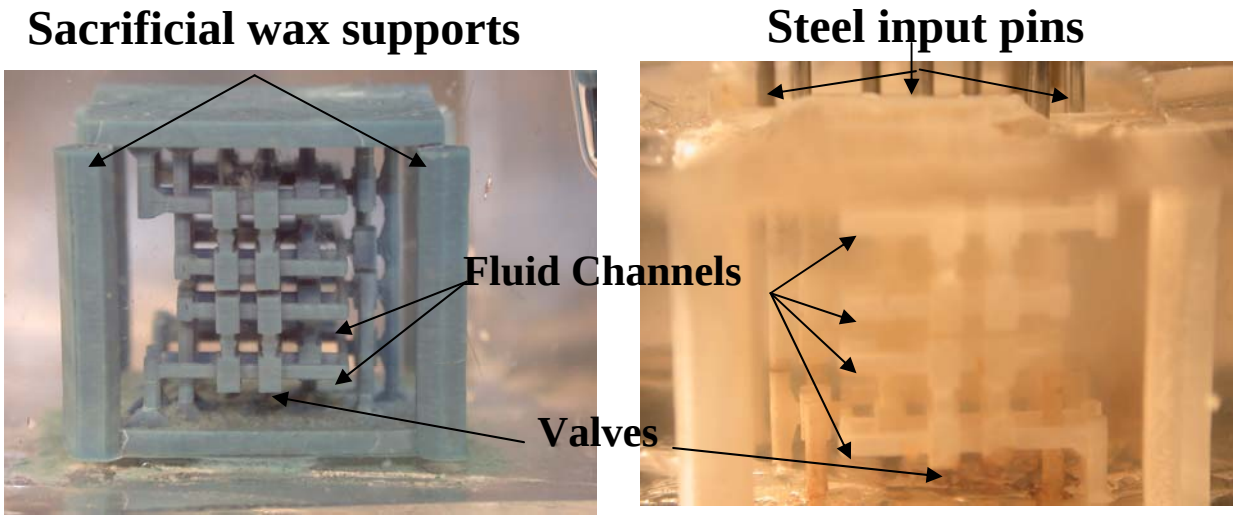

Figure 5. Micrograph of a wax mold before and after pdms replication molding showing the geometry of the flow channels and the pneumatic actuation valves for a 36 valve, 16 to 1 fluidic multiplexer. The chip is made entirely of pdms without the need for bonding to glass, and pressure inputs are made via steal pins on both sides (only the top side show

geometry (Fig. 2 and 3). This approach was used to construct fluidic conduits that require structural supports only every few centimeters, as well as robust, tunable, three-dimensional valves (Fig. 3-4) which can control flow pressures of over 220 kiloPascals (33 psi). The 3-D replication-molded microfluidic design is also very resistant to swelling caused by aggressive solvents. Three-dimensional printing eliminates the need for bonding the pneumatic control layer to the flow layer as both are formed in the same monolithic mold. This enables the use of elastomers that can be bonded only once or do not satisfy the adhesion requirements of multi-layer fabrication such as

the highly solvent-resistant perfluoropolyether (PFPE) The elimination of multiple bonding steps also avoids the need for aligning multiple elastomeric layers and compensation for polymer shrinkage. Additionally, components can be embedded into the device in a three-dimensional fashion and pin input holes can be formed as part of the mold in situations where punching would crack brittle polymer layers. Solvent-resistant microfluidic components enable the use of organic solvents incompatible with polydimethylsiloxane (PDMS), thus opening up a vast array of potential microfluidics applications in organic chemistry and combinatorial synthesis.

Result

We have designed a truly three-dimensional normally open valve geometry (Fig. 3). A suspended fluid flow tube is surrounded by a doughnut-shaped pressure chamber. The valve is actuated by increasing the pressure in the doughnut chamber surrounding the fluid flow tube by a predictable amount dependent on the precise valve geometry. Figure 3 has a schematic diagram of the wax mold, onto which PDMS is poured and cured, and the wax is then melted out. The closing pressure in the “pressure chamber” communicates with the “flow channel” via a thin “valve membrane” formed by a gap in the wax mold. Typical flow curves of a three-dimensional pneumatic valve constructed in PDMS can be observed. In Figure 4, the flow rate is shown as a function

of the actuating pressure of the pneumatic ring for various flow pressures applied to the fluidic channel. From this data, it is evident that the 3-D valve is able to perform even at relatively very high pressures of ~250 kPa (35psi). At all tested pressures, the valve can be closed by applying a pneumatic pressure 62kPa (9psi) above the flow pressure applied to push fluids through the flow channel. The maximum pressure range as well as the control over the valve actuating pressure compares very favorably with traditional planar valves constructed through multi-layer soft lithography. In comparison, our multi-layer soft lithography layers delaminate at approximately 82kPa (12psi). Figure 4 also shows that the 3-D valve can be predictably tuned over a large range of flow rates by controlling the actuating pressure and initial flow pressure. The graph depicts a family of curves that represent a variety of different initial flow pressures. In general, we observe 3 important regions: (a) toward the left part of the valve response plot, at low actuation pressures, we note a region within which the valve is unaffected by the actuating pressure. In this case, the flow pressure is significantly larger than the actuating pressure. As the actuating pressure becomes comparable to the flow pressure, (b) the valve enters a tunable region where the flow is linearly sensitive to actuation pressure. Finally, (c) the valve is pinched off when the difference between the actuating pressure and flow pressure reaches 62kPa (9psi). Flow rates were

experimentally measured with a 10ml graduated cylinder and a stopwatch. After the pneumatic valve actuator pressure was established, the fluid flow valve was opened and simultaneously a timer was used to measure flow rates. When 1.0 ml of fluid flowed through the valve and was accumulated in a collection reservoir, the time was measured and a flow rate was calculated. Measurements were conducted for several devices to confirm good reproducibility. Flow hysterisis was found to be negligible and did not influence the measurements as the valve was always open at the beginning of each experiment.

Our pneumatic 3-D valve was also tested in solvents that are known to deteriorate PDMS channels. For example, the valve performance was evaluated when metering toluene, a material known to result in swelling of PDMS and deterioration and distortion of conventional PDMS fluidic systems. As our 3-D valve definition procedure does not rely on multi-layer PDMS films that could delaminate, no leakage or deterioration could be observed in our 3-D valve after exposure to toluene. Although the tenability suffered due to swelling over time, the valve performance was not influenced. Figure 5 shows an optical micrograph of a three dimensional multiplexer mold consisting of an integrated bi-level array of 18 3-D pneumatic valves. From this image, it is clear that large plumbing systems consisting of integrated arrays of microfluidic valves can be constructed by 3-D microvalve definition. In such a valve network, the

density of fluidic elements can be significantly increased beyond what is available for more traditional 2-D microfluidic networks constructed from PDMS. In such 3-D fluidic chips, the smallest flow pressure line that can be defined by the lateral and vertical resolution of the wax printer is 115 microns wide by 12.5 microns high (although some difficult geometries require more material strength and must be made larger). These dimensions match well with geometries suitable for the definition of useful microfluidic "laboratory on a chip" applications. It is well known that in geometries much below 10 microns the Reynold's number is very low and the differential fluid flow velocity in the center of the channel versus at the channel wall can be significant. These effects limit the usefulness of fluidic systems with dimensions much below the 100x10 channels and valves that we describe here.

Conclusion

Three-dimensional soft lithography offers many advantages over the more conventional multi-layer soft lithography, which is based on 2-D valve and pump definition. One key advantage of developing devices from 3-D replication molding is that it enables the use of a wide variety of elastomers and plastics that are more corrosion resistant than PDMS. Moreover, the pressure in the flow channels can be increased and the actuation pressure of the pneumatic lines can be decreased by implementing designs that do not involve layers

that may delaminate and can close the valve by applying pneumatic pressure from all sides. The most important opportunity obtained from 3-D definition is the increase in inter-connectivity of the fluidic components and improvement in the flow channel integration in all three dimensions through the use of via holes that can jump over a fluidic layer with a commercially available wax molding system. Our first results on this new kind of microfluidics indicates that denser integration with larger numbers of components and more complex fluidic multiplexing systems can be implemented through 3-D replication molding.

References:

[1] J.P. Brody and P. Yager, “Low Reynolds number microdevices”, In Proc. Of Solid State Sensor and Actuator Workshop, pp. 105-8. Hilton Head, June 1996.

[2] S.R. Quake and A. Scherer, “From Micro to Nano Fabrication with Soft Materials”, Science 290, 1536 (2000).

[3] H.P. Chou, M.A. Unger, A. Scherer and S.R. Quake, “A Microfabricated Rotary Pump”, Biomedical Microdevices 3, 323 (2001).

[4] J. Liu, M. Enzelberger, and S.R. Quake, “A nanoliter rotary device for PCR”, Electrophoresis, in press.

[5] Jeon NL, Chiu DT, Wargo CJ, Wu HK, Choi IS, Anderson JR, Whitesides GM, “Design and fabrication of integrated passive valves and pumps for flexible polymer 3-dimensional

microfluidic systems", BIOMEDICAL MICRODEVICES 4 (2): 117-121 MAY 2002

[6] Wu HK, Odom TW, Chiu DT, Whitesides GM, "Fabrication of complex three-dimensional microchannel systems in PDMS", JOURNAL OF THE AMERICAN CHEMICAL SOCIETY 125 (2): 554-559 JAN 15, 2003

[7] M.A. Unger, H.P. Chou, T. Thorsen, A. Scherer and S.R. Quake, "Monolithic Microfabricated Valves and Pumps by Multilayer Soft Lithography", Science 288, 113 (2000).

[8] K. Ikuta, S. Maruo, Y. Fukaya, T. Fujisawa, "Biochemical IC chip toward cell free DNA protein synthesis", MEMS 2000, Miyazaki, Japan, Jan. 23-27 2000, pp.131-136.

[9] K. Ikuta, T. Hasegawa, T. Adachi, S. Maruo, "Fluid drive chips containing multiple pumps and switching valves for Biochemical IC Family", MEMS 1998, Heidelberg, Germany, Jan. 25-29 1998, pp. 739-744.

[10] H. Morgan, N.G. Green, M.P. Hughes, W. Monaghan and T.C. Tan, "Large area traveling-wave dielectrophoresis particle separator", J. Micromech. Microeng. 7, 65 (1997).

[11] S. Fiedler, S.G. Shirley, T. Schnelle, and G. Fuhr, "Dielectrophoretic sorting of particles and cells in a microsystem", Anal. Chem. 70, 1909 (1998).

[12] M.U. Kopp, A.J. deMello, A. Manz, "Chemical amplification: continuous flow PCR on a chip", Science 280, 1046 (1998).

[13] L.C. Waters, S.C. Jacobson, N. Kroutchinina, J. Khandurina, R.S. Foote and J.M. Ramsey, "Microchips devices

for cell lysis, multiplex PCR amplification, and electrophoretic sizing", Anal. Chem. 70, 158 (1998).

[14] P.H. Li and D.J. Harrison, "Transport, manipulation and reaction of biological cells on-chip using electrokinetic effect", Anal. Chem. 69, 1564 (1997).

[15] A.G. Hadd, D.E. Raymond, J.W. Halliwell, S.C. Jacobson and J.M. Ramsey, "Microchip device for performing enzyme assays", Anal. Chem. 69, 3407 (1997).

[16] A.G. Hadd, S.C. Jacobson and J.M. Ramsey, "Microfluidic assays of acetylcholinesterase inhibitors", Anal. Chem. 71, 5206 (1999).

[17] N.H. Chiem and D.J. Harrison, "Microchip-based capillary electrophoresis for immunoassays: analysis of monoclonal antibodies and theophylline", Electrophoresis 19, 3040 (1998).

[18] A.Y. Fu, C. Spence, A. Scherer, F.H. Arnold and S.R. Quake, "A microfabricated fluorescence-activated cell sorter", Nature Biotech. 18, 309 (2000).

[19] T. Thorsen, S.J. Maerkl, S.R. Quake, "Microfluidic Large-Scale Integration", Science 298, 5593 (2002).

2. Chemically robust three-dimensional monolithic SIFEL fluoropolymer microfluidics

Abstract

A current problem in microfluidics is that the standard poly(dimethylsiloxane) (PDMS) polymer used to make microfluidic devices is not compatible with most organic solvents. Fluorinated compounds are more chemically robust but in the past it was nearly impossible to construct valves out of them by multilayer soft lithography. With our new three-dimensional (3D) valve design we can fabricate microfluidic devices using fluorinated compounds in a single monolithic layer that is resistive to these chemicals by virtue of the polymer and the design itself is swell tolerant. This paper describes the design and development of 3D microfluidic valves by molding of a perfluoropolyether, known as Sifel, onto printed wax molds encapsulated by PDMS. The above mentioned fabrication has the potential to expand the use of microfluidic applications in such areas as organic chemistry.

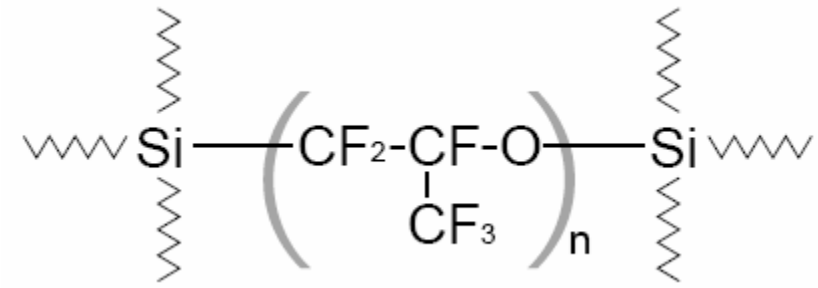

The perfluoropolyether backbone with terminal silicon crosslinking groups of sifel

Introduction

In the past decade soft polymers, such as PDMS, have emerged as the material of choice for microfluidic and soft lithography applications.[1-6] PDMS offers the advantages of being less expensive and simple to fabricate using the methods of soft lithography.[2-4] It exhibits elastomeric properties with a surface energy of ~20erg/cm2 and low Young's modulus value of ~750kPa; thus, allowing the material to conform and easily seal to other surfaces, both reversibly and irreversibly.[5] In addition, PDMS is optically transparent in the UV-visible light region. Despite the advantages of PDMS in microfluidic applications, one of the most prominent drawbacks with the use of this polymer is its incompatibility with most organic solvents including acyclic and cyclic hydrocarbons (pentanes, hexanes, heptane, cyclohexane), aromatic hydrocarbons (xylenes, toluene, benzene), halogenated compounds (chloroform, trichloroethylene), ethers (diethyl ether, dimethoxyethane, tetrahydrofuran), and amines (diisopropylamine, dipropylamine, triethylamine).[6] These solvents can cause swelling in the material, leading to changes in the cross-sectional area of microchannels and, therefore, changes in the rate of flow. Swelling can also alter surface properties and cause the device to delaminate.[6] As a result, applications involving organic

solvents require the use of other materials that do not interact directly with the polymer.

To solve these limitations we have developed a novel solvent-resistant microfluidic device based on a fluoroelastomeric material and 3D microvalves from printed wax molds. Numerous methods have previously been utilized to create 3D structures; one of the most common techniques is known as the “membrane sandwich” method.[5,7-10] This procedure involves the fabrication of three-dimensional systems by curing multiple layers together so that they create 3D patterned structures composed entirely of a single elastomer.[7-8] This method is limited, however, by the difficulty of making effective interconnections between layers during fabrication including aligning, stacking, and bonding patterned membranes of PDMS. An alternative, non-photolitographic technique for producing masters is solid-object printing.[11] By using this technique we were able to print 3D wax molds without the need for masks or alignment and required only a computer file to direct the wax printer. Here, we used a perfluorinated elastomer, known as Sifel,[12] to create a solvent-resistant system (Figure 1).

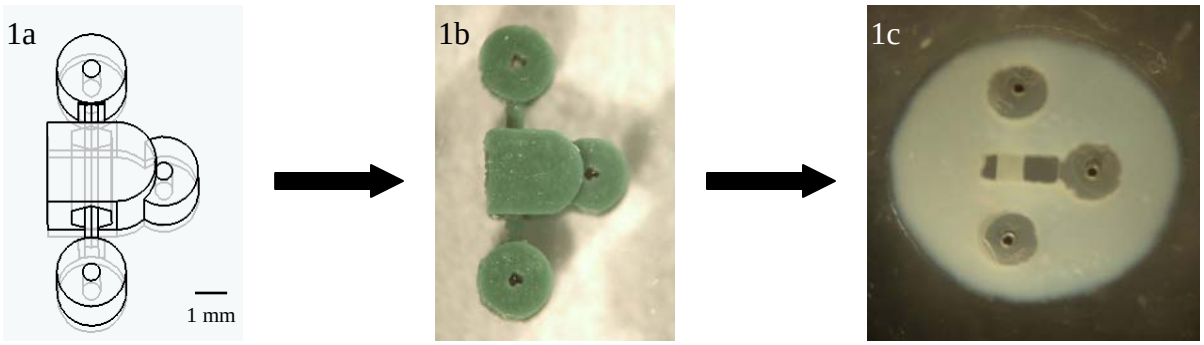

Figure 1. Scheme for fabricating devices in Sifel using a wax printer. (a) A Solidworks file is generated that defines the system in 3D. (b) The object is then printed onto a glass substrate using a commercial wax printing system. (c) Once the object is printed, Sifel is poured over the mold and cured at 60˚C for 24 h. Once cured, the building wax is removed to reveal the completed structure.

Similar studies have used photocurable perfluoropolyethers to fabricate microfluidic devices.[13-14] However, our particular design eliminates the intricacies involved with adhering partially cured perfluoropolyether layers. Since bonding the control layer and flow layer to one another which is extremely difficult in fluorinated compounds. Our 3D valves have the flow and control regions formed in the same monolithic mold. This technique enables the use of elastomers that do not satisfy the adhesion requirements of multi-layer fabrication. After curing by heat, Sifel becomes a high-performance elastomer with extraordinary levels of resistance to chemicals, oil, and heat; thus opening up a vast array of potential microfluidic applications in organic chemistry.

Here, we have designed three-dimensional pneumatic valves with a suspended fluid flow tube surrounded by a doughnut shaped pressure chamber. In this design, pressure was applied around the entire fluid channel, deflecting a thin Sifel membrane inward. This deflection closed the suspended channel and stopped fluid flow. Valve actuation was controlled by varying the pressure applied to the control channel (Figure 2).

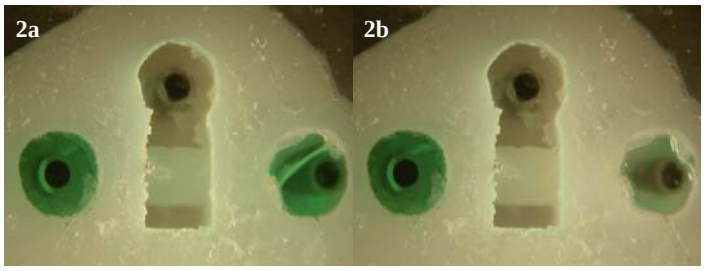

Figure 2. (a) Fluid tube filled with green dye solution. (b) Actuation of valve was accomplished by introducing pressurized air (~3psi) into the doughnut-shaped pressure chamber.

As a result, these valves could be used for microfluidic metering and flow control. Introduction of fluid into this device was accomplished through steel pins inserted into holes formed through the material. These holes where formed by 25 guage steel pins melted into the wax mold. These pins where taken out after the Sifel cured and 21 guage tubes where used to form a tight seal around the input pins, readily accepting pressures up to 21psi without leakage. This hole-molding method solves one difficult problem with

fluoropolymers in that they cannot be hole-punched without cracking and leaks.

Four samples of polymer- Sifel 610, Sifel 611, Sifel X-71-6030, and Sifel X-71-6054, where cured and tested for adhesion to glass surfaces. Since fluid flow was pressure-driven, it was necessary to form an irreversible seal between the glass and Sifel. Both Sifel 610 and Sifel 611 adhered very strongly to glass surfaces upon curing. However, the two materials were too viscous which made it difficult to completely de-gas and remove all air bubbles. Sifel X-71-6054 was less viscous but easily peeled off from the glass. Sifel X-71-6030 adhered well to the glass and was considerably less viscous than the other materials which made it ideal for pouring over the wax molds. The viscosity of sifel and its tendancy to form pinholes and retain air was a major problem which required several design changes over the course of our research. In order to prevent malformations and decrease the risk of pinholes in the fluid channel the thickness of the valve membrane needed to be at least 400µm. Because Sifel is one of the few liquid castable perfluoroelastomers available, further investigation may prove fruitful.

This technique for fabricating Sifel-based microfluidic valves was difficult to miniaturize due to the sizes needed to guarantee leak free valves. In addition, Sifel is opaque to UV-visible light so conventional optical methods of

detection must be done through the glass substrate. Some of these limitations result from properties of the material being used for the devices, whereas others depend on fabrication or design limitations. As device complexity increases, similar design rules will evolve to yield high performances despite the limitations of the particular material and fabrication technology being used.

By replacing PDMS with Sifel, this novel three-dimensional wax printing method allows for making topological complex 3D microfluidic structures and offers many advantages over multi-layer soft lithography. These include ease of fabrication, rapid response time, and high levels of integration. The major advantage of developing devices from 3D molding is that it enables the use of fluoroelastomers that are more solvent-resistant than PDMS. Microfluidic devices constructed from Sifel provide many of the same advantages of PDMS with the added advantage of chemical resistance. Since Sifel consists of a perfluoropolyether backbone, the elastomer is particularly stable due to the strength of the carbon-fluorine bond and steric hindrance arising from the strong forces between hydrogen and fluorine atoms. [12] As a result, these chemically robust valves have the potential to increase the number of solutions available for device applications. Because PDMS is not compatible with a broad range of solvents as reported by Lee et al.,[6] future work will

involve the analysis of solvent compatibility of the listed organic solvents with swelling ratios above 1.20 (Table 1). This technology makes the fabrication of more complex structures possible and has the potential to expand the field of highly integrated microfluidics to many new applications in chemical synthesis and analysis.

Table 1. Solubility parameters and swelling ratios of various solvents used in organic synthesis.

Table 1. Solubility Parameters, Swelling Ratios, and Dipole Moments of Various Solvents Used in Organic Synthesis

solvent	δ^a	S^b	μ (D)	ref[c]	rank[d]
perfluorotributylamine	5.6	1.09	0.0	10	32
perfluorodecalin	6.6	1.09	0.0	10	33
pentane	7.1	1.44	0.0	10	3
poly(dimethylsiloxane)	7.3	∞	0.6–0.9	8, 14	
diisopropylamine	7.3	2.13	1.2	10	1
hexanes	7.3	1.35	0.0	10	8
n-heptane	7.4	1.34	0.0	10	10
triethylamine	7.5	1.58	0.7	8,10	2
ether	7.5	1.38	1.1	10	6
cyclohexane	8.2	1.33	0.0	10	11
trichloroethylene	9.2	1.24	0.9	10	9
dimethoxyethane (DME)	8.8	1.32	1.6	10	12
xylenes	8.9	1.41	0.3	10	4
toluene	8.9	1.31	0.4	10	13
ethyl acetate	9.0	1.18	1.8	8,10	19
benzene	9.2	1.28	0.0	10	14
chloroform	9.2	1.39	1.0	10	5
2-butanone	9.3	1.21	2.8	10	18
tetrahydrofuran (THF)	9.3	1.28	1.7	10	7
dimethyl carbonate	9.5	1.02	0.9	8,10	26
chlorobenzene	9.5	1.22	1.7	10	15
methylene chloride	9.9	1.22	1.6	10	16
acetone	9.9	1.06	2.9	8,12	22
dioxane	10.0	1.16	0.5	10	20
pyridine	10.6	1.06	2.2	10	23
N-methylpyrrolidone (NMP)	11.1	1.02	3.8	10	25
tert-butyl alcohol	10.6	1.21	1.6	8,12	17
acetonitrile	11.9	1.01	4.0	10	31
1-propanol	11.9	1.09	1.6	8,10	21
phenol	12.0	1.01	1.2	8,12	29
dimethylformamide (DMF)	12.1	1.02	3.8	8,10	27
nitromethane	12.6	1.09	3.5	10	34
ethyl alcohol	12.7	1.04	1.7	8,12	24
dimethyl sulfoxide (DMSO)	13.0	1.00	4.0	10	35
propylene carbonate	13.3	1.01	4.8	10	30
methanol	14.5	1.02	1.7	8,12	28
ethylene glycol	14.6	1.09	2.3	8,12	36
glycerol	21.1	1.09	2.6	13,15	37
water	23.4	1.09	1.9	8,12	38

[a] δ in units of $cal^{1/2}\ cm^{-3/2}$. [b] S denotes the swelling ratio that was measured experimentally: $S = D/D_0$, where D is the length of PDMS in the solvent and D_0 is the length of the dry PDMS. [c] References refer to literature values of δ and μ. [d] Rank refers to the order of the solvent in decreasing swelling ability (see Figure 1).

Methods

The wax molds were designed in 3D in a Solidworks program, and the file was printed directly onto a glass substrate using a commercial wax printing system (Solidscape T66). Printing was carried out with two waxes – the building wax (blue) which formed the structure of the desired microchannels and the supporting wax (red) which acted as a sacrificial material and supported suspended structures during fabrication. The supporting wax was removed by placing the molds in a petri dish containing VSO precision cleaner for approximately 1 h at 65˚C. Next, the wax molds were dried at 40˚C for approximately 3 h. Once the molds were dry, 25 gauge pins were soldered into each valve. PDMS blocks were created by pouring a liquid PDMS pre-polymer (mixture of 1:10 base polymer:curing agent) onto a petri dish and allowing the mixture to cure at 80˚C for 1 h. 1cm holes were then punched through the PDMS and these PDMS blocks were then placed around each wax mold. Next, Sifel was poured over the models and allowed to cure at 60˚C for approximately 24 h. Finally the building wax was melted away at 150˚C to provide the completed structure.

Conclusion

Sifel Microfluidics promises to allow an unprecedented number of chemical reactions in microfluidic devices.

Problems with pinholes and bubbles and through hole cracking were solved and robust microfluidic valves were made. These valves were tested with the solvents most incompatible with PDMS and were found to be robust to these chemicals.

A Swell < 10% after exposure. Suitable
B Swell > 10% & < 20% after exposure. Generally suitable
C Swell > 20% & < 40% after exposure . May be suitable in some situations
D Swell >40% after exposure. Not suitable
N Insufficient data
Test: full immersion, Room Temperature, 3 days
Performance in some chemical depend on the type of SIFEL products: LIMS vs. HCR. In such cases, chemical performance is shown as "A/B".

Recommendations made in the chart are based on our best experience and knowledge of the applications for these products and shall not constitute a guarantee or warranty of performance nor a modification or alteration of our standard product warranty which shall be applicable to all products. Prior to any actual use compatibility tests should be run to determine suitability to a specific application, particularly where failure could result in injury or catastrophic failure.

acetaldehyde	A	ammonium phosphate	A
acetic acid,		ammonium stearate	A
glacial	A	ammonium sulfate	A
hot	A	ammonium thiocyanate	A
5%	A	amyl acetate	A/B
acetic anhydride	A	amyl alcohol	A
acetone	A	amyl nitrate	A
acetone cyanohydrin	A	aniline	A
acetyl chloride	A	aniline hydrochloride	A
acetylene gas	A	anti-freeze, alcohol or glycol based	A
acrylonitrile	A	aqua regia	N
adipic acid	A	argon gas	A
alcohol, denatured	A	arsenic acid	A
alkyl benzene	A	ash slurry	A
alkyl-arylsulphonic acid	A	asphalt	A
alumina trihydrate	N	barium chloride	A
aluminum acetate	N	barium hydroxide;	
aluminum chloride	N	mono-, octa-, pentahydrate	A
aluminum nitrate	N	barium nitrate	A
aluminum potassium sulfate	N	beer	A
aluminum sulfate	N	beet sugar	A
amines, mixed	A/B	benzaldehyde	A
ammonia,		benzene	A
gas, cold	A	benzenesulfonic acid	A
gas, hot	N	benzochloride	A
liquid, (anhydrous)	N	benzoic acid	A
ammonium acetate	A	benzotrifluoride	C
ammonium bicarbonate	A	bleach solutions	A
ammonium bifluoride	N	blood	A
ammonium bromide	A	bone oil	A
ammonium carbonate	A	boric acid	A
ammonium chloride	A	boron trichloride	N
ammonium hydroxide	A	bromine	N
ammonium nitrate	A	bunker fuel oil	A

butadiene	A/B	cement	A
butane	A/B	chloric acid	A
buttermilk	A	chlorinated solvents	
butyl acetate	A/B	dry	B
butyl alcohol	A	wet	B
butylamine	A/B	chlorine dioxide	N
butylene	A/B	chlorine,	
butylene glycol	A	dry	N
butyl ether	B	wet	N
butyric acid	A	chloroacetic acid	B
calcium acetate	A	chloroacetone	B
calcium carbonate	A	chlorobenzene	A
calcium chlorate	A	chloroform	B
calcium cyanide	A	chlorosulfonic acid	A
calcium hydrogen sulfite	A	chocolate	A
calcium hydrosulfide	A	chromic acid	N
calcium hydroxide, aqueous	A	chromic oxide	A
calcium hypochlorite	A	chromium potassium sulfate	A
calcium liquors	A	citric acid	A
calcium magnesium chloride	A	clay slurry	A
calcium nitrate	A	coal-tar	A
calcium phosphate;		coal-tar distillate	A
dibasic, monobasic, tribasic	A	coconut oil	A
calcium sulfate, aqueous	A	cod-liver oil	A
carbamate	A	copper acetate	N
carbon dioxide,		copper ammonium acetate	N
dry	A	copper chloride	N
wet	A	copper cyanide	N
carbon disulfide	A	copper nitrate	N
carbon monoxide	A	copper sulfate, <50%	N
carbon tetrachloride	B	corn oil	A
carbonic acid	A	cottonseed oil	A
castor oil	A	creosote, coal-tar	A
catsup	A	cresol	A

crude oil - sour	A	ethane	A
cumene	A	ethanethiol	A
cutting oil	A	ethanolamine	A
cyanogen	A	ethyl acetate	A
cyclohexane	A/B	ethyl alcohol	A
decahydronaphthalene	A	ethylamine	B
detergent, H2O solution	A	ethylbenzene	A
diacetone alcohol	A	ethylene	A
diallyl phthalate	A	ethylene dibromide	B
dibromoethyl benzene	N	dethylene dichloride	B
dibutylamine	A/B	ethylene glycol	A
dibutyl Cellosolve adipate	A	ethylene oxide	B
dibutyl phthalate	A	ethyl ether	B
dichlorobenzene	B	ethyle formate	A
diesel oil	A	fatty acids	A
diethanolamine	A	ferric sulfate, aqueous	A
diethylamine	B	ferrous sulfate, aqueous	A
diethyl carbonate	A	fluorine, gas, dry < 300°F	D
diethylene glycol	A	fluosilicic acid	N
diethylenetriamine	A	formaldehyde	A
diethyl phthalate	A	formic acid < 160 °F	A
diisobutyl ketone	A	Freon 11®	D
dimethylamine	A	Freon 113®	D
dimethyl formamide	A	Freon 114®	D
dimethyl phthalate	A	Freon 12®	D
dimethyl terephthalate	A	Freon 22 ®	D
dinitrochlorobenzene	A	Freon 502 ®	D
dioctyl phthalate	A	fruit juices	A
diphenyl	A	fuel oil,	
Dowtherm® (DOW chemical)		#1 , #2,	A
A	A	#5 Light, #5 heavy , #6	A
E	A	fumaric acid	A
209	A	furfural	B
epichlorohydrin	A	gas oil	A

gasoline	A/B	isopropyl acetate	A/B
gelatin	A	isopropyl alcohol	A
glucose	A	isopropyl ether	B
glycerol	A	jet fuel	A
glycine	A	kerosene	A
helium	A	lacquer	A
heptane	A/B	lactic acid,	
hexyl alcohol	A	cold	A
hydraulic oil, petroleum based	A	hot	A
hydrazine	A	lard	A
hydrobromic acid	A	latex	A
hydrochloric acid ,		ligroin	A/B
concentrated	A	lime slurry	A
diluted	A	linoleic acid	A
<20%, well service	A	linseed oil	A
20% - 30%, well service	A	liquefied petroleum gas	B
hydrocyanic acid	A	lubricating oil, petroleum base	A
hydrofluoric acid,		magnesium chloride	A
SIFEL has poor compatibility with strong acids.		magnesium hydroxide	A
Cold, < 65%	C	magnesium sulfate	A
Cold, > 65%	C	maleic acid	A
hot, <65%	N	maleic anhydride	A
hot, > 65%	N	malic acid	A
hydrogen	A	manganous chloride	A
hydrogen chloride, gas, dry	A	melamine resin	A
hydrogen fluoride, anhydrous	N	mercuric chloride	A
hydrogen peroxide	A	mercury	A
hydrogen sulfide,		mesityl oxide	A
dry, cold	A	methane	B
dry, hot	A	methyl acetate	A/B
wet, cold	A	methyl alcohol	A
wet, hot	A	methyl benzoate	A
hypochlorous acid	A	methyl bromide	B
isobutane	A/B	methyl chloride	B

methylene bromide	B	paper stock	A
methylene chloride	B	paraffin wax, molten	A
methyl ethyl ketone	A/B	peanut oil, vegetable	A
methyl formate	A	pectin, liquor	A
methyl isobutyl ketone	A/B	pentane	A/B
methyl methacrylate	A	perchloric acid	A
methyl propionate	A	perchloroethylene	B
methyl tertiary butyl ether	B	phenol, 10%	A
milk	A	phenylacetic acid	A
mineral oil	A	phosphoric acid,	
molasses	A	concentrated	A
naphtha, crude	B	diluted	A
naphthalene	A	phthalic anhydride	A
natural gas, sour	B	picoline, alpha	A
nickel chloride	A	picric acid,	
nickel sulfate	A	H20 solution	A
nitric acid,		molten	A
SIFEL has poor compatibility with strong acids.		pine oil	A
diluted	A	polyethylene glycol	A
concentrated	A	polypropylene slurry	A
red fuming	N	polyvinyl acetate emulsion	A
nitrobenzene	A	polyvinyl alcohol	A
nitrogen gas	A	potassium bromide	A
nitromethane	A	potassium carbonate	A
oleic acid	A	potassium chlorate	A
olive oil	A	potassium chloride	A
oxalic acid	A	potassium cyanide	A
oxygen, gas	A	potassium dichromate	A
-10°F to 200 °F	A	potassium hydroxide, diluted	A
200 °F to 400 °F	A	concentrated	A
ozone	A	potassium nitrate	A
paint, oil based	A	potassium permanganate	A
palm oil	A	potassium phosphate,	
palmitic acid	A	dibasic, monobasic, tribasic	A

potassium sulfate	A	sodium phosphate,	
propane	A/B	dibasic, monobasic, tribasic	A
propionic acid, <150 °F	A	sodium silicate	A
propyl acetate	A/B	sodium sulfate	A
propyl alcohol	A	sodium sulfide	A
propylene	A/B	sodium sulfite	A
propylene oxide	B	sodium thiocyanate	A
pulp stock	A	sodium thiosulfate	A
pyridine	A	soybean oil	A
quenching oil	A	starch	A
rapeseed oil	A	steam, <350 °F	A
red liquor	A	steam, > 350 °F - 500°F	A
refrigerator oil	A	stearic acid	A
sewage	A	styrene	A
silver nitrate	A	sulfite waste liquor	A
soap solutions	A	sulfur,	
soda ash	A	molten	A
sodium acetate	A	in water	A
sodium bicarbonate	A	sulfur chloride	A
sodium bisulfate	A	sulfur dioxide,	
sodium bisulfite,		wet	A
< 200 °F	A	dry	A
sodium carbonate		sulfuric acid,	
> 200 °F	A	SIFEL has poor compatibility with strong acids.	
sodium chloride		diluted	A
> 200 °F	A	concentrated	A
sodium cyanide, aqueous	A	fuming	D
sodium dichromate	A	sulfurous acid	A
sodium dithionite	A	tall oil,	
sodium hydroxide, diluted	A	< 450°F	A
sodium hypochlorite, 20%	A	tallow	A
sodium nitrate	A	tartaric acid, aqueous	A
sodium peroxide	A	terephthalic acid	A
		tetrachloroethane	B

tetrahydrofuran	B
thiols	A
titanium dioxide	A
titanium tetrachloride	N
toluene	A
trichloroethane	B
trichloroethylene	B
tricresyl phosphate	A
triethanolamine	A
triethylamine	A/B
tung oil	A
turpentine (oil)	A
urea	A
urea-formaldehyde resin	A
varnish	A
vinegar	A
vinyl acetate	A/B
vinyl chloride	B
vinylidine chloride	B
water,	
chlorinated	A
fresh	A
heavy	A
salt or sea	A
whiskey	A
white liquor	A
wine	A
wood pulp stock	A
wort	A
xylene	A
yeast	A
zinc chloride	A
zinc nitrate	A
zinc sulfate	A

References:

1. Whitesides, G. M. The origins and the future of microfluidics. Nature 442, 368-373 (2006).

2. Whitesides, G. M., Stroock, A. D. Flexible methods for microfluidics. Physics Today, 42-48 (2001).

3. Sia, S., Whitesides, G. M. Microfluidic devices fabricated in poly(dimethylsiloxane) for biological studies. Electrophoresis 24, 3563-3576 (2003).

4. Weibel, D., Kruithof, M., Potenta, S., Sia, S., Lee, A., Whitesides, G. M. Torque-actuated valves for microfluidics. Anaytical Chemistry 77, 4726-4733 (2005).

5. McDonald, J., Whitesides, G. M. Poly(dimethylsiloxane) as a material for fabricating microfluidic devices. Accounts of Chemical Research 35, 491-499 (2002).

6. Lee, J., Park, C., Whitesides, G. M. Solvent compatibility of poly(dimethylsiloxane)-based microfluidic devices, Analytical Chemistry, 75, 6544-6554 (2003).

7. Clark, T., Boncheva, M., German, J., Weck, M., Whitesides, G. M. Design of three-dimensional, millimeter-scale models for molecular folding. Journal of American Chemical Society 124, 18-19 (2002).

8. Anderson, J., Chiu, D., Jackman, R., Cherniavskaya, O., McDonald, J., Wu, H., Whitesides, S., Whitesides, G. M. Fabrication of topologically complex three-dimensional microfluidic systems in PDMS by rapid prototyping. Analytical Chemistry 72, 3158-3164 (2000).

9. Jeon, N., Chiu, D., Wargo, C., Wu, H., Choi, I., Anderson, J., Whitesides, G. M. Design and fabrication of integrated passive valves and pumps for flexible polymer 3-dimensional microfluidic systems. Biomedical Microdevices 4, 117-121 (2002).

10. Wu, H. Odom, T., Chiu, D., Whitesides, G. M. Fabrication of complex three-dimensional microchannel systems in PDMS. Journal of American Chemical Society 125, 554-559 (2003).

11. McDonald, J., Chabinyc, M., Metallo, S., Anderson, J., Stroock, A., Whitesides, G. M. Prototyping of microfluidic devices in poly(dimethylsiloxane) using solid-object printing, Analytical Chemistry, 74, 1537 -1545 (2002).

12. Waksman, L., Kishita, H., Sato, S., Tarumi, Y. The evolution of a fluoroelastomer: sifel a new class of easily processed high performance elastomer, adhesive and sealant, SAE Transaction: Journal of Materials and Manufacturing 110, 849-856 (2001).

13. Rolland, J., van Dam, R., Schorzman, D., Quake, S., DeSimone, J. Solvent-resistant photocurable "liquid teflon" for microfluidic device fabrication, Journal of American Chemical Society 126, 2322-2323 (2004).

14. Rolland, J., Zhou, Z., Kelly, J., Denison, G., van Dam, R., Hagberg, E., Carter, K., Quake, S., DeSimone, J. Liquid precursors for applications in microfluidics, soft lithography, and fuel cells. J. M. Polym. Prep. 91, 254-255 (2004).

3. Microfluidic Valves for customized radioactive positron emission dyes

The "lost wax" process was used to create specialized chips and newly designed, chemically robust high pressure microfluidic valves for making radioactive positron emission dyes. This is important because these species typically have very short half lives and all PET scan machines must be within a certain time-distance from a central manufacturing site. In turn this causes the central plant to only produce the standard dye, even though researchers have been able to create target specific dyes for use in more informative diagnostics. The development of local capacity to create dye as needed in a microfluidic device would also easily be able to make the more specific dyes in order to improve patient outcomes.

Figure 1 shows the chemical reaction that must be carried out in order to create the PET scan dye. This represents a very difficult reaction for microfluidics. Not only must the chip be compatible with the solvents used, but it also must retain as little of the radioactivity as possible in order to increase yield from the reaction.

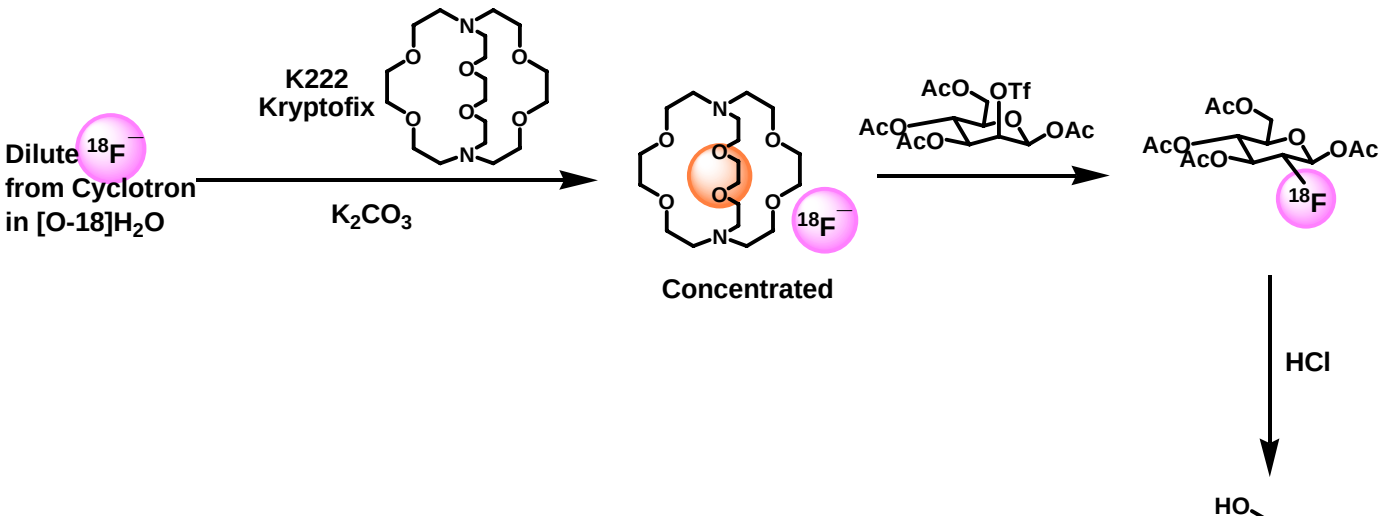

Figure 1 The reaction that must be carried out In the microfluidic chip in order to perform PET scans

The primary advantages of using the rapid prototyping device where

- very rapid/inexpensive evaluation of new designs, esp. valve shapes
- more controlled thickness of deep features than e.g. SU8
- 3D molds eliminate adhesion step; therefore wider range of materials possible (bond is unescesary). Also, there is no need to add functional groups to the material (to provide bonding) -- we saw in some cases the added functional groups interfere with the chemistry.

This method of developing microfluidics allowed new designs to be tested quickly and efficiently while being compatible with all polymer systems tested.

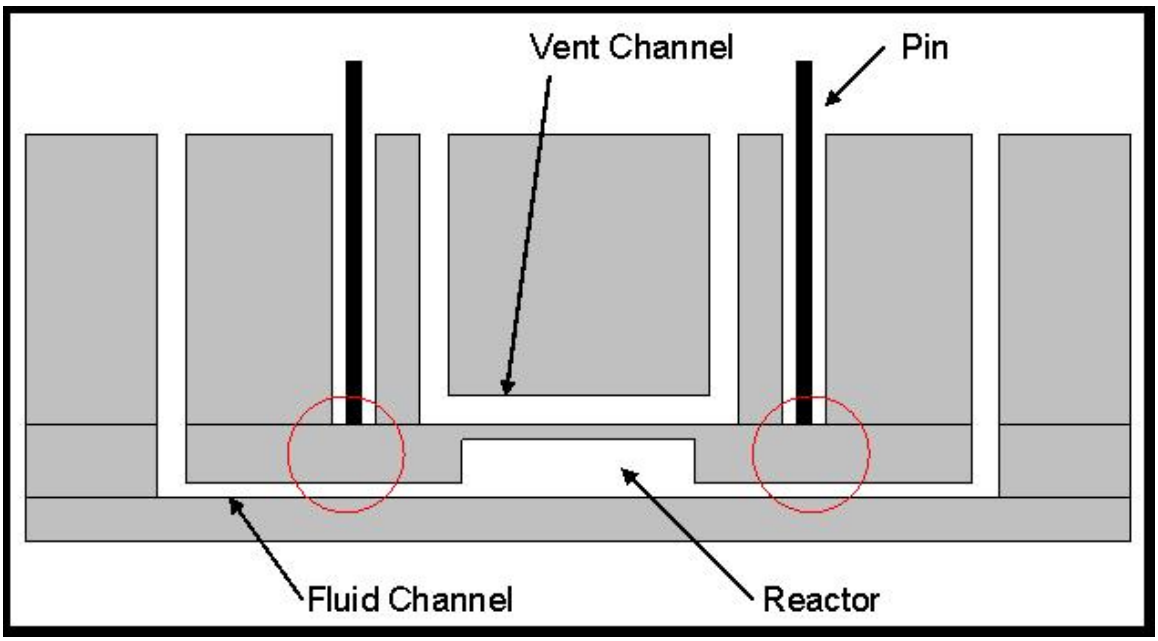

Figure 2 A side cutout view of the pin operated valves. The pin is forced down by compressed air, deforming the proprietary catalyst-compatible norbornene-based elastomeric polymer and creating a seal to block the flow of liquid

The Valve design can be seen in figures 2-6. Figures 3-5 show the steps of fabrication from the 3D printer, to the removal of the red support wax, to finally the casting in DCPD (dicyclopentadiene) for the hard outer layers and a proprietary catalyst-compatible norbornene-based elastomeric polymer for the deformable membrane sandwiched between the hard layers. These polymers where shown to be compatible with the solvents involved as well as non-absorbing of the radioactive ion.

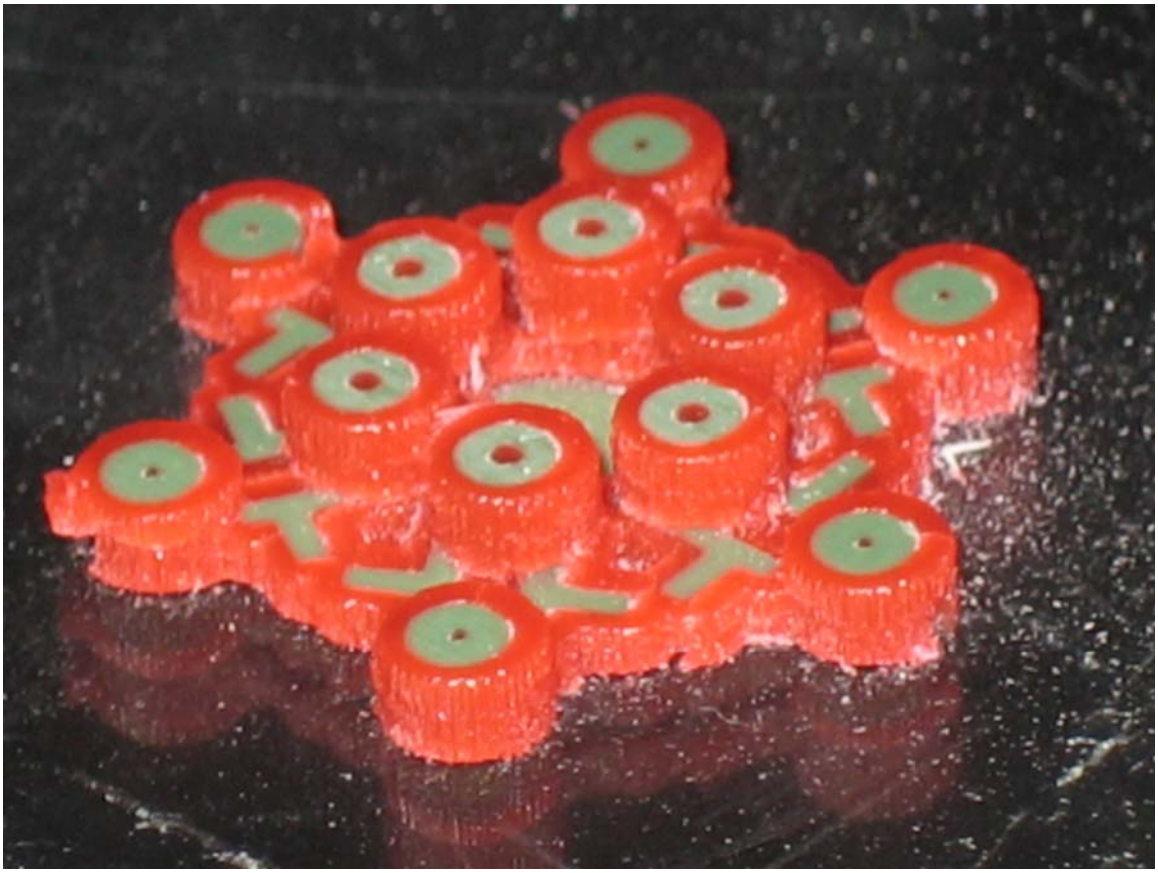

Figure 3 The wax mold before the red support wax is removed

Figure 4 The wax mold after it has had the support wax removed from it

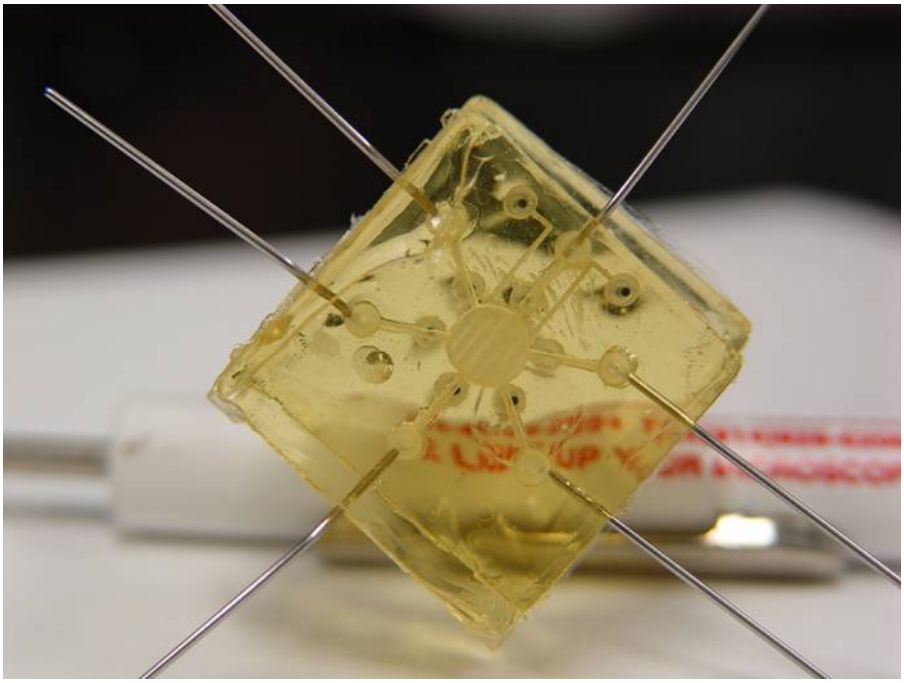

Figure 5 The completely assembled device in dicyclopentadiene and catalyst-compatible norbornene-based elastomeric polymer

Figure 2 shows the valve design from a side cutout view. The pin is a wire that is guided by metal tubes of a slightly larger guage that guide the pin into the correct position over the membrane. The position of the valve is defined by wax supports that hold the metal tube as the polymer is being cured and then the wax is melted out. These valves exhibited the following properties and were used under the following conditions:

- closing pressure: we used our mechanical valve setup. With 280um diameter pins, and 1.1mm diameter heads on the pins, our closing pressure (to push the pins) was typically 40-80 psi.

- flow pressure: typically 10-20 psi

- chemicals: for this application, we have mostly water or acetonitrile.

In particular: K_2CO_3/H_2O containing F-18 ion, kryptofix in acetonitrile, mannose triflate ('FDG' precursor) in acetonitrile, hydrochloric acid.

- valve size: channels about 250um wide, valves up to 500um wide. The valve membrane thickness was typically 200-600um with the wax molding approach.

Figure 6 shows an image of a closed valve. The pin can be seen clearly deforming the membrane, creating a seal and closing the valve.

Figure 7 is a validation of the chip-based ^{18}FDG synthesis using an earlier chip design by in vivo microPET imaging. The tumor is located on the left shoulder of the mouse and is clearly visible in the scan.

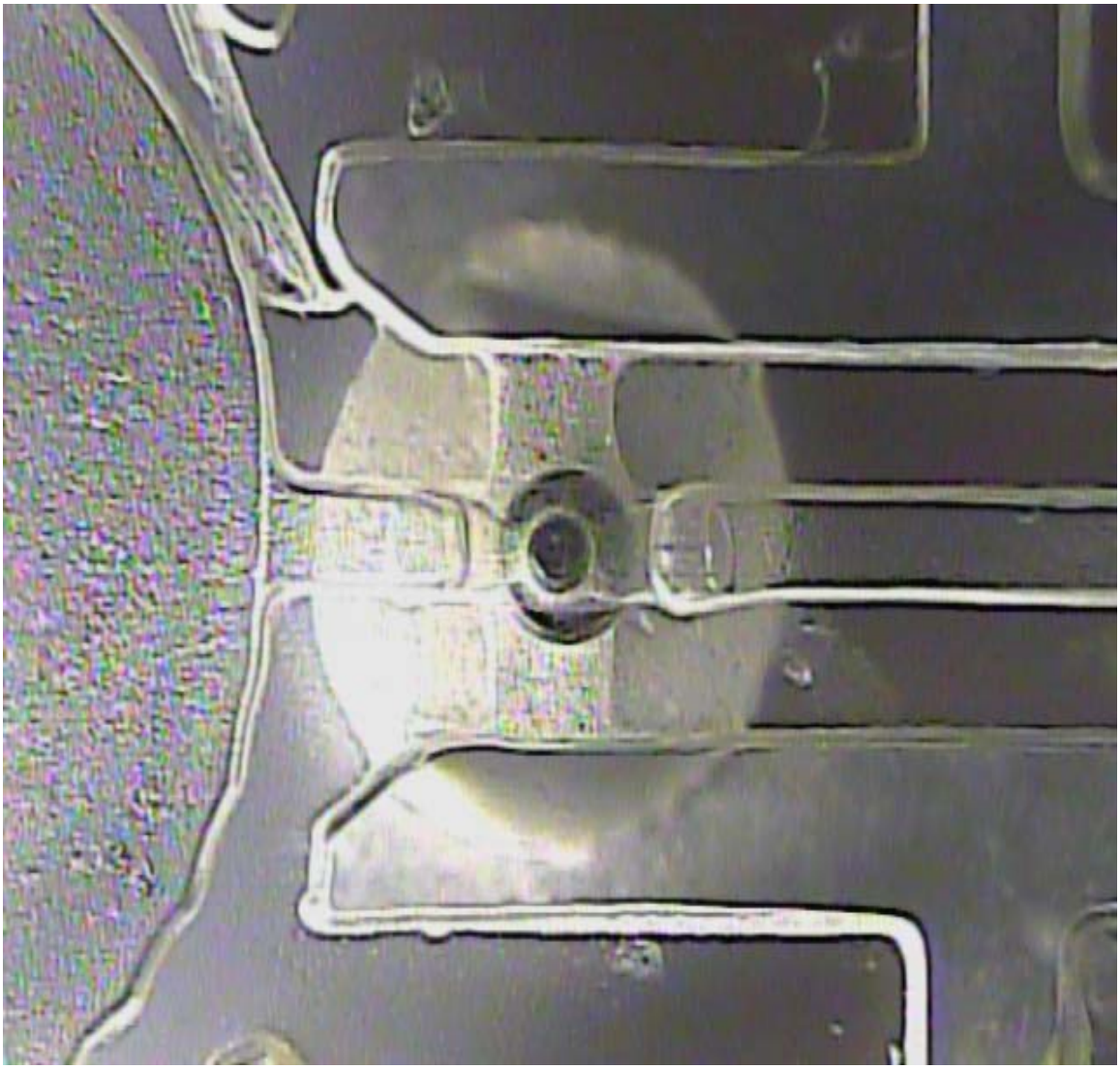

Figure 6 A pin operated valve in the completely closed position

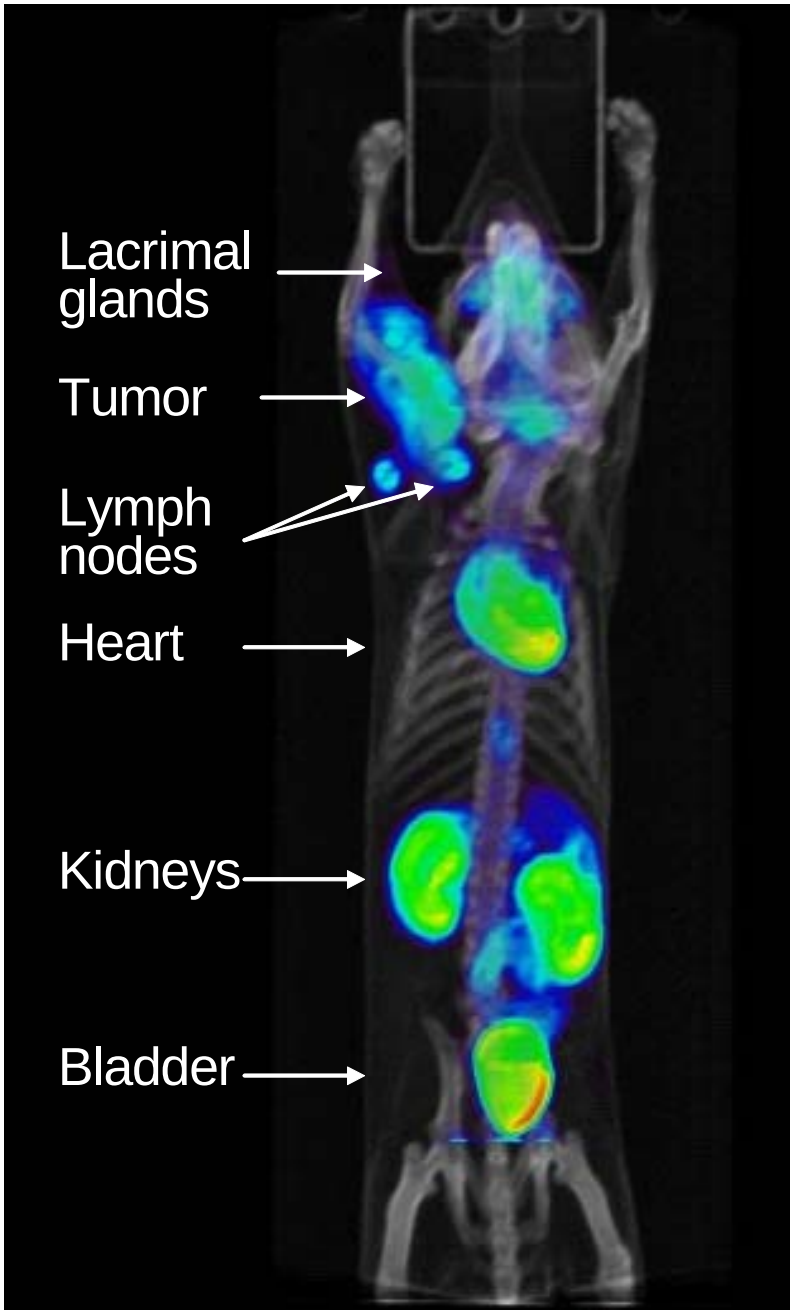

Figure 7 Validation of the chip-based ^{18}FDG synthesis by in vivo microPET imaging.(The tumor is located on the left shoulder of the mouse.)

References

[1] (a) D. M. Roberge, L. Ducry, N. Bieler, P. Cretton and B. Zimmerman, Chem. Eng. Technol., 28, 318, 2005. (b) P. Watts and S. J. Haswell, Curr. Opin. Chem. Biol., 7, 380, 2003. (c) T. Kawaguchi, H. Miyata, K. Ataka, K. Mae and J. Yoshida, Angew. Chem. Int. Ed., 44, 2413, 2005. (d) J. Liu, C. Hansen and S. R. Quake, Anal. Chem., 75, 4718, 2003.

[2] S.-Y. Lu, P. Watts, F. T. Chin, J. Hong, J. L. Musachio, E. Briard and V. W. Pike, Lab Chip, 4, 523, 2004.

[3] (a) M. Phelps, P. Natl. Acad. Sci. USA, 97, 9226, 2000. (b) R. Nutt, Mol. Imaging Biol., 4, 11, 2002.

[4] K. Hamacher, H. H. Coenen and G. Stocklin, J. Nucl. Med., 27, 235, 1986.

[5] H. C. Padgett, D. G. Schmidt, A. Luxen, G. T. Bida, N. Satyamurthy and J. R. Barrio, Appl. Radiat. Isot., 40, 433, 1989.

[6] C.-C. Lee, G. Sui, A. Elizarov, C. J. Shu, Y.-S. Shin, A. N. Dooley, J. Huang, A. Daridon, P. Wyatt, D. Stout, O. N. Witte, H. C. Kolb, N. Satyamurthy, J. R. Heath, M. E. Phelps, S. R. Quake and H.-R. Tseng, Science, 310, 1793, 2005.

[7] S. R. Cherry, Y. Shao, R. W. Silverman, A. Chatziioannou, K. Meadors, S. Siegel, A. Boutefnouchet, T. Farquhar, J. Young, W. F. Jones, D. Newport, C. Moyers, M. Andreaco, M. Paulus,

D. Binkley, R. Nutt and M. E. Phelps, IEEE Trans. Nucl. Sci., 44, 1161, 1997.

[8] (a) T. C. Merkel, V. I. Bondar, K. Nagai, B. D. Freeman and I. Pinnau, J. Polym. Sci., Part B: Polym. Phys., 38, 415, 2000. (b) J. C. Lötters, W. Olthius, P. H. Veltink and P. Bergveld, J. Micromech. Microeng., 7, 145, 1997.

[9] D. C. Duffy, J. C. McDonald, O. J. A. Schueller and G. M. Whitesides, Anal. Chem., 70, 4974, 1998.

[10] (a) M. A. Unger, H.-P. Chou, T. Thorsen, A. Scherer and S. R. Quake, Science, 288, 113, 2000. (b) V. Studer, G. Hang, A. Pandolfi, M. Oritz, W. F. Anderson and S. R. Quake, J. Appl. Phys., 95, 393, 2004.

[11] Supplied by Explora RN Nucleophilic [18F]Fluorination System, courtesy of Siemens Biomarker Solutions, Culver City, CA.

[12] J. M. Gillies, C. Prenant, G. N. Chimon, G. J Smethurst, B. A. Dekker and J. Zweit, Appl Radiat. Isot., 64, 333, 2006.

[12] E. D. Agdeppa, V. Kepe, J. Liu, S. Flores-Torres, N. Satyamurthy, A. Petric, G. M. Cole, G. W. Small, S.-C. Huang and J. R. Barrio, J. Neurosci., 21, 189, 2001.

[13] J. P. Rolland, R. M. van Dam, D. A. Schorzman, S. R. Quake and J. M. De Simone, J. Am. Chem. Soc., 126, 2322, 2004.

[14] A. M. Elizarov, H. C. Kolb, R. M. van Dam, J. R. Heath, H. C. Padgett, J. Huang and A. Daridon, Coin-Shaped Reactor in Microfluidic Devices Used for Radiopharmaceutical Synthesis, IN PRESS

[15] A. M. Elizarov, M. R. van Dam, J. R. Heath, Microfluidic Device with “Coin-Shaped Reactor” for Radiopharmaceutical Synthesis, IN PRESS

4. Reducing Microfluidic Control Inputs Through the Use of Pressure Multiplexing

An important problem in microfluidics is reducing the number of input pins needed to control as many valves as possible. Each input pin takes up space on the chip and requires a leak free connection to outside plumbing and large control valves. Using our new three-dimensional valves created by rapid prototyping we were able to conceive of and prove a new system of pressure multiplexing that can greatly reduce the number of needed inputs beyond the previously reported minimum of controlling n valves with 2 $\log_2 n$ inputs. We were able to control n valves with 2 $\log_x n$ inputs, where x is the number of different pressures that different valves in the array close at. Furthermore, our pressure multiplexing technique is general and can be applied to standard 2D microfluidics. Minimizing the number of control inputs is extremely important in creating simplified and more robust microfluidic chips for practical purposes.

Our microfluidic multiplexer reduces the number of control inputs – the number of control inputs to control n number of valves given by 2 $\log_{24} n$. Where 24 is the number of different closing pressure we were able to create with our 3D valves. Or rather, in different terms, $24^{\frac{4}{2}} \geq n$. The two multiplexer chips are similar in theory, but our microfluidic multiplexer is able to increase the number of

valves to be manipulated through the fact that different sized valves with different membrane thicknesses will close at different pressures. This allows pressure to be used as an additional control instead of just on/off used previously. Using a microfluidic chip with twenty-four different valve styles of varying sizes, membrane thicknesses, and therefore closing pressures, we were able to create a multiplexer that is more efficient in terms of required input ports. An analysis of the family of curves (Fig 1.)

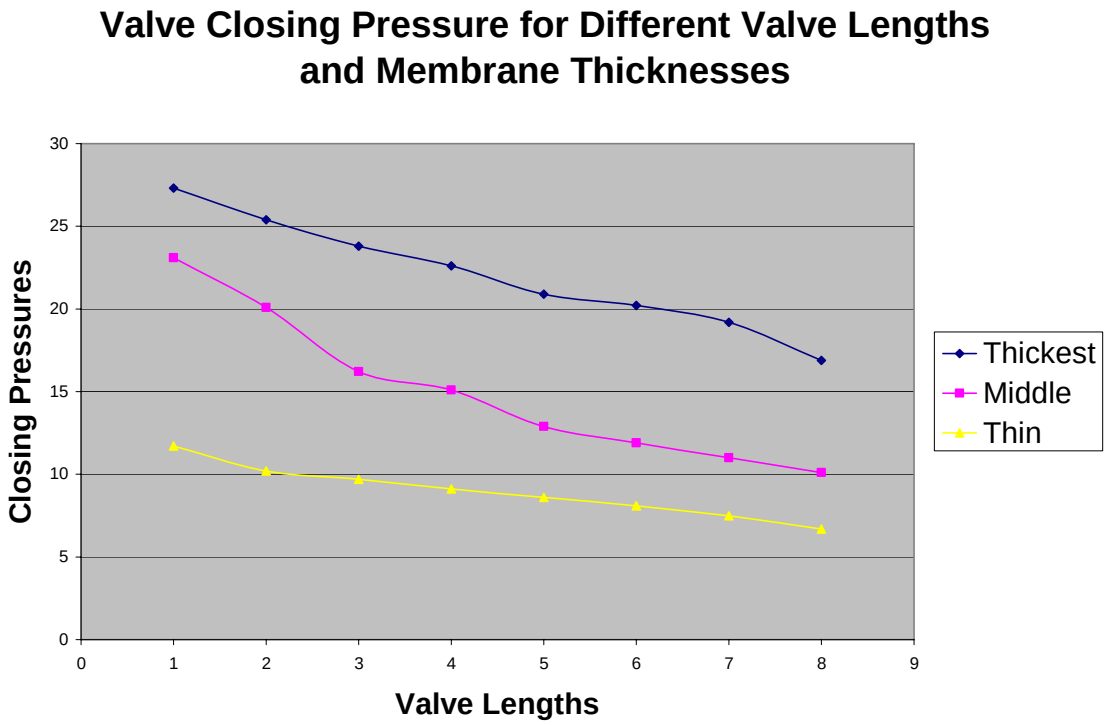

Figure 1 Family of closing pressure curves created by changing the membrane thickness and the valve length. Each valve has a distinct closing pressure and this information

can be used to reduce the number of input lines needed for a microfluidic multiplexer

created by spanning the parameter space of width and membrane thickness was created. Using a subset of this parameter space consisting of 12 evenly spaced closing pressure, a forty-six multiplexer was created using four control channels. This is significantly different from the previous microfluidic multiplexer in that our chips are not restricted to simply two degrees of freedom: on or off. Rather, through the use of various pressures and twenty-four different valves – different in width, membrane thickness, and closing pressures – we were able to create twenty-four different degrees of freedom. Using twenty-four different degrees of freedom, it is thus possible to manipulate up to 576 input lines using our scheme.

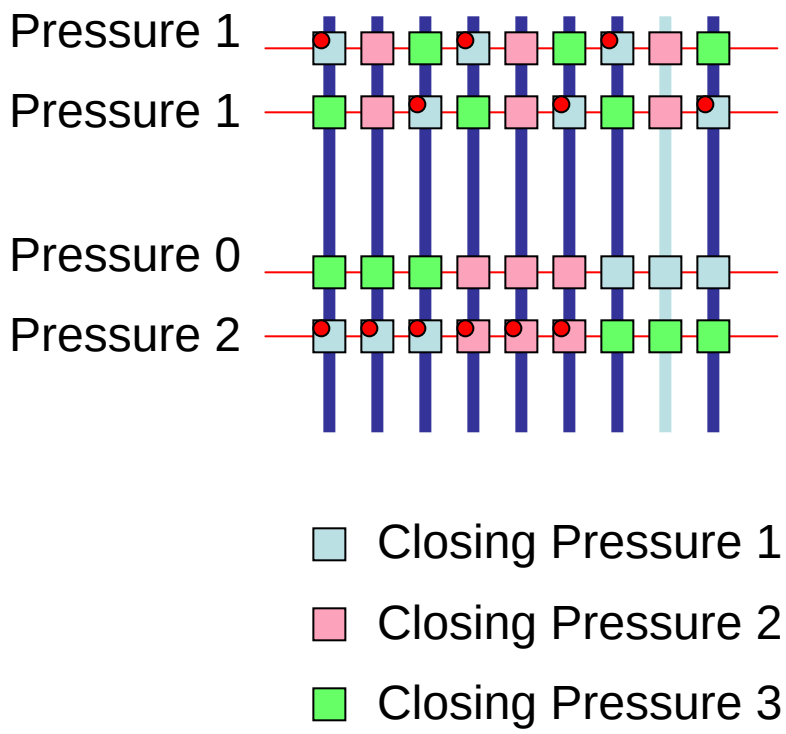

Figure 2 A simple demonstration of our pressure multiplexing scheme. The red dots show valves which are closed. The light blue path is open and fluid can flow only through it. The traditional multiplexing scheme would require 7 input valves to control these 9 flow lines

Figure 2 shows the multiplexing scheme we used with a smaller number of valves. There are three different valves with 3 different closing pressures controlling 9 flow channels. The power of our multiplexing scheme can be seen in this simple example as we require only 4 control lines where the traditional multiplexing scheme would require 7 control valves. Closing pressure 1 is the lowest and closing pressure 3 is the highest. When pressure 1 is put on the top 2 control lines only the valves which close at

pressure 1 are shut, this allows flows through the channels without a red dot. When no pressure is applied to the third control line all the valves remain open. Pressure 2 applied to the fourth valve set closes all valves except for the closing pressure 3 valves, thus selecting only one channel to have an open path from top to bottom.

The general equation used in the creation of a multiplexer is given by the following: $\log_k n = \frac{m}{2}$. The variable *k* is the degrees of freedom: on/off, various closing pressures of valves, etc. The variable *n* is given by the number of lines controlled, whereas the variable *m* is the number of control lines – or inputs, as it were. The 2 in the equation is a factor which accounts for the nature of the control input. A single input being on or off would open or close all the lines in contact with the input. However, with the use of a pair of inputs to control a line, it is possible to leave on or off half the lines. In this way, it is possible to control and manipulate the valves to allow a pathway for fluid, thus requiring the factor 2 in the equation. This equation can be manipulated to create a more correct, or more logical, equation: $k^m \geq n$. This equation is more correct, for it allows a *minimum* possible number of control lines, whereas the previous equation suggests an absolute number of control lines. The savings in number of control inputs is illustrated by figure 3 in which the top line (blue) is the number needed with traditional

multiplexing and the lower curves which need fewer controlling channels per controlled channel represent multiplexers using a larger and larger pressure space.

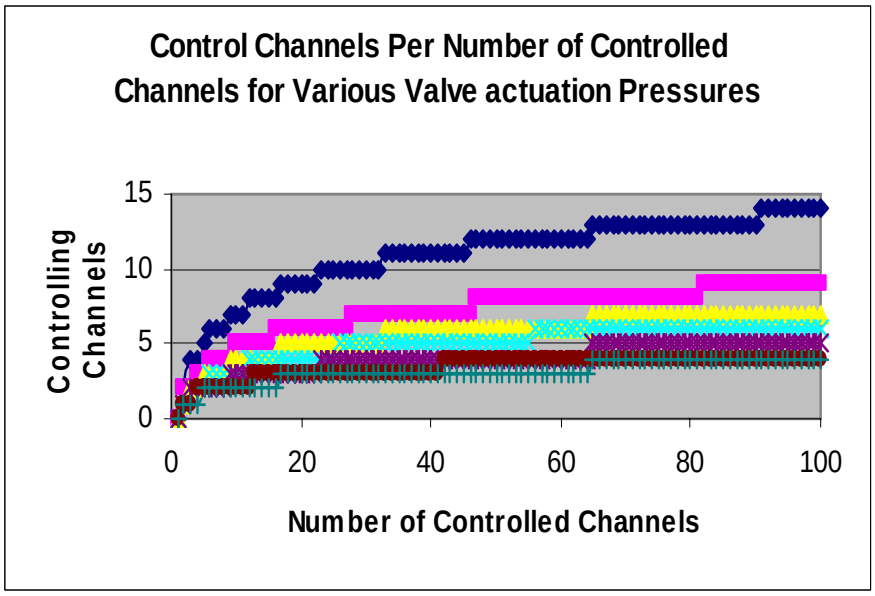

Figure 3 A graph representing the number of control channels required per controlled line. Each line reresents a different number of valve closing pressures with the top line being only on/off. This graph clearly demonstrates the advantage of pressure multiplexing over standard multiplexing for reducing the number of input channels.

A multiplexer that no longer simply functions on a binary valve system, but rather on various pressures is more efficient than the previous microfluidic multiplexers. A microfluidic multiplexer is only as important as its

efficiency. Microfluidic multiplexers have multiple applications, in applied physics, chemistry, engineering, and biotechnology. It is used in the production of DNA chips, micro-propulsion, and more recently, lab-on-a-chip technology. The previous multiplexers were created to asuage the inefficiencies of simple microfluidic arrays in which each fluid channel is controlled by its own individual valve control channel, however these designs cannot be efficiently scaled up. These problems are eradicated through the use of multiplexing, or more efficiently, through pressure multiplexing.

We created an array of 46 microfluidic lines, and two pairs of two control inputs, (figs. 4 + 5) it is possible to manipulate the valves using the various pressures, to control the flow of a liquid – in our case, dye – through various channels. As a result, complex manipulation of the

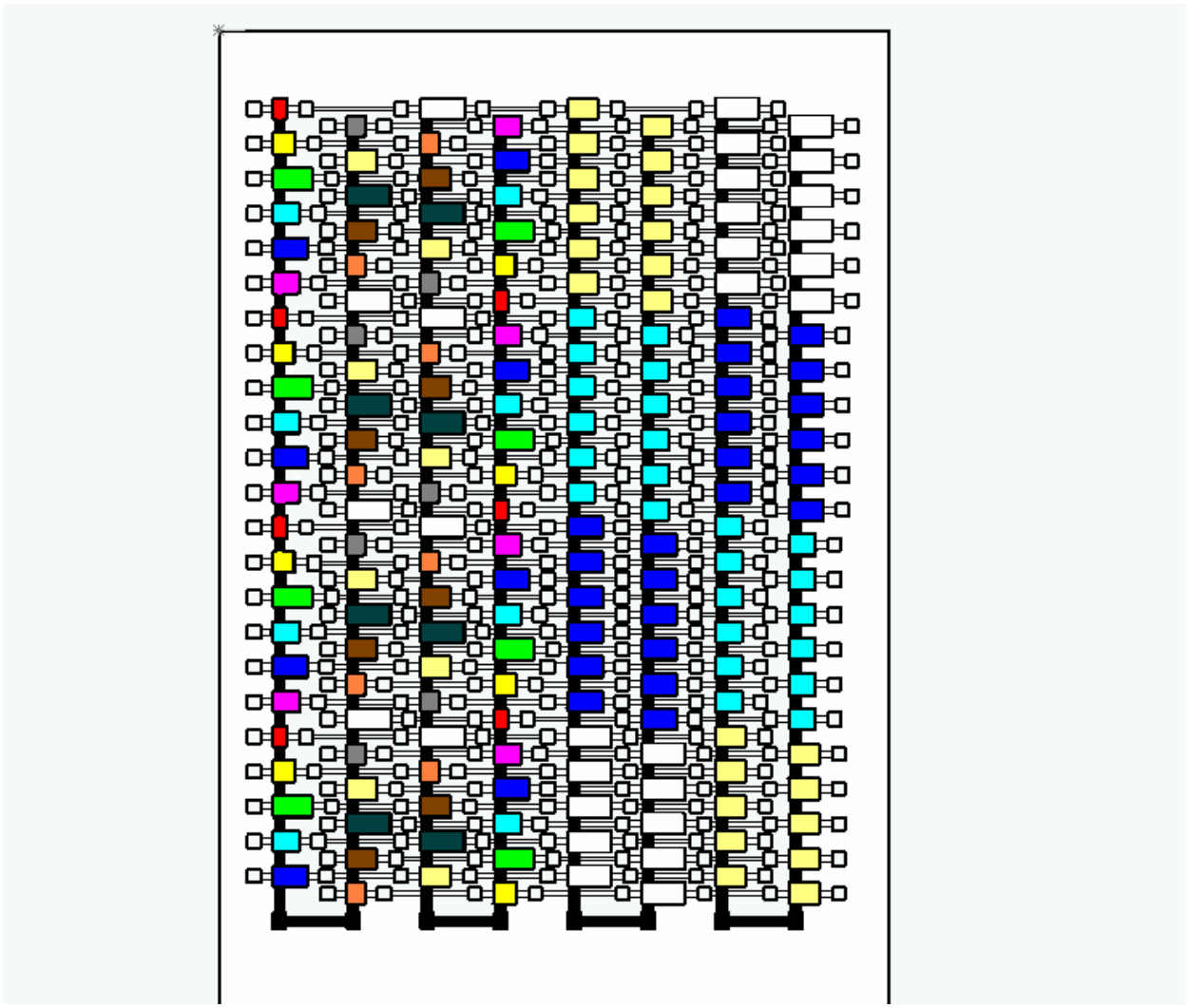

Figure 4 Our multiplexer design with 46 input and outputs controlled by only 4 control lines. Each individual color represents a valve with a distinct closing pressure. The valves have both different membrane thicknesses and valve lenghths in order to make them close at different pressures.

array is efficient and more specific. Control of the channels can be done in several combinations, with different pressures in the control inputs. In a simple array, one pair of control inputs is inserted with high pressure gas,

effectively closing all the channels with valves that close at high pressures. A second pair of control inputs can be designed to assign to different combinations of channels. To understand this, it is necessary to understand the design of the multiplexer. There are 46 channel lines, which are sorted through the twenty-four different valves that close at

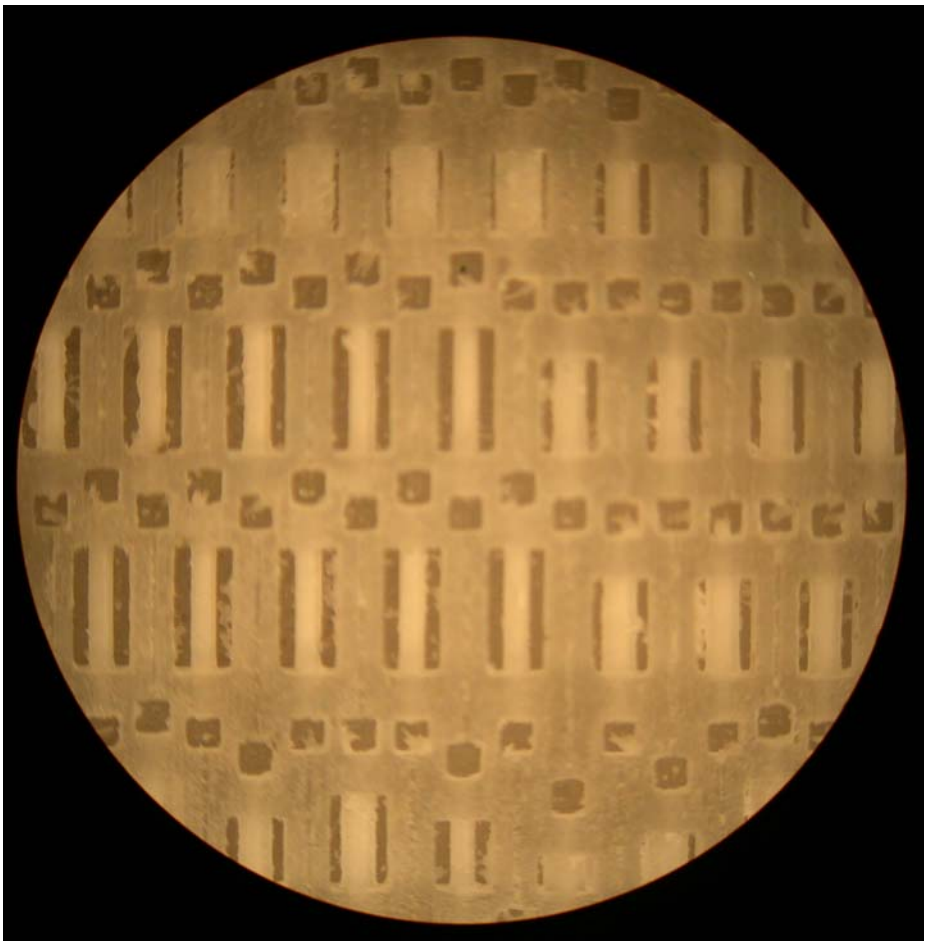

Figure 5 Micrograph of a section of our multiplexer chip. The different valve lengths and thickneses are clearly visible in this view from underneath the valves.

different pressures. They do not necessarily have to be in the order of valve pressure; however, they are placed in an order. This is due to the following reasons: the control inputs, through which pressure travels to close valves, correspond to various valves, so as to allow for the selection of specific valves and fluid pathways. Therefore, the usage of several control inputs – four, in our multiplexer – can be used to single out a single fluid pathway, or can be manipulated for a pathway of our choosing. Also, with the use of pressure multiplexing and twenty-four different valves that close at twenty-four different pressures, it is also possible to create more than one single pathway from one end of the multiplexer to the other. That is to say, it is possible now to use multiple, consecutive or even nonconsecutive lines to reach their respective ends through different pathways concurrently. Whereas the previous paper allowed for only one pathway to open at a time on one multiplexer, our multiplexer allows for several pathways to be created at the same time, on one multiplexer, through the use of pressure multiplexing. It is more efficient than a binary on/off microfluidic multiplexer, because twenty-four different degrees of freedom allow for more channel lines with less control inputs.

We have demonstrated a general technique for increasing the efficiency of microfluidic multiplexers that takes advantage of pressure information to reduce the number of control

inputs necessary to control *n* fluid lines. We have demonstrated this in PDMS using our three-dimensional valves which allowed a greater pressure space than traditional planar microfluidics, although the principals we outline are also applicable to planar microfluidics. Additionally our multiplexing scheme allows for groups of control lines to be selected instead of just one. This multiplexer design will find broad applications in microfluidics in order to decrease the “tyranny of numbers” associated with large scale microfluidic integration and will allow ever more complicated chips to be made.

5. Bicuspid inspired Microfluidic Check Valve

Complicated “check valves” can be made using the “lost wax” process which mimic the operation of the heart’s valves. These one way valves promise to be a robust check valve for an electrically operated microfluidic valve. All of the variables for making these complex three-dimensional valves are analyzed and a one input pump is demonstrated, as opposed to the three normally required for traditional peristaltic microfluidic pumps.

Complicated “check valves” can be made using the “lost wax” process which mimic the operation of the heart’s valves. These one way valves promise to be a robust check valve for an electrically operated microfluidic valve. All of the variables for making these complex three-dimensional valves are analyzed and a one input pump is demonstrated, as opposed to the three normally required for traditional peristaltic microfluidic pumps.

The three dimensional microfluidic check valves are designed by solidworks—a 3d structure design software. The overall size is 2mm*2mm*2.4mm, but it can be easily integrated with channels which are at the minimum resolution of 115µm by 12.5µm. The material used to build our device is poly(dimethylsiloxane) (PDMS). Other polymers, such as Sifel or PFPE can be used as well, but the properties of the valves are dependant on the spring constant of the material used to make them.

The valves are designed in such a way that the water is blocked when it flows from the top part to the bottom part of the valves or visa versa. There is one flap in the top part and a which mates with a sealing surface 50 microns underneath the flap. The sealing structure is part of the monolithic PDMS that forms the valve flap and has a square hole in the center. No alignment is necessary as the entire valve is molded from the same wax piece (Figure 1-2).

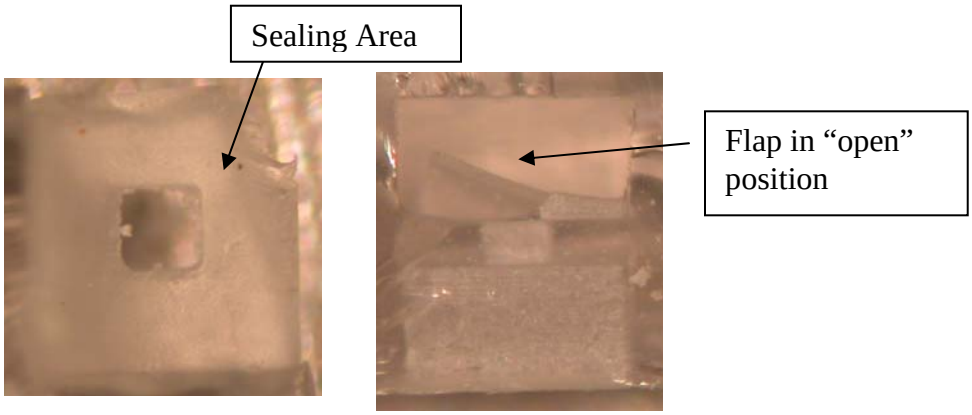

Figure 1. Optical micrographs of the 3D check valve showing the sealing area where the flap is forced against during reverse flow and the flap in the open position.

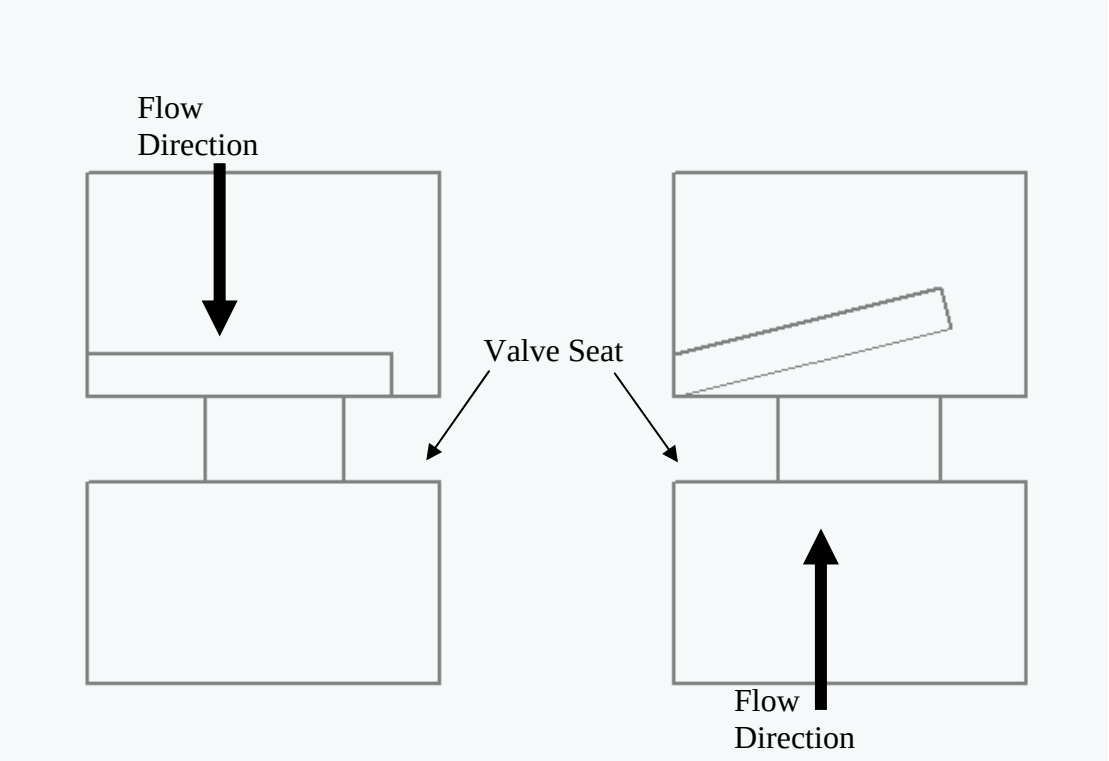

Figure 2. A side view of the check valve. The image on the left is the valve in the "closed" position where flow is coming from the top, down through the valve and forcing the flap against the sealing lip in order to create a seal. When the flow of liquid is reversed and comes from the bottom to the top, the flap is forced open and the fluid can flow freely through the structure.

The area around the hole is the valve sealing area. When the water flows in reverse through the check valve, the pressure of the water will push the flap toward the well structure and it will seal against the lip. At the same time, the square hole will be blocked by the flap. No water can come down in this mode. When the water flows up, it will go through the hole first and push the flap to open.

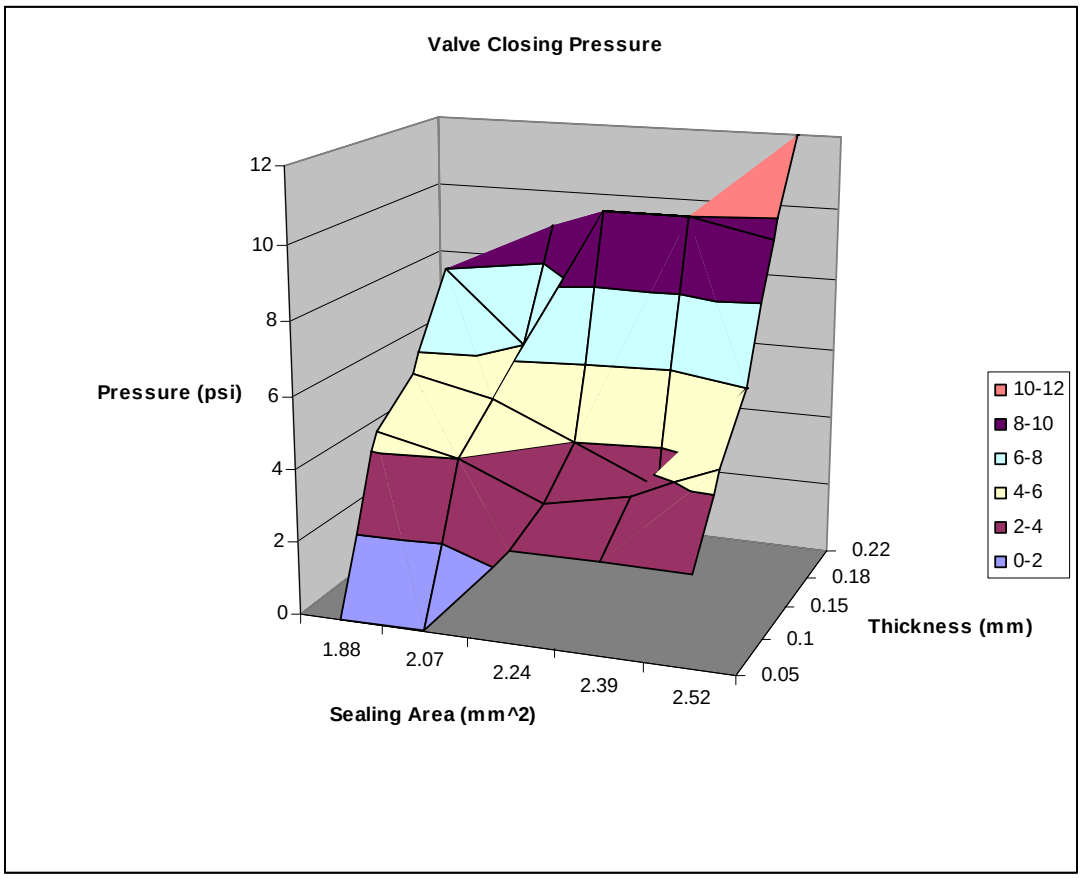

Figure 3 A graph of closing pressure with regards to the sealing area and flap thickness. The greater the amount of sealing area (corresponding to the interaction area between the flap and the valve seat) the lower the pressure needed to close the valve. At the same time as the flap thickness increases the amount of pressure required to tightly seal the valve also increases.

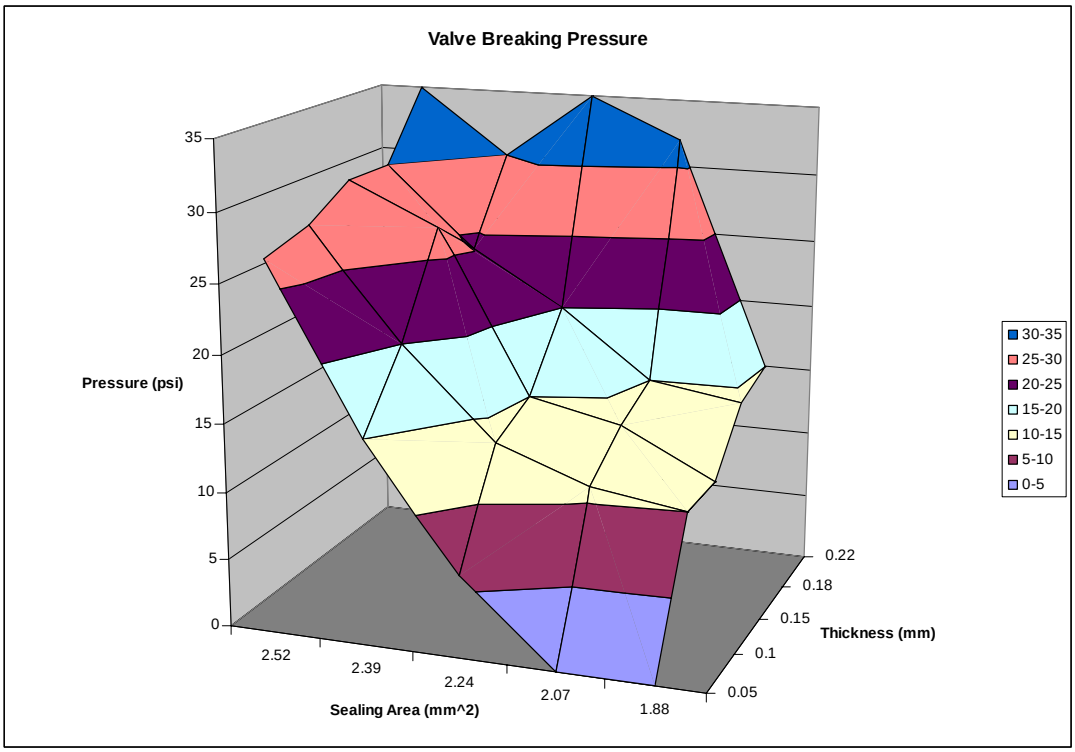

Figure 4 A graph of reverse valve breakthrough pressure when the valve is operated in reverse. Greater valve thickness and sealing area servs to prevent higher pressure reverse flows up to 35psi.

In the experiment, we vary the thickness of the flap and the size of the sealing area to find under what pressure the valves will be closed and broken. The thickness of the flaps where choosen as 50µm, 100µm, 130µm, 160µm, and 200µm and the sealing area is 0.36mm^2, 0.5476mm^2, 0.81mm^2, 1.04mm^2, and 1.44mm^2. 25 valves spanning the parameter space where built simultaneously on the same chip. The apparatus to test the valves consisted of a pressure source (compressed air), a sealed bottle of water, graduated cylinder and stop watch. The water in the bottle was pushed by the pressure source into the top part of the valves. When doing the experiment the pressure began at 1psi and was increased in 0.5 psi

increments in order to find the pressure under which the valve is sealed. Sealed valves remained leak tight for greater than 10 minutes.

The pressure was then increased to determine the valve breaking pressure. The mode of failure is quite sudden, with the flap quickly slipping past the valve seat and allowing water to suddenly pass the valve.

From the experimental data, we find that:

1. The closing pressure is highly related to the thickness of flaps and is not very dependant on the size of sealing area very much.

2. The thicker the flap is, the higher pressure needed to close it. The pressure ranges from 2.5 psi to 10 psi. (2.5, 4 , 6, 9, 10psi)

3. As the sealing area is small, no matter what the thickness of flaps is, valves can afford large pressure like 30 psi. But when the sealing area is big, the breaking pressure drops fast to a low value like 10 psi. Generally, the thicker the flap is, the higher pressure we need to break it.

4. For large sealing area, the valves with the thinnest flap (0.05mm) will never be sealed. This is represented by 0 psi on both graphs.

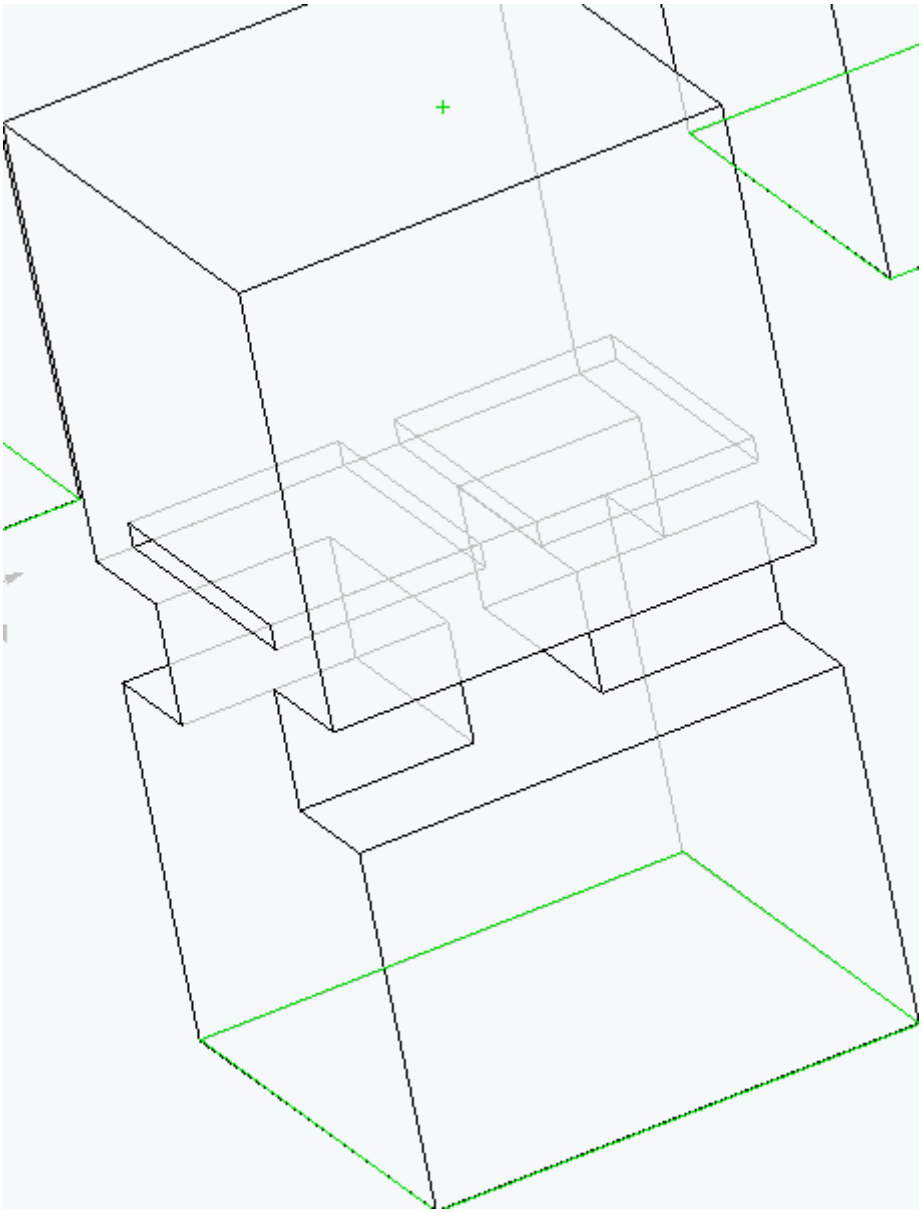

Figure 5. A 2 flap implementation of the check valve

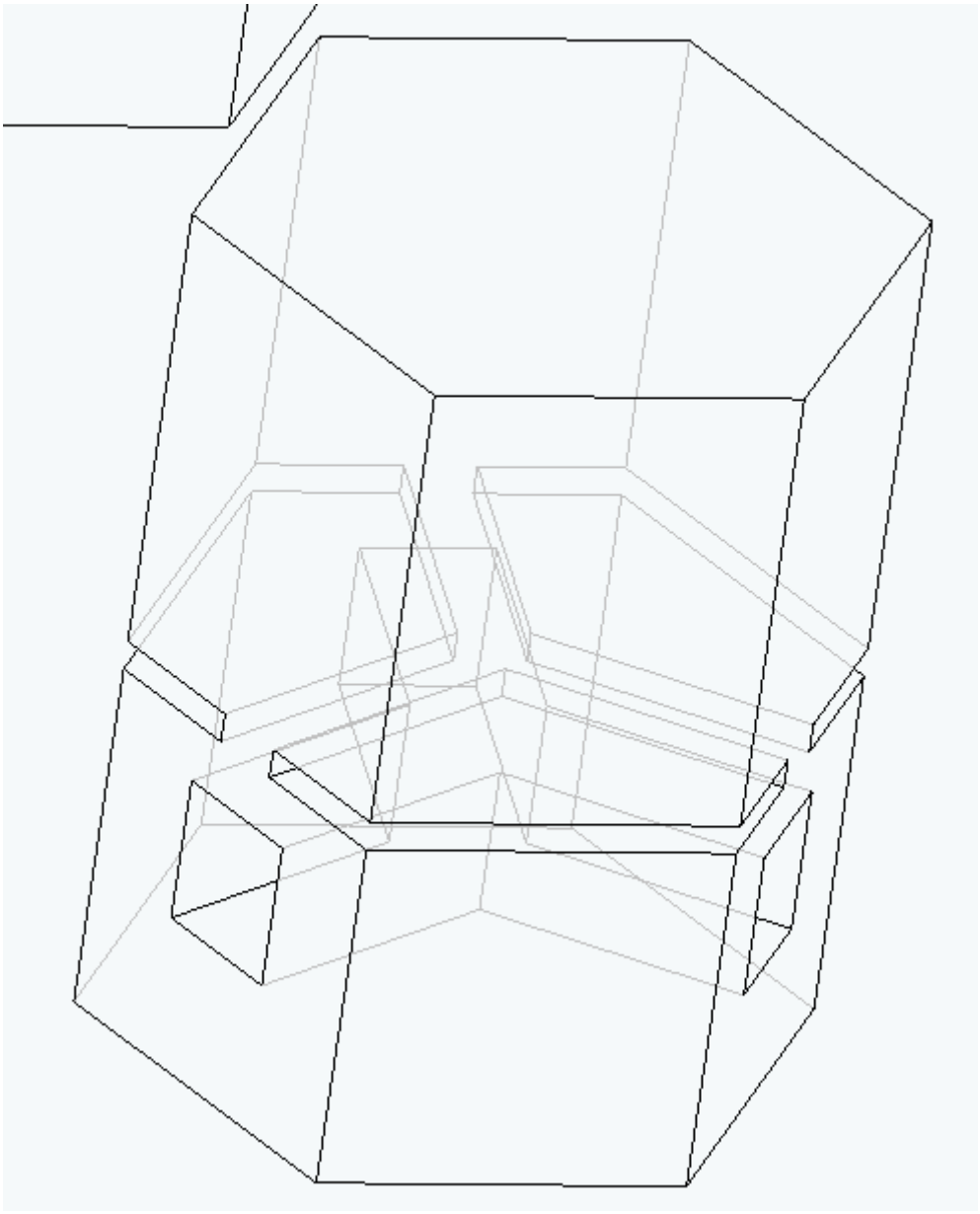

Figure 6. A 3 flap implementation of the check valve

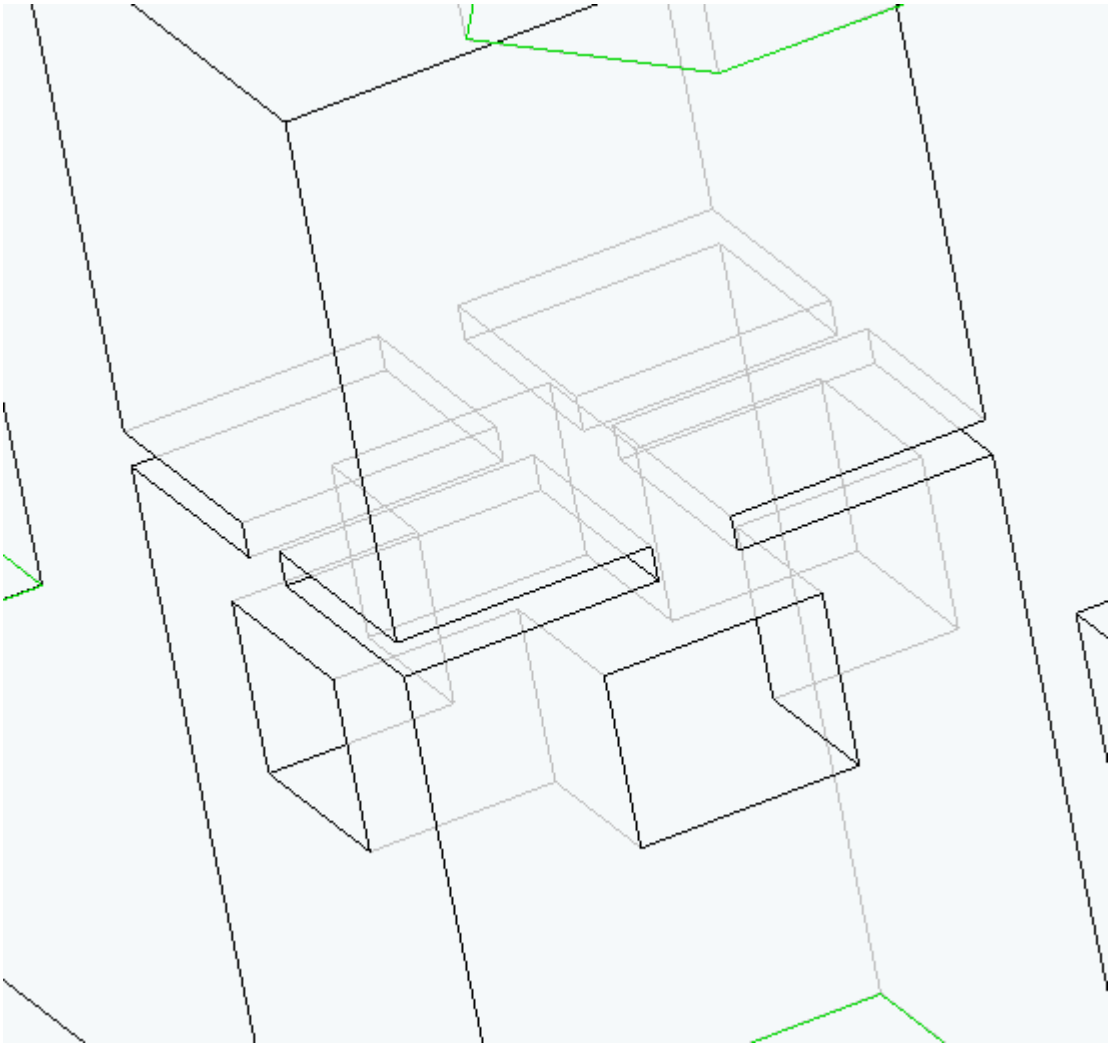

Figure 7. A 4 flap implementation of the check valve

We also explored other geometries (Figures 5-7) that involved two, three and four flaps, However none of these sealed as well as the 1 flap device. We believe that this is because the X-Y resolution of the wax printer was not sufficient to build leak tight structures on this size scale, and also because the area for leaks increases with each additional flap.

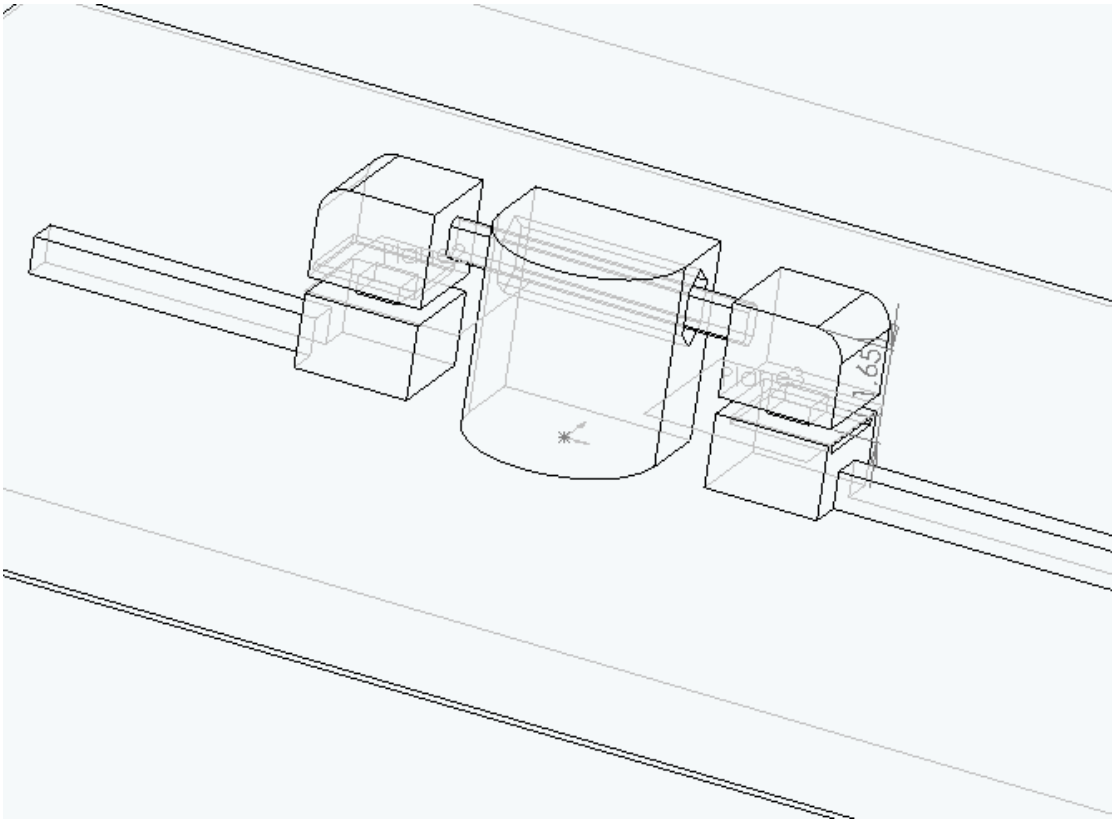

Figure 8. A one input valve can be made with two check valves and a 3D valve

A one input pump is also possible with a check valve and is shown in Figure 8. This is a 3 dimensional valve combined with two check valves that give direction to the fluid flow. The valve is squeezed, expelling fluid in the only direction the valves allow, and then the valve is relaxed, sucking fluid in from the opposite direction in order to form a pump.

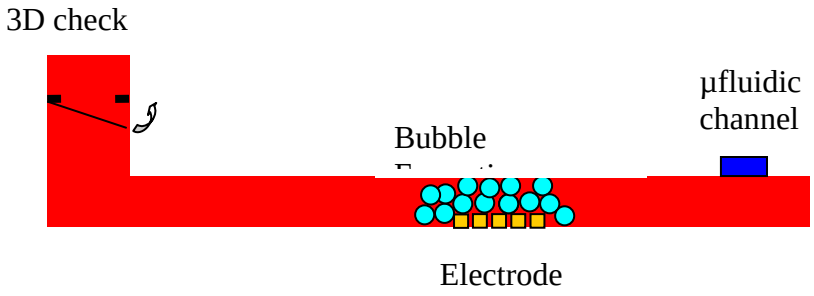

The most usefull application of these check valves is to integrate them with traditional microfluidics in order to eliminate the need for large off chip solenoid valves. In Figure 9 we show an electrically actuated valve in which a dead end microfluidic channel is connected to the one way valve. The channel has elecrodes in it that will create bubbles through electrolysis of the liquid when a voltage is applied to them. These bubbles occupy more volume than the liquid they replace and therefore will create pressure in the chamber, closing the check valve. Up to 8psi has been created in such a setup, more than enough to actuate the check valve. This pressure will then build in the channel. If this channel is in communication with another microfluidic channel through a thin membrane in the typical fashion, the membrane will deform and pinch off the microfluidic channel. This will create an electrically activated microfluidic valve without the need for off chip hardware.

6. Microfluidic Three-Dimensional separation column

The separation of mixtures using column chromatography is a widely used method in analytical chemistry. In column chromatography, molecules travel through a gel (stationary phase) placed in a column and the mobile phase, a solvent in which the materials to be separated are miscible in, flows down the column. Different substances will flow at different speeds, allowing for the mixture to be separated. Here, a method known as flash chromatography is used. It differs from common gravity chromatography in the sense that is uses pressure to run the molecules through the packed column. In this case, using the our three-dimensional “lost wax” approach for microfluidics, we developed a method for miniaturizing a chromatographic column.

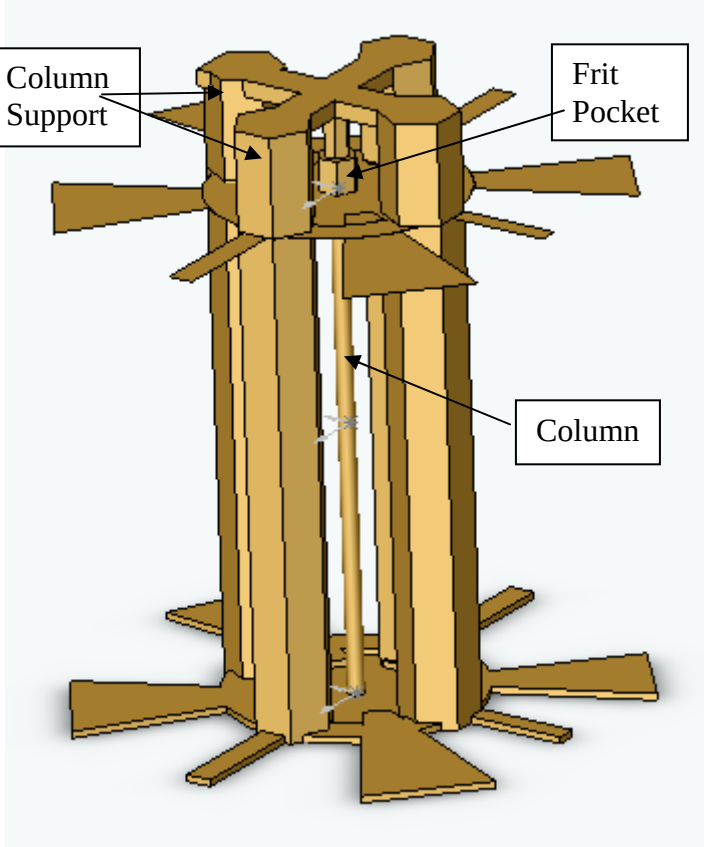

Figure 1 A computer model of the wax structure used to make the microfluidic chromatography columns

First we created a 3D computer model (fig. 1) and then realized it using a rapid prototype machine (solidscape T66). The micro column has dimensions of 600 microns in diameter by 15,000 microns in length. The ratio of these dimensions (1/25) is comparable to a very long benchtop separation column in order to ensure good separation. In order to make such a thin vertical column, with good reliability, it was necessary to place larger supports around the column and a cross bar over the top in order to secure it through the processing steps. At the end this connection was cut, leaving us with just the column. The wax model also has a "frit pocket" in order to hold a sodium

silicate frit in place. This wax model was then embedded into a poly(dimethylsiloxane) (PDMS) elastomer. Once the wax is melted away a micro column is created inside the PDMS elastomer with the same dimensions as the wax model. A glass frit like material is embedded into the column to serve as a base for the silica that will be the stationary phase. It was very difficult to embed a traditional glass frit into the monolithic structure of the pdms with the necessary leak tight fit, so we devised an alternative method using sodium silicate. Sodium silicate is liquid at room temperature. This allows us to construct the frit by placing a wire of the appropriate diameter into the colum, up to the point where a space has been made for the frit (the “frit pocket” fig 1.). The wire serves as a seal to hold the liquid sodium silicate in the frit pocket. Sodium silicate is then injected into the frit pocket and is then heated at 175 degrees for 10 minutes. Under these conditions sodium silicate crystallizes and forms a porous solid with ideal properties for use as a column frit. Silica is then carefully pured into the column, either dry or by means of a slurry (fig. 2).

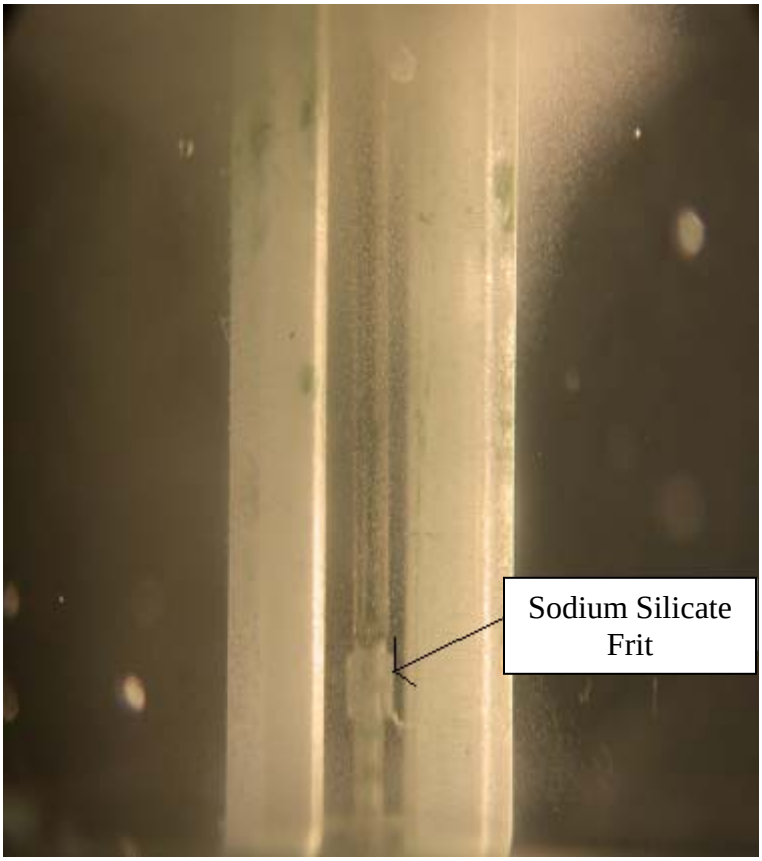

Figure 2 The completed column cast in PDMS. The sodium silicate frit is visible and the column is packed with silica

Our initial experiment consisted of separating two food dyes. They were mixed and introduced into the column. 2psi of pressure was then connected via a 23 guage steel pin and used to move the dyes through the column. A typically separation took less than 20 minutes from start to finish

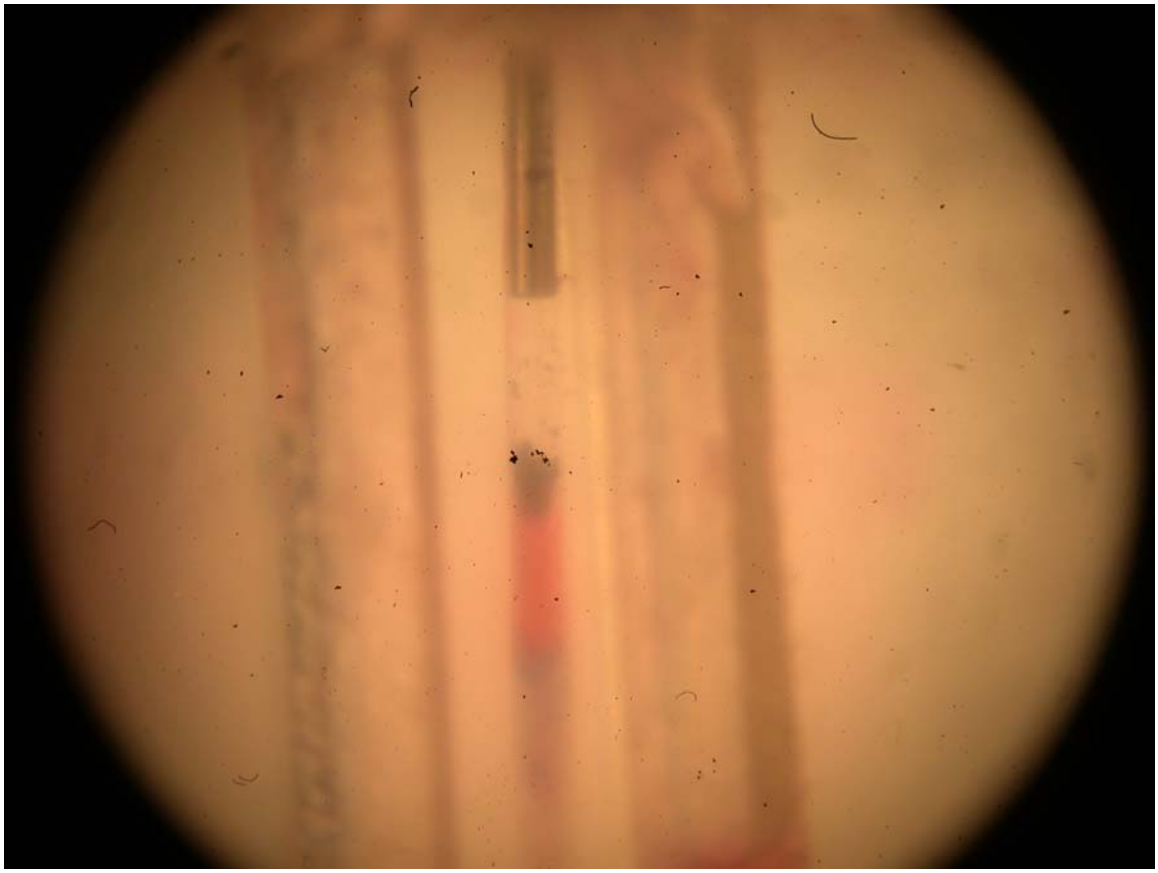

Figure 3 A column separating blue, green and red dyes. The three bands are visible traveling down the column

A 0.2 •L plug of a mixture of dyes was introduced to the top of the tube via pipette. The dyes were observed to separate in the colum and were collected at the bottom. The pattern was similar to a thin layer chromatography done on the same dyes. We have not yet found ideal conditions and solvents for separating these dyes so our seperations have been slightly "smeared" but the columns do show promise. Collection is also a concern due to the fact that the column lacks a mouth from where the purified material can drip easily from. This was solved by using micro slides (concave slides commonly used in microbiology) attached to the bottom

of the column allowing it to drip and be collected for further TLC plate studies.

Future research will see better separation using a larger number of solvents. These columns can be made in fluorinated polymers such as sifel and PFPE and should allow the majority of organic solvents to be used. Other types of columns can also be made such as elution and affinity columns. Additionally a multilayer stack of two and three-dimensional microfluidics can be aligned to the columns in order to introduce fluids into the columns and extract it afterwards. Additionally it is quite easy to make large arrays of these columns and the possibilities for combinatorial chemistry and other applications in which multiple reactions need to be carried out and purified are apparent.

References

1. www.chem.ualberta.ca/~orglabs/Shirley's%20Webpages/WebChem/ColChrom/colchrom.htm
2. T Uchida and CR Filburn, "Affinity chromatography of protein kinase C-phorbol ester receptor on polyacrylamide-immobilized phosphatidylserine". J.

Biol. Chem., Vol. 259, Issue 20, 12311-12314, 10, 1984.

3. Desgres J, Boisson D, Padieu P, “Gas-liquid chromatography of isobutyl ester, N(O)-heptafluorobutyrate derivatives of amino acids on a glass capillary column for quantitative separation in clinical biology”. J Chromatogr. 1979 Feb 21;162(2):133-52.
4. McDonald JC, Duffy DC, Anderson JR, Chiu DT, Wu H, Schueller OJ, Whitesides GM, **“**Fabrication of microfluidic systems in poly(dimethylsiloxane)”. Electrophoresis. 2000 Jan;21(1):27-40.

III

Devices created to analyze blood

1. Microfluidic Device to extract Blood Plasma from a finger Stick

Abstract

The promise of microfluidic medical testing requires the extraction and analysis of small quantities of patient's blood. Here we describe a device that uses the standard method of a finger stick blood draw using a capillary tube to provide a microfluidic circuit with blood plasma or serum that is ideally suited for downstream microfluidic evaluation. When working with on-chip microsystems for whole blood analysis, it is important to process the whole blood into components that can be analyzed using microfluidic technology. Blood typically must be anticoagulated and filtered in order to yield plasma, often necessary for microfluidic applications. Plasma will not coagulate in the channels, nor will large blood cells clog the microfluidic chip. The blood filter used in this work was created from poly (dimethylsiloxane), or PDMS, and commodity off the shelf blood filter paper. The blood filter was tested with mouse blood and was able to filter more than a milliliter of whole blood at a low constant pressure of 0.5 psi. The blood Plasma was then passed onto a traditional microfluidic circuit via a 23 guage connector pin.

Introduction

With the increased use of microfluidic technology in the fields of physics, chemistry, engineering, biotechnology, and especially medicine, it has become increasingly more important to discover more viable and more efficient means through which to incorporate existing technology into a microfluidic context. One such example is the analysis of blood through microfluidics. For the practical application of microfluidic analysis, it is necessary to create a system of blood filtration and anti-coagulation, a procedural practice necessary for microscale whole blood analysis.

In the context of microfluidic blood analysis, the system of blood filtration and anti-coagulation is necessary to handle blood samples in a miniaturized format. That is to say, there must be a way to separate blood cells and plasma from whole blood, on a microfluidic scale, for proper microfluidic blood analysis.

It is well known that cell inclusion may lead to cell lysis affecting the reproducibility and standardization of blood tests [1]. A second reason to remove the blood cells in an initial step is that miniaturized downstream systems, such as on-chip detection modules, protein analysis, PCR etc are prone to be clogged by cells and coagulation. Blood filtration is necessary for all assays requiring plasma as well. Viral screening and other blood-type analysis may not deal specifically with blood cells, but what else may be

found in blood – such as proteins or antibodies. In that context, it is necessary to filter whole blood, not only for individual blood cells, but also for the plasma.

Poly (dimethylsiloxane), or PDMS, was the material used for the blood filter, as it is more cheap and disposable, and has little affinity for proteins, RNA, DNA etc [2-4]. The device can also be made from a variety of polymers including fluorinated Sifel and PFPE if the specific application requires the highest capture rate and sensitivy for rare species[5]. PDMS is a good choice because it seals well to the filter, is compatible with traditional microfluidics and is flexible enough to seal to both the glass capillary tube and the standard metal pins used to introduce samples to microfluidic chips.

In this design, the purpose was the create a microfluidic blood filter that could, on one end – the receiving end – be integrated with a capillary tube with an anti-coagulate – in this case ethylene-diamine-tetra-acetic acid, (EDTA) – on it. These capillaries of the type that are commonly used for finger stick blood draws and are available with a variety of anti-coagulants depending on the intended analysis to be performed. The blood comes from a single prick on a fingertip onto a capillary tube. The other end of the blood filter, the end through which filtrate passes through, was made to interface with any standard microfluidic chip, through a 23 gauge pin. Whole blood would pass through the specially designed filter paper embedded in

the PDMS blood filter, separating whole blood from the plasma, which would be used in the microfluidic chip.

Experimental

Device fabrication

The PDMS blood filter is made from a machined aluminum mold, shown next to the actual PDMS device in figure 1.

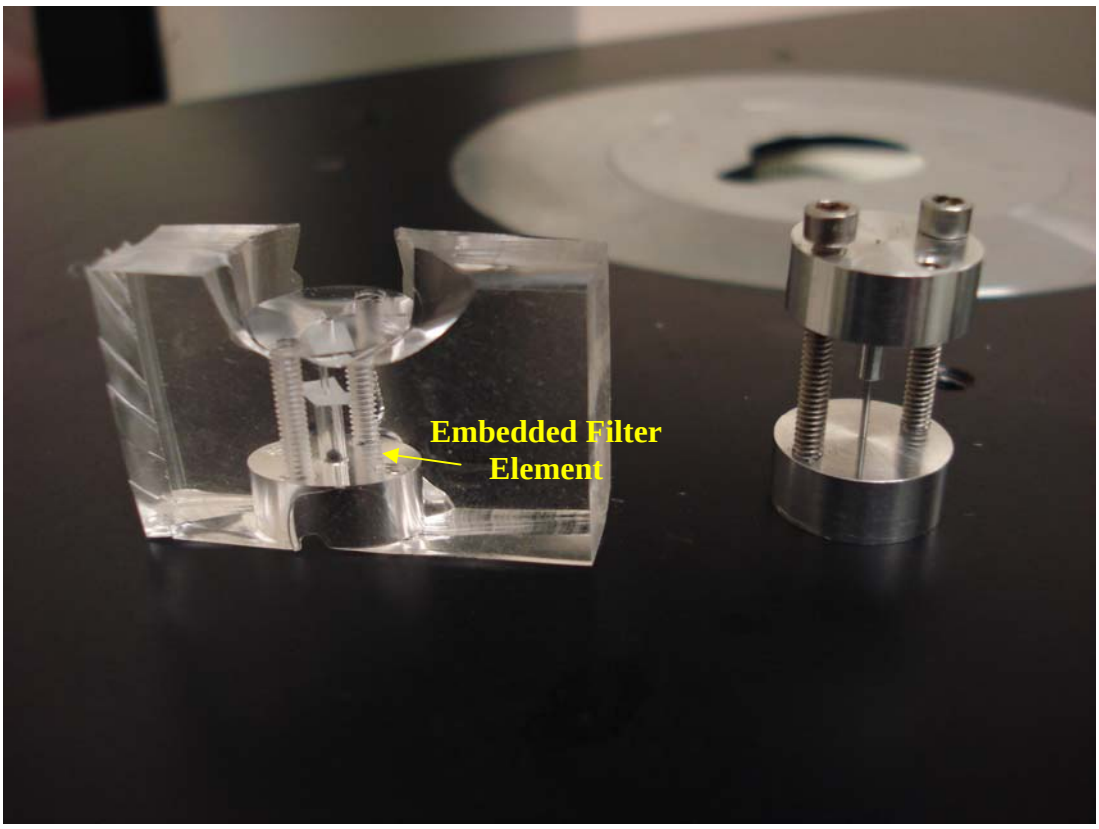

Figure 1 The aluminum mold and the cast PDMS with the filter material embedded in the flow channel. The aluminum mold was designed to be separated and a piece of filter material was placed between the top and bottom halfs and then cast in polymer. This enabled a leak tight seal to be created around the filter in order to force blood through the filter only

The mold is made of two pieces, that are brought together by alan bolts. The top piece has a cylinder designed to mold the PDMS such that the capillary tubes can be pushed in and sealed. The bottom piece has a 24 guage steel pin press fit into the aluminum in order to mold a hole that will seal tightly to the standard 23 guage pins typically used for microfluidics. The top piece has 4 holes, two of which are not threaded and correspond to tapped holes on the bottom piece and are used to compress the filter between the top and bottom cylinders. This ensures that a leak tight channel will be created in which blood must pass through the filter only. The other two holes are threaded and have no corresponding holes on the bottom piece and are used to gently back the mold out of the PDMS when the casting process is finished.

When the two rounds of the mold are connected, the two pieces, which mold for the capillary tube integration and the 23 gauge pin interface, serve to sandwich the blood filter. The filter paper is placed in between the top and bottom pins and then the alan bolts are used to squeeze and hold the filter in place. This method will creat a monolithic PDMS device. These sorts of three dimensional device has a large advantage over traditional planar microfluidics for filtration in that a leak tight seal can be formed by virtue of the fact that the entire device is in

one piece of PDMS. All other filters in planar PDMS require registration and sealing between two layers and the filter. This is difficult because only the thinnest of filters can be sealed this way, and leakage is a problem.

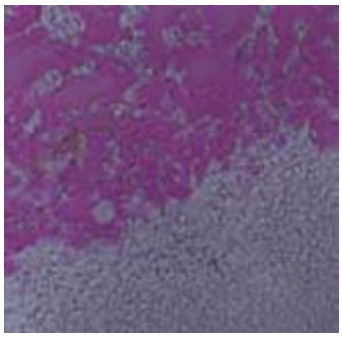

Figure 2 A micrograph of the BTS-SP filter media. Note the graduated pore structure from top to bottom. The larger pores at the top serve as a cell exclusion zone, trapping red and white blood cells while wicking the blood plasma past the filter.

There are several commonly available filters, all of which are very cheap, especially in the small size needed for this device. We chose BTS-SP series from Pall Corporation (East Hills, NY). The BTS-SP media (figure 2), features a highly asymmetric membrane that is specifically engineered for serum separation of whole blood. The graduated pore structure of the filter consists of more open pores on the upstream side with finer pores on the downstream side. The high degree of asymmetry allows red and white blood cells to be captured in the larger pores while the plasma wicks into the smaller pores on the downstream side of the membrane.

The large pore side of the media serves as an absolute cell exclusion zone and performed very well in our device.

When the mold has been prepared, it is placed sideways into a standard Petri dish. PDMS is then poured into the Petri dish, carefully to completely cover the mold. The PDMS is mixed in a 10:1 ratio. After the mold is completely covered by the PDMS mixture, it is left to degas in vacuum, until all air bubbles have been separated. At this point, the mold and the PDMS in the Petri dish are left to cure in an 80 degree Celsius oven for 1 hour. After curing, the PDMS blood filter was cut out of the dish and the allen bolts where removed from the mold, freeing the two halfs. The allen bolts where then inserted into the tapped separation holes and the mold was slowly backed out of the PDMS. This left the blood filter paper intact in the PDMS filter.

The choice of capillary tube is specific to the test to be carried out on the blood because different anticoagulants are needed for different analysese. The capillary tube, StatSampler Capillary Blood Collectors from StatSpin (Iris Sample Processing, Westwood, MA) used had EDTA as an anti-coagulant to keep the blood sample from drying out or otherwise becoming unusable. These capillary tubes are used in doctor's offices as a standard finger prick blood draw and are available with several different anticoagulants. EDTA was not strictly necessary because the mouse blood sample from Bioreclamation Inc. (Hicksville, NY) had EDTA as its anticoagulant.

Whole blood filtration

20 ml of mouse blood from was stored and refrigerated at 4°C when not used. There were two-10 ml samples, drawn a week from each other. EDTA was used to keep the blood from clotting.

The mouse blood was then drawn, 1 ml at a time, into a capillary tube. The capillary tube was then inserted into the upper portion of the filter (figure 3).

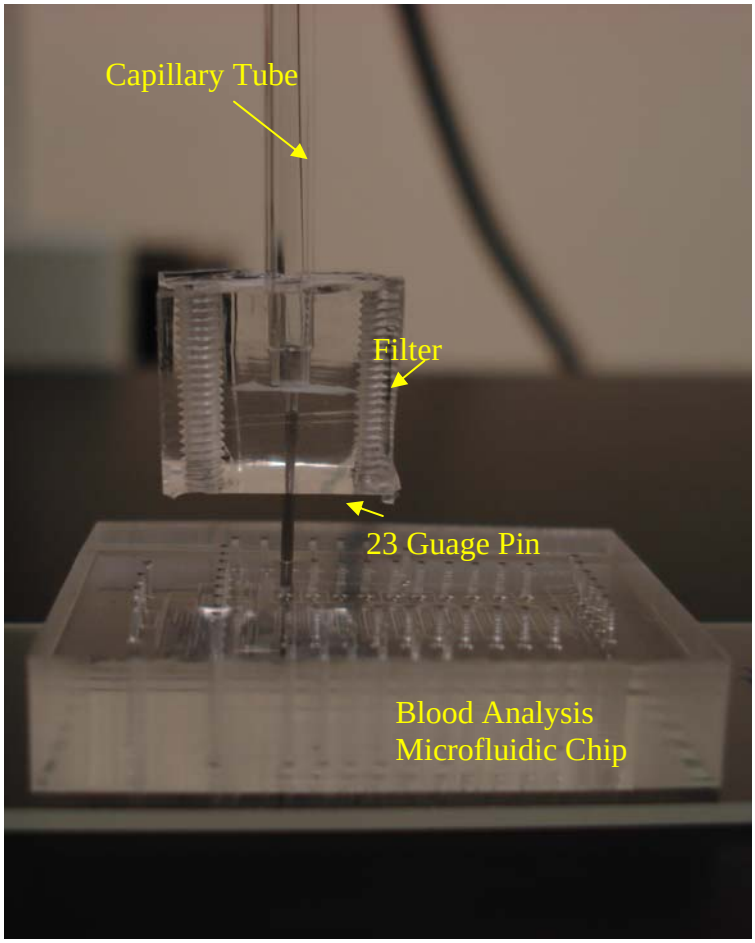

Figure 3 The PDMS blood filter integrated with a microfluidic blood analysis chip and a blood draw capillary tube

The capillary tube was attached to hose supplied with dry nitrogen and the blood was pumped through the filter at a constant pressure of 0.5 psi. This pressure was chosen for safety and to demonstrate that very little pressure is necessary to flow blood through the filter. It is also important to stabilize the pressure by which blood is filtered. Increasing the pressure from this low level does serve to speed the blood flow, but 1ml of blood went through the filter quickly. The filter was shown to collect 80-100% of the available blood plasma which is typically half the total volume of the blood. 500 microliters of blood plasma is a very large amount of blood for most microfluidic applications which typically require nanoliters to microliters of fluid in order to perform analysis.

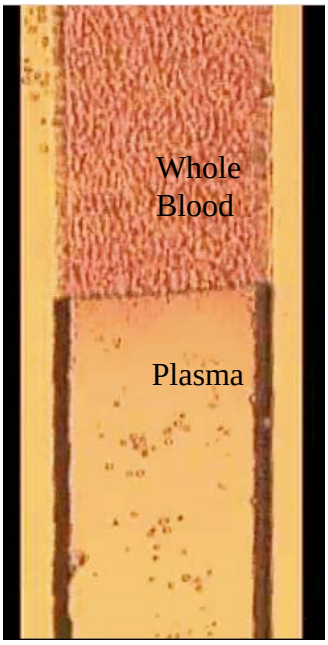

Figure 4 The blood filter during simulated use. The blood cells are all kept above the filter and plasma passes through below

One advantage of this design is that the same pressure which pushes blood through the filter can also be used to push the blood through an attached microfluidic chip. Figure 4 shows a simulated side view of the blood filter device during operation. The blood cells are stopped by the filter material and plasma continues to flow past the filter. Figure 5 shows two microfluidic channels with dimensions of 100µm in width and 10µ in height, one with anti-coagulated mouse blood flowing through it and the other with the filter directly connected to its input port. The channel with no filter attached to it is full of blood cells and the filtered channel is clear and is flowing only plasma.

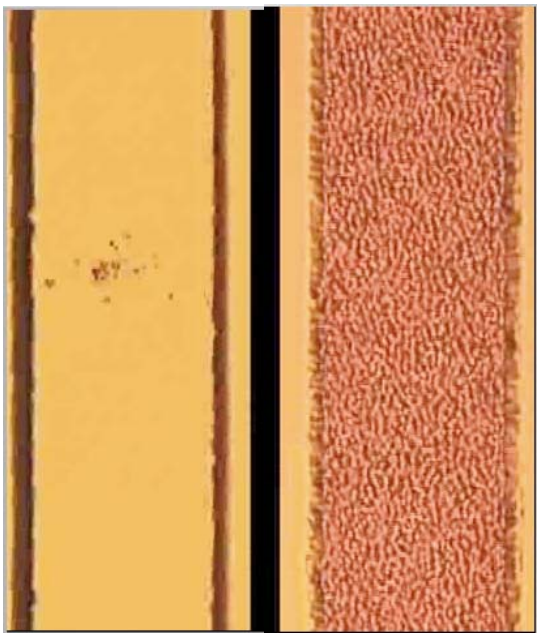

Figure 5 The channel on the left is connected to the microfluidic blood filter and the chanel on the right is directly connected to the blood source without the filter. Only plasma is flowing on the left while whole blood flows on the right

Conclusions

From the study, we were able to fabricate a simple, disposable, and sanitary PDMS blood filter for use with on-chip whole blood filtration for microfluidic blood analysis. The PDMS blood filter was able to filter the necessary volume of blood in an acceptable time frame. It should be noted that this PDMS chip was created specifically for use with standard microfluidic chips. The PDMS blood filter is effective in separating plasma and blood cells from whole blood. The ability to collect whole blood from a simple finger prick and directly insert it into a microfluidic chip will allow blood analysis to be brought closer to the patient and eliminate the need for painful venipuncture and trained phlebotomist and simplify the collection and analysis of blood.

2. Inexpensive, Portable Immunoassay Device

ABSTRACT

We have developed an inexpensive and rapid read-out system for multi-antigen microfluidic fluorescence immunoassay systems. The fluidic analysis chips can be fabricated in polydimethylsiloxane PDMS, and have been shown to perform high throughput analysis on multiple analytes and require the measurement of over 100 fluorescent readings with sensitive detection down to .01mg/ml concentrations. In a fluorescence assay, the intensity of fluorescence is used to read the concentration of the antigen, and is typically measured with a fluorescence microscope or a laser scanner. This serial measurement process is both time-consuming and expensive, and limits the speed with which an immuno-assay can be completed. Here we show that it is possible to perform fluorescence detection with digital imaging to obtain multiple immunoassay readings in parallel.

INTRODUCTION

Miniaturization of diagnostic tools often results in improved cost, manufacturability and ease of operation. Medical immuno-assay test chips benefit in this way from such reduced sizes, as multi-analyte high-throughput formats have can be developed to perform fluorescence identification

of many proteins in many blood samples. Many approaches for such chips using glass (2-8), TiO_2 (8), silicon (9, 10), and silicone (9, 11-19) fluidics have so far demonstrated the opportunities of more complex fluidic systems. However, until now, the read-out mechanism for such chips has involved the use of rather large fluorescence microscopes or laser scanners. Ideally, more compact handheld devices are desirable for point of care diagnostic immunoassays that can evaluate fluorescence form 100 chambers in parallel by using multi-element imaging cameras. This leads to an opportunity for enabling easier operation through massively redundant and automated measurement systems, followed by a simple readout that can compare fluorescence intensities with high sensitivity and accuracy.

High-throughput multi-antigen fluorescence immuno-assay chips made from PDMS microfluidic systems promise quantitative blood analysis at the clinically relevant levels of 10-100pM. In our most recently developed immunoassay chips, active microfluidic matrix (20) formats utilize arrays of integrated micromechanical valves (21) to direct pressure-driven flow and to multiplex analyte samples with immunoassay reagents. ELISA-like fluorescence immunostacks are formed in the microchambers at the intersections of sample and reagent channels. Here we show that the fluorescence signals from these microchambers can be measured with a digital camera to captured antigens. This

test matrix can be expanded to significantly larger numbers by exploiting the capabilities of PDMS microfluidic technology (22), resulting in even greater advantages of parallel fluorescence measurement.

EXPERIMENTAL

PDMS microfluidic chips with integrated micromechanical valves were built using soft lithography as described previously (21) with the following modifications. Silicon wafers were exposed to HMDS vapor for 3 min. Photoresist SPR 220-7 was spun at 2,000 rpm for 60 sec on a Model WS-400A-6NPP/LITE

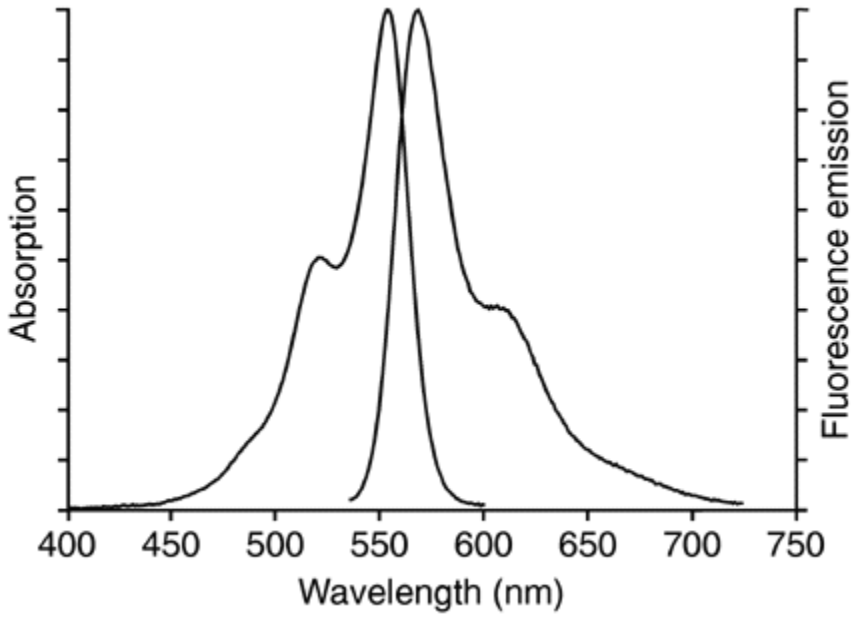

Figure 1 The emission and excitation curves of Alexafluor 555

spinner from Laurel Technologies Corp. The wafers were baked at 105 degC for 90 sec on a hotplate. UV exposure through

black-and-white transparency masks was performed for 1.75 min on a mask aligner (Karl Suss America Inc., Waterbury, Vermont). The molds were then developed for 2 min in 100% 319 MicroChem developer. Flow layer molds were baked at 140 degC for 15 min on a hotplate to melt and round the flow channels. Molds were characterized on an Alpha-Step 500 (KLA-Tencor, Mountain View, CA 94043). Channel height was between 9 and 10 µm. Control channel profile was oblong, while flow channel profile was parabolic. Except for the height measurements, the mold fabrication was conducted in a class-10,000 clean room.

Molds were exposed to TMCS vapor for 3 min. PDMS in 5:1 and 20:1 ratios were mixed and degassed using an HM-501 hybrid mixer and cups from Keyence Corp. (Long Beach, CA 90802). Thirty-five grams of the 5:1 was poured onto the control mold in a plastic petri dish wrapped with aluminum foil. Five grams of the 20:1 was spun over the flow mold at 1,500 rpm for 60 sec on a Spincoater P6700 (Specialty Coating Systems, Indianapolis, IN 46278). Both were baked in an 80degC oven for 30 min. The control layer was taken off its mold and cut into respective chip pieces. Control line ports were punched using a 20-gauge luer-stub adapter (Beckton-Dickinson, Franklin Lakes, NJ 07417). Control layer pieces were washed with ethanol, blown dry with filtered air or nitrogen, and aligned on top of the flow layer under a stereoscope. The result was baked in an 80degC oven for one hour. Chip pieces were then cut out and peeled off the flow

layer mold. Flow line ports were punched with a 20-gauge luer-stub adapter. Chip pieces were washed in ethanol and blown dry before binding to the epoxide glass slides. The now assembled chips underwent final bake in an 80degC oven overnight.

Sylgard PDMS elastomer was mixed with concentration (10:1), poured onto a silicon/photoresist mold, and used in a replication molding procedure. Once PDMS channels were completed, holes were mechanically punched to access the PDMS channels, and the elastomer was bonded to glass substrates at 80C. Following this soft lithography procedure, the glass was covered with black electrical tape to avoid stray light penetration. Then, different concentrations of Alexa Fluor 555 solution were injected into the channels and a digital image of the PDMS chip was obtained with an imaging camera shown in figure 2. Images taken with the setup are shown in figure 3 The intensity in the resulting digital image matches the concentration of the Alexa dye, and follows a linear relationship for higher dye concentrations (Figure 4). At lower concentration, this intensity/concentration graph reveals an anomalous peak in fluorescence intensity can be observed at lower concentrations. This peak, which indicates that the fluorescence drops with increasing dye concentration, can be explained by quenching mechanisms between dye molecules bonded to the surface of the flow channels. We have

carefully analyzed the anomalous intensity peak, shown in Figures 5 and 6.

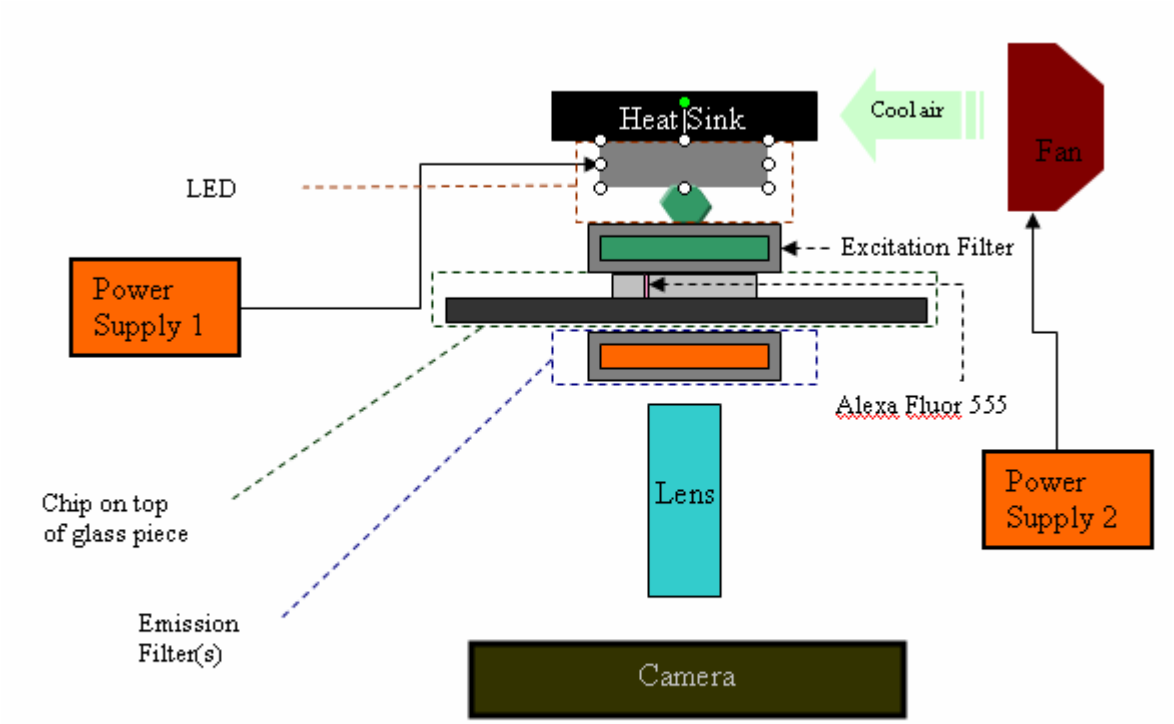

Figure 2 A schematic view of our device. The parts are all commodity off the shelf pieces and a very sensitive immunoassay detector can be built for a few hundred dollars.

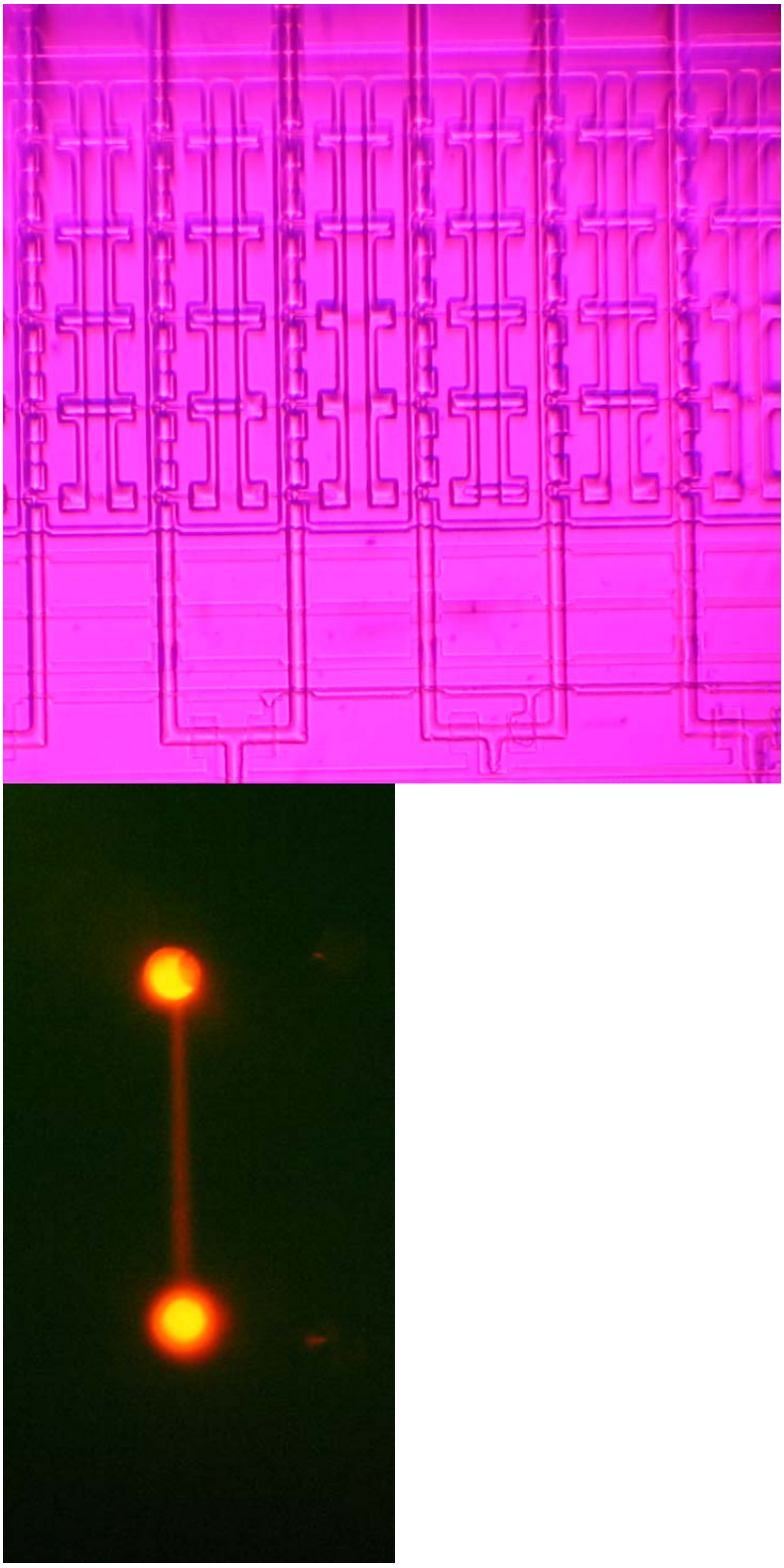

Figure 3 On the left is a view of a microfluidic chip with 100 micron wide fluid channels taken with only the emission

filter in plce in order to demonstrate the resolution of our device. On the right is a 100µm wide by 10µm tall channel filled with Alexafluor 555 in a fluorescent image from our device.

MEASUREMENTS

In this study, we measured fluorescence from a wide range of concentration of Alexa Fluor 555 with a Canon EOS digital "Rebel" camera and excited by either a light emitting diode (LED) or a mercury lamp in the geometry described by Figure 2. Concentrations of the fluorophore were prepared to range from 0.01g/ml to 300g/ml in water. When combined with a light emitting diode source, the digital camera provides a compact portable fluorescence imaging system, as 2 6V lantern batteries in series connection can be used to power the electronics. The camera was protected from the excitation light source by an excitation filter (HQ 545/25 by Chroma), and by selecting a LED or mercury light source emitting at a wavelength of approximately 545nm. This choice in source and filter wavelengths guarantees that only the fluorescent light matching the filter reaches the PDMS chip. The 545nm wavelength then excites the Alexa Fluor 555 dye (Figure 4), which emits at 555nm. Emission Filters ford other wavelengths (HQ605/75, HQ610/75, HQ620/60) were also tested to obtain superior signal to noise values. To improve the quality of the pictures and eliminate stray light, an

opaque rectangular aperture was placed above the PDMS chip. The dimensions of the aperture were chosen to be slightly larger than those of the PDMS chip, and this aperture ensured that only filtered light emission from the chip reaches the camera.

Digital images of the PDMS chips were taken at ISO settings of 100, 400 and 1600 and with shutter speeds ranging from the 1/100 seconds to 20 seconds. These pictures were analyzed and the ones that result in the highest S/N with clearly visible channels were chosen. Image analysis software (Astra Image

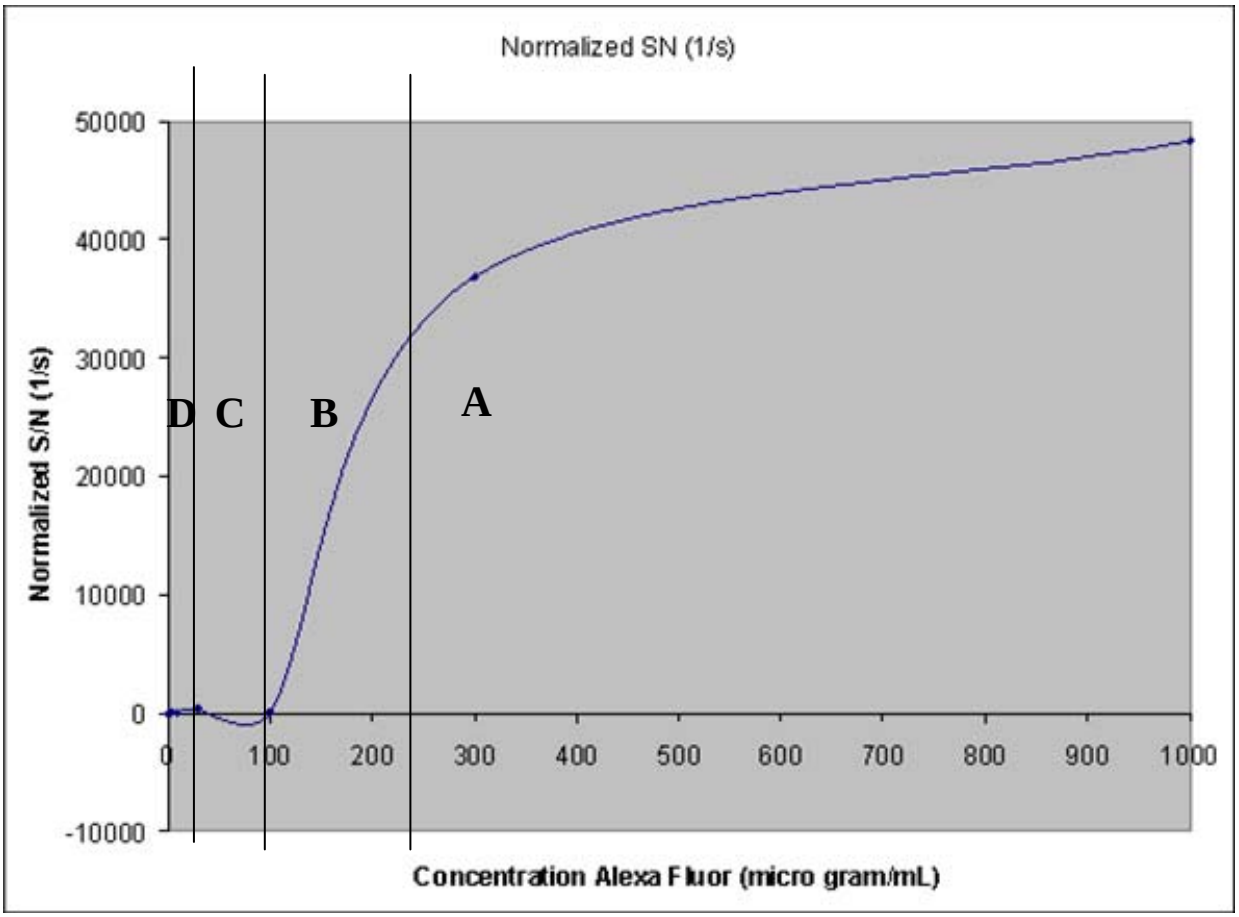
Normalized SN (1/s)
50000
40000
30000
20000
10000
0
-10000
Normalized S/N (1/s)
D
C
B
A
0
100
200
300
400
500
600
700
800
900
1000
Concentration Alexa Fluor (micro gram/mL)

Figure 4

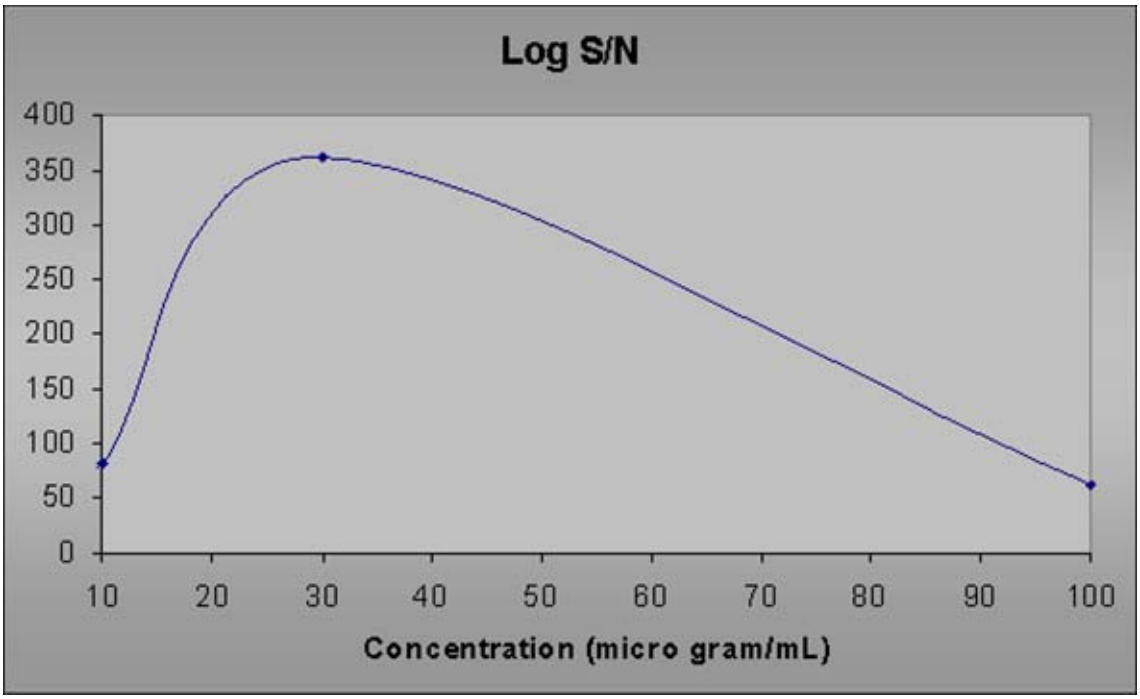

Figure 5

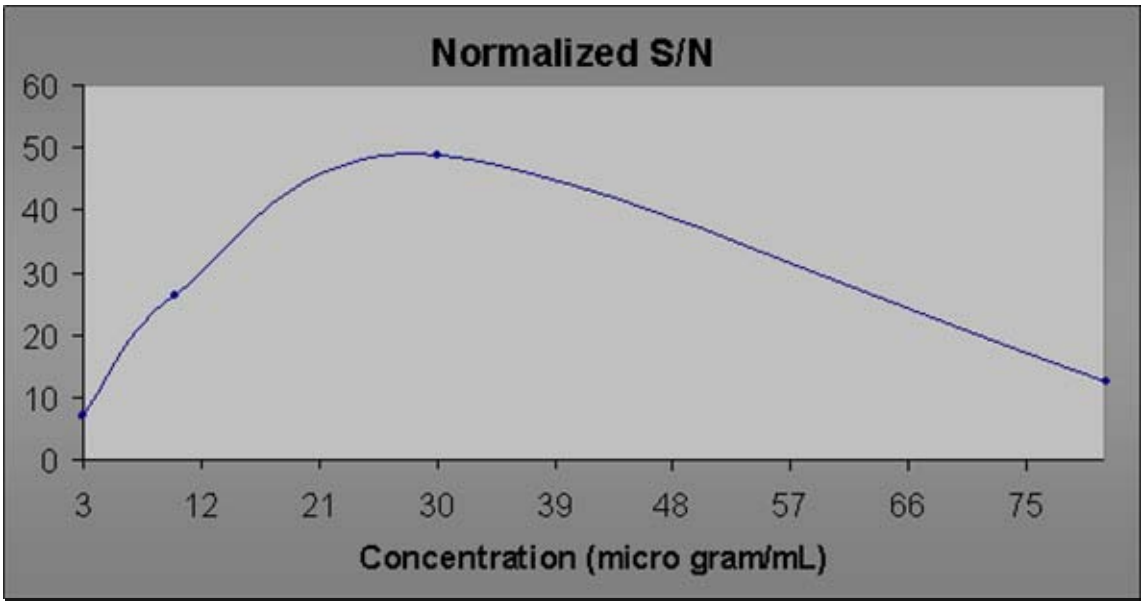

Figure 6

2.0 (Phase Space Technology)) was used to analyze these pictures. The measured red signal of the channel was

compared to the red signal from the background to evaluate the signal to noise using this software. The following equation was employed:

$$S/N = \frac{\mathrm{Re}\,d\_mean\_channel - \mathrm{Re}\,d\_mean\_background}{(\mathrm{Re}\,d\_deviation\_background)(Shutter\_speed)}$$

RESULTS AND DISCUSSION

Signal to noise values of the fluorescence signal were normalized and plotted as a function of concentration. This number was found to generally increase with concentration when measuring the chip during UV lamp illumination. Above concentrations of 0.1mg/ml, a linear relationship between fluorescence signal/noise and concentration is observed (Figure 3). At lower concentrations however, we observe an anomalous intensity peak at 0.030mg/ml. The SNR is not saturated in the intensity and concentration range of this measurement. If, instead of a mercury lamp, a LED (with a 2.5x larger intensity) is employed as a fluorescence source, the SNR values are improved and the fluorophore is found to saturate. (Figure 4). Four interesting regions can be identified in this fluorescence SNR graph from highest concentration to lowest (from right to left).

A. Saturation: At sufficiently high concentrations, saturation occurs in both the volume of the liquid and at the surface of the flow channels as the dye molecules are close enough to result in fluorescence quenching. Saturation on the surface results in significant fluorophore quenching

as the fluorophores are very closely spaced. As the concentration of fluorophore is increased, non-specific sites can be driven towards fluorophore attachment. At even higher concentrations, the CMOS detector elements may saturate, leading to further nonlinearities in the fluorescence measurement. Moreover, at high concentrations, horizontal scattering of light out of the channel sides leads to a decrease in SNR.

B. First linear region: At lower concentrations, the CMOS detector array response becomes linear and volume quenching is largely avoided. However, surface FRET energy transfer still occurs, but this term is expected to be linear with respect to concentration.

C First rise in graph: Above a critical concentration, the fluorophore density in the volume is sufficiently high to ensure that the surface dye molecules are saturated and experience quenching. As the concentration decreases, fluorophores molecules are released from the surface layer and, as a result, dye molecules that were previously quenched now contribute to the fluorescence signal.

D. second linear decrease: as the concentration is further decreased, the fluorescence signal from the liquid and the surface are linearly related as no quenching compromises the fluorescence signal.

To avoid uncertainties with the nonlinear intensity behavior resulting from fluorescence quenching, it is possible to bleach the fluorophores. If the signal is reduced after

optical irradiation, fluorophore concentrations are below the ones relevant for quenching. However, if the fluorescence intensity is increased, fluorescence quenching influences the signal. During optical irradiation, both free fluorophores contributing to the fluorescence signal as well as fluorophores that quench neighboring molecules are bleached. In most realistic clinical cases, surface treatments that decrease nonspecific attachment to the surface and result in contributions from the surface will not be very important as the fluorescence dependence on concentration is linear for dilute concentrations. However, non-specific attachment to a surface can be characterized by observing the fluorescence quenching.

Concentration in solution

One of the advantages of conducting an antibody assay is the high specificity offered by the epoxide chemistry used to prepare the surface. After the analyte containing the antigen to be identified is flowed over that carefully prepared surface, the antigen is selectively removed from

Table 1. Cancer markers and their clinically relevant concentrations within human blood.

Albumin	3.5-7.5 g/dL	7	normal range	4 hours	66	5.50E+11	9.14E-04
C3 complement	70-150 mg/dL	7	normal range	4 days	174	3.80E+09	6.31E-06
Ceruloplasmin	21-50 mg/dL	5	normal range	36 hours	132	1.60E+09	2.66E-06
beta2 Microglobulin	>2.0mg/L	7	is abnormal	1 day	11.8	1.00E+08	1.66E-07
Thyroxine (T4)	5-12 ug/dL	7	normal range	72 hours	777	6.60E+07	1.10E-07
C-reactive protein	<1.2 mg/dL	5	is abnormal	4 hours	114	6.60E+07	1.10E-07
Ferritin	30-300 ng/mL	7	male range	72 hours	474	2.10E+05	3.49E-10
AFP	>20 ng/mL	7	is abnormal	96 hours	70	1.70E+05	2.82E-10
PSA	>4.0 ng/mL	7	is abnormal	96 hours	30	8.00E+04	1.33E-10
VEGF	2500 pg/mL	vary	plasma normal	days	26	5.80E+04	9.60E-11
Creatin Kinase MB	>5.0 ng/mL	7	indicates infarct	4 hours	84	3.60E+04	5.98E-11
Thyroglobulin	5-50 ng/mL	5	normal range	7 days	670	2.50E+04	4.15E-11
CEA	>3.0 ng/mL	7	is abnormal	72 hours	180	1.00E+04	1.66E-11
Calcitonin	>40 pg/mL	5	is abnormal	4 days	3,500	6.80E+03	1.13E-11
Vasopressin	2-12 pg/mL	10	plasma normal	7 days	1,084	3.30E+03	5.48E-12

the flow and concentrated on the antibody-treated regions of the flow channels. Of course, the probability of binding can be increased by using microfluidic channels that pump the solution over the antibody-coated surface many times. It is important to ensure that many more binding sites are available than antigen molecules in the analyte, so that the fluorescence or absorption intensity can be quantitatively related to the antigen concentration. In a fluorescence immuno-assay, the fluorescence intensity can be obtained with a digital image, and after careful calibration and appropriate selection of antibody chemistries deposited on the surface of an immunoassay chip, a simple snapshot image suffices to provide analytical information about many antigens within a fluidic specimen. The concentration obtained by the antibody surface treatment can lead to 1000x increases in the local concentration and thereby the fluorescence intensity of the surface compared with that of the liquid analyte.

In Table 1, we have summarized the clinically relevant concentrations that need to be measured within blood samples for the particular application of cancer marker detection. As can be seen from this table, concentrations ranging from the 10pg/mL-150mg/dL need to be measured, compared to 100μg/mL minimum sensitivity demonstrated with our present digital camera instrument. Therefore, antigens have to be concentrated significantly before such small concentrations can be measured, but this is enabled through microfluidic

delivery of large volumes of sample over the functionalized surface. This observation renders the microfluidic immuno-assay approach much more sensitive than typical micro-array technologies, in which diffusion must take place before antigens can react with the functionalized surface. Thus, in micro-arrays, either much higher concentrations or longer times are needed to obtain similar sensitivities, limiting the use of simple digital cameras with limited signal to noise performance.

Table 1 also indicates the time required for a typical clinical analysis to be completed, and this ranges from several hours to several days. It is naturally desirable to reduce the time required to obtain test results and this is enabled through the use of inexpensive fluidics and imaging systems.

We have shown that concentrations of .01-1000mg/ml can be measured with a simple commodity off the shelf CCD camera well below the ranges needed for clinical evaluations of blood samples in microfluidic chips. When combined with fluorescent assays and finger prick to plasma technologies this represents the core of a cheap, accessible medical testing.

REFERENCES

1. Gilbert, H.C. & Szokol, J.W. (2004) *Intl Anesthesiology Clinics* **42(2)**:73-94
2. Wang, J., Ibanez, A., Chatrathi, M.P. & Escarpa, A. (2001) *Anal.Chem.* **73**, 5323-5327
3. Fruetel, J.A. et al. (2005) *Electrophoresis* **26**, 1144-1154
4. Angenendt, P., Glokler, J., Konthur, Z., Lehrach, H. & Cahill, D. (2003) *Anal.Chem.* **75**, 4368-4372
5. Ngundl, M.M., Shriver-Lake, L.C., Moore, M.H., Lassman, M.E., Ligler, F.S. & Taitt, C.R. (2005) *Anal.Chem.* **77**, 148-154
6. Delehanty, J.B. & Ligler, F.S. (2002) *Anal.Chem.* **74**, 5681-5687
7. Sapsford, K.E., Charles, P.T., Patterson Jr., C.H. & Ligler, F.S. (2002) *Anal.Chem.* **74**, 1061-1068
8. Sydor, J.R., Scalf, M., Sideris, S., Mao, G.D., Pandey, Y., Tan, M., Mariano, M., Moran, M.F., Nock, S. & Wagner, P. (2003) *Anal.Chem.* **75**, 6163-6170
9. Wolf, M., Juncker, D., Michel, B., Hunziker, P. & Delamarche, E. (2004) *Biosensors and Bioelectronics* **19**, 1193-1202
10. Yakovleva, J., Davidsson, R., Lobanova, A., Bengtsson, M., Eremin, S., Laurell, T. & Emneus, J. (2002) *Anal. Chem.* **74**, 2994-3004

11. Delamarche, E., Bernard, A., Schmid, H., Michel, B. & Biebuyck, H. (1997) *Science* **276**:779-781

12. Eteshola, E. & Leckband, D. (2001) *Sensors and Actuators* **72**, 129-133

13. Eteshola, E. & Balberg, M. (2004) *Biomedical Microdevices* **6:1**, 7-9

14. Phillips, K.S. & Cheng, Q. (2005) *Anal.Chem.* **77**, 327-334

15. Piyasena, M.E., Buranda, T., Wu, Y., Huang, J., Sklar, L.A. & Lopez, G.P. (2004) *Anal. Chem.* **76**, 6266-6273

16. Murakami, Y., Endo, T., Yamamura, S., Nagatani, N., Takamura, Y. & Tamiya E. (2004) *Anal.Biochem.* **334**, 111-116

17. Kanda V., Kariuki, J.K., Harrison, D.J. & McDermott, M.T. (2004) *Anal. Chem.* **76**, 7257-7262

18. Sia, S.K., Linder, V., Parviz, B.A., Siegel, A. & Whitesides, G.M. (2004) *Angew. Chem. Int. Ed.* **43**, 498-502

19. Jiang, X., Ng, J.M.K., Stroock, A.D., Dertinger, S.K.W. & Whitesides, G.M. (2003) *J. Am. Chem. Soc.* **125**, 5294-5295

20. Liu, J., Hansen, C. & Quake, S.R. (2003) *Anal. Chem.* **75**, 4718-4723

21. Unger, M.A., Chou, H.-P., Thorsen, T., Scherer, A. & Quake, S.R. (2000) *Science* **288**, 113-116

22. Thorsen, T., Maerkl, S.J. & Quake, S.R. (2002) *Science* **298**, 580-584

23. Maeda, K., Chung, Y.S., Ogawa, Y., Takatsuka, S., Kang, S.M., Ogawa, M., Sawada, T. & Sowa, M. (1996) *Cancer* **77**, 858-863

a. Use in small cell lung carcinoma

Abstract: Here we describe the application of a microfluidic fluorescent noncompetitive immunoassay system for the detection of the CRMP5 protein, a marker for SCLC (Small Cell Lung Carcinoma), and the miniaturization of the detector. Using monoclonal rat antibodies, an immunoassay stack specific to the CRMP5 marker was built and tested for specificity and sensitivity. A microfluidic filter able to separate serum from blood allowed for tests to examine marked blood. A detector consisting of an excitation and emission filter set, lens, LED, and CCD digital camera replaced bulkier optical microscope detectors and allowed for images to be taken simultaneously off all chambers in the microfluidic device. By achieving appropriate signal to noise ratios with the miniaturized detector and using the immunoassay chip in tandem with microfluidic blood filters we approach cost efficient handheld devices capable of detecting SCLC with high specificity and sensitivity.

Introduction

The high cost and time requirements for medical testing restrict prompt detection and efficient treatment of ailments. Modern medical technology remains large and expensive, requiring centralized healthcare systems which increase delays, price, and the probability of clerical error and often cause prolonged hospital stays[1]. By

utilizing microfabrication techniques such medical devices can be miniaturized and fully automated, lowering costs, removing human error, and creating the advent of "point of care" testing through which such tests can be quickly performed at any clinic or home[2].

The field of microfluidics provides the foundation for such advances. Soft-Lithography allows for the cheap and efficient creation of poly(dimethylsiloxane) (PDMS) chips able to perform Sandwich Enzyme-Linked ImmunoSorbent Assay (ELISA) tests on a microscopic scale. Such systems can run with less than a drop of patient blood serum and synthesized proteins unlike the current macroscopic versions which require significant amounts of both. By reducing the size of devices, cost of manufacturing, and amount of material needed these chips prove essential in the creation of point of care medical testing[2].

Using a two-layered PDMS chip for microfluidic fluorescence immunoassay as our platform[3], we investigate the creation of a point of care testing device capable of detecting the presence of the antigen CRMP5, a protein marker for small-cell lung carcinoma (SCLC) and in some cases thymona[4]. We conducted a sandwich immunoassay test on a sample containing CRMP5 for proof of concept testing on the device's ability to detect a specific antigen. Collected data was analyzed for specificity and sensitivity. A miniaturized fluorescence

detector was constructed from an inexpensive CCD camera, LED, lens and emission and excitation filter[5]. A chip with fluorescence signal was observed through this system to show such a device was capable of simultaneously inspecting all chambers and still retain appropriate signal to noise ratio. The use of a microfluidic blood filter to filter a sample to serum is discussed but investigated elsewhere.

Background

For years medical professionals have conducted macroscopic fluorescent noncompetitive, or "sandwich", immunoassays, an efficient and effective method of detecting a variety of diseases and conditions. The technique hinges on the ability of synthesized antibodies to bond tightly and specifically to antigens. In traditional sandwich immunoassays we flow antibodies specific to the target antigen across a substrate coated with a protein bonding substance. Sample (blood serum) from the patient is then allowed to flow across the substrate such that any antigen present in the serum will bond to the stationary antibodies. A wave of biotinylated antibodies, either polyclonal (able to bind to any location on the antigen) or specific to a different location on the antigen then the previous sample of antibodies, is allowed to flow over the substrate to construct a sandwich of antibody -> antigen -> biotin attached antibody. Finally fluorescently tagged streptavidin is allowed to pass over the substrate and attach to the biotin molecules. The result

is excited by an appropriate light source such that a fluorescent signal is produced for each immunoassay stack. The combined signal is analyzed and used to determine the concentration of antigen present in the patient's sample.

With the microfluidic chip sandwich immunoassays have been performed on a microscopic level and at antigen concentrations as low as 10 picoMolar and saturation concentrations in the 100 nanoMolar range[3]. Here we conducted a proof of concept experiment; using the chip to detect the CRMP5 antigen, a marker of small-cell lung carcinoma, in the saturation range. In order to simplify the process fluorescently pre-tagged antibodies were used instead of biotinylation or tagged streptavidin. In order to investigate the practicality of a point-of-care testing apparatus constructed around such a platform a portable and low cost detector was developed and tested.

Materials

Chip Fabrication

The materials and fabrication instructions for the manufacturing the chips are describe elsewhere[3]. The chip consisted of a control (top) layer and flow (lower) layer. The flow layer contained a 5 by 10 matrix of pathways 10μm tall and 100μm wide.

Antibodies and Antigen

IgG rat monoclonal antibodies in ascites fluid were obtained from the Mayo Clinic in three variations. CR-1 binds to residues ~369-564 of CRMP-5, CR-3 binds to residues ~1-64, and CR-5 binds to residues ~57-376. CRMP-5 antigen, a 62 kilaDalton molecule[6], prepared from E. Coli in a 4.7 mg/mL concentration in dilute Phosphate Buffered Saline (PBS) was obtained from the Mayo Clinic.

Fluorescent Tag

Samples of each antibody were tagged with DyLight 547 using the Pierce Protein Labeling kit supplied by Pierce Biotechnology (Rockford, IL, USA). The dye excites at 557nm and emits at 570nm.

Buffers

PBS from (Irvine Scientific Located Santa Anna, CA., USA) and bovine serum albumin purchased from Sigma (St Louis, MO., USA) were used to create the solution buffers. Tagged antibodies and the CRMP-5 antigen were reconstituted in PBS 0.1% BSA solution. Untagged antibodies were reconstituted in pure PBS 1x solution. Trishydroxymethylaminomethane (Tris Buffer) from Sigma-Aldrich (St. Louis, MO., USA) was used as a flushing and pacifying agent.

Detection Systems

An Olympus IX71 inverted microscope (Olympus America Inc. Melville, NY, USA) equipped with mercury lamp, Texas Red emission and excitation filter set (Absorption wavelength 595 nm, Emission wavelength 620 nm), and DFW –V500 Digital CCD cool charged-coupled device (CCD) from Sony, served as the primary means of detection. A miniaturized detector consisting of a 520nm-535nm (Green) Cree XLamp 3 7090 LED from ETG Corp (Los Angeles, CA, USA), an emission and excitation filter set from Chroma (Excitation: HQ535/50x Emission: HQ610/75M; Rockingham, VT, USA), and a Cannon EOS digital Rebel camera, was constructed and tested. Astra Image 2.0 software (Phase Space Technology) analyzed fluorescent signal captured from both systems[5].

Experimental Setup

As described elsewhere[3], the microfluidic chip was mounted upon Super Epoxy SME glass slides from TeleChem International, Inc. (Sunnyvale, CA., USA). We plugged 23 gauged tubes from New England Small Tubes (Litchfeld, NH., USA) into the control and flow input ports and used ID: 0.020 inch, OD: 0.060 inch Tygon Tubing from Cole-Parmer (Vernon Hills, IL., USA) to connect the control channels to Lee-valve arrays (Fluidigm; San Francisco, CA., USA) and the flow channels to the reagent supply. Fluidigm uChip control software was used to control the Lee-valve arrays and operate the control valves.

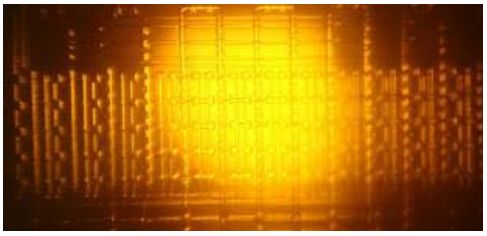

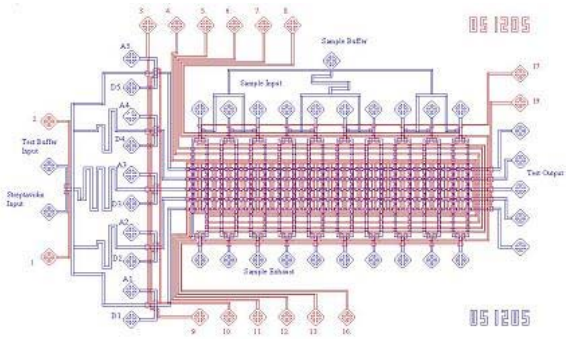

Left: Unfiltered image of microfluidic chip taken with miniaturized detector

Right: Schematic diagram of microfluidic chip; Red – control layer; Blue –flow layer

Method

Pressurized water filled the control layers until all air had diffused out of the channels. Applying pressure to any control input port via the software controlled valve arrays closed a microfluidic valve and shut off the flow in the corresponding reagent channel[7]. Untagged monoclonal

antibodies (CR5) were sent into the A5 input port and allowed to flow directly to the Test Output ports for several minutes. The horizontal flow channels were then flushed with Tris Buffer from the Test Buffer Input port to pacify any free epoxide locations and remove excess antibodies from the channel. Next, two samples were sent through the first and second Sample Input Ports. The first solution consisted of 5% CRMP5 by volume in a PBS .1% BSA mixture, the second a control contained only PBS .1% BSA. The vertical channels were filled and then circulated clockwise with a series of peristaltic pumps with a lap time of 20 seconds for 10 laps. This process was repeated 10 times with the vertical channels being replenished after each cycle in order to ensure the antigens bonded to the antibody locations thoroughly. The vertical channels were then flushed with Tris Buffer from the Sample Buffer Input to the Sample Exhaust to remove the sample solutions. Fluorescently tagged monoclonal antibodies (CR1) were sent through the D5 input port and allowed to flow into the Test Output port for several minutes, completing the stack. Tris Buffer was sent through the Test Buffer Input to remove standing fluorescence.

The chip was placed upon the stage of the Olympus inverted microscope, excited by the mercury lamp, and examined through the Texas Red emission/excitation filter cube. Using a simple CCD camera images were taken using the microscope setup of the chambers containing both the antigen present

sample and the control sample, and examined with Astra Image 2.0 software to determine the signal to noise ratio.

In order to determine the quality of signal capture from the miniaturized detector in comparison to the bulkier microscope setup, a chip with a chamber of saturated signal was illuminated by the Green ETG LED through the HQ535/50x excitation filter and the signal captured by the EOS digital Rebel camera through the HQ610/75M emission filter. The image was likewise analyzed with the Astra Image 2.0 Software to determine the strength of the signal to noise ratio.

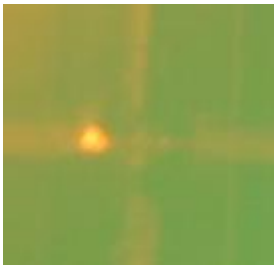

Left: Signal from CRMP5 positive chamber viewed from microscope detector
Right: Saturated fluorescent signal as observed with miniaturized detector

Results

The images of the CRMP5 present chamber and CRMP5 absent chambers were analyzed using Astra Image 2.0 software. The mean red signal of the chamber was compared with the mean red signal of the background. The signal to noise ration (SN) was determined by dividing the net signal by the standard deviation of the background noise[3]. Using the microscope setup a SN of 107 was found from the CRMP5 positive chamber and a SN of 0.86 resulted from the CRMP5 negative chamber, showing a high level of specificity.

Results from the miniaturized detector proved practical though less proficient. Images taken from this portable setup of chambers saturated with fluorescence yielded a SN of 53.4. However the miniaturized detector proved capable of examining multiple chambers simultaneously and provided adequate qualitative data capable of differentiating between antigen present chambers and antigen absent chambers. Additionally the detector proved able to produce images of the chip with high clarity and good focus while requiring less space and costly materials than the microscope detection system.

Discussion

The experiment described here provides proof of concept results showing our ability to detect the CRMP5 antigen with the microfluidic fluorescent immunoassays. Furthermore the test demonstrates that tagging antibodies directly with a protein dye proves as effective as attaching fluorescent streptavidin without the need for biotinylated antibodies and simplifying the immunoassay process. Due to time constraints and the shelf life of the proteins used the sensitivity of the system with regards to CRMP5 has yet to be fully explored. Previous tests of the system with other antigens showed reliable detection as low as 10 pM^3.

The miniaturized detection system proved able to detect signal strength up to saturation while requiring dramatically less power, space, and expense the microscope/mercury lamp detector, however the system suffered from a high degree of background light interference and ultimately proved unable to achieve similar signal to noise ratios. Future attempts at constructing a miniaturized detector will focus on further methods to eliminate noise and investigate the use of a dichroic mirror, a factor present in the microscope filter system.

With the development of microfluidic blood filters able to separate serum from blood, miniaturized detectors and microfluidic immunoassay platforms give us the ability to

construct point-of-care testing devices able to yield analytical results from a single drop of blood. With insightful application of microfabrication techniques the cost, efficiency and size of medical technology can be greatly reduced.

References

1. **Kartalov, Emil**, *Journal of In-Vitro Diagnostics*, in press.

2. **Gilbert, H.C. and J.W. Szokol.** 2004. Point of care technologies. Int. Anesthesiol.
Clin. 42:73-94.

3. **Kartalov, Emil. Zhong, Jiang. Scherer, Axel. Quake, Stephen. Taylor, Clive.**
Anderson, French. 2006. High-throughput multi-antigen microfluidic fluorescence immunoassays. BioTechniques. 40:85-90.

4. **Yu, Zhiya. Kryzer, Thomas. Griesmann, Guy. Kim, Kwang-Kuk. Benarroch,**
Eduardo. Lennon, Vanda. 2001. CRMP-5 neuroonal autoantibody: Marker of lung cancer and thymona-related autoimmunity. Annals of Neurology. 49: 146-154.

5. **Maltezos, George. Kartalov, Emil. Vinh, Nguyen. Taylor, Clive. Scherer, Axel.**
2005. Portable Fluorescence Detection for Decentralized Point-of-Care Diagnostics. Unpublished.

6. **Thambisetty, Madhav R. MD, DPhil; Scherzer, Clemens R. MD; Yu, Zhiya MD,**
PhD; Lennon, Vanda A. MD, PhD; Newman, Nancy J. MD. 2001. Paraneoplastic Optic Neuropathy and Cerebellar Ataxia With Small Cell Carcinoma of the Lung. Journal of Neuro-Opthalmology. 21(3):164-167.

7. **Unger, M.A., H.-P. Chou, T. Thorsen, A. Scherer, and S.R. Quake.** 2000.
Monolithic microfabricated valves and pumps by multilayer soft lithography. Science 288:113-116.

b. Use in Multiple Sclerosis

Recent advances in microfluidics have allowed for the fabrication of miniaturized, highly efficient immunoassay chips that minimize the quantities of reagent and patient serum needed for disease detection. This technology is especially applicable for detection and diagnosis of multiple sclerosis (MS), a debilitating auto-immune disease. We were able to demonstrate disease detection by identifying matrix metalloproteinase 9 (MMP-9), a biomarker for MS, in simulated patient serum. This is a proof-of-concept for the viability of a handheld multiple sclerosis symptom detector. Such a detector could prove invaluable in the treatment of this disease. Multiple sclerosis is a disease that progresses through a series of excacerbations. If these excacerbations can be predicted through constant monitoring of blood species, treatments can be developed for use at the onset of MS attacks in order to minimize or eliminate the damage caused by the attack.

Discussion

Multiple sclerosis is a debilitating auto-immune disease that affects the function of the central nervous system (CNS). An antibody response targets oligodendrocytes cells that are responsible for the myelination of neural axons. The immune response critically damages oligodendrocytes, halting production of myelin and leading to the rapid

demyelination and eventual disintegration of the axons. Ultimately, the affected neurons lose the ability to conduct electrical impulses [1].

Diagnosis of multiple sclerosis is done through characterization of the symptomatic response, which varies with each patient. More common symptoms, associated with the loss of neural function, include fatigue, numbness, spasticity, vision loss, and depression. Most patients fall into one of the four identified symptom motifs for multiple sclerosis: relapsing-remitting (RR), primary-progressive, secondary-progressive, and progressive relapsing (*see Figure 1)*.

Approximately 85% of multiple sclerosis patients are initially diagnosed as relapsing-remitting; characteristics of these patients include episodes of acute symptoms followed by remissions of partial to complete recovery. Within ten years of the initial diagnosis about 50% of RR patients go on to exhibit secondary-progressive multiple sclerosis, which is characterized by a steady increase in symptom intensity with brief periods of acute symptoms and recovery [2]. A smaller percentage of patients, diagnosed as primary-progressive, exhibit a steady increase in symptom intensity from the onset of the disease. However, a very small percentage of patients with multiple sclerosis demonstrate a progressive relapsing syndrome, wherein

symptom intensity steadily increases along with intermittent periods of partial recovery.

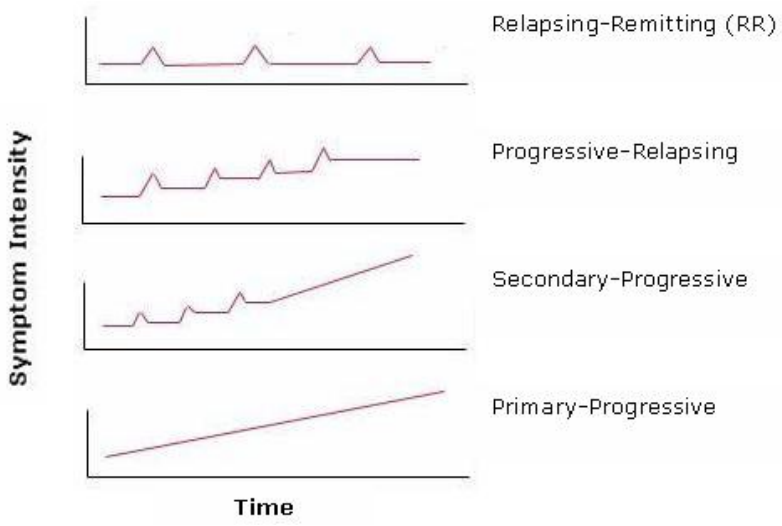

Figure 1 Multiple Sclerosis Symptom Motifs

Currently, there is no definitive serological test for multiple sclerosis. However, recent research has demonstrated the existence of specific biological markers for multiple sclerosis, which include matrix metalloproteinase 9 (MMP-9), a gelatinase enzyme that has the ability to cleave myelin [3], and Galactocerebroside (GalC), a transmembrane glycoprotein in oligodendrocyte cells that is a known target for demyelinating antibody responses [4-5]. Furthermore, these markers have a demonstrated presence in the blood stream, making them promising candidates for immunological testing.

We built a simple two-layer immunostack, using a high-throughput microfluidic immunoassay chip to illustrate a proof-of-concept of multiple sclerosis disease detection. A serum of MMP-9 was flowed through the coliseums of the fluidic chip and allowed to bond to free expoxide sites along the flow layer (*see Figure 2*). After passivating the remaining epoxide sites with TRIS buffer, fluorescently-tagged monoclonal anti-MMP-9 antibodies were pumped throughout the coliseums. Subsequently, the coliseums were flushed with TRIS buffer to liberate and remove and free-floating antibodies. Finally, the fluidic chip was illuminated with light of wavelength 547 nm, and the fluorescence emission was captured by a CCD (*see Figure 3*). We inferred the presence of MMP-9 because of the luminescence of the fluorphores.

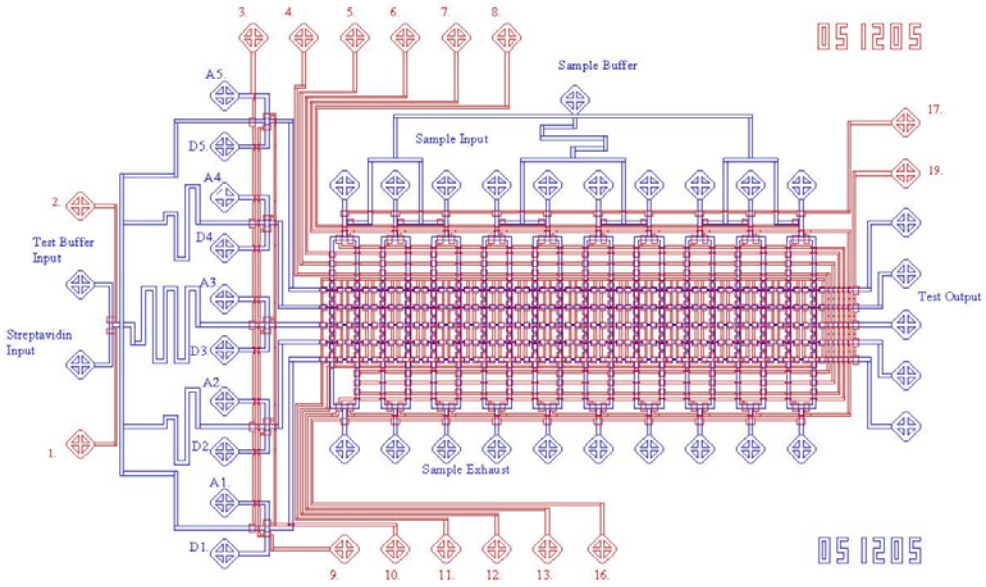

Figure 2 Microfluidic Immunoassay Chip Layout (Control channels RED, flow channels BLUE) [6]

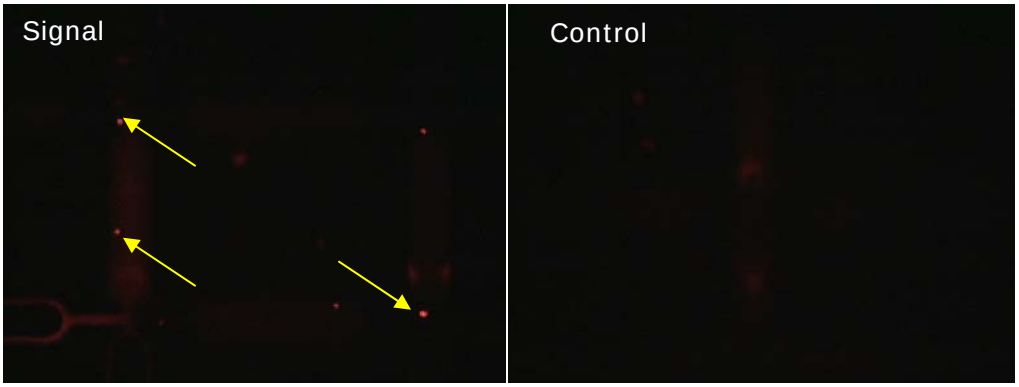

Figure 3 *MMP-9 Half Stack Immunoassay*

Controlled detection of MMP-9 was done by fabricating a selective, three-layer protein stack (*see Figure 4*) for MMP-9. First, polyclonal goat anti-human MMP-9 molecules were flowed through the coliseums and allowed to bond to the epoxide layer of the immunoassay chip. After passivating the remaining epoxide sides with TRIS buffer, simulated patient serum (consisting of a 470 nM solution of MMP-9) was flowed through the coliseums. The MMP-9 was immediately captured by the polyclonal anti-MMP-9 antibodies. Finally, fluorescently tagged monoclonal anti-MMP-9 antibodies were flowed through and mated with the MMP-9. Fluorescence imaging confirmed the presence of MMP-9 (*see Figure 5*). Furthermore, luminescence was observed only in coliseums which had exposure to MMP-9, validating the selectivity of the protein-stack.

Since only fully formed protein stacks have fluorescently tagged antibodies, the intensity of the fluorescence

emission corresponds to the strength of the signal. In one assay, we measured the red mean of the signal to be 227 with a standard deviation of 39.2. In comparison, the red mean of the noise was 9.224 with a standard deviation of 9.23. This resulted in a signal to noise ratio (SNR) of 24 to 1. In another assay, we observed a red mean of the signal to be 72.6 with a noise floor of 7.01, resulting in a SNR of 10 to 1. Successful immunoassays consistently had signal to noise ratios of 10 to 1 or greater.

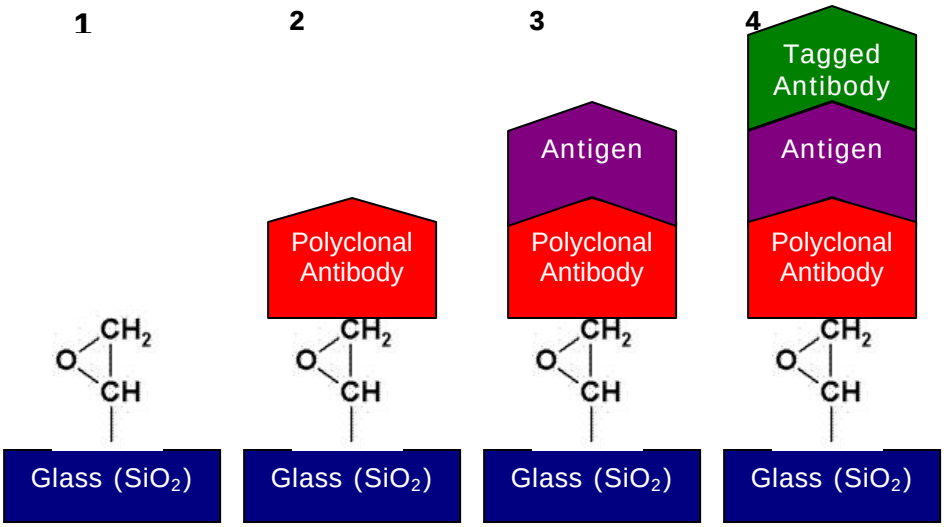

Figure 4 Three Layer Protein Stack

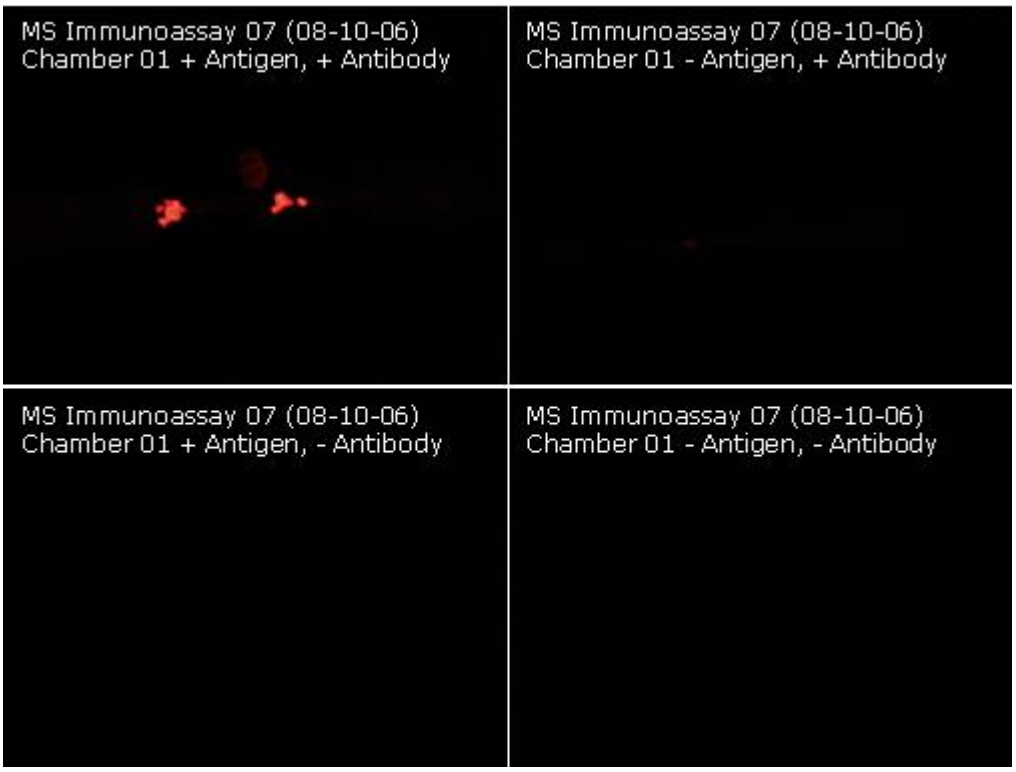

Figure 5 MMP-9 Full Stack Immunoassay

Conclusions

We have demonstrated a proof-of-concept of multiple sclerosis disease detection through successful detection of the biomarker MMP-9. Furthermore, fluorescence detection of MMP-9 yielded SNR in excess of 24 to 1, with a minimum SNR of 10 to 1. Subsequent testing has suggested that MMP-9 antigen detection is possible with concentrations as low as 65 nM.

In future tests, we will attempt to do a more thorough characterization of the detection of antigens at ultra-low concentration. Additionally, we will attempt a three-stage

characterization of multiple sclerosis through the detection of MMP9, myelin oligodendrocyte glycoprotein (MOG), GalC in the patient blood serum. Finally, we plan on integrating the microfluidic immunoassay chip with an elastomeric blood filter and CCD image capture device to illustrate the feasibility of a hand-held multiple sclerosis symptom monitor.

Methods and Materials

A high throughput immunoassay chip (*see Figure 6*) [6] was used to perform the microfluidic immunoassays. Soft lithography was used to fabricate the chips in polydimethylsiloxane (PDMS), an organic elastomer. The PDMS chips were then mounted and bonded on SuperEpoxy SME glass slides from TeleChem International.

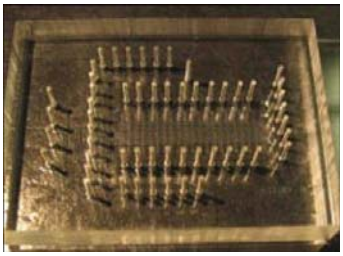

Figure 6 Microfluidic Immunoassay Chip [6]

The immunoassays were carried out using human MMP-3, MMP-9 antigens, anti-MMP-9 polyclonal antibodies, and monoclonal human anti-MMP-9 and anti-MMP-3 antibodies manufactured by R&D Systems. Subsequent immunoassays were

performed with human GalC and anti-GalC antibodies provided by a collaborator.

The MMP proteins were reconstituted with TCNB buffer solution containing 50 mM Tris buffer, 10 mM $CaCl_2$, 150 mM NaCl, and Brij 35 (a stabilizing detergent manufactured by VWR Scientific.) The reconstituted proteins were aliquot into single-use centrifuged tubes, and refrigerated at -27 °C until needed. Furthermore, monoclonal human anti-MMP-9 and anti-MMP-3 were tagged with a Dylight 547 protein fluorescence labeling kit from the Pierce Corporation. The antibodies were stabilized with pure PBS buffer from Irvine Scientific.

The actual immunoassay was controlled with a Fluidigm BOB3 pressure-flow controller and was interfaced to the user with the Fluidigm uChip software. Antigen and antibody solutions were gently vortexed before input. Tris buffer was used to passivate epoxide groups in reagent channels. Excitation of the fluorophores was performed with a green light of 552 nm. Pictorial data was obtained using a Sony DFW-V500 Fire-i digital microscope camera. Statistical image analysis was performed using

References

[1] Website: <http://www.nationalmssociety.org>

[2] N. Tanuma, H. Sakuma, A. Sasaki. "Chemokine Expression by Astrocytes Plays a Role in Microglia Macrophage Activation and Subsequent Neurodegeneration in Secondary Progressive Multiple Sclerosis." *Acta Neuropathol*. Vol. 112, No. 2, 2006.

[3] M. Ram, Y. Sherer, Y. Shoenfeld. "Matrix Metalloproteinase-9 and Autoimmune Diseases." *Journal of Clinical* Immunology. Vol. 26, No. 4, 2006.

[4] P. Lalive, T. Menge, C. Delarasse, B. Gaspera, D. Pham-Dinh, P. Villoslada, H. von Budingen, and C. Genain. "Antibodies to Native Myelin Oligodendrocyte Glycoprotein are Serological Markers of Early Inflammation in Multiple Sclerosis." *PNAS*. Vol. 103, No. 7, 2006.

[5] T. Menge, P. Lalive, H. Budingen, B. Cree, S. Hauser, and C. Genain. "Antibody Responses Against Galactocerebroside are Potential Stage-specific Biomarkers in Multiple Sclerosis." *Journal of Allergy and Clinical Immunology*. Vol. 116, No. 2, 2005.

[6] E. Kartalov, J. Zhong, A. Scherer, S. Quake, and C. Taylor. "High-throughput multi-antigen microfluidic fluorescence." *BioTechniques*. Vol. 40, No. 1, 2006.

3. Device to screen metastasizing cancer cells

Abstract

With nanofabricated microfluidic systems, we studied the migration behaviors of two cell lines *in vitro*. Cells were allowed to migrate through areas of 15 µm in height, containing a microfluidic channel of 15 µm (height) by 15 µm (width) and 45 µm to 1cm in length. We observed that cells left their monolayer origin as individual cells to enter the entrance of the channel. After migration through the channel, the daughter cells resulting from the first division migrated away from each other to form two colonies. When each of the two colonies expanded into 32-cell colonies, the colonies disassociated into multiple small colonies. Our results indicate that cells can break off from the monolayer to actively search their environment, and the dissociation of cells from each other is highly regulated. Future gene expression profiling study on cells prior and post disassociation should reveal genes that regulate the disassociation of cells from the monolayer. These genes are potential candidate genes which regulate cancer cells to leave the original tumor and become the metastasis. We demonstrated here that a microfluidic system can be a powerful means to study genes that regulate cell disassociation, which is a first step of cancer metastasis. Our system can be easily converted to an inexpensive high throughput device to screen drugs for inhibiting metastasis in the pharmaceutical industry.

Introduction

Cell migration has been well studied in conventional tissue culture systems with Boyden chambers[1], substrates (collagen, fibrin gel, and agarose)[2,3], Dunn chambers [4] and microfluidic chamber[5] assays. It is known that cells can respond to chemical gradients such as chemotaxic and cytokines in their culture environments. In these studies, a chemical gradient of chemotaxic or cytokines was established for allowing cells to respond to the chemicals and migrate toward or away from the source of the chemicals. An interesting question of cell migration is whether cells can act like insects such as ants or bees to search the environments. The ability to search the environment, i.e. moving randomly, is critical for cells to find chemical signals as well as respond to their gradients. The searching ability also allows cells to move through the

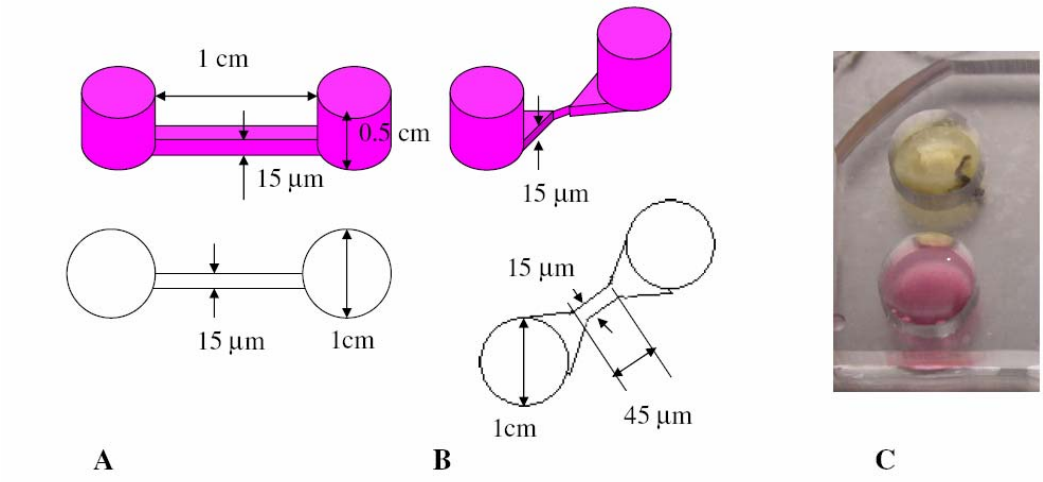

Figure 1 Designs of the microfluidic systems for cell migration study. A. Two wells connected by a 15 mm width by

15 mm height and 1cm in length. B. In another system, two triangular areas with the height of 15 mm were placed between the wells and the connecting channel. The length of the connecting channel is 45 mm. C. A picture of cell cultures, the diffusion is minimal between the two wells. As shown in the picture. The well (on top) turned into yellow due to the growth of the monolayer of 293T cells, but the well which has no cells is still in normal pH. The connecting channel does not allow efficient diffusion of H+ and OH- between the two wells.

extracellular matrix (ECM) and around obstacles, such as other cells, or nerve fibers. Understanding the molecular mechanism of cell migration is critically important in studying cancer metastasis, the transfer of cancer cells from one organ or tissue to another not directly connected with it. It was estimated that approximately 90% of cancer patients die from metastases.[6] In fact, the presence of tumor cells in lymph nodes near the original tumor is a major prognosis factor in many cancers.

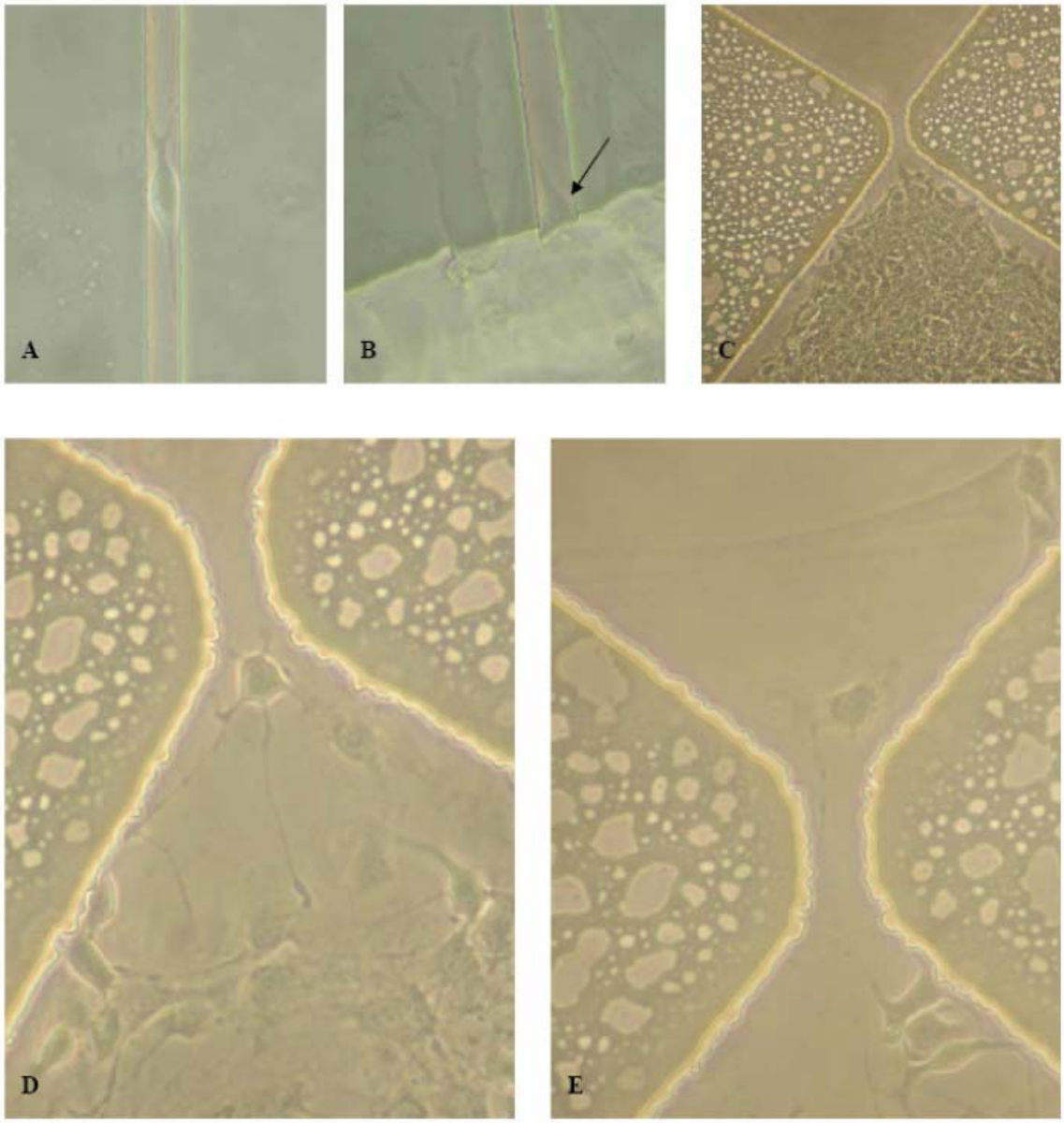

Figure 2 Cell migration in microfluidic systems. A) A cell inside a 15 μm channel. The cell body almost completely occupied the channel. B) A cell entering the channel. C) The monolayer next to the channel entrance. D) and E) showed a cell broke off from the monolayer to migrate through a channel (width: 15μm; height:15μm and length: 45 μm).

Metastasis involves intravasation (the entry of cancer cells into the vasculature), extravasation (exit from the vessels), and growth in target organs.[7] Most of studies of metastasis have been on steps after intravasation. Little

effort has been put on the first step of metastasis, the disassociation of cancer cells from the original tumor. With nanofabrication technology, we created a microfluidic system with polydimethylsiloxane (PDMS) to study the process of transformed cells breaking off from the monolayer and getting into small channels. It has been demonstrated that microfluidic systems can be used to precisely control, monitor and manipulate cells in microenvironments.[8-11] The transparent nature of PDMS and the simple fabrication procedure with replica molding, make microfluidic systems, like those reported here, an ideal system to study cell disassociation. Our results suggest that cell disassociation is highly regulated. Identification of the genes which regulate cell disassociation in a colony should provide vital information in designing and screening chemicals to inhibit the first step of metastasis, the disassociation of cancer cells from tumor. We have used microarray gene expression profiling to identify genes that regulate stem cell activity.[12] Similar

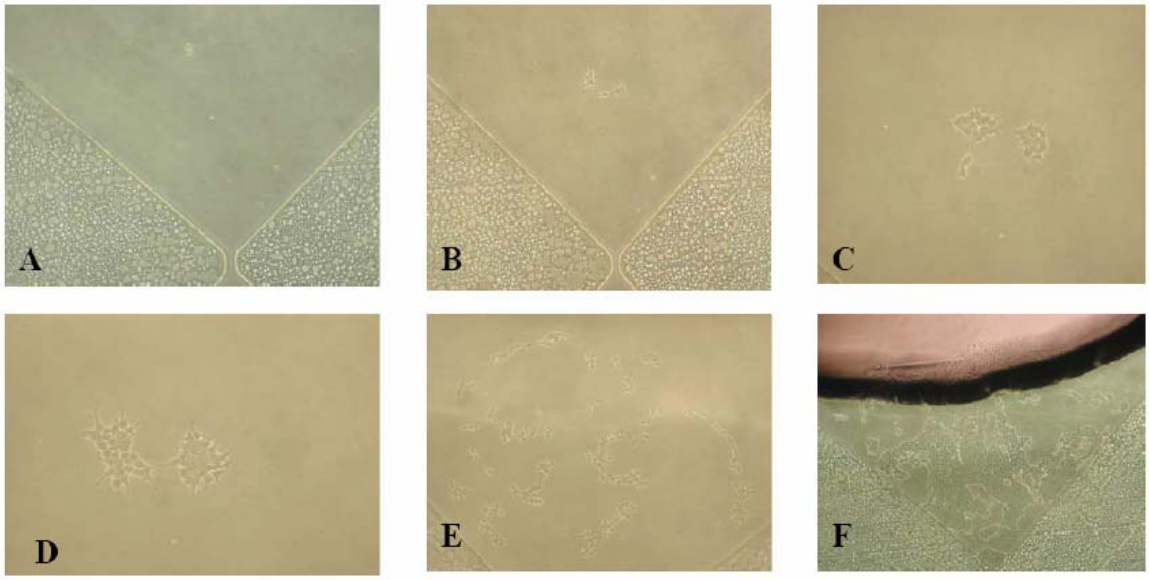

Figure 3 The re-establishment of monolayer after a cell migrated through a channel. Images of cells after migrating through a channel were taken to monitor the formation of the new monolayer. Cell doubling time is approximately 12 hrs. A) One cell migrated through a 45 μm channel and divided to be tow daughter cells. B) The two daughter cells migrated away from each other to form two colonies. Cell division of these two daughter cells resulted in connected cells rather than cells migrated away from each other as the first cell division. C) and D) The cell numbers in both colonies increased with cell division but remain associated. There are 32 cells in each of the two colonies. E) Twentyfour hours later, we observed multiple small colonies. The total cell number is 256 which is two doubling from D. F) The small colonies grew and were connected to form a monolayer

approaches could be used to identify genes regulate cell disassociation in microfluidic system.

Material and methods

Fabrication of microfluidic systems

The microfluidic systems were fabricated by using soft-lithography technology and replication molding at the microfluidic soft lithography foundry at Caltech. The connecting channels and triangular areas were defined on a

chrome photolithography mask with a Heidelberg dwl 66 direct write laser system using the 20mm write head. Then a blank sillicon wafer was coated with su8 2010 (microchem) and spun at 2000rpm for 60 seconds (Lavrell ws-400A) to result in the 15•m high mold of the channel and triangular areas. PDMS (Sylgard 184, Dow Corning) was poured directly on top of the mold and cured at 80 ^{0}C for 2 hours. The cured PDMS was peeled off the mold, and 1 cm diameter holes were punched to generate the wells for cell growth. The PDMS chip was then bonded to glass by cleaning with ethanol and baking at 80 ^{0}C for several hours.

Cell cultures

The NIH/3T3 cells were cultured in Dulbecco's Modified Eagle's Medium (DMEM) (Mediatech, USA) supplemented with 10% bovine calf serum. The 293T cells were cultured in DMEM supplemented with 10% fetal bovine serum. The microfluidic system with cells was put into a tissue culture incubator with 5% $CO_{2.}$ After the initial seeding of cells into one of the two wells, images of the cell migration were taken every 24 hrs right before daily medium changes.

Results

Microfluidic system

Two Microfluidic systems were designed and fabricated to study cell migration behavior of human 293T and murine NIH/3T3 cell lines (Figure 1A). The two wells had different growth conditions, one had the cell monolayer where nutrients were depleted rapidly while the other had no cells in and nutrients were plentiful. The two wells were connected by a micro channel. Two cell lines, murine NIH 3T3 and human 293T cell lines, were studied in this microfluidic system. NIH/3T3 is a highly contact-inhibited mouse fibroblast line established from disaggregated swiss albino mouse embryos in 1962. [13,14] The human 293T cell line is from human embryonal kidney fibroblasts transformed by adenovirus type 5 (Ad 5).[15]

Because of the small dimension and the length of the connecting channels (15 •m width by15 •m high with 45 •m or 1 cm in length) between the two wells, there is minimal diffusion between these two areas, and the diffusion is not sufficient to establish a significant chemical gradient before the daily medium change. As shown in Figure 1C, the two wells have a different pH indicated by the color of the medium. The well with the monolayer has completely turned yellow (acidic condition produced by the cells) while the connected empty well still has a normal pH (pink).

Migration of cells

As shown in Figure 2 A and B, single 3T3 cells migrated out from the monolayer and into a 15 µm channel. A cell is able to find the entrance of the 15 µm by 15 µm channel entrance. The cells are roughly 10 µm in diameter after being trypsinized off the monolayer. As shown in Figure 2 A, the cells almost completely occupy the width of the channel. The migration is not likely guided by a chemical gradient as evidenced by no cells following the single migrating cells into the channel. This migration behavior is similar to carcinoma cells migrating in vivo.[16] In conventional *in vitro* cell migration systems, carcinoma cells migrate as a collection of cells which is likely an artifact of these *in vitro* systems.[17] There is also almost no fluid flow between the two wells as evidenced by the different pH between the two connected wells (Figure 1C). To further study the migration behavior, we constructed two triangular areas with the height of 15um between the wells and the connecting channel (Figure 1B). Cells broke off from the monolayer to migrate into the triangular areas (Figure 2C to 2D). The cell close to the channel entrance originally has tight cell junctions with the cell around it. Before breaking off, the cell lost cell junctions with the cells around it, and only contacted with other cells in the monolayer by long pseudopods as shown in Figure 2D. After migrating into the triangular areas, cells divided to establish colonies. Finally the colonies contacted with each other to form a new monolayer.

A serial time-lapse image showed the reestablishment of a monolayer (Figure 3). The doubling time for the NIH 293T cells in our system is approximately 12 hours. Every 24 hours, an image was taken to monitor the cell which migrated through a channel into the connected triangular area. After migrated through a connecting channel (15 µm by 15 µm by 45 µm in length), a cell divided into two cells. These two cells each became a colony (Figure 3B). The two colonies expanded to 32 cells, then cells in both colonies were disassociated and migrated around the original position. As showed in Figure 3E, many different sizes of colonies were formed. The total number of cells is 256, which is the result of two divisions from the original two 32 cells colonies. But the number of cells in the individual colonies is not an even number and different from each other. This suggested that these colonies were not formed by cell division; rather different number of cells migrated as a group and divided to form these new colonies. Some single-cells also existed.

Discussion

With nanofabrication technology, we constructed microfluidic systems to study cell migration behavior *in vitro*. With this microfluidic system, we found that cells can find the 15 µm by 15 m entrance to enter the channel and migrate through the channel. We did not observe the migration of groups of cells, rather individual cells break off from the monolayer

and then actively migrate through the channel individually. It has been reported that carcinoma cells migrate as solitary amoeboid cells *in vivo,* but as collections of attached cells *in vitro*.[16,17] The data in our previous stem cell migration study in bone marrow transplantation models also support the theory that cells actively migrated *in vivo* rather than being carried by the blood circulations.[18] This underscores the importance of using microfluidic channels to study cell migration. After migrating to a new environment, first cell division resulted in two daughter cells migrating away from each other to form two colonies. Then the following cell divisions did not result in detached daughter cells. Instead, daughter cells remained bound after cell divisions to form a colony. But once the cell number of the colonies reached 32, cells began to dissociate after cell division and resulted in multiple small colonies with different cell numbers. Our study indicated that cells actively break off from their monolayer to move away, and there are cellular signals which direct certain cells to leave the group. The timing of the disassociation of a colony, and the fact that cells leave the monolayer one at a time, rather than as a group of cells, indicate that the association and disassociation from surrounding cells are highly regulated. Genes regulating cellular association and disassociation may also affect cancer cells to disassociate from their original tumor. With gene expression profiling, it should be possible to identify these genes. These genes

may be important for the development of drugs to control cancer metastasis.

References

1. Boyden S. The chemotactic effect of mixtures of antibody and antigen on polymorphonuclear leucocytes. Journal of Experimental Medicine. 1962;115:453-466

2. Brown AF. Neutrophil granulocytes: adhesion and locomotion on collagen substrata and in collagen matrices. J Cell Sci. 1982;58:455-467

3. Nelson RD, Quie PG, Simmons RL. Chemotaxis under agarose: a new and simple method for measuring chemotaxis and spontaneous migration of human polymorphonuclear leukocytes and monocytes. J Immunol. 1975;115:1650-1656

4. Zicha D, Dunn GA, Brown AF. A new direct-viewing chemotaxis chamber. J Cell Sci. 1991;99 (Pt 4):769-775

5. Li Jeon N, Baskaran H, Dertinger SK, Whitesides GM, Van de Water L, Toner M. Neutrophil chemotaxis in linear and complex gradients of interleukin-8 formed in a microfabricated device. Nature Biotechnology. 2002;20:826-830

6. Wittekind C, Neid M. Cancer invasion and metastasis. Oncology. 2005;1:14-16

7. Fidler IJ. The organ microenvironment and cancer metastasis. Differentiation. 2002;70:498-505

8. Chung BG, Flanagan LA, Rhee SW, Schwartz PH, Lee AP, Monuki ES, Jeon NL. Human neural stem cell growth and differentiation in a gradient-generating microfluidic device. Lab on a Chip. 2005;5:401-406

9. Tourovskaia A, Figueroa-Masot X, Folch A. Differentiation-on-a-chip: a microfluidic platform for long-term cell culture studies. Lab on a Chip. 2005;5:14-19

10. Hung PJ, Lee PJ, Sabounchi P, Lin R, Lee LP. Continuous perfusion microfluidic cell culture array for high-throughput cell-based assays. Biotechnology & Bioengineering. 2005;89:1-8

11. Gu W, Zhu X, Futai N, Cho BS, Takayama S. Computerized microfluidic cell culture using elastomeric channels and Braille displays. Proceedings of the National Academy of Sciences of the United States of America. 2004;101:15861-15866

12. Zhong JF, Zhao Y, Sutton S, Su A, Zhan Y, Zhu L, Yan C, Gallaher T, Johnston PB, Anderson WF, Cooke MP. Gene expression profile of murine long-term reconstituting vs. short-term reconstituting hematopoietic stem cells. Proceedings of the National Academy of Sciences of the United States of America. 2005;102:2448-2453

13. Jainchill JL, Aaronson SA, Todaro GJ. Murine sarcoma and leukemia viruses: assay using clonal lines of contact-inhibited mouse cells. J Virol. 1969;4:549-553

14. Andersson P, Goldfarb MP, Weinberg RA. A defined subgenomic fragment of in vitro synthesized Moloney sarcoma

virus DNA can induce cell transformation upon transfection. Cell. 1979;16:63-75

15. Graham FL, Smiley J, Russell WC, Nairn R. Characteristics of a human cell line transformed by DNA from human adenovirus type 5. J Gen Virol. 1977;36:59-74

16. Condeelis J, Segall JE. Intravital imaging of cell movement in tumours. Nature Reviews. Cancer. 2003;3:921-930

17. Friedl P, Wolf K. Tumour-cell invasion and migration: diversity and escape mechanisms. Nature Reviews. Cancer. 2003;3:362-374

18. Zhong JF, Zhan Y, Anderson WF, Zhao Y. Murine hematopoietic stem cell distribution and proliferation in ablated and nonablated bone marrow transplantation. Blood. 2002;100:3521-3526

IV

Devices created to perform polymerase chain reactions

1. Evaporative cooling in microfluidic channels

Evaporative cooling is an effective and energy efficient way to rapidly remove heat from a system. Specifically, evaporative cooling in microfluidic channels can provide a cost-effective solution for the cooling of electronic devices and chemical reactors. Here we present microfluidic devices fabricated by using soft-lithography techniques to form simple fluidic junctions between channels carrying refrigerant and channels carrying N2 gas. The effects of channel geometry and delivery pressure on the performance of refrigeration through vaporization of acetone, isopropyl alcohol, and ethyl ether were characterized. By varying gas inlet pressures, refrigerants, and angles of the microfluidic junctions, optimal cooling conditions were found. Refrigeration rates in excess of 40 °C/s were measured, and long lasting subzero cooling in the junction could be observed.

Miniaturization of components has been the defining trend in the world of electronics and optics for the past 50 years. Moore’s law predicts a doubling of transistor density in approximately every 18 months,[1] and transistor resolution is now well below 100 nm.[2] With this rapid

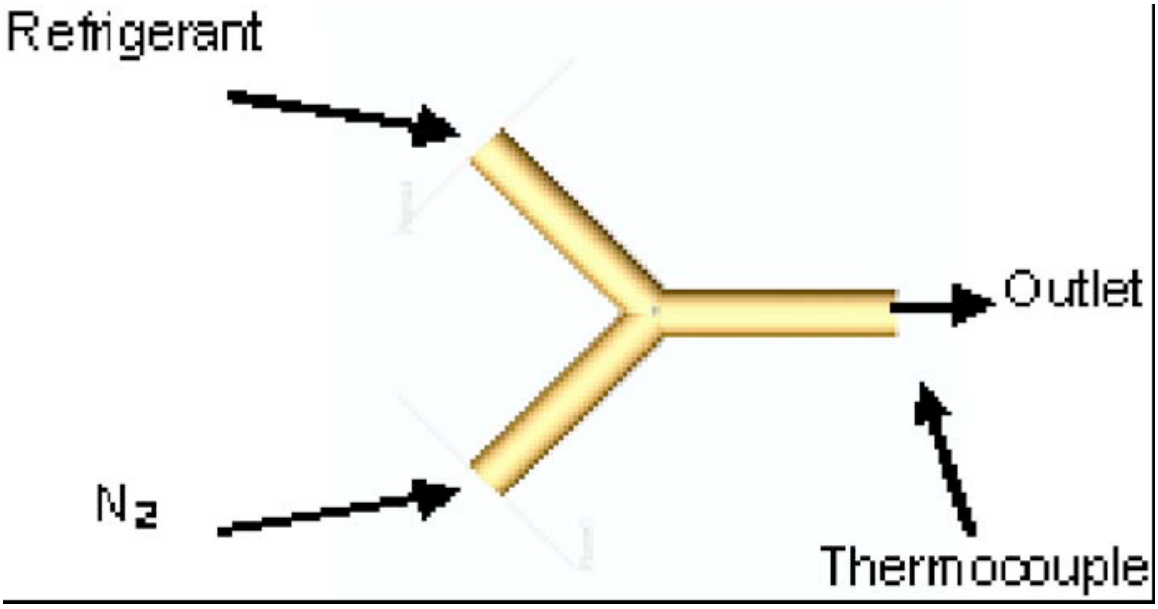

Figure 1 A diagram of the Y junction and inlet/outlet connections

increase in transistor density, the fundamental problem of heat dissipation places ultimate limitations on processing power and device speed. Attention to energy consumption and heat dissipation is of paramount importance [3] when designing electronic and optical architectures. So far, heat dissipation has been addressed in a variety of ways, from "sleep" transistors[4] to on-chip microrefrigeration.[5–7] Apart from the electronic applications of refrigeration, there are many other
needs for miniaturized refrigerators, including optical and microwave detector cooling, polymerase chain reactor cycling, and thermal stabilization of high power telecommunication lasers. Temperature control has also

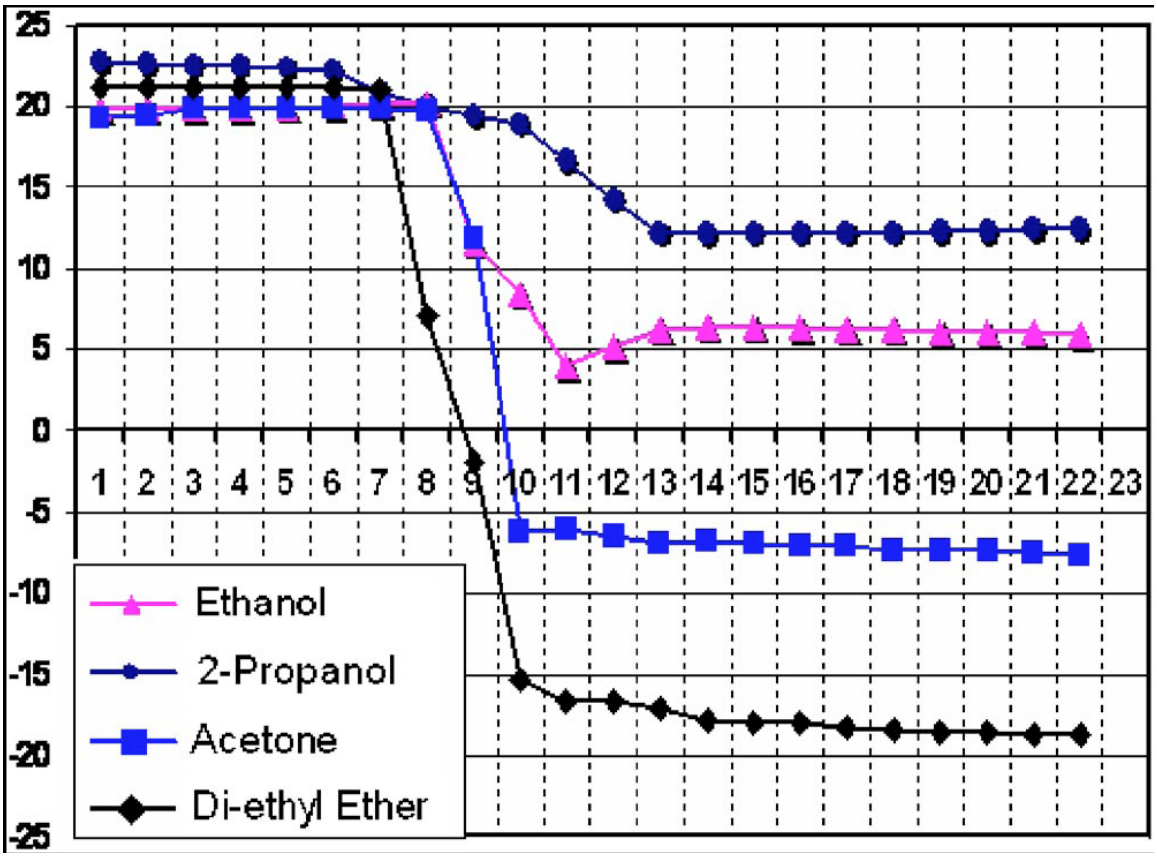

Figure 2 Temperature drop vs time for four refrigerants.

become extremely important in ensuring the precise control of thermally sensitive reactions within the framework of microfabricated chemical "laboratories"[8–10] in which subnanoliter volumes of reagents are reacted on microfluidic chips. Here we will describe the integration of evaporative cooling through microfluidic channels to address the needs of these applications.

We present a unique solution to the problem of heat dissipation: localized cooling through evaporation of volatile materials within microfluidic channels. It is well

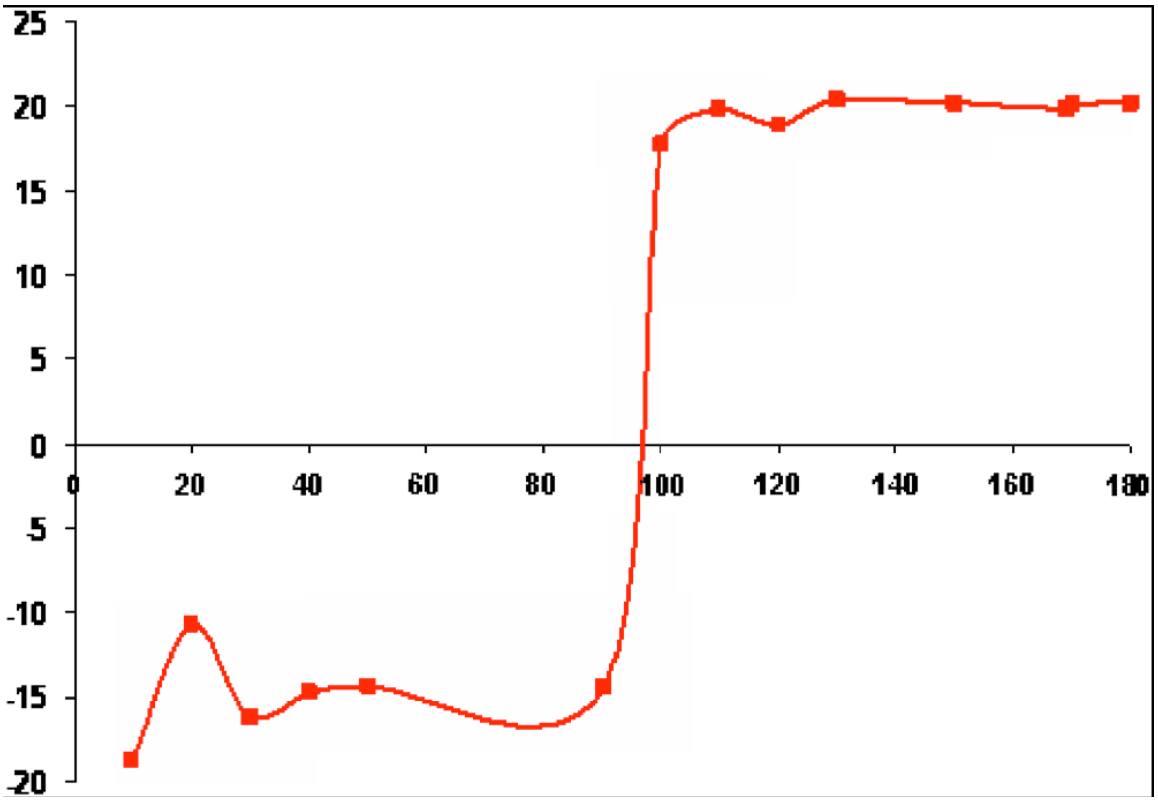

Figure 3 Minimum attainable temperature •centigrade• vs angle of junction.

known that refrigeration can be achieved through the endothermic mixing of compressed gas with an evaporating liquid.[11] To show that this also applies in microfluidic geometries, small channels were fabricated to carry out the refrigeration, and connected to form simple *Y* junctions with two input channels (see Fig. 1)—one for the refrigerant and the other for the gas. Evaporation occurs throughout the outlet channel. In our experiments, each channel has a length of 6.5 mm and a diameter of 0.650 mm. The angle of the *Y* junction was varied between 10° and 180°, and the cooling effect was characterized as a function of angle, inlet gas pressure (N2), and type

of refrigerant. Furthermore, we characterized the refrigeration using ethyl ether, acetone, ethyl alcohol, and isopropyl alcohol. The fluidic channels were initially designed on a computer using SOLIDWORKS, a three-dimensional modeling tool. These models were then converted to a usable file format using SolidScape's MODELWORKS software. Wax molds of the fluidic channels were created using a SolidScape T66 wax printer. The wax molds were then chemically cured (to remove unwanted build wax) with Petroferm Bioact VS-0 precision cleaner, and thermally cured by overnight heating at 37 °C. Sylgard Dow-Corning 184 polydimethalsiloxane (PDMS) elastomer was mixed in a Keyence hybrid mixer HM501 to fabricate the fluidic channels. The PDMS was then cured in a two step process. First, a 0.3 mm thick initial layer of elastomer was degassed in a vacuum chamber for 10 min and thermally cured at 80 °C for 8 min. A second, thin layer of PDMS was then poured on top of the first layer. The wax junction mold was then placed on the second layer of PDMS. Finally, a 3 mm thick layer of PDMS was poured on top of the wax mold. The setup was finally pumped down in a vacuum chamber for 25 min and then heated at 54 °C for 4 h to degas the elastomer.

The PDMS blocks were then cropped and dewaxed (by heating to 90 °C for 15 min). Acetone was rinsed through the fluidic channels to remove residual build wax. The fluidic chips were then attached to a refrigerant and N2 gas inlets.

An Omega Precision fine wire, *K*-type thermocouple was inserted into the outlet of the fluidic channel. The thermocouple had a diameter of 0.125 mm—small enough not to interfere with the outlet of refrigerant and gas. The thermocouple was attached to an Omega iSeries i/32 temperature controller that logged the temperature in the junction at a rate of approximately three times a second. Temperature measurements were made using this controller which was interfaced to a computer via serial port and Microsoft HyperTerminal. The inlet pressures of the refrigerant and the gas were monitored by TIF Instruments digital pressure meters. Preliminary characterization of the channels indicates that the lowest refrigeration temperatures were achieved by evaporating ethyl ether. We believe that this is due to the very low specific heat and boiling point of ethyl ether— enabling rapid vaporization. Refrigeration rates recorded for the vaporization of ethyl ether _ethyl ether pressure was 1.2 psi and N2 inlet pressures were in excess of 20 psi_ were approximately 40 °C/s. The evaporation of ethyl ether also enabled temperatures as low as −20 °C to be sustained for several minutes prolonged cooling effects in excess of 15 min were recorded (see Fig. 2).

The rates of temperature decrease in the mixing chambers were also characterized with respect to the gas inlet pressures. We incremented gas inlet pressures from

0 to 36 psi in steps of 3 psi, and found that there was a positive relationship between the gas inlet pressure and the refrigeration rate. However, we noted that inlet pressures in excess of 21 psi did not significantly increase the cooling effect further (see Fig. 3). We suspect that such increases in the gas inlet pressure create back pressure within the inlet channels, and a corresponding disruption in the flow of the refrigerant. Such back pressure contributes to erratic temperature
fluctuations and a minimized cooling effect.

We also characterized *Y*-junction geometries with respect to angle between the channels. We found that the slowest refrigeration occurs when the angle between the channels forming the *Y* branch is large _180°_, and the refrigerant supply and nitrogen evaporation gas sources point at each other. Conversely, the most efficient cooling was measured when the angle between these two supply channels was 10° *Y* junction. We think that this is due to the fact that in smaller angles, flow congestion at the junction can be minimized.

Smaller angles allow the vaporized refrigerant and heat to leave the system faster. Furthermore, larger angles exhibit significant back pressure problems at pressures in excess of 15 psi (see Fig. 4). Back pressure prevents proper refrigerant flow, thereby dampening the cooling effect. This was most clearly demonstrated in a test _gas inlet was 25

psi and ethyl ether inlet was 1.2 psi_ for the 180° junction, where little or no cooling was observed. Localized evaporative cooling in fluidic channels provides an elegant and low-cost solution to the problem of cooling electronics, optics, and chemical reactions. We optimized the geometry of a *Y*-junction and the gas/evaporant ratios for this purpose. We found that the optimal refrigeration took place in a 10° *Y* junction when using ethyl ether as an evaporant. Maximum temperature drops were measured when gas inlet pressures were between 21 and 36 psi. Gas inlet pressures above 36 psi resulted in dampened cooling effects. We also investigated the increase of the size of the outlet channel (outlet channel had a diameter of 2 mm) in hopes of promoting the expansion associated with volatilization of the refrigerant. However, we found that widening the outlet channel did not result in faster refrigeration.

A copper heat sink was also embedded into a fluidic chip. In this chip, it was observed that the cooling effect in the *Y*-junction channel results in a cooling effect in a second channel. The copper heat sink acts as a thermal bridge between the two channels. With this model, it is possible to demonstrate the cooling of an external heat source. This experiment confirms that it is possible to apply the evaporative coolers for electronic and optical cooling purposes. Ultimately, we hope to develop self-sustaining, closed systems in which refrigerant is

conserved. One possibility for refrigerant conservation would employ a selective, organic membrane at the output channel. Furthermore, in order to provide an applicable solution for the cooling of electronics, we plan on integrating microfluidic cooling systems into silicon.

References

[1] V. Zhirnov, R. Cavin, J. Hutchby, and G. Bourianoff, Proc. IEEE **91 (**2003).

[2] Intel Corporation; http://www.intel.com/technology/silicon/mooreslaw/

[3] HP Development Company; http://www.hpl.hp.com/news/2003/oct_dec/energy_talk.html

[4] J. Park, V. Moony, and P. Pfeiffenberger, Manuscript: http://codesign.ece.gatech.edu/publications/jcpark/paper/patmos_2004.pdf

[5] A. Shakouri and Y. Zhang, IEEE Trans. Compon. Packag. Technol. **28 (**2005).

[6] S. Borkar, IEEE Micro. **19**, 23–29 (1999).

[7] G. Guijt, A. Dodge, G. van Dedem, N. Rooij, and E. Verpoorte, Lab Chip **3**, 1–4 (2003).

[8] E. Hasselbrink, Jr., T. Shepodd, and J. Rehm, Anal. Chem. **74**, 4913 (2002).

[9] J. Xie, Y. Miao, J. Shih, Q. He, J. Liu, Y. Tai, and T. Lee, Anal. Chem. **76**, 3756 (2004).

[10] A. Pattekar and M. Kothare, J. Micromech. Microeng. **13**, 337 (2003).

[11] *CRC Handbook of Chemistry and Physics* 76th edition (CRC Press, New York, 1999), pp. 6-120.

2. Thermal management in microfluidics using micro-Peltier junctions

We report refrigeration and heating of nanoliter fluid volumes with micro-Peltier junctions. The temperature of small liquid reservoirs can be rapidly changed and controlled within a range between −3 °C to over 120 °C with good long-term stability. These thermal management systems enable the fabrication of complex chip-based chemical and biochemical reaction systems in which the temperature of many processes can be controlled independently.

The dense integration of microfluidic components for the construction of compact and monolithic chip-sized laboratories and reaction systems requires many different functions to be miniaturized and combined on the same substrate. Some useful chip-based operations could include mixing, filtering, metering, pumping, reacting, sensing, heating, and cooling of nanoliter volumes of fluids.[1–3] In such systems, smaller amounts of samples can be analyzed in less time, as little material is lost by transferring samples from one reaction vessel to another. So far, much work has been performed on defining and integrating fluidic

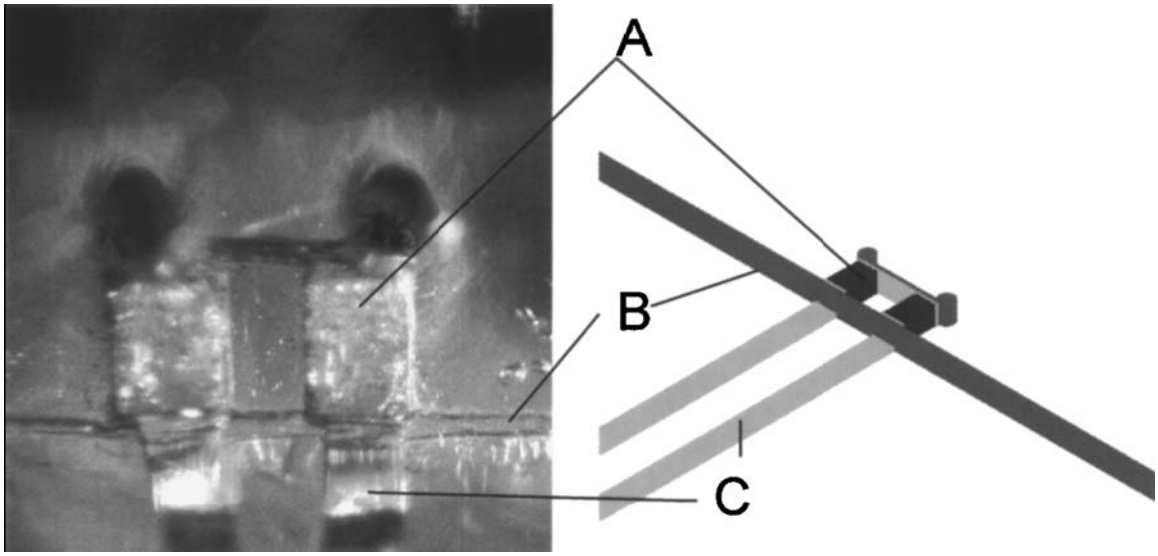

Figure 1 Optical micrograph of the 168 nL chamber Peltier cooler embedded between the PDMS chamber and the 200 µm heat exchanging channel. A three-dimensional drawing of the device is depicted with A pointing to one of the Peltier devices, B pointing to the heat exchange channel, and C points to the copper heat sink and electrical connection. The two holes at the top of the picture allow access to the chamber for fluid and the thermocouple.

components that can perform such on-chip mixing, sorting, and reacting of fluids. By combining thousands of lithographically defined pumps and valves into chip-based systems, it is possible to obtain unprecedented control over reagent concentrations and perform many reactions in parallel. However, one largely unexplored area for microfluidic devices has been the miniaturization of thermal management systems,[4-7] such as refrigerators and heaters to control the local temperature of a reaction. Typically, the entire chip must be heated or cooled, which

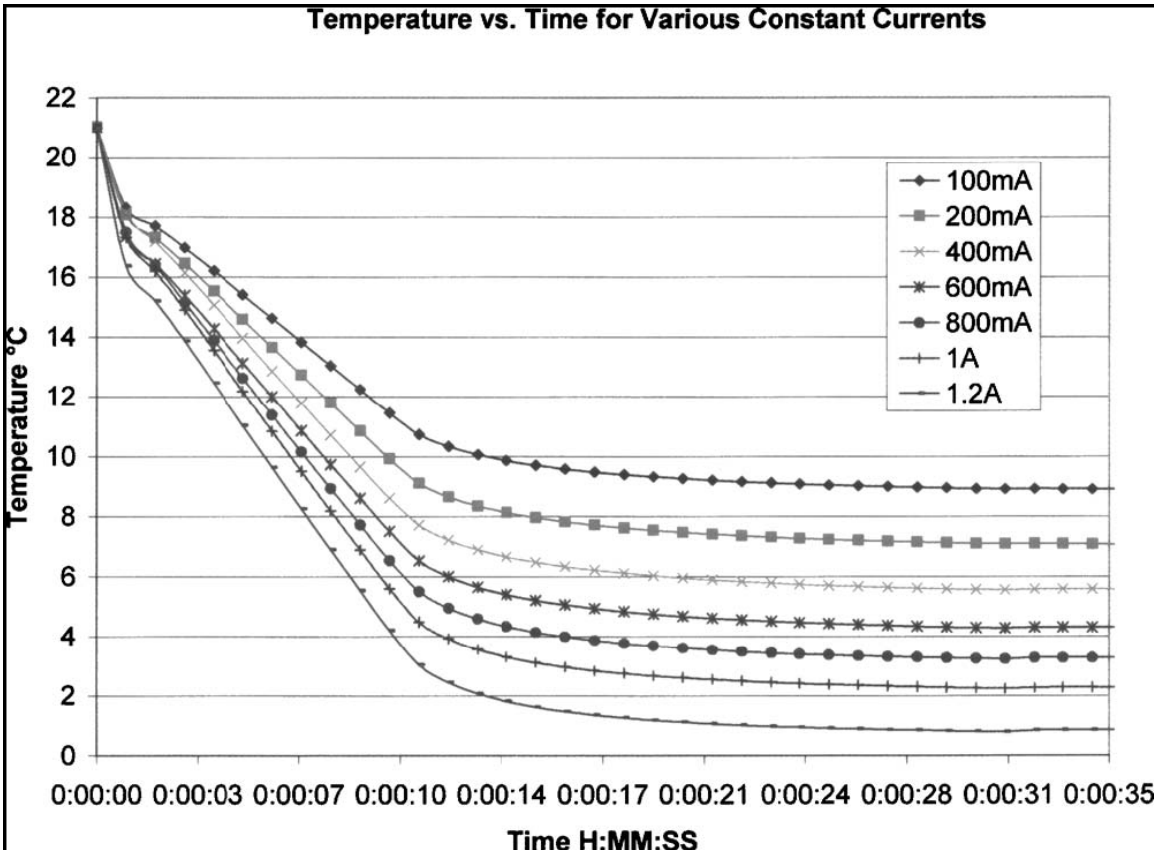

Figure 2 Time dependence of the sample temperature as a function of the current applied to the thermoelectric junction.

seriously limits the kind of independent operations that can be performed on such chips. As a result of the recent demand for performing more complex procedures with greater temperature flexibility and accuracy, as well as the need for sample accumulation and chromatographic analysis, we have investigated methods for independent thermal control over individual reaction chambers on a fluidic chip.

Many different approaches have so far been explored for thermal control, including the construction of

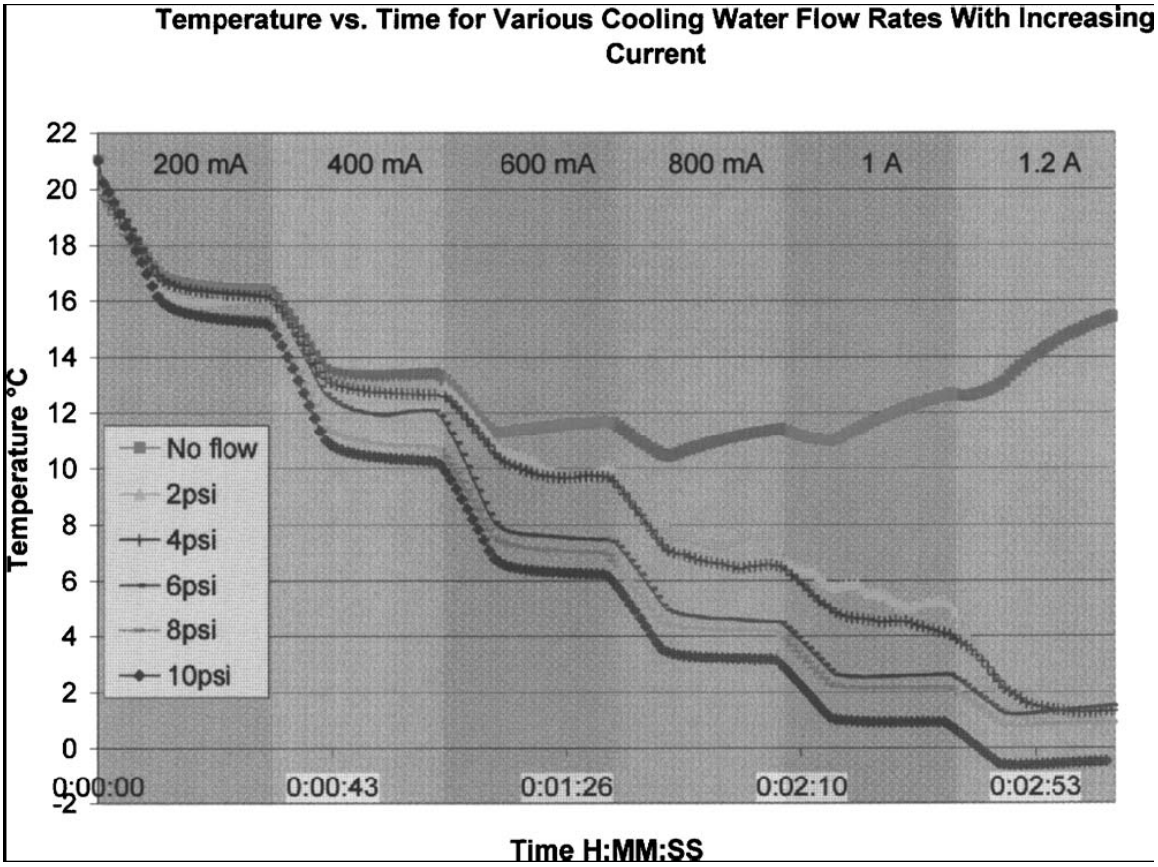

Figure 3 Time-dependent plot showing several temperature curves for different thermal transfer cooling rates. The applied current was incrementally increased by 200 mA every ~30 s. Note the curve which increases at 600 mA was with no cooling water flow showing, and that increased cooling water flow leads directly to improved cooling.

resistive heating elements within fluidic chambers, and immersing the entire chip into coolant. For example, polymerase chain reaction (PCR) systems for deoxyribonucleic acid (DNA) amplification have been fabricated with volumes as small as 12 nanoliters based on lithographically defined resistive tungsten heaters.[8,9]

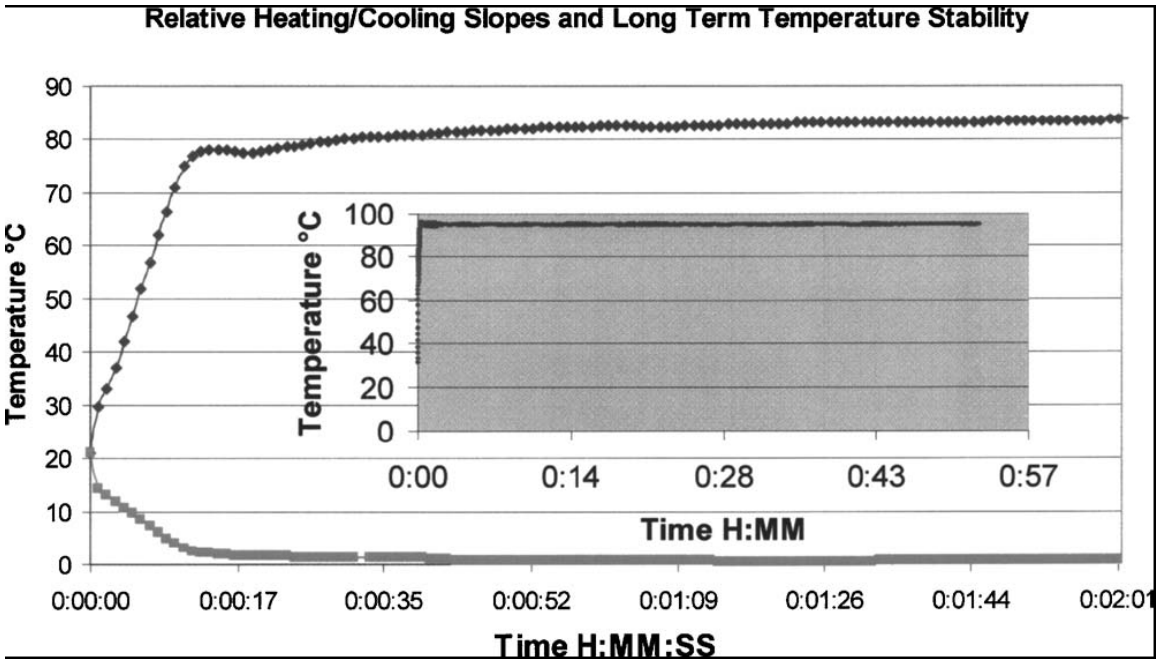

Figure 4 Temperature ramp rates for both thermoelectric heating and cooling.Inset graph shows a heating run at 94.7 °C with a standard deviation of 0.2° over almost 1 h.

We believe that the use of micro-Peltier junctions provides an even more versatile method of thermal control, which permits both local heating and cooling of reaction chambers and the controlled redistribution of heat loads on microfluidic chips. Here, we demonstrate the integration of such refrigeration systems with microfluidic valves and pumps, and describe the temperature dependence on the current applied to the thermoelectric cooler as well as the microfluidic heat exchange flow. The technology described here is expected to be particularly useful for the definition of micro-PCR systems, as well as for many analytical biochemical reaction and testing systems. Figure 1 shows a picture of a micro-Peltier cooler encapsulated within a replication molded elastomeric chip.

In the resulting chips, the Peltier junction is used as a heat pump to transfer heat from a microfluidic chamber into an adjacent channel which uses water as a microfluidic heat exchanger.

The Peltier device is embedded within a standard poly(dimethylsiloxane) (PDMS) replication mold, making this device compatible with the most common microfluidic material. The molds for this device are made by three-dimensional fabrication, which allows for a large surface area to be presented to the face of the Peltier device while still minimizing volumes of the chamber and channel. A copper busbar joins *p* and *n* junctions in the Peltier chamber to improve thermal transfer, while a similar copper/fluid heat exchanger was introduced on the cooling channel side to maximize the thermal transfer from the warm side of the Peltier device to the heat sink. Thermal isolation is achieved through the low thermal conductivity of PDMS. The Peltier device itself is a 0.6_0.6_1.0 mm3 diced pieces of *p*- and *n*-type thermoelectric materials with nickel and gold applied to the end faces to facilitate solder connections, obtained from Marlow Industries Incorporated and soldered to wires that are sealed
and isolated through two-component elastomer and connected to a constant current power supply. To conduct measurements of the refrigeration temperature and rate, one side of the Peltier junction is heat sunk with a microfluidic flow channel in which the flow rate was measured to observe

the effect of heat exchange on this device. The sample side of the junction consists of a small fluidic chamber, 169 nl in volume, which also contains a .001 in. diameter bare wire type *K* thermocouple to measure the temperature of the refrigerated material. As a current is applied to the micro-Peltier junction, the chamber can be cooled down within approximately 10 s (Figs. 2 and 4). The ultimate temperature depends on the current applied to the thermoelectric cooler, as well as the flow rate and temperature of the heat exchanger liquid. Figure 3 demonstrates such a temperature dependence of the refrigerated liquid as a function of current and flow rate with the cooling water kept at 25 °C. Several temperature curves are shown for various heat exchange flow rates as the Peltier current is increased in steps of 200 mA.

As the cooling water flow is increased, the better the effectiveness of the Peltier junctions at lowering the temperature in the chamber. The effect of no cooling water flow is shown by the curve which heats up after 800 mA, in which case the resistive heating overwhelms the cooling power due to the lack of an effective heat sink. A subzero temperature can be obtained when the highest heat exchange flow rates and large currents (of approximately 1.2 A) are applied to the cooler.

Ultimately, this temperature is limited by a balance between the resistive heating of the junctions at high

applied currents and the cooling action from the Peltier effect, as described in the following equation:[10]

$$q_c = \alpha_n I T_1 - \frac{\lambda A \Delta T}{L} - \frac{I^2 R}{2}$$

where *R* is the resistance, *I* is the applied current to the Peltier device, • is the Seebeck coefficient, • is the thermal conductivity, *A* is the surface area, and *L* is the length.

During our measurements, the chamber temperature was monitored by a thermocouple embedded in the chamber, to obtain response results as functions of electrical current, heat exchange fluid flow, and time. The resulting curves can be used to optimize the temperature and ramp rate of the micro-Peltier device. For many applications, such as quantitative PCR, it is also important to demonstrate constant temperatures with accuracies of 0.1 °C, and we have measured the time-dependent response of the chamber temperature over several hours of refrigeration or heating.

The inset graph of Fig. 4 shows a typical thermal stability plot for our refrigerator when operated with a simple labview program to control temperature. These preliminary temperature control results are already promising, reaching an average temperature of 94.7 °C with a standard deviation of .2° over almost an hour, however the goal of a temperature control of 0.1° C will require more complex active feedback to adjust the Peltier current.

We report an on-chip refrigerator and heat exchanger for microfluidic devices. The microfluidic chamber was cycled between −3 and over 120 °C, thus spanning water freezing and boiling, and the entire PCR temperature range. For smaller chambers, we also show that it is possible to cool reagent from room temperature to freezing within 10–20s, and to obtain relatively good temperature __±.2 °C_ stability over long periods of time. The ability to localize heating and cooling in microfluidic chambers and channels will enable massive parallelization of chemical reactions in which the temperature of each reaction vessel can be independently controlled. This enables more complex chemical and biochemical reactions, which require precise temperature schedules, to be performed on miniaturized fluidic chips. Moreover, important analytical and functional temperatures can be changed very rapidly or held constant. For instance, one chamber can be frozen in order to store a cell, while another can be boiled in order to sterilize it, whereas yet another chamber can cycle the temperature in order to perform a PCR reaction.

References

[1] J. P. Brody and P. Yager, *Proceedings of the Solid State Sensor and Actuator Workshop, Hilton Head, SC, June 1996*, pp. 105–108.

[2] S. R. Quake and A. Scherer, Science **290**, 1536 (2000).

[3] H. P. Chou, M. A. Unger, A. Scherer, and S. R. Quake, Biomed. Microdevices **3**, 323 (2001).

[4] J. Lee and I. Mudawar, Int. J. Heat Mass Transfer **48**, 928 (2005).

[5] J. Lee and I. Mudawar, Int. J. Heat Mass Transfer **48**, 941 (2005).

[6] A. M. Clark, N. A. Miller, A. Williams, S. T. Ruggiero, G. C. Hilton, L. R. Vale, J. A. Beall, K. D. Irwin, and J. N. Ullom, Appl. Phys. Lett. **86** 173508 (2005).

[7] X. Fan, G. Zeng, C. LaBounty, J. E. Bowers, E. Croke, C. C. Ahn, S. Huxtable, A. Majumdar, and A. Shakouri, Appl. Phys. Lett. **78** 1580 (2001).

[8] J. Liu, M. Enzelberger, and S. R. Quake, Electrophoresis **23**, 1531 (2002).

[9] E. T. Lagally, P. C. Simpson, and R. A. Mathies, Sens. Actuators B **63**, 138 (2000).

[10] H. J. Goldsmid, in *CRC Handbook of Thermoelectrics*, edited by D. M. Rowe _CRC Press, Boca Raton, FL, 1995_, p. 20.

3. Microfluidic Polymerase Chain Reaction

ABSTRACT.

We implement Microfluidic technology to miniaturize a thermal cycling system for amplifying DNA fragments. By combining microfluidic thermal heat exchanger to cool a Peltier junction, we have demonstrated very fast heating and cooling of small volumes of solution. We use a miniature K-type thermocouple to provide a means for in-situ sensing of the temperature inside the micro-refrigeration system. By combining the thermocouple, two power supplies controlled with a relay system, and computer automation, we reproduce the function of a commercial PCR thermal cycler and have demonstrated amplification of a DNA sample of about 1000 bp.

INTRODUCTION

Since its first demonstration in the late 1980s, Polymerase Chain Reaction (PCR) has emerged as one of the most sensitive analysis tools available to researchers in molecular diagnostics. DNA genotyping, virus identification, and forensic applications represent only a few of the applications that heavily rely on PCR amplification and analysis. Clearly, thermal cycling PCR is one of the leading techniques for the amplification of DNA fragments[1]. It is a rapid and straight-forward method for generating many copies of DNA molecules. PCR amplification typically consists of thermally cycling DNA fragments through many heating (denaturation), cooling (annealing) and extension

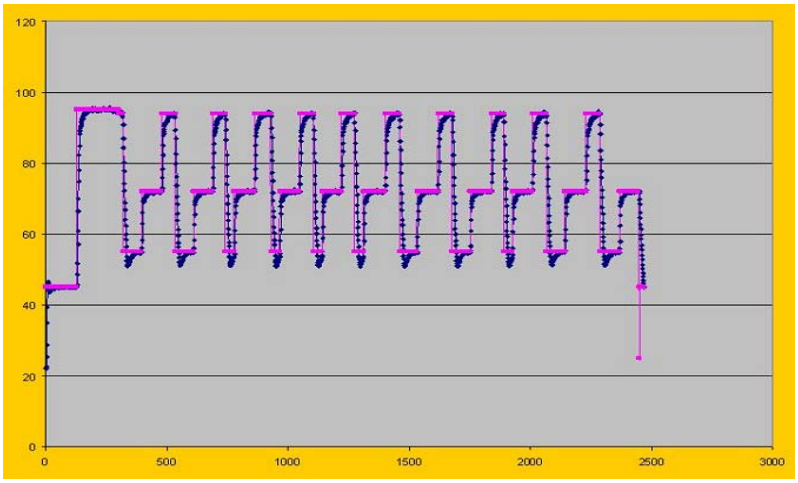

Figure 1 A graph of temperature verses time showing the typical temperature control temperature we can achieve. The actual temperature control in the tube is better as the glass tube behaves as a low pass filter

temperatures of target DNA mixed with a primer and a polymerase (involved in the catalysis of DNA). To obtain accurate amplification of the desired DNA chains, it is necessary to carefully control the temperature of the three temperatures and to ensure good temperature uniformity in the thermal cycling process. Traditionally, resistive heating or forced air heating have been used to control the temperature, but more recently Peltier junctions have been the refrigeration and heating system of choice for PCR applications. This choice is a result of the relative simplicity of integrating electrically controlled Peltier junctions within electronic feedback loops using thermocouple measurement data.

Here, we compare two alternatives of combining thermocouple device with thermovoltaic solid state devices (a Peltier junction) to form a miniaturized PCR cycling system within a

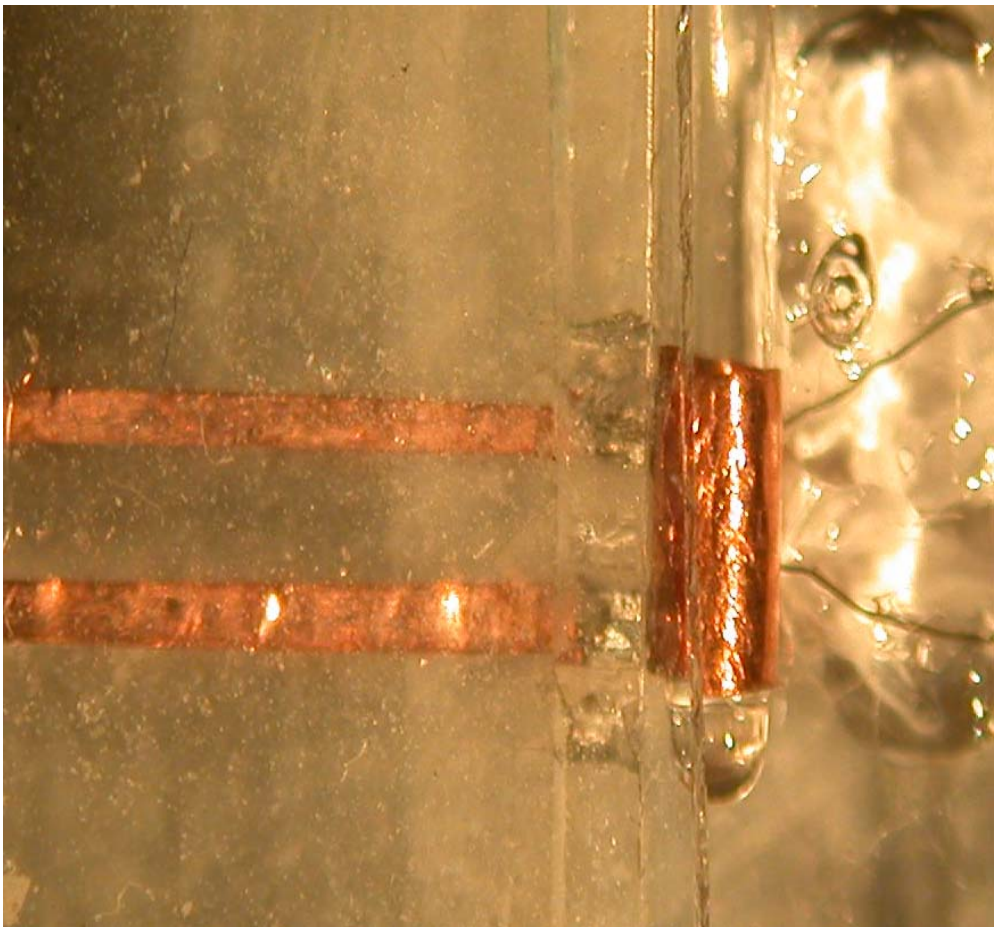

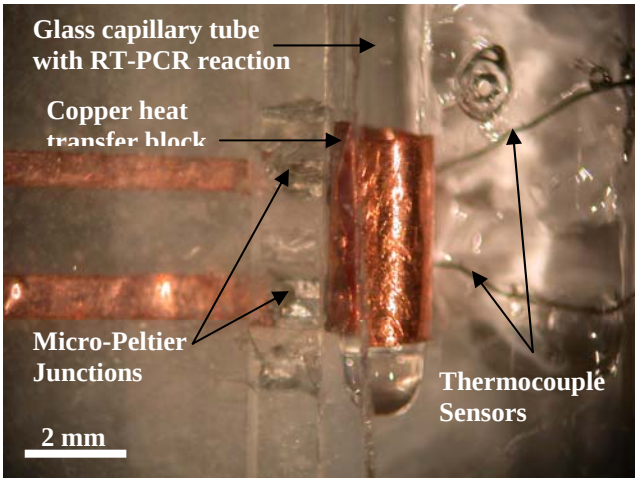

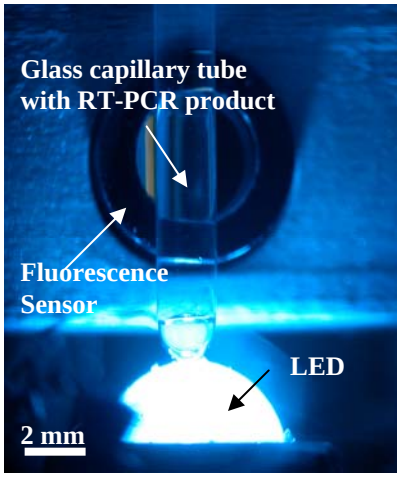

Figure 2 An optical micrograph of our microfluidic PCR system. The glass capillary tube is heated and cooled by the P and N peltier jnctions attached to the copper jacket. Also visible to the right is the control thermocouple.

microfluidic and glass capillary systems with rapid ramp rates. One of the advantages of developing such a

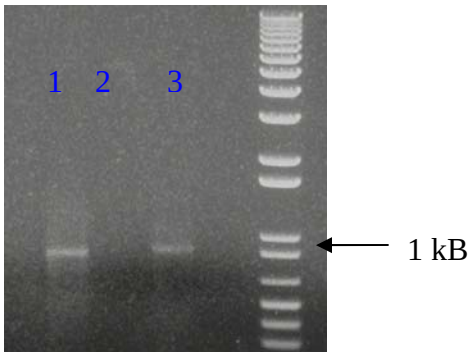

2 ul PCR products were loaded into each lane
Lane 1: Beta-Actin amplified with lightcycler
Lane 2: Negative control with templete
Lane 3: Beta-Actin amplified with Caltech device

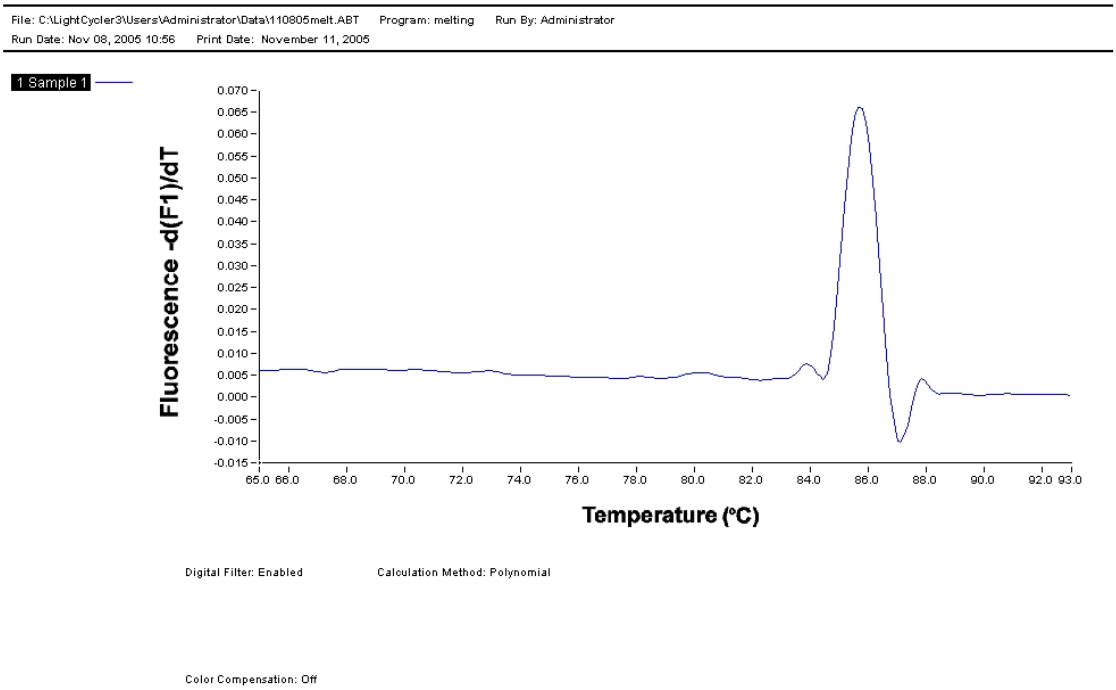

Figure 3 Electrophoresis Gel of he amplified product and Melting curve of the amplified product

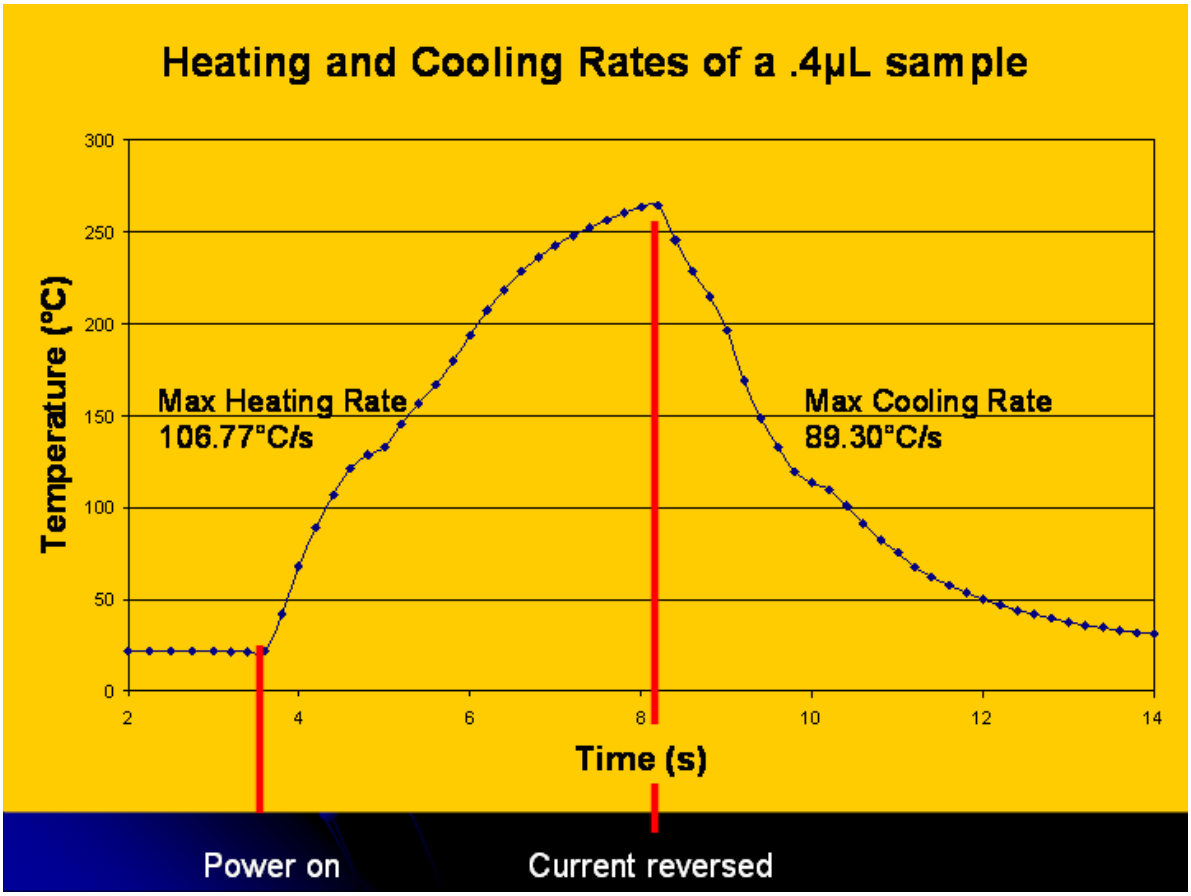

Figure 4 Maximum heating and cooling rates of a 400 nanoliter sample in our microfluidic thermal cycler

microfluidic cooling system is that liquid cooling can be used for effective heat-sinking of the Peltier junctions. The other opportunity of integrating PCR cyclers within microfluidic systems is that rather complex sample preparation can be performed microfluidically and the transfer of amplicon from the fluidic chip into a capillary-based thermal cycler can be avoided. However, more conventional glass capillary tubes offer the great advantage of well-defined surface chemistries and the avoidance of evaporation through porous elastomer channels – a major problem with previous PDMS approaches.

EXPERIMENTAL METHODS AND RESULTS

First, we have constructed two Peltier junction system: One was based on a multi-layer replication molded polydimethylsiloxane (PDMS) microfluidic chip developed for the purpose of integrating fluidic sample delivery, where both the junction and the thermocouple are assembled to run a DNA sample using the PCR technique described above. Therefore, the process of incorporating different elements such as the junction and the thermocouple into the chip can be thought as a "lab on a chip" device that can both miniaturize and reduce costs when dealing with the nowadays expensive techniques of PCR. An alternative system, in which a commercially available glass micro-capillary tube (Polymicro Technologies TSG320450) with a 320 micron inner diameter is inserted into a copper heat-exchanger, was also constructed. PCR amplification was demonstrated on large DNA molecules and the ramping speed of the system was characterized. The microfuidic device was able to perform very fast cycling that consisted of a rise in temperature from 22 °C to 95 °C and then holding at 95 °C for 900 seconds, followed by a 35-cycle PCR amplification reaction. The schedule for this experiment is summarized as follows:

50°C for 1200 sec

95°C for 900 sec

PCR(35 cycle):

94°C for 15 sec,

55°C for 20 sec

72°C for 40 sec

A solution with 1000bp DNA molecules was run through 35 cycles, and the amplified product was passed through a gel using the gel electrophoresis technique to determine whether or not the PCR run amplified the appropriate DNA sample. A silica capillary tube, was prepared with the amplicon, and mineral oil were used to avoid evaporation of the sample at the high denaturation temperature. When single or double Peltier junctions were used on the copper heat-sink holding the capillary tube, 20°C/s ramp rates were measured, whereas the introduction of 4 parallel Peltier junctions resulted in ramp rates of approximately 100°C/s per second, measured in the amplicon mixture. Figure 2 shows a time-temperature plot in which heating rates of above 100°C/s and cooling rates of 90°C/s were measured. In this system, the direction of current flow was reversed for heating and cooling of the primer/sample mixture. The 0.32mm capillary enabled the amplification of 0.4 μL DNA+primer samples. A 1000bp beta-Actin DNA mixture, as well as a DNA positive control, and a DNA ladder were tested in parallel by using agarose gel electrophorsis after the DNA sample was amplified. Figure 3 shows the gel electrophoresis results, indicating that the amplified product did consist of 1000bp molecules. Furthermore, once the DNA sample was cycled and gel electrophoresis tests were complete, the same sample was used to obtain a melting curve to determine the melting

temperature of the amplified DNA mixture. Figure 4 shows the resulting melting curve, indicating a very sharp melting temperature at approximately 85°C, indicative again of the amplification of rather large DNA fragments. It is of interest to note that no primer-dimer signals could be detected from this melting curve, indicating a uniform temperature within the amplification system.

Conclusions

Much work has been recently done to reduce the size of PCR systems. Clearly, the power of PCR amplification to improve sensitivity to DNA and RNA molecules makes its use in microfluidic analysis chips very appealing. For on-chip PCR amplification, the amplicon is often pumped over constant temperature heaters located in the path of the fluidic channels. However, three important problems arise when such microfluidic flow-controlled PCR systems are to be used: (a) of all, the flow rate of DNA molecules within a channel depends on the distance between the molecule and the side-walls of the channel, (b) the PDMS commonly employed is porous to air and steam, and water evaporation at high temperatures requires careful designs to avoid fluid loss during the PCR amplification and (c) the surface to volume ratios of such fluidic systems is very large and not well understood. These factors have led us to building miniaturized PCR systems that are based on chambers that can be rapidly heated and cooled rather than fluid flow based

thermal cycling systems, and to the use of Peltier junctions. Indeed, we show that modern Peltier junctions can be used for rapid thermal control with heating and cooling rates of 100°C/s – with temperature control accuracies of 0.1°C.

Fig 1. Temperature cycling using PCR microchip

Fig 2. Peltier Junction and thermocouple set up
The PCR microchip was used to amplified 1000 bp sample of Beta actin

REFERENCES

1) Mullis, Kary B. The Polymerase Chain Reaction. La Jolla, CA.: Birkhäuser, 1994.

2) P M Holland, R D Abramson, R Watson, and D H Gelfand, "Detection of specific polymerase chain reaction product by utilizing the 5'----3' exonuclease activity of Thermus aquaticus DNA polymerase". Proc Natl Acad Sci U S A. 1991 August 15; 88(16): 7276-7280.

4. Accessible Polymerase Chain Reaction

Since the mid-1990s, real-time polymerase chain reactions (PCR) have been used with selective primers to amplify and identify DNA and RNA molecules within large and expensive thermal cyclers. Recently, it has become possible to build compact heating and cooling systems for the amplification of DNA with greater accuracy at a 100 times lower cost. Such inexpensive PCR identification could serve remote regions of the world, leading to an early warning system for pandemic outbreaks. Here we compare a portable PCR system with a conventional desk-top unit. We show that H5N1 (avian influenza) and HIV (AIDS), as well as many other common virus strains can be identified within a clinical setting at low viral loads. Our portable instrument results in superior amplification as more precise temperature control is possible. This improvement in performance also enables the use of less expensive intercalating dyes as fluorescent probes, further reducing the cost of PCR tests.

Since the first report of specific DNA amplification using the polymerase chain reaction (PCR) in 1985, this technique has had a revolutionary impact on biochemistry [1-4]. The introduction of real-time PCR in the 1990s [5,6] removed many of the limitations of earlier end-point PCR instruments. Several systems have recently become commercially available, and techniques for the precise and rapid thermal control of nano- and micro-liter analyte

volumes with Peltier junctions have been demonstrated over the past several years [7-10]. The excellent control provided by Peltier coolers and heaters now enables the miniaturization and improvement of PCR-analysis tools. In particular, reverse transcriptase RT-PCR [11,12], has recently emerged as unrivalled in sensitivity for the identification of RNA virus strains.

The introduction of smaller and less expensive instruments with the capability to use lower-cost fluorophores is expected to lead to a more widespread availability of PCR testing, with the goal of more effective monitoring of viral epidemics so important to pandemic prevention [13]. If the cost of thermal cycling systems can be radically reduced, and the speed of the PCR amplification process can be increased by utilizing higher thermal ramp rates, point-of-care PCR analysis may eventually lead to earlier diagnosis of viral diseases and more efficient patient monitoring.

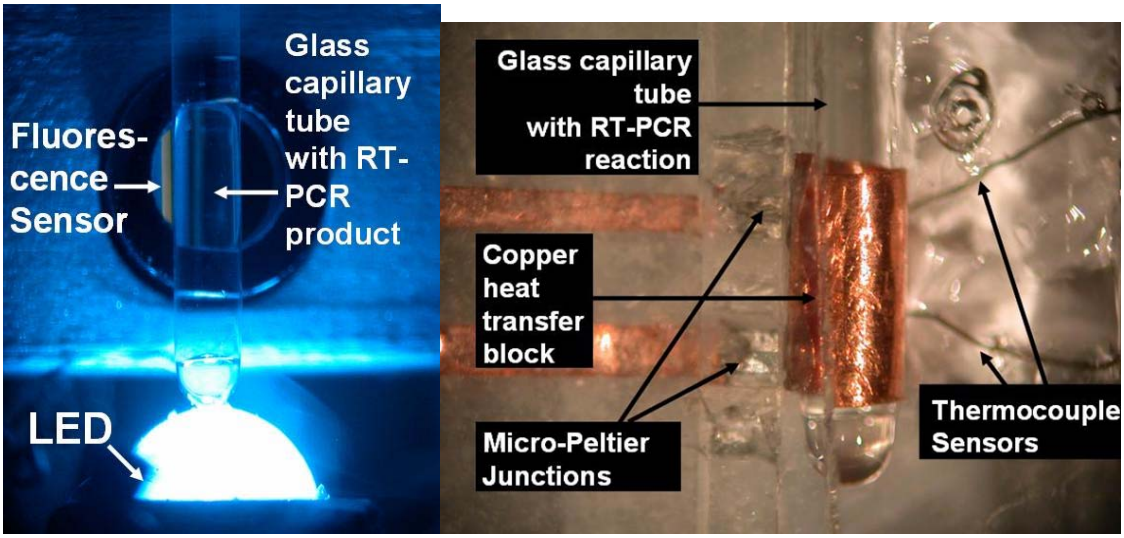

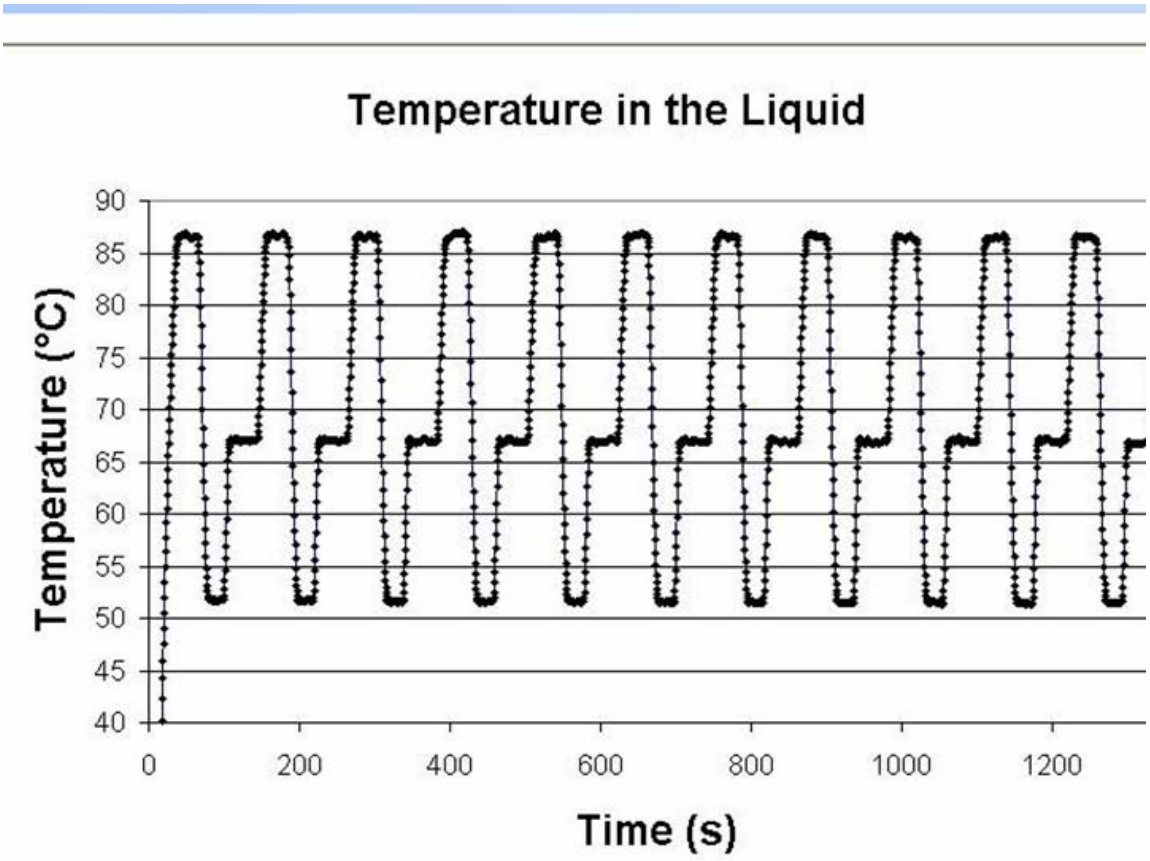

Figure 1A. Picture of a portable PCR system showing the Peltier junctions for high-rate heating and cooling
Figure 1B. Photograph taken of the portable PCR system during operation with a blue InGaN LED and a silicon photo-detector
Figure 1C. Thermal ramping curve displaying temperature measured inside of a 20uL capillary tube sample with a thermocouple during PCR amplification

Our effort is not the only one aimed at miniaturizing PCR systems. In alternative approaches [14-16], the analyte and primer are pumped over heaters within microfluidic channels to perform annealing, extension and denaturing of DNA [17-21] have been demonstrated to result in PCR amplification. However, uncertainties in the time taken for DNA molecules moving from one temperature bath to another result in non-specific binding events and errors during the amplification process. This problem can be addressed by using immiscible solutions (oil and primer-target mixture) to ensure control over thermal ramping, or by cycling the entire microfluidic chip with relatively lower ramp speeds. In polymer systems, surface reactions and evaporation through the channel walls can lead to problems with the PCR reactions, especially at the high denaturing temperatures. Here, we avoid these problems by heating and cooling the primer/analyte mixture within well-characterized glass capillary tubes.

We have constructed a small and inexpensive RT-PCR system for the identification of virus strains. Our device heats and cools glass capillary tubes also used in real-time LightCycler (Roche Diagnostics, Mannheim, Germany) [7] instruments. The prototype system consisted of a Peltier junction controller along with coolers (Marlow Inc., Peltier elements) soldered to a copper heat-exchange jacket into which a glass capillary tube is inserted. The picture in

Figure 1A illustrates the illuminating light emitting diode, the chamber and silicon detector for fluorescence measurement. Figure 1B shows the programmable thermal cycling controller (model 5c7-197, by Oven Industries Corp) used to ramp the current passed through the Peltier elements and obtain temperature ramp sequences. This portable PCR system was constructed for $500 in parts.

A typical temperature ramp curve measured within the primer-sample mixture is shown in Figure 1C, and illustrates accurate thermal cycling with 0.1°C control over annealing, extension and denaturing temperatures. As the ramp rate typically determines the overall time for a PCR amplification, it is possible to reduce that time by ramping the Peltier coolers at above ~30°C/s and there is great potential for reducing the total time needed for PCR analysis below 20 minutes. In this paper, however, we apply the standard ramping recipes optimized for benchtop PCR systems. The high accuracy of the temperature reading in the primer-analyte mix also relies on a careful calibration of the system, and we use a thermocouple probe inserted into the solution within a micro-capillary tube for that purpose.

After temperature calibration, our portable PCR instrument was tested on real virus samples in a hospital. The sensitivity and selectivity of the portable PCR system were compared to desk-top PCR systems by performing

amplifications with standard primers, prepared as a batch and then aliquoted into two identical samples to be run on a LightCycler I desk-top system (Roche Diagnostics, Mannheim, Germany) and in our portable PCR system. Both products were examined by performing melting curves after amplification within the LightCycler instrument and compared by gel electrophoresis. All of the amplifications and measurements were conducted in triplicate. To prepare the specimens, 200 μl of plasma, whole blood, or cerebrospinal fluid (CSF) were prepared for extraction with a commercially available spin column. Then, DNA, RNA, or total nucleic acid were eluted from the column using 30-50 μl of elution buffer and one or two μl were mixed with an appropriate primer to perform the RT-PCR analysis.

H5N1 Birdflu: The potential for an international pandemic resulting from the H5N1 strain of avian influenza has recently caused great concern among policy makers in search of effective identification techniques. We therefore tested our portable PCR instrument on samples from H5N1 infected chickens to determine whether H5N1 outbreaks within the poultry industry could be identified. By using a previously optimized RT-PCR primer set and temperature profile, we first analyzed in vitro transcribed H5 gene RNA as positive control, and real H5N1 samples in infected

chicken samples. The following primer pairs were employed, with an amplicon size of 200 base pairs:

Forward primer: AtgCCCCAAATATgTgAAATCA and

Reward primer TTgTCTgCAgCgTACCCACTC

The thermal profiles used during amplification were 1200s at 61°C, 120s at 95°C, 45 cycles at 95°C/5s-53°C/15s-72°C/8s followed by 90s at 40°C. Several concentrations of H5N1 equivalent were amplified with our system to simulate the effects of different viral loads. Thermal cycling led to amplification after 45-65 cycles, depending on the concentration, and the resulting product was measured by running melting curves within the LightCycler instrument. Figure 2 shows melting traces of H5N1 chicken samples, comparing the derivative of the fluorescence signal as a function of the temperature for product from both Roche LightCycler and the portable PCR system (Figure 2A). The traces do not differ greatly, indicating a melting temperature of 62.9°C (+/-2.5°C). Close examination also reveals a reduced shoulder peak in the portable instrument that can be attributed to lower non-specific binding and primer-dimer interaction.

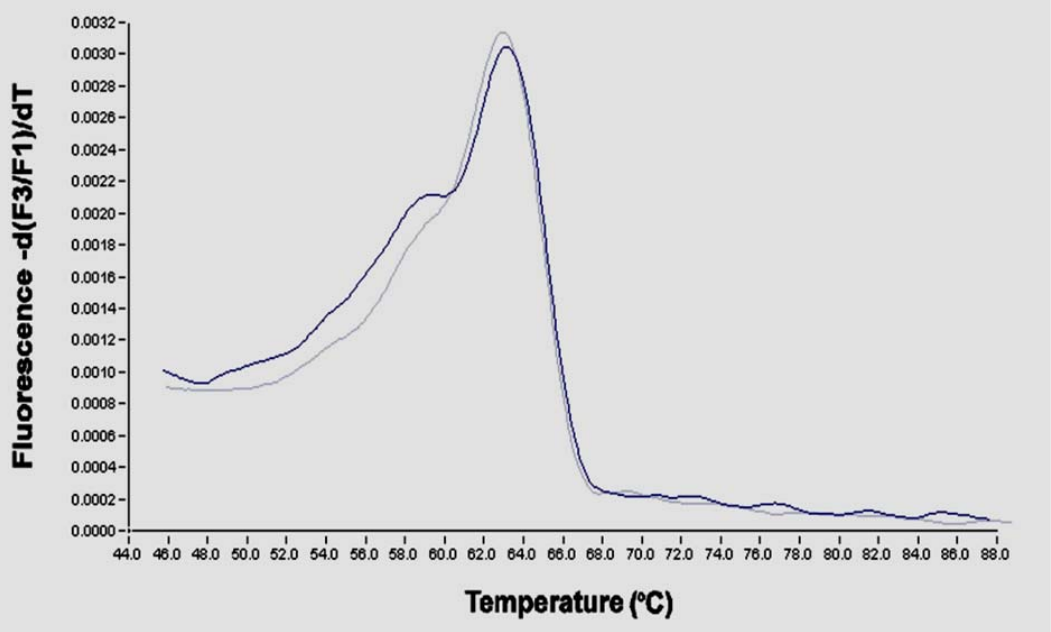

Figure 2A. Derivative fluorescence melting curves of H5N1 (Avian Influenza) amplified with 45 PCR cycles from chicken samples in the Roche LightCycler (black line) and portable PCR system (grey line).

HIV (AIDS): The effective treatment and prevention of HIV transmission relies on early detection, which could be offered through the introduction of inexpensive PCR testing within clinics throughout the world. PCR detection is the only method presently available to detect this disease only two weeks after infection. We investigated the amplification of blood samples containing AIDS at several viral loads with both PCR instruments by using the following RT-PCR primer set:

Forward Primer: TCAgCCCAgAAgTAATACC

Reward Primer: gCAgCTTCCTCATTgAT

with amplicon size of 150bp. The temperature profile consisted of 1800s at 60°C, 120s at 95°C, 65 cycles at 95°C/5s-50°C/15s-72°C/7s followed by 90s at 40°C. Of course,

as the viral load is reduced, more cycles have to be completed before amplification is observed. A typical set of melting curves for very dilute viral loads is shown in Figure 2B, after 65 thermal cycles. From this data, the DNA melting temperature measured from both PCR systems are similar, leading to a measured melting temperature of approximately 56.0°C (+/-2.5°C). As the treatment of patients with fairly expensive drug cocktails often varies from patient to patient, it is also of benefit to be able to monitor viral loads of patients by frequent measurements during treatment, and we find that the ultimate sensitivity of both instruments is similar by exploring the lowest limits of the viral load.

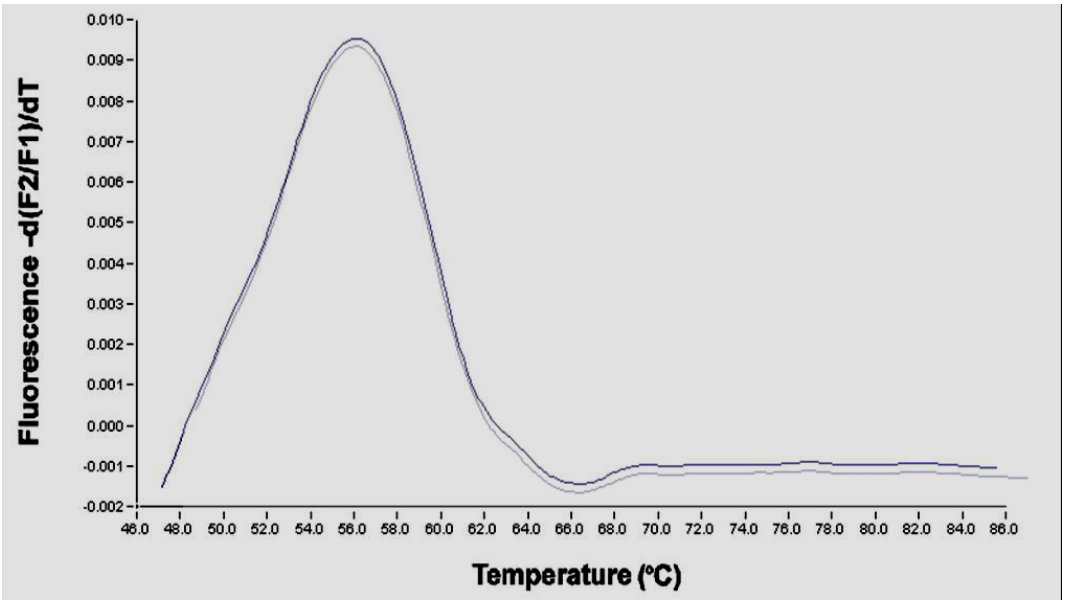

Figure 2B. Derivative fluorescence melting curves of HIV (AIDS) amplified with 65 PCR cycles from human blood sample in the Roche LightCycler (black line) and the portable PCR system (grey line)

Hepatitis B (HBV): To confirm that our PCR instrument can be used to amplify both DNA and RNA virus samples, we

performed amplification experiments on HBV, a common DNA virus. Again, inexpensive detection methods for Hepatitis B could lead to effective monitoring of this common disease. Human blood samples containing the Hepatitis B virus were amplified within the LightCycler and our system using the following PCR primer set:

Forward primer: TACTAgTgCCATTTgTTCAgTgg

Reward primer: CACgATgCTgTACAgACTTgg

with amplicon size of 100bp. In this amplification procedure, the temperature profile consisted of 600s at 95°C, 45 cycles of 94°C/10s-64°C/10s-72°C/30s followed by 30s at 75°C and 30s at 40°C. Figure 2C shows the melting curves of samples amplified in the benchtop and portable systems, respectively, after 45 cycles. The melting temperature was measured to be 79.6°C (+/- 3.0°C).

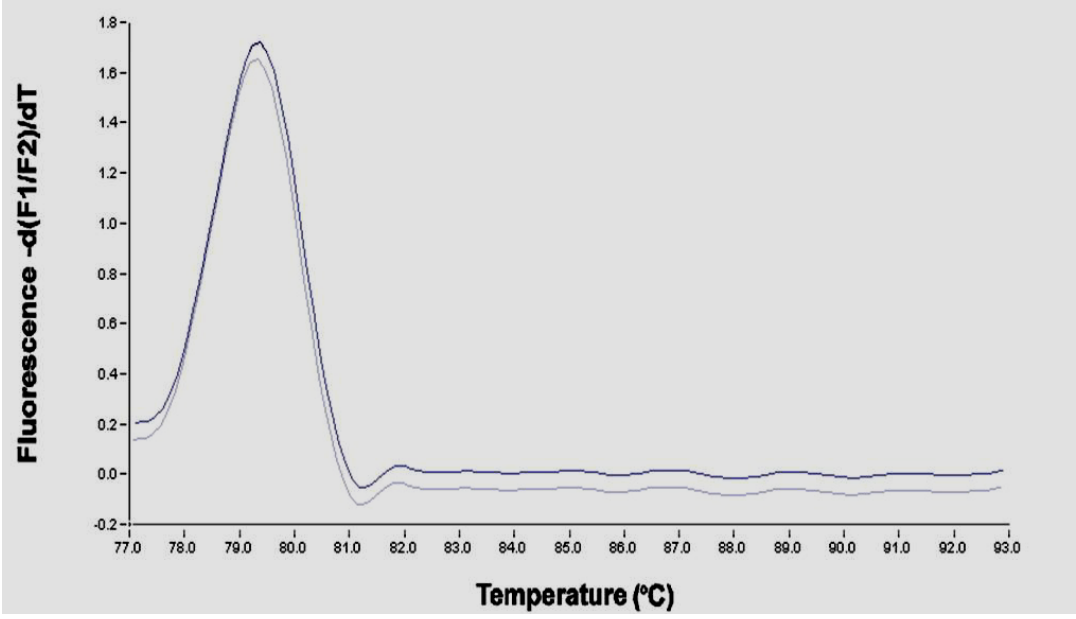

Figure 2C. Melting curves of HBV (Hepatitis B) amplified with 45 PCR cycles from human blood sample in the Roche

LightCycler (black line) and the portable PCR system (grey line)

Herpes Simplex I and II (HSV): We demonstrate that the portable PCR system is also able to amplify and genotype two or more virus strains within the same sample by testing human cerebral spinal fluid containing both HSV-I and HSV-II strains. After 45 cycles of amplification using a commercially available PCR primer set (LightCycler HSV ½ Detection Kit LightMix reagent TIB MOLBIOL GmbH, Eresburgstrasse, Berlin) with amplicon size of 200bp and temperature profile of 600s at 95°C, 45 cycles of 95°C/10s-55°C/15s-72°C/15s followed by 40°C/90s, When melting curves of the amplified samples were measured, two peaks appeared in the melting curves at 54.0°C (+/-2.5°C) and 67.2°C (+/-2.5°C). These peaks correspond to HSV-I and HSV-II (Figure 2D). The ability to distinguish these two peaks indicates that our system can amplify dual or co-infection of viruses within the same sample. Rapid diagnosis with good selectivity between these two common diseases could prevent the spread of HSV-I and II and avoid associated complications.

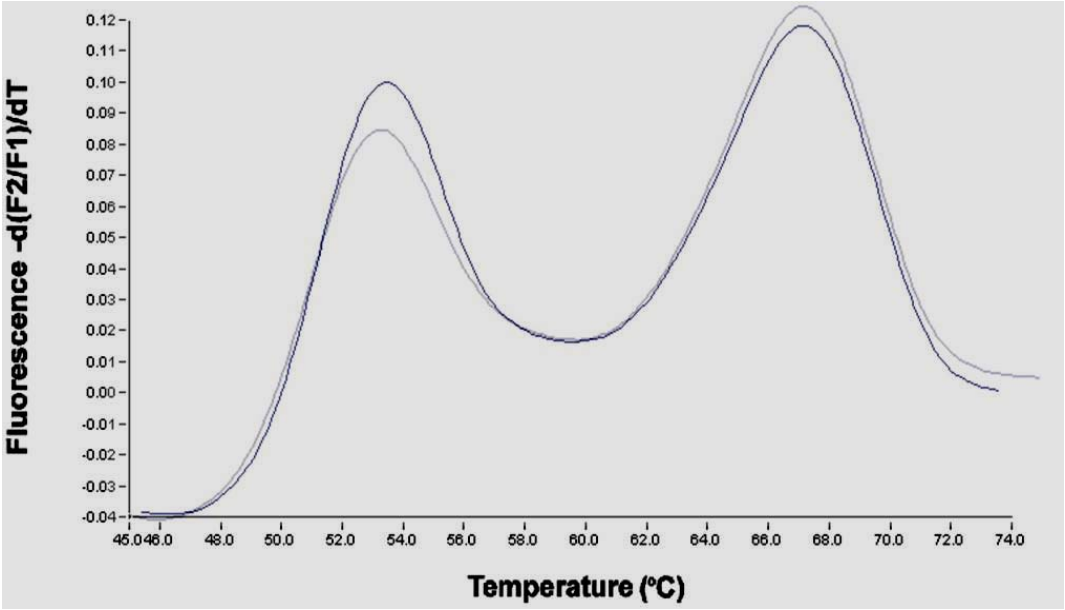

Figure 2D. Melting curves of HSVI and HSVII (Herpes Simplex) mixture from human blood sample with 45 PCR cycles in the Roche LightCycler (black line) and the portable PCR system (grey line)

Cytomegalovirus (CMV): This is another common member of the herpes virus family that is time-consuming to diagnose with antibody tests. We amplified CMV in human blood samples within the following primer set:

Forward primer: gCACCATCCTCCTCTTCCT

Reward primer: ggCCTCTgATAACCAAgCC

and amplicon size of ~380bp. The temperature profile consisted of 720s at 95°C followed by 45 cycles of 90°C/2s-65°C/5s-72°C/10s followed by 75°C/30s-40°C/30s. Figure 2E shows comparative melting curves of amplified products after 45 PCR cycles, generated by the LightCycler and the portable system, with melting temperature of approximately 85.8°C (+/- 3.0°C).

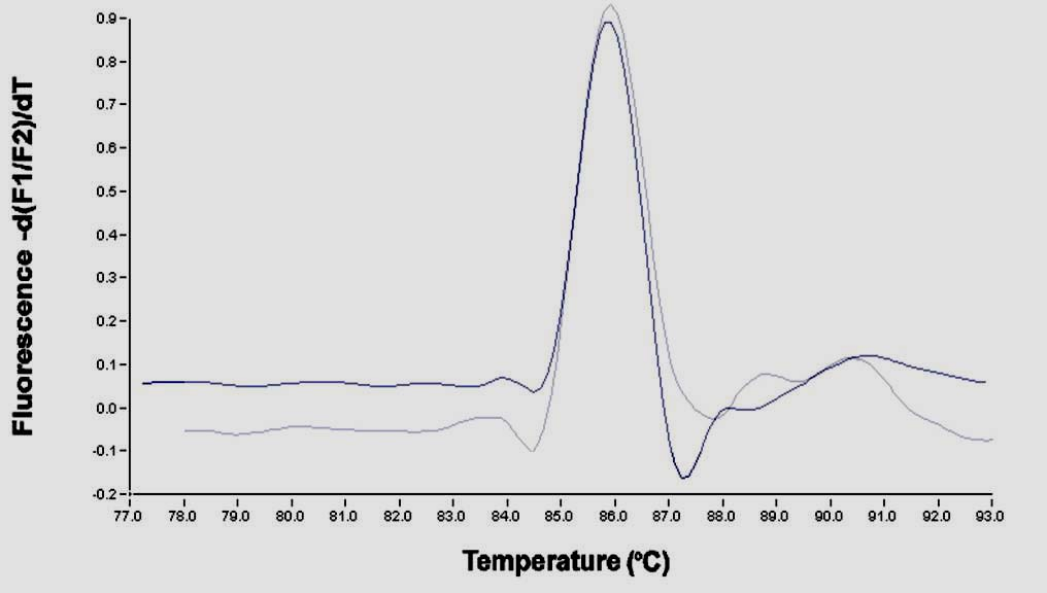

Figure 2E. Melting curves of CMV (Cytomegalovirus) from human blood sample with 45 PCR cycles in the Roche LightCycler (black line) and the portable PCR system (grey line)

Careful analysis of the negative control sample during the CMV test reveals one of advantages of our more compact system when using intercalating dye probes such as SYBR Green I (FastStart SYBR green kit; Roche Diagnostics, Mannheim, Germany) rather than more expensive FRET (Fluorescent Resonance Energy Transfer) probes. In the negative control amplified with the Roche LightCycler system, a modest primer-dimer peak at 80.7°C is observed after amplification, whereas no such peak appears in the miniaturized system (Figure 3). The avoidance of such "false" peaks, also found in the HBV negative samples, suggests that both speed and accuracy of amplification were significantly improved when using our Peltier design in the PCR reactor. The lower thermal mass of the portable PCR system results in a higher precision and smaller thermal

gradients within the capillary tube. Eliminating the SYBR Green I fluorescence signal in negative control samples reduces the risks of false positive identification and opens the door to the confident use of intercalating dyes for human virus diagnostics.

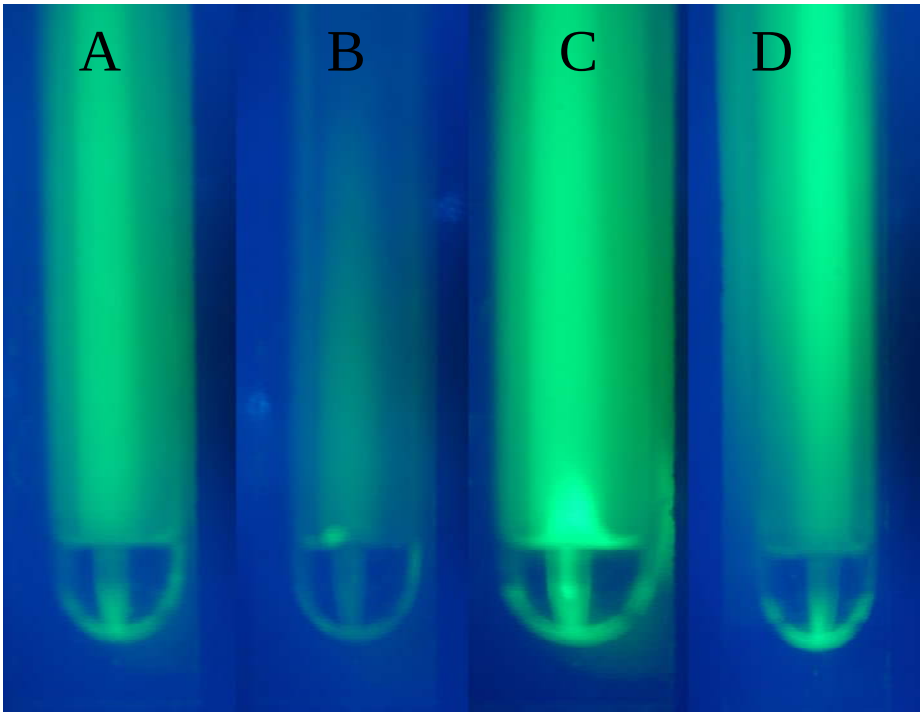

Figure 3A-D Fluorescence images of CMV capillary tubes with SYBR-green fluorophore-primer showing (A) Positive CMV sample portable unit, (B) Negative control portable unit, (C) positive CMV sample LightCycler (D) Negative control LightCycler

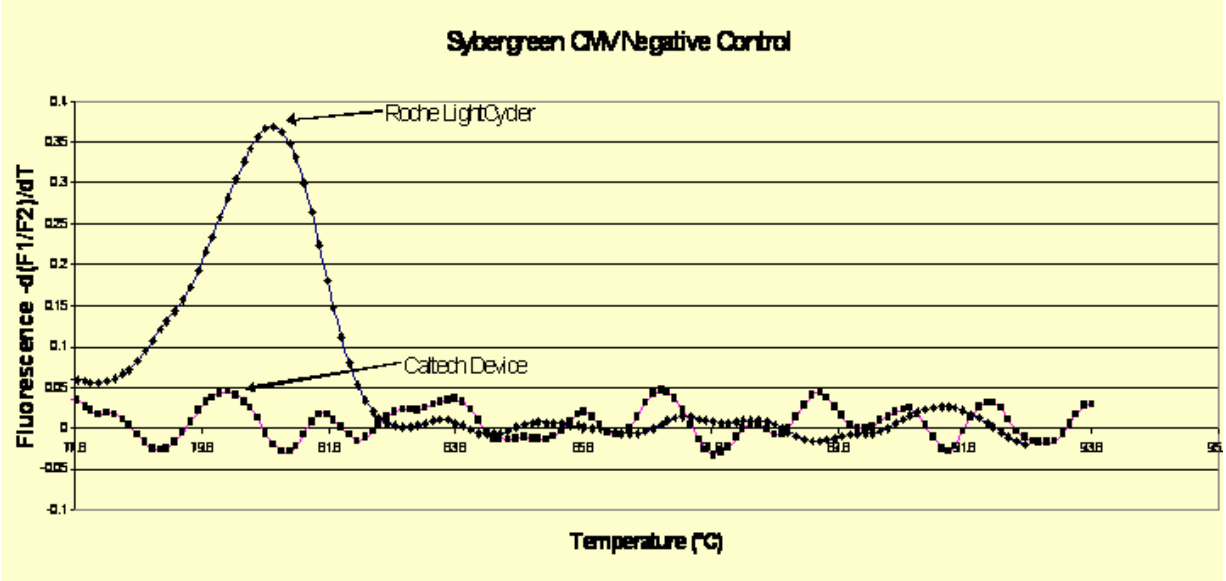

Figure 3E. Melting curve of negative control for CMV using SYBR-green dye. The LightCycler fluorescence is compared with the signal from the portable unit described in the text

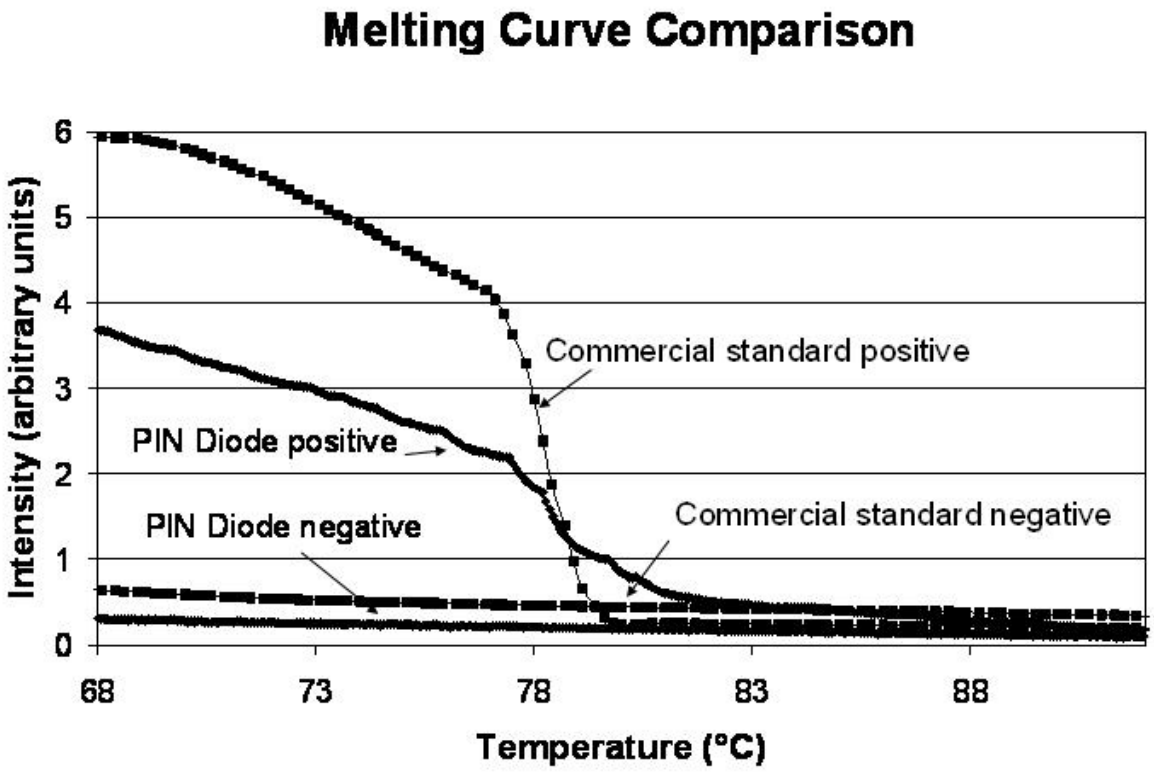

Figure 4. Melting curves taken with (a) commercial instrument, (b) Silicon p-n diode replacement of the commercial photomultiplier

Real-time fluorescence monitoring and melting curve measurements were also conducted in the portable device (Figure 5). During the amplification process, the fluorescence intensity of the sample-primer mixture was measured and recorded. As long as false-positive intensity readings from primer-dimer formation can be avoided, real-time measurements can be used for the rapid screening for virus infection in a sample. Real-time measurements also

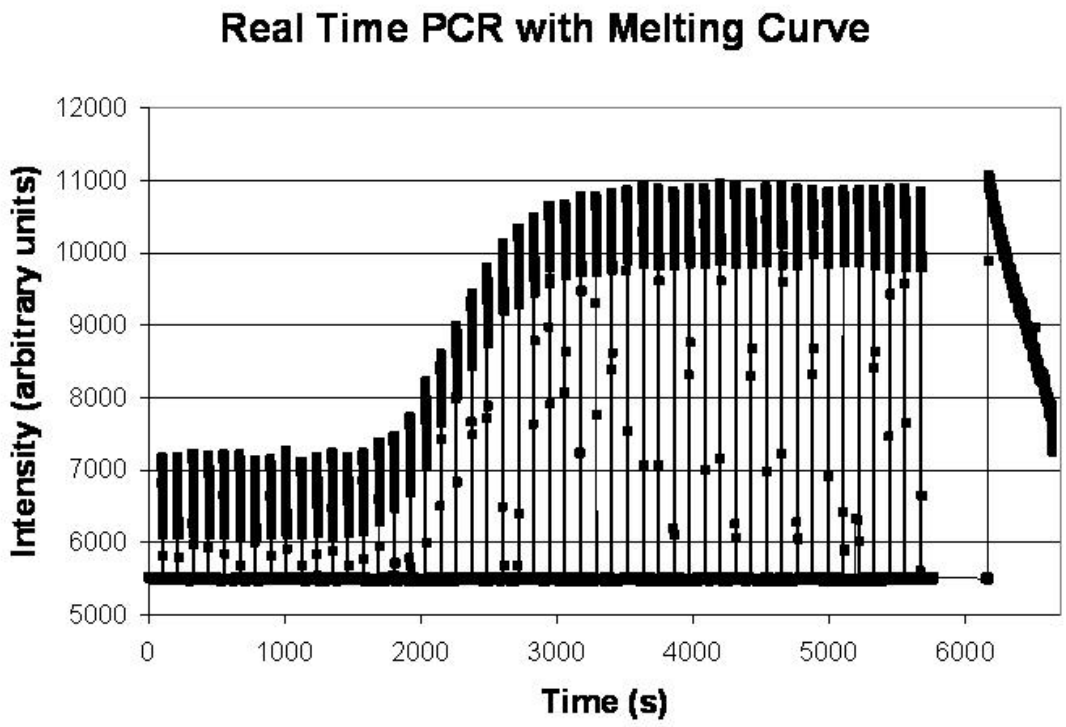

Figure 5. Real-time fluorescence monitoring system showing the amplification of Lentivirus DNA

provide information on the viral load or the concentration of DNA or RNA within the primer/viral nucleic acid target mixture, as the number of cycles before the onset of significant fluorescence can be recorded and compared. After integration of a InGaN LED light source and a photodetector within our PCR instrument, real-time measurements were obtained (Figure 5). The intensity of the fluorescence intensity of the amplicon is observed to increase after approximately 14 cycles. The performance of photomultiplier and silicon PIN photodiode detectors were compared for intensity monitoring, and we find that solid state detectors

provide an adequate solution for real-time measurement of typical fluorescent signal during PCR amplification.

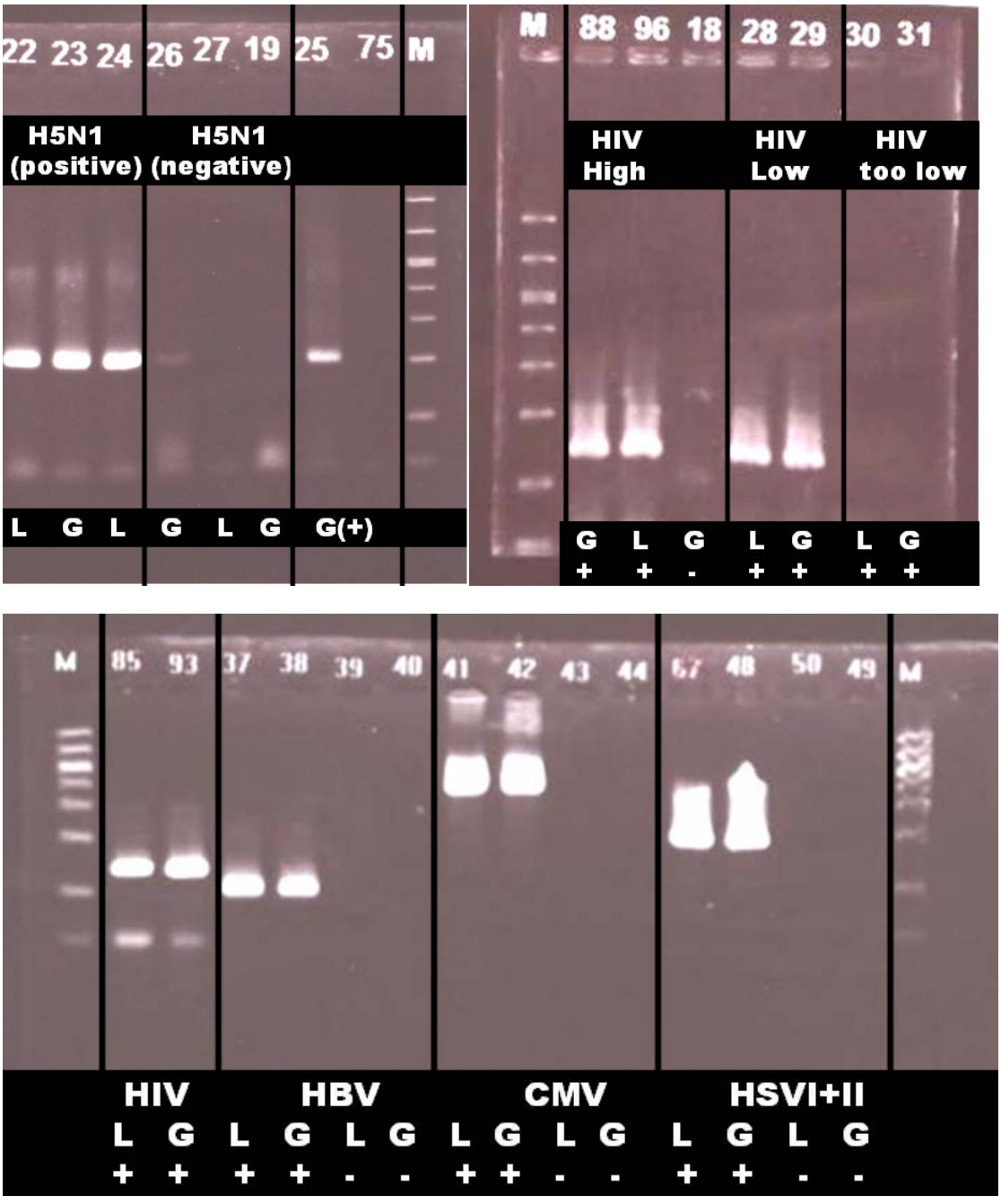

Figure 6. Electrophoresis plates with agarose gel showing the fluorescence signal from the amplified products. Measurements of amplified product generated in the light-cycler are denoted with an L, whereas product generated in the portable device (+) indicates a positive sample containing the specified virus whereas (-) denotes a negative controls experiencing the same ramping procedure.

Vertical lines were included to separate the electrophoresis columns to guide the eye.
Figure 6A. H5N1 virus positive and negative gel electrophoresis tests on chicken samples.
Figure 6B. HIV sensitivity tests for different viral loads ranging from very low to high
Figure 6C. Gel electrophoresis confirmations of amplified product for other viruses

Our melting curve measurements were accompanied by agarose gel electrophoresis data on the amplified PCR product, and the PCR melting curves from all of the virus strains matched well with gel electrophoresis panels, summarized in Figure 6. Similar tests were run on negative samples with no false positive results in the gel electrophoresis measurements.

The most significant advantage of miniaturization is the obvious reduction in the thermal response time as the thermal mass of a PCR reactor is reduced. Miniaturized systems can heat and cool 20 μl samples at ~30°C/s ramp rates, and smaller sample volumes lead to further rate increases. Fast ramping reduces the overall time required for the PCR amplification process from hours to minutes, and improves the feedback control over the temperature. However, the advantage of reducing analyte volumes must be carefully weighed against the problem of amplifying samples containing dilute viral loads.

As at least a single RNA virus must theoretically be present for successful amplification, it is desirable to work with larger sample volumes for improved sensitivity. 10-20 μl

constitutes a good compromise for current PCR systems and 20 μl volumes were used in this study. We note that if low viral loads are expected from a sample, some concentration of the sample can be accomplished by using a combination of high speed centrifugation (of 1ml samples) to pack the viral particles in the blood sample, and permitting the rest of the sample to be decanted. Smaller volumes (~0.1ml) of buffer can be added, resulting in a reduction of the final reaction mixture volume after spin column extraction from 20 μl to 5-10 μl. 7-10 μl of PCR/RT-PCR reaction mixture are typical for many routine PCR or RT-PCR viral assays, whereas for SNP detection, only 3 μl are needed.

We have described a portable PCR system with highly precise temperature control and thermal cycling speed, and demonstrated the identification of several important viruses with this system. When automatic sample preparation system are integrated with this RT-PCR instrument, low-cost and rapid PCR amplification will lead be possible for medical diagnostics, livestock monitoring and forensic testing.

References

[1] Saiki, R, Scharf, S., Faloona F., Mullis, K., Horn, G., Erlich, HA, and Arnheim N. Science, 230, (1985), 1350,

[2] Saiki, RK, Bugawan, TL., Horn, GT, Mullis, KB, Erlich, HA, Nature 324, (1986), p163/ Mullis, KB, Faloona, FA "Specific synthesis of DNA in vitro via a polymerase catalyzed chain reaction, Meth. Enzymol., (1987), 155, p335-351

[3] Erlich, H. A., *PCR Technology,* Stockton Press, New York, 1989, pp.1-5.

[4] Edwards, K, Logan, J, Saunders, N., editors, "Real-time PCR - An essential guide", Horizon Bioscience, Wymondham, Norfold, UK

[5] Higuchi, R., Dollinger, G., Walsh, PS. And Griffith R. "Simultaneous amplification and detection of specific DNA sequences", Biotechnology (NY), 10, (1992), p413-417

[6] Higuchi, R., Fockler, C. Dollinger G., and Watson, R., "Kineticc PCR analysis: real-time monitoring of DNA amplification reactions", Biotechnology (NY), 11, (1993) p1026-1030

[7] Wittwer, CT, Ririe, KM., Andrew, RV, David, DA, Gundry, RA, Balis, UJ, "The LightCycler: a microvolume multisample fluorimeter with rapid temperature control", Biotechniques, 22, (1997), 176-181

[8] Northrup, MA. Benett, B., Hadley, D., Landre, P., Lehew, S., Richards, J. and Stratton, PA, "A miniature analytical instrument for nucleic acid acids based on micromachined silicon reaction chambers,", Anal. Chem., 70, (1998), p918-22

[9] Belgrader, P, Benett, W., Hadley d., Long, G., Mariella, R., Milanovich, F, Nasarabadi, S., Nelson, W., Richards, J., and Stratton, P. "Rapid pathogen detection using a microchip PCR array instrument", Clin. Chem. 44, (1998) p2191-4

[10] Wittwer, CT Reed, GH, Gundry CN, Vandersteen, JG, Pryor, RJ, "High resolution genotyping by amplicon melting analysis using lCGreen, Clin. Chem., 49 (2003), p853-860

[11] Simpson D, Crosby RM, Skopek TR, "A method for specific cloning and sequencing of human hprt cDNA for mutation analysis, Biochem. Biophys. Res. Commun., 151, (1988), p487-492

[12] Vrieling H Simons JW, van Zeeland AA, "Nucleotide sequence determination of point mutations at the mouse HPRT locus using in vitro amplification of HPRT mRNA sequences, Mutat. Res., 198, (1988), p107-113

[13] Enserink, M, "Veterinary scientists shore up defenses against birdflu", Science, Vol 308, (April 2005) p341

[14] Nature pandemic paper

[15] Kopp, M. U., de Mello, A. J., Manz, A., *Science* 1998, *280*, 1046–1048.

[16] Quake, S. R., Scherer, A., *Science* 2000, *290*, 1536–1540.

[17] Chou, H. P., Unger, M. A., Scherer, A., Quake, S. R., *Biomed.Microdevices* 2001, *3*, 323–330.

[18] Chou, H. P., Unger, M. A., Scherer, A., Quake, S. R., *Proceedings of the Solid State Actuator and Sensor Workshop*, Hilton Head, S.C. 2000.

[19] Dabiri, D., Gharib, M., *Experim. Fluids* 1991, *11*, 77–86.

[20] Burns, M. A., Johnson, B. N., Brahmansandra, S. N., Handique, K.,Webster, J. R., Krishman,M., Sammarco, T. S.,Man, P. M., Jones, D., Heldsinger, D., Mastrangelo, C. H., Burke, D. T., *Science* 1998, *282*, 484–487.

[21] Woolley, A. T., Hadley, D., Landre, P., deMello, A. J., Mathies, R. A., Northrup, M. A., *Anal. Chem*. 1996, *68*, 4081–4086.

[19] Hong, J. W., Fujii, T., Seki, M., *Electrophoresis* 2001, *22*, 328–333.

[20] Legally, E. T., Mathies, R. A., *Anal. Chem.* 2001, *73*, 565–570.

[21] Belgrader, P., Benett, W., Hadley, D., Richards, J., Stratton, P., Mariella, R., Milanovich, F., *Science* 1999, *284*, 449–450.

[22] Khandurina, J., Mcknight, T. E., Jacobson, S. C., Waters, L. C., Foote, R. S., Ramsey, J. M., *Anal. Chem.* 2000, *72*, 2995–3000.

[23] Chiou, J., Matsudaira, P., Sonn, A., Ehrlich, D., *Anal. Chem*.2001, *73*, 2018–2021.

[24] Nakano, H.,Matsuda, K., Yohda, M., Nagamune, T., Endo, I., Yamane, T., *Biosci. Biotechnol. Biochem.* 1994, *58*, 349–352.

[25] Chaudhari, A. M., Woudenberg, T. M., Albin, M., Goodson K., E., *J. Microelectromech. Syst.* 1998, 7, 345-355.

[26] Protocol of TaqMan PCR Reagent Kit with AmpliTaq Gold DNA Polymerase, 2001, Applied Biosystems. http://www.appliedbiosystems.com.

[27] Ibrahim, M. S., Lofts, R. S., Henchal, E. A., Jahrling, P.,Weedn, V. W., Northrup, M. A., Belgrader, P., *Anal. Chem*.1998, *70*, 2013-2017.

[29] Gordon, F. B., *Immobilization of Enzyme and Cells*, Humana Press, Totowa, NJ 1997. 1536 J. Liu *et al.* *Electrophoresis* 2002, *23*, 1531-1536